EQUAL CHANNEL ANGULAR PRESSING OF ELEMENTAL & ALLOYED P/M ALUMINIUM SYSTEMS

by

NICHOLAS HARRISON

A thesis submitted to
The University of Birmingham
For the degree of
DOCTOR OF PHILOSOPHY

Department of Metallurgy and Materials
The University of Birmingham
May 2014

PREFACE

The experimental work described in this thesis was carried out by the author in the School of Metallurgy and Materials at the University of Birmingham, from October 2008 to January 2014 under the supervision of Dr. Isaac Chang.

The material presented here is original and none of it has been submitted for a degree at the University of Birmingham or any other academic establishment. Where information has been drawn from other published works by other authors, it has been acknowledged and cited according to the numbered referencing format at the end of the document.

This thesis includes preliminary work presented at the PM2010 Powder Metallurgy World Conference & Exhibition in Florence, Italy, 2010 as:

"Harrison, N., Chang, I.T.H. (2010) *Consolidation of Elemental Aluminium Powders using Equal Channel Angular Pressing (ECAP),* **PM2010 World Congress on Powder Metallurgy, Florence, 10-14 October 2010**."

These results were also published as a paper in the **PM2010 World Congress Proceedings Volume 1, p 565-572, ISBN: 978-1-899072-10-1.**

Two journal papers based on the results from Chapter 4 are in preparation.

ACKNOWLEDGMENTS

I would like to acknowledge Dr. I. T. H. Chang for his supervision throughout the PhD and my co-supervisor Dr. Yu Lung Chiu. I am grateful for the provision of the facilities to carry out the work at the University of Birmingham and funding by Professor Paul Bowen and the EPSRC respectively.

I would like to thank all the technical staff in the School of Metallurgy and Materials at the University of Birmingham for their assistance: Mr. Mick Cunningham; Miss Avril Rogers; Mr. Jaswinder Singh; and all the staff of the Centre for Electron Microscopy.

Finally, I am indebted to my friends; Mark Blevins, Soroosh Bagheriasl, Praveen Ramakrishnan, Claire Wait, Kyle Burrows, Kylie Owen, Luke Hughes, Rich Wyse, Richard Sheridan, Andy Ward, Peter Squire, Josh Vines, Lydia Pickering, Laura Witherden, Edward Labuschagne, Ian Congdon, Jitin Verma, Lucian Falticeanu, Caragh King, Casey Brown and to my family for their support and encouragement, which helped me to persevere throughout my time in Birmingham.

SYNOPSIS

Aluminium powder metallurgy finds increasing use in automobile and aerospace applications, such as low friction bearing alloys, due to the use of lightweight parts for reduced energy consumption. Conventional press-and-sinter methods are used to produce dense components although porosity issues remain, which have a debilitating effect on strength, hence appropriate alloying additions need to be considered to optimise sintering. Severe plastic deformation via Equal Channel Angular Pressing (ECAP) can be applied to green compacts or pre-sintered samples to achieve full densities and refine the microstructure to improve strength of powder metallurgical (P/M) aluminium alloys.

Sintering of aluminium powder is difficult due to the surface oxide layer preventing adequate contact between neighbouring particles for the densification mechanisms to occur. Therefore a liquid phase needs to be present to assist with sintering processes. In this thesis, solid state sintering of pure aluminium and liquid phase sintering of an Al-Sn bearing alloy were analysed in collaboration with industrial support. Furthermore, the use of room temperature ECAP to produce fully dense parts from these sintered materials was investigated. The microstructure, density, and hardness of samples were characterised as a function of sintering time and ECAP processing conditions. This provided an understanding of the effect of processing conditions on the resultant microstructure (e.g. grain size, porosity level, type/amount of phases) and properties (hardness).

Cold compaction produced a non-uniform distribution of density with a more porous region on the outside of the samples as a result of increased friction at the die wall surface.

Solid state sintering of pure aluminium powders is not effective due to the oxide layer preventing adequate particle to particle contact. However, the application of ECAP to green and sintered pure aluminium samples induced severe plastic deformation and broke down the oxide layer, exposing fresh surfaces of particles to be in contact with each other and work hardened the grains. This caused elongation in the longitudinal section and a relatively equiaxed microstructure in the transverse section. The grains were refined from 160.77μm to 118.57μm while density and hardness were increased by 4% and 200% respectively after ECAP processing of sintered pure Al samples.

For the Al-Sn bearing alloy material, sintering at or below 10 hours gave a poor response as the liquid tin is unable to wet the aluminium. Instead it forms at the grain boundaries, weakens the material and does not increase the density or homogenise the microstructure. After ECAP of the sintered samples, density and hardness improved and aluminium grain sizes were refined with the formation of two distinct regions; a denser, deformed core region and a non-deformed skin region. The core region had tin whiskers protruding from the surface and the skin region showed pore closure.

LIST OF ABBREVIATIONS

Abbreviation	Meaning
ECAP	Equal Channel Angular Pressing
SPD	Severe Plastic Deformation
P/M	Powder Metallurgy
SEM	Scanning Electron Microscopy
EDX	Energy Dispersive Microanalysis
MPIF	Metal Powder Industries Federation
EBS	Ethylenebisstearamide compounds
UFG	Ultra-Fine Grains
LAGB	Low Angle Grain Boundaries
HAGB	High Angle Grain Boundaries
EBSD	Electron Back-Scatter Diffraction
CIP	Cold Isostatic Pressing
BP	Back Pressure
T-ECAP	Torsional Equal Channel Angular Pressing
FE-ECAP	Forward Extrusion- Equal Channel Angular Pressing
AlPoCo	Aluminium Powder Company
SEI	Secondary Electron Imaging
BSEI	Back-Scatter Electron Imaging
ECD	Equivalent Circular Diameter

CONTENTS

1. INTRODUCTION

1.1. Brief history of Powder Metallurgy (P/M)

After the Second World War, the use of P/M increased due to cost savings and production of net shape parts with close dimensional control and a series of press-and-sinter methods have been developed since. The pressing capacity has increased from a few tonnes to several thousand tonnes and better sintering furnaces have allowed a precise control of sintering temperatures and atmospheres, which has led to advancement in P/M techniques [1, 2].

The development of P/M parts using new powders, improved compaction presses, sintering furnaces and post-sintering treatments are areas of high interest in modern P/M research. It has been shown that P/M can be used to achieve comparable tensile properties, hardness and aging response to a high performance wrought alloy, for example, AA4032 (Al-12.2Si-1Mg-0.9Cu-0.9Ni) [3].

More recently, P/M components are used in the automotive industry in applications such as pistons, belt pulleys, pump gears and connecting rods. A significant development of P/M was the self-lubricating bearing, where the network of pores is filled with lubricating oil, which takes up 20-25% of the total volume [2].

1.2. The principles of P/M

The term ‘powder metallurgy’ refers to the process of converting metallic powders to a useful shape via various means of consolidation into semi-finished or finished products. Semi-finished products can be further treated by sintering or additional consolidation techniques until a finished part is reached [4, 5]. Basic steps in the traditional process involve producing the powder, compaction into an appropriate pre-form and sintering, which involves “heating the pre-form to a temperature below the melting point of the major constituent”, or additional deformation, as shown in Figure 1.1 [4, 6-8].

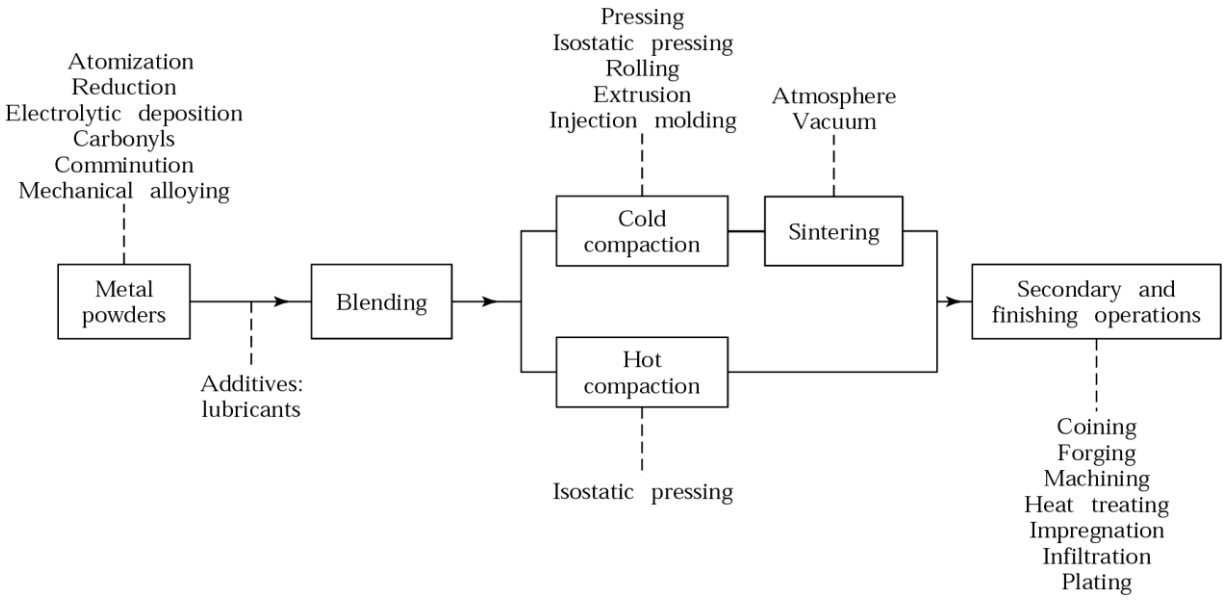

Figure 1.1: The process of powder metallurgy from start to finish [6, 7].

1.2.1. The conventional PM process

The first step is powder production, followed by blending with or without lubricant, where commercially pure elemental powders are blended together to give the desired alloy, described in more detail in section **2.1**. The powders used to generate the alloy can either be commercially pure elemental powders or master alloys, which are composed of two or more elements. Another type of particle available is pre-alloyed powder, where the composition of the particle is the same throughout and can reduce the need for blending, thus saving time. However, the pre-alloyed powder can be more expensive to produce compared to commercially pure powders and is more difficult to compact.

Also at this stage, sieving and other processes are used to precisely control the size of the particles, an important consideration for the way in which the powders flow and fill the die, described in more detail in section **2.1.5** [4, 9].

The next stage of the process is compaction using specially designed die sets to produce a green compact that has sufficient strength to be handled. In section **2.2**, consolidation techniques are described that have been developed to optimise consolidation so that better properties can be achieved at the compaction stage [4, 9].

The samples are then subject to sintering in a controlled atmosphere, at a specific heating rate, temperature and holding time to metallurgically bond the powder particles together, which gives the required physical and mechanical properties, explained in more detail in **2.3** [4, 9].

Sintering and heat treatments are usually the final stage of the P/M process. However, the properties can be further enhanced by using severe plastic deformation processing, such as Equal Channel Angular Pressing, ECAP. The sample is pushed through a die with a channel that bends between 60° and 160°, which can increase the density further and refine the grains by shear deformation [10-12]. The use of ECAP as a means to consolidate aluminium powders is described in more detail in section **2.5**.

1.2.2. Aluminium Powder Metallurgy

Aluminium powder metallurgy products are mainly used in automobile and aerospace applications due to the need for light weight parts to reduce energy consumption during operation of components [9, 13, 14]. Such applications include camshaft belt pulleys and bearing caps, shock absorber pistons, oil pump gears, sprockets and connecting rods [13-21]. Components that use aluminium P/M benefit from high mechanical and fatigue properties, corrosion resistance, thermal and electrical conductivity, excellent machinability and low density. These parts can be processed further to reduce the amount of porosity and improve the bonding of the particles so that the properties can be enhanced [9].

1.3. The benefits of using P/M

Powder metallurgy is mainly used in order to manufacture reliable net-shaped products and is very cost effective to produce parts, which are at, or close to, the final dimension as shown in Figure 1.2 [9, 22]. A component can be made with minimal scrap loss compared to casting processes as any powders that have not been consolidated can be re-used. The mechanical and physical properties can be modified by close control of the starting materials as well as the processing conditions and these properties can also be further improved by secondary processing operations such as heat treatments or mechanical means [9].

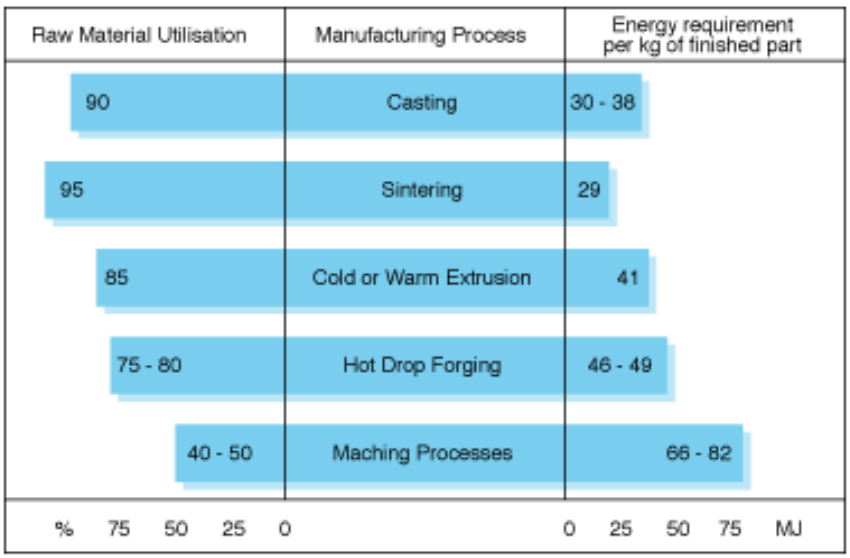

Figure 1.2: Raw material utilisation and energy requirements of conventional manufacturing processes compared to P/M (sintering) [22]

Porosity is the main problem associated with compacted powder components as this decreases the strength, density and ductility of the part. Local stresses build up at the pores, which act as sites for crack initiation leading to premature failure of the component [19, 23-25]. Techniques have been researched extensively such as sintering [26-28] and severe plastic deformation [10, 29] as a means to produce near full dense, high strength PM components in aluminium parts, which will be described in more detail in **2.3** and **2.5** respectively.

1.4. Aims and objectives of the PhD

This thesis aimed to explore the use of severe plastic deformation processing to produce fully dense Al components from powdered starting material; to understand the microstructural development during the ECAP process and; the relationship between microstructure and mechanical properties such as hardness.

The aims were achieved by applying ECAP at room temperature to uni-axially compacted and pre-sintered samples. Various aluminium powders ranging from pure aluminium to pre-alloyed Al-20Sn-7Si-1Cu bearing alloy were used in this study. The microstructure of the samples processed by ECAP were characterised using a combination of optical microscopy, Scanning Electron Microscopy (SEM), and Energy Dispersive Microanalysis (EDX) to quantify density, grain size, size distribution and confirmation of phases. The mechanical properties of these samples were determined using Vickers hardness.

2. LITERATURE REVIEW

2.1. Production of aluminium powders

The production method of the powder has a significant influence on the final product as it can determine particle size distribution, particle shape, size and surface oxide. Powders can be produced by solid state techniques, such as milling. They can also be produced by liquid state techniques such as atomisation. A brief description of mechanical milling is given in section **2.1.1** and atomisation processes in sections **2.1.2** to **2.1.3**.

2.1.1. Mechanical milling

Ball milling involves mechanically breaking solid metal into smaller particles of hard materials such as iron, beryllium and stainless steel [30]. Jars containing steel balls (12-16mm) and the metal are rotated at high speed for several hours and the subsequent collisions crush the metal into fine powder sizes, shown in Figure 2.1 [4, 31]. These collisions cause fractures, deformation and cold welding of the impacted particles [30, 32-34]. This process can be done in wet conditions using a surface-active grinding liquid, which reduces the surface energy of the particles and decreases particle size, although the fluid might contaminate the powders [35]. Ball milling can be used to produce ultrafine or nano-crystalline aluminium powders, where micron sized particles with nanometre grain sizes are formed, as well as producing composite powders such as carbon nanotubes in an aluminium matrix [36, 37].

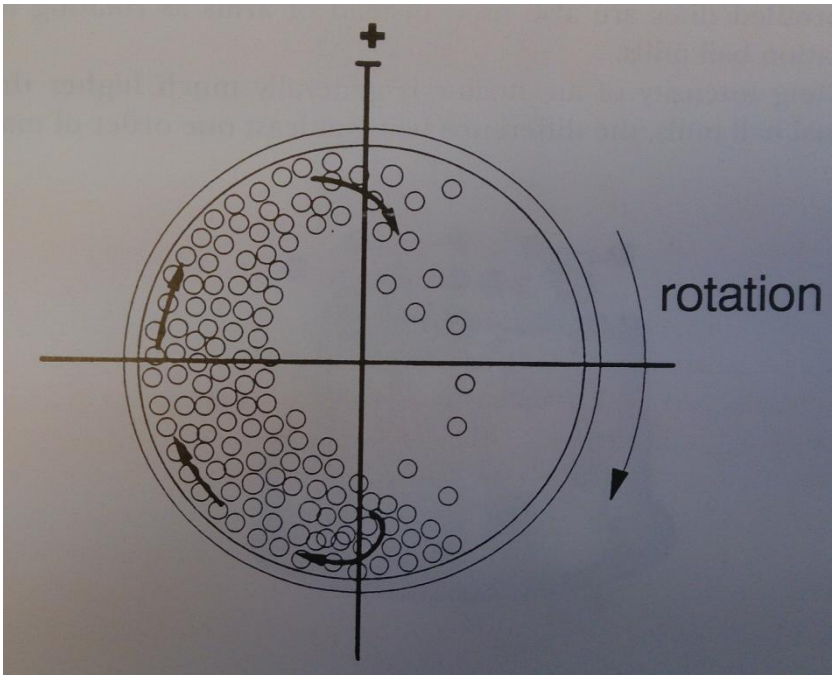

Figure 2.1: Ball milling procedure [4]

2.1.2. Gas atomisation

This is the most frequently used method for producing powdered aluminium alloys [38-41]. The process consists of using high velocity jets of non-inert gas (air) or inert gases (nitrogen, argon, helium) to disintegrate a molten stream of metal into powder particles, shown in Figure 2.2 [42]. The gas pressure ranges from 0.5MPa to 4MPa and velocity ranges from Mach 1 to 3. The other parameters that determine the shape and size of the solidified powders are shown in Table 2.1 [4, 38, 43]. The liquid stream is broken up by rapid gas expansion into a thin sheet that forms ligaments, which are further broken down into spheroids to minimise the surface energy, shown in Figure 2.3 [42]. The particles are separated from the gas by a cyclone separator.

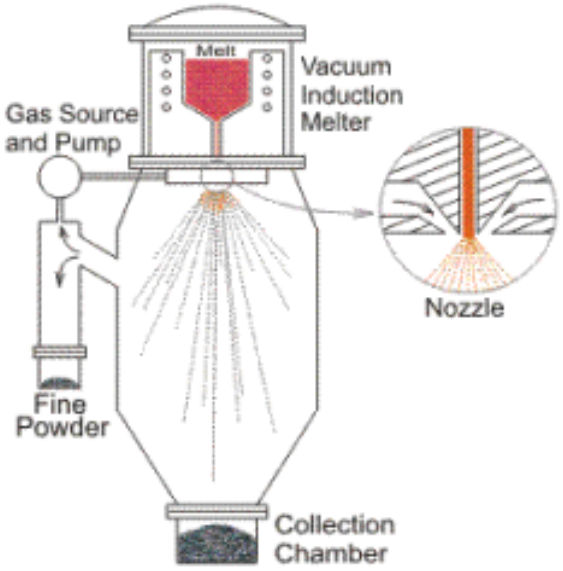

Figure 2.2: The gas atomisation process [42].

Table 2.1: The effect of the different parameters of water and gas atomisation on the particle size and morphology. A plus sign represents a direct relationship between particle property and a negative sign represents an inverse relationship. A zero indicates no strong relationship [38, 43].

Parameter	Mean particle size	Width of particle size distribution	Particle irregularity	Particle oxygen content (including air atomisation)
Melt viscosity	+	0	-	-
Melt surface tension	+	0	-	-
Melt stream diameter	+	+	-	0
Melt flow rate	+	+	-	0
Melt velocity	+	+	-	0
Water/gas flow rate	-	-	+	0
Water/gas velocity	-	-	+	+
Angle	-	0	+	+

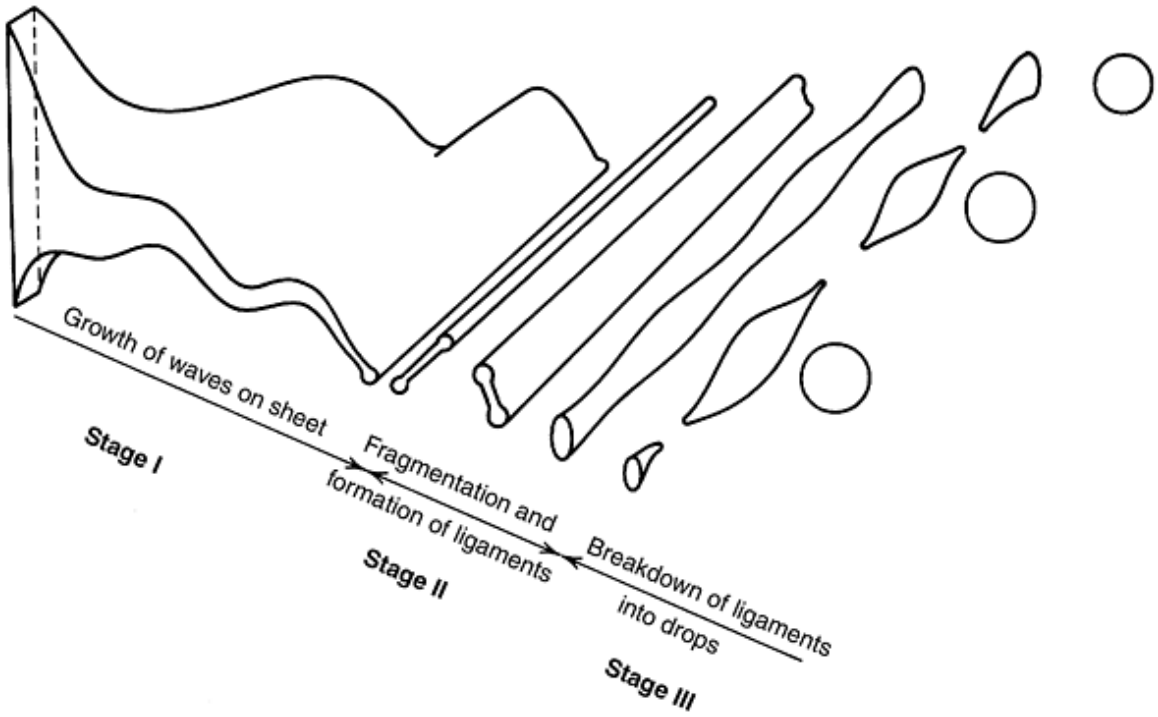

Figure 2.3: The three stages of break-up during atomisation [38].

A significant parameter that controls particle size is specific gas consumption, shown in equation (2.1):

$$\delta_m = KF^{-1/2} \qquad (2.1)$$

where; δ_m is the median diameter of the particle after atomisation; K is a function of alloy properties and design of the nozzle; and F is specific gas consumption, which is expressed as a ratio of gas volume to metal mass m^3/kg. Therefore, the median particle diameter can be decreased from approximately 250µm to below 50µm by increasing the mass-flow ratio of gas to metal from 0.3 to 2 respectively [39].

Generally, only spherically shaped particles are produced from gas atomisation when an inert gas is used and this tends to be used more for the production of aluminium alloys [4, 35, 44, 45]. However, when air is used for atomisation, the shape of the particles tends to be more irregular and the presence of oxide is observed resulting from the exposure of molten metal to air [4, 35, 44, 45]. Despite this, it was found that the oxide on aluminium alloys was similar to that formed from inert gas atomisation [46, 47].

2.1.3. Water atomisation

Similar to gas atomisation, the material is melted in a detached furnace, then fed into a funnel allowing a constant flow of liquid metal towards the chamber [44]. This liquid flow is shot at by water jets positioned at a variable angle to the downward flow of the melt and the resulting particles are collected at the bottom of the chamber as illustrated in Figure 2.4 [4]. The velocity of the water needs to be very high ($250ms^{-1}$) in order that the flow of metal can be suitably disintegrated.

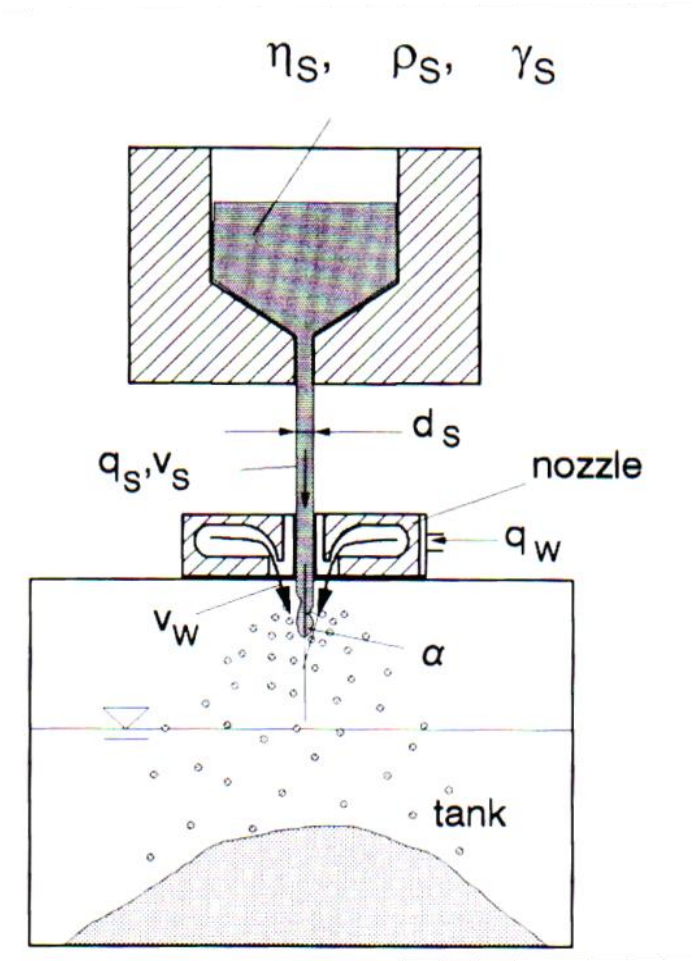

Figure 2.4: The water atomisation process [4]. The symbols in the image are as follows:

η_s – melt viscosity

ρ_s – melt density

γ_s – melt surface tension

d_s – melt stream diameter

q_s – melt flow rate

v_s – melt velocity

q_w – water flow rate

v_w – water velocity

α - angle between water jets and the metal stream

The degree of disintegration depends on the pressure and velocity of the water, the angle of the water jet to the melt flow, melt viscosity, melt flow diameter and density, shown in Table 2.1 [38, 48]. The pressure of the water jets is the main parameter that influences particle size. Generally, water pressures between 5MPa and 20MPa produce particle sizes between 30-150µm, which can be reduced to 5-20µm by increasing the pressure to between 50-150MPa [4, 38, 49]. Powders produced by water atomisation include iron, nickel and its alloys, copper and copper alloys and stainless steels, which are used in, for example, thermal spray coatings [4, 38, 49].

Although water atomisation is a cheaper atomisation process, powder purity and the irregular particle shape are the primary limitations, as well as oxygen contamination and formation of hydrated layers, meaning that time spent for degassing and drying is longer compared to gas atomisation [45, 50-53].

2.1.4. Particle analysis

Sieving and optical microscopy are commonly used to determine the size of powder particles [4, 35, 54, 55]. Although there are various other means of measuring particle size, only sieving and optical microscopy will be considered as these are widely used [54, 56-59].

Characterising particle size is difficult when powder particles are not spherical in shape [35]. The size of spherical powders can be defined using the diameter of the particle whereas other shape factors such as length, volume and mass are considered when determining non-spherical powders [35, 54]. For irregular particles, the 'equivalent diameter of a sphere or circle' is calculated from measurements in optical microscopy [35, 54, 55]. The main problem with referring to particle size in this manner is that the shape of the particle is not taken into consideration and different results can be seen for the same particle [35, 54, 55, 60]. There are many shapes that powders can form, which are shown in Figure 2.5 and these morphologies affect the way the powder flows during packing as described in section **2.1.5.**

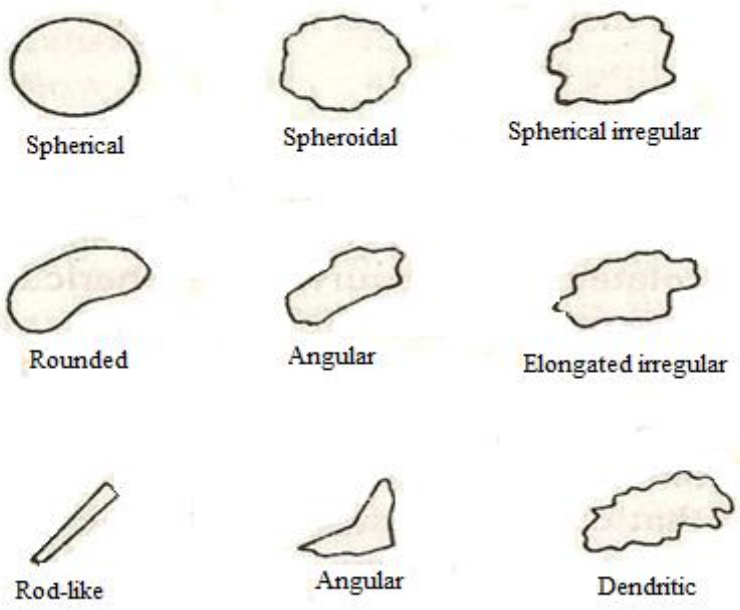

Figure 2.5: The different particle shapes that can form [35].

2.1.5. Flow properties

Physical properties, such as density, compressibility and how well the powder flows, are directly related to the particle size and how particles are distributed [61, 62]. In industry, it is very important that the die is filled quickly and uniformly with loose powder to provide consistent samples by mass, therefore the way the particles flow needs to be considered [35, 62-64]. Dies can be filled by gravity filling, where powder is conventionally poured in to a moving or vibrating die, or suction filling, where punches are moved across the die opening causing suction of the powder in to the die [65]. The flow of powder is defined as the time taken for a mass of powder to flow through a standard sized funnel [4, 35]. The standards have been set out in the MPIF Standard 03, where the mass of powder is 50g and the diameter of the orifice of the funnel is 2.54mm [66, 67].

Flow is influenced by friction between the powder particles themselves and against the funnel wall and also by the surface of the powder [62]. Finer particles, less than 60μm, have a larger surface area, which increases the frictional force of the powder and causes the formation of stagnant regions or bridges, thus preventing free-flow through the funnel illustrated in Figure 2.6 [35, 62]. Different proportions of particles in a ‘bimodal’ size blend can provide a powder with optimal flow properties, where the small particles fill the voids created by the large particles as shown in Figure 2.7 [35].

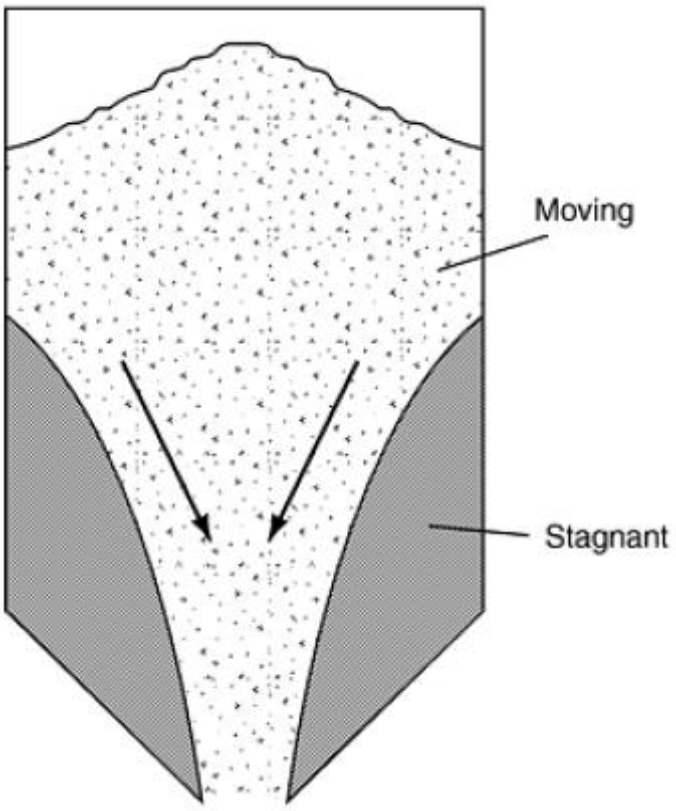

Figure 2.6: Particle bridging forms stagnant regions where powders do not flow [62].

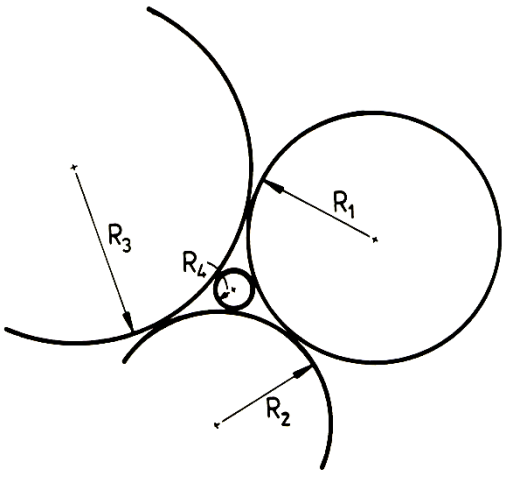

Figure 2.7: Mixture of large and coarse spherical powders

Particle shape and surface roughness also have an influence, for example, coarse dendritic shapes have poor flow characteristics due to mechanical interlocking of particles, especially when the width and height vary significantly [68]. For a particle to reach a mechanical equilibrium with an ordered packing structure, it needs to have at least three points of contact with neighbouring particles. Spherical particles are more desirable as they increase the relative movement between particles during die filling by reducing the number of contact points in the dynamic state [68]. Rougher surfaces cause mechanical interlocking of neighbouring particles in the early stages of die fill, as well as increased surface area to volume ratio, which increases friction and reduces flow [68].

2.1.6. Apparent Density

The volume occupied by the mass of powder affects the ability of industrial presses to mass produce compacts. Apparent density is defined as the mass per unit volume of bulk powder [35, 62]. It can be determined from the MPIF standard 04, where a cylindrical container with a volume of 25 ± 0.03cm^3 is filled with powder via a standard Hall Flowmeter funnel as described in section **2.1.5**. The apparent density is calculated by dividing the mass of the powder by the volume of the container [66].

The efficiency of powder packing depends on particle size, distribution and shape. The volume that gets filled depends on how the particles are aligned as they are poured [4, 62, 68]. This relates to whether or not pores will form due to mechanical interlocking or if smaller particles position themselves in the voids between larger particles. The strongest influence on apparent density is particle size [68]. Smaller particles have a higher specific surface, meaning that there is more area of contact between neighbouring particles, which increases the friction and prevents adequate flow and filling of dies [4, 35, 62]. Particle sizes under 20µm show a significant effect on aluminium apparent density shown in Table 2.2 [62, 69].

Table 2.2: Different particles sizes giving different apparent density for aluminium powder [62]

Average particle diameter µm	Apparent density (g/cm^3)
5.8	0.62
6.8	0.75
15.5	0.98
17.0	1.04
18.0	1.09
55.5	1.22
70.2	1.25

The limit of apparent density is reached when all of the particles have fallen into the optimum position, although when using different size ranges, more time is spent vibrating the die to settle these particles into place [4]. Having a higher proportion of spherical powder particles increases the apparent density as they will move past other spherical particles without bridging as shown in Figure 2.8 [4]. However, irregular shaped particles create empty spaces that cannot be reached during packing [4, 62]. An excessive amount of fine particles may also cause bridging.

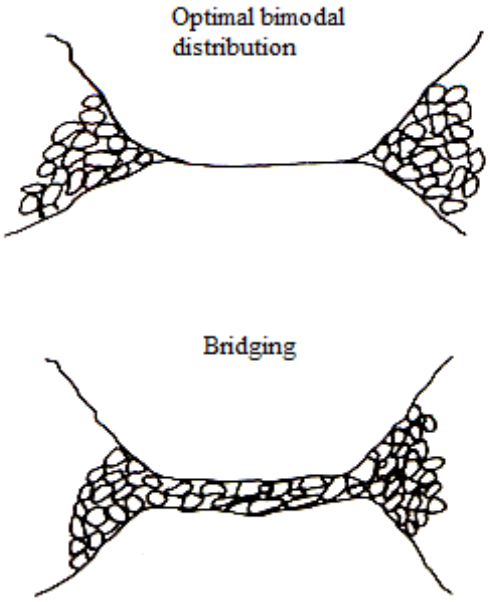

Figure 2.8: Bridging can occur in bimodal mixtures of powders if fine particle size content is excessive [4].

2.2. Compaction processing

Using an external force, the bulk powder is pressed into a green compact, or a pre-form, with a desired shape and density. These compaction techniques involve particle deformation and breaking the bridges that are formed during die fill [35, 70, 71]. The aim of compaction is to achieve as high a density as possible, which will usually result in better green strength and less dimensional changes during sintering [9]. A process that is widely used to produce green compacts with high densities is uni-axial compaction.

2.2.1. Lubricant application

It is important for the powders to flow during compaction, therefore a suitable lubricant is required that can either be blended with the powder particles (admixing) or solely applied to the die wall and punches [72, 73]. The lubricants should not react with the aluminium powder or the other alloying elements and it must burn off at relatively low temperatures during sintering [21, 74]. Using admixed lubricant can have a detrimental effect on the density and mechanical properties if the correct proportions are not used [75-78]. Typically, between 0.5%wt and 1.5%wt lubricant is used for admixed powders [75-77, 79] In ferrous P/M, some of the lubricants used are lithium stearates, which leave deposits during sintering that have an adverse effect and cannot be used in aluminium P/M processing [74, 80]. These deposits prevent metallurgical bonding during sintering and therefore the admixed lubricant needs to be completely removed at temperatures below 420°C in a non-oxidising atmosphere [81].

The main role of lubricant is to reduce die wall friction rather than inter-particle friction [82]. Kenolube and Acrawax C (Ethylenebisstearamide (EBS) compounds) are generally used for die wall lubrication in aluminium powder metallurgy, the compositions of which are shown in Table 2.3 [79, 83, 84] These lubricants decrease ejection forces and reduce wear of the tooling, an important consideration as powder particles can be quite abrasive depending on hardness of the material [77, 81]. At room temperature, the green density achieved for Alumix 231 alloy (Al-14Si-2.5Cu-0.5Mg), did not vary significantly when using Kenolube or Acrawax for die wall lubrication [79, 85].

Table 2.3: Composition of Kenolube used for die wall lubrication of aluminium powders [79, 84, 86]

Lubricant	Density g/cm^3	EBS %wt	Zn-Stearate %wt	Stearic acid %wt	Melting point °C	Boiling point °C
Kenolube	1.006	75	25	0	~100-145	250-450
Acrawax C	0.97	98	0	2	140-145	285

2.2.2. Uni-axial compaction

This is the most common method to compact powders and is shown in Figure 2.9. First, the lubricant is applied to the die wall then the die is filled with powders. Pressure is transmitted via punches that move in the vertical direction in a rigid die. Either one punch is moved or both can be moved to apply the pressure for consolidation in a floating die set-up, illustrated in Figure 2.10 and Figure 2.11 respectively [6, 70]. Then the sample is ejected from the die.

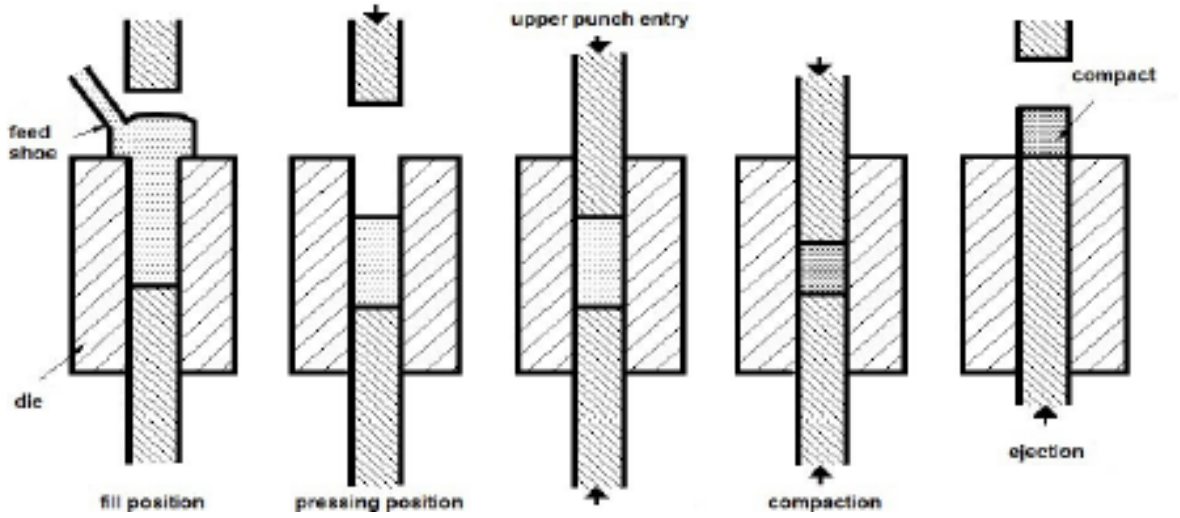

Figure 2.9: The die fill, pressing and ejection stage of cold compaction [4]

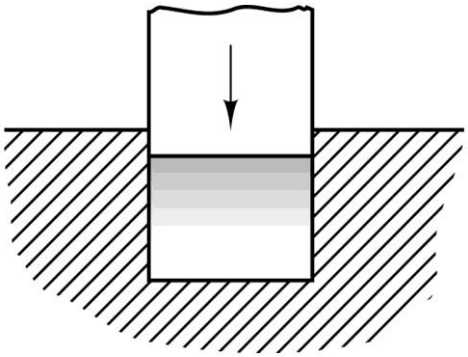

Figure 2.10: Single acting punch applying pressure in compactions. There is non-uniform densification of the powders, where the shaded area shows highest densification [6].

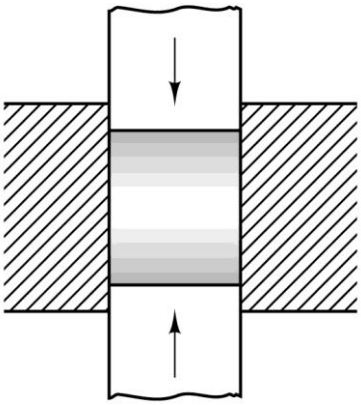

Figure 2.11: A floating die set-up with two moving punches. Densification is more uniform but still not homogenous [6].

In uni-axial die compaction, there are four stages of densification as shown by the compressibility curve in Figure 2.12 [17, 42, 87, 88]. The first involves particle rearrangement, whereby particles move past each other and settle in the optimum position, depending on their size and shape characteristics [8, 17, 87-91]. As was mentioned in section **2.1.5**, higher friction exists between smaller particles, which restricts their ability to flow past each other and this is also the case during compaction [8, 17, 65, 87-90]. When the powders are loosely settled upon die filling, there is an interconnected porous network. As densification proceeds, more contact points or asperities are created between the powder particles, which subsequently cause isolated porous networks in the compact and breaks down the bridges that were formed in die filling [8, 70, 71, 76, 90]. The asperities on the surface of the particles merge together and form bonding surfaces between neighbouring particles, which develops several cold welding spots due to the strong shearing along the contact surfaces [8, 76, 87, 90].

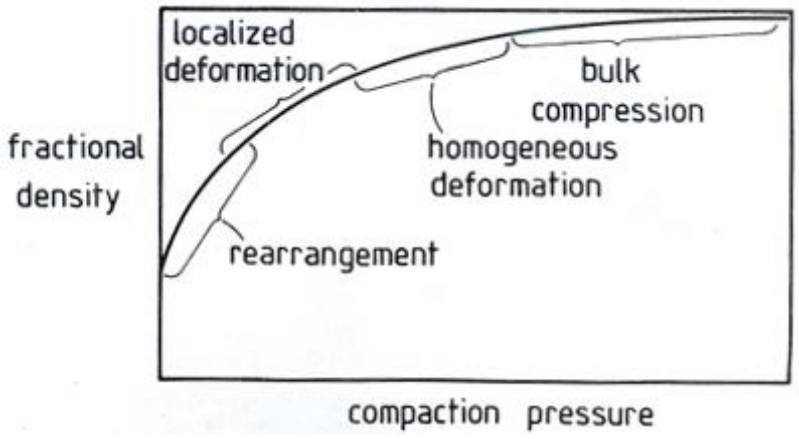

Figure 2.12: Compressibility curve showing the different stages of compaction [42].

The second stage involves localised elastic deformation of the particles, where compression occurs at the asperities between neighbouring powders, isolating the pore network via neck growth of the deformed contact region [17, 65, 87-92]. As compaction increases past the yield strength of the material, local plastic deformation of the contact points occurs and the material begins to flow in to inter-particle voids.

Strain hardening occurs due to the plastic deformation, which increases the particles resistance to further deformation and prevents additional densification as compaction processing increases [71, 76, 77, 88, 89]. The work hardening effect is described in more detail in section **2.5.2.4**. The points of contact between the particles, at this instant in the compaction process, have grown and created isolated pores [91]. This gives high local density where pores remain closed, as shown in Figure 2.13b for pure aluminium powder particles cold compacted at 245MPa [93]. The final stage generally occurs at very high pressures where plastic deformation cannot proceed due to a lack of porosity and the compact behaves like a fully dense body [71, 76, 88].

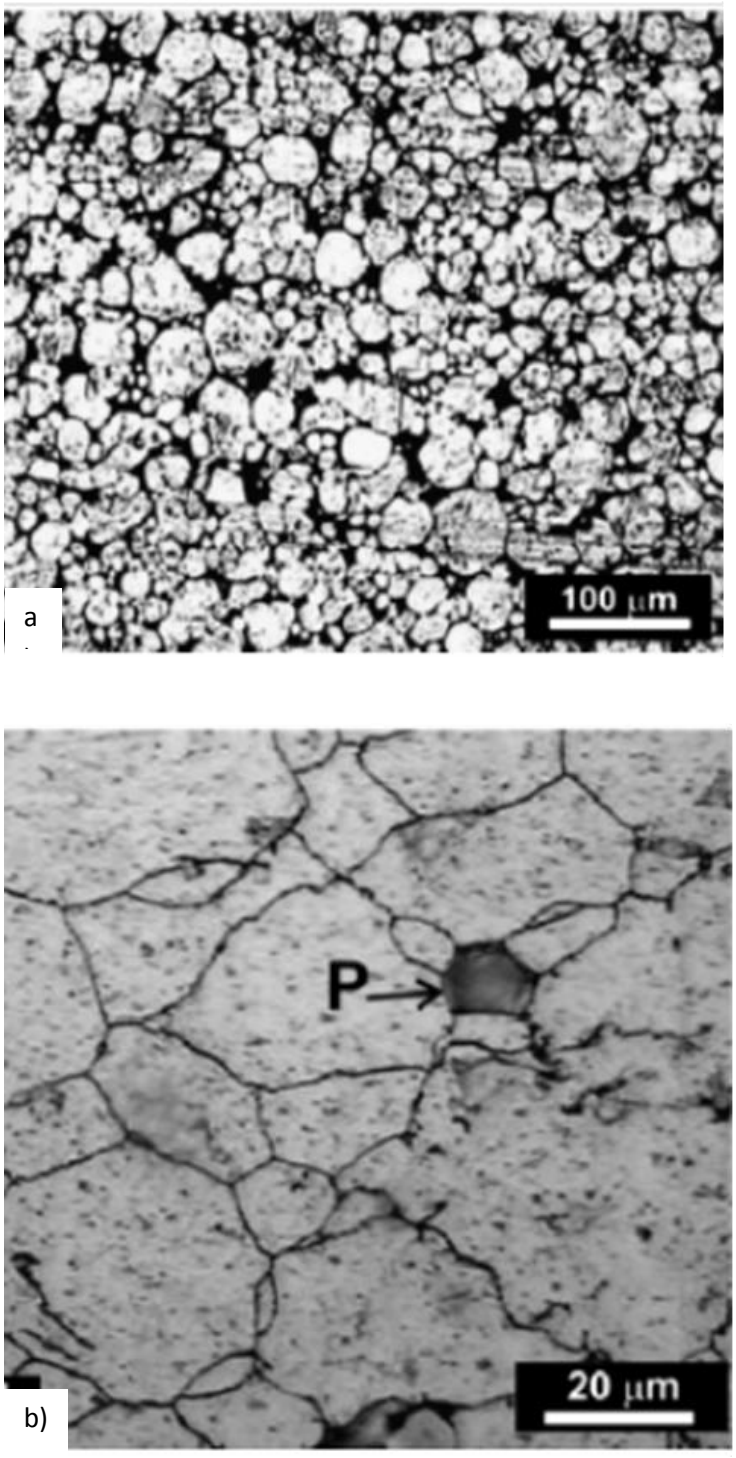

Figure 2.13: Etched pure aluminium powder compacted at 245MPa where a) shows the top surface of the compact with many pores (black regions) and b) shows local areas of higher density inside the sample [93].

2.2.2.1. The Heckel relationship

The Heckel relationship is used to describe the relationship between relative density and compaction pressure, shown in equation (2.2) [94, 95];

$$ln\frac{1}{1-D} = A + k_H P \tag{2.2}$$

where, ln is natural logarithm, D is the relative density of the compact ($\rho_{measured}/\rho_{theoretical}$), P is compaction pressure, k_H and A are constants. By plotting $ln\frac{1}{1-D}$ against P, a linear relationship is given and the gradient gives the value for k_H which is related to yield stress, σy, by equation (2.3) [79, 95]:

$$k_H = \frac{1}{3\sigma_y} \tag{2.3}$$

The value k_H is used to determine the mechanism of deformation of a material and if the gradient is shallow then yield strength of the material is high [79, 96]. This means it is more difficult to induce plastic deformation of the powder particles during compaction [79, 96]. A Heckel plot generally has a linear part with curves at the low and high pressure end, as shown in Figure 2.14. The linear region of the curve describes plastic deformation of the material, whereas the non-linear region at low pressure is related to particle movement. The transition between these two regions relates to the minimum pressure required to form a compact [79, 96].

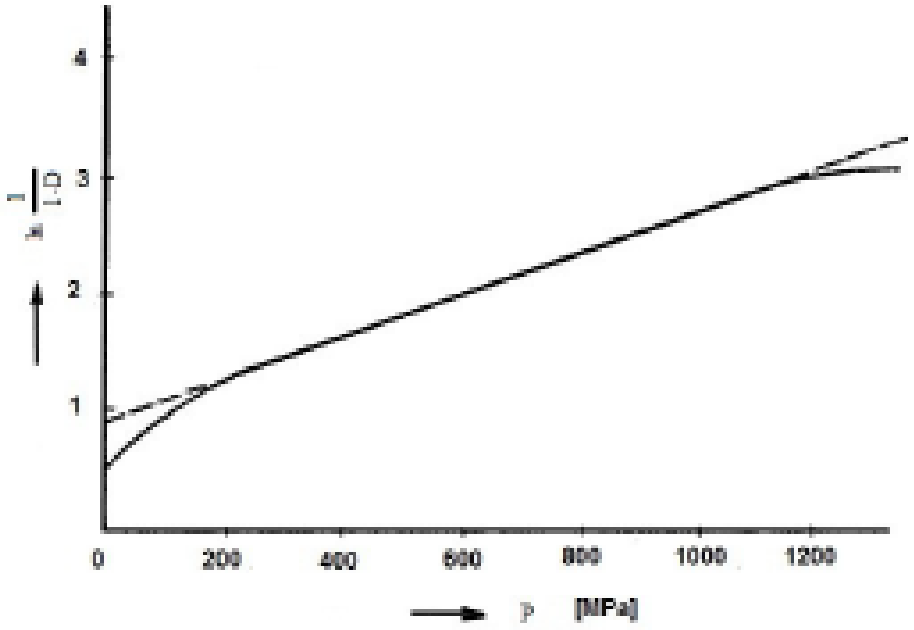

Figure 2.14: A typical Heckel plot of $ln\frac{1}{1-D}$ versus compaction pressure [79, 96].

2.2.3. Non-uniform transmission of pressure throughout compaction

During the uni-axial compaction process, the pressure transmitted may not be uniformly distributed throughout the sample, shown in Figure 2.13 [87, 88]. When the pressure is only applied by one punch, the maximum densification occurs directly below the punch surface as that is where the force is applied from and the particle movement is greatest [97]. Friction between the particles prevents adequate re-arrangement, which means that the powder may not be consolidated in the central section of the part as the force has not been transmitted all the way through as shown in Figure 2.10 [6, 98]. For compaction of thicker parts a double-acting press and two moving punches in the floating die arrangement can provide better densification but the transmission of force is still not uniform throughout the compact, shown in Figure 2.11 [6, 99].

The way the powders flow in to the die also has an influence on the transmission of pressure. Although pressure is in the longitudinal direction of the sample, there can be variations of density around the edges of the transverse cross-section as shown in Figure 2.15 [100]. This results from high areas of friction at the die wall preventing uniform flow, even with applied die wall lubricants, and it is this friction between the tool and the powders that affects the compaction process in terms of density distribution, pressing forces and cracks [100, 101].

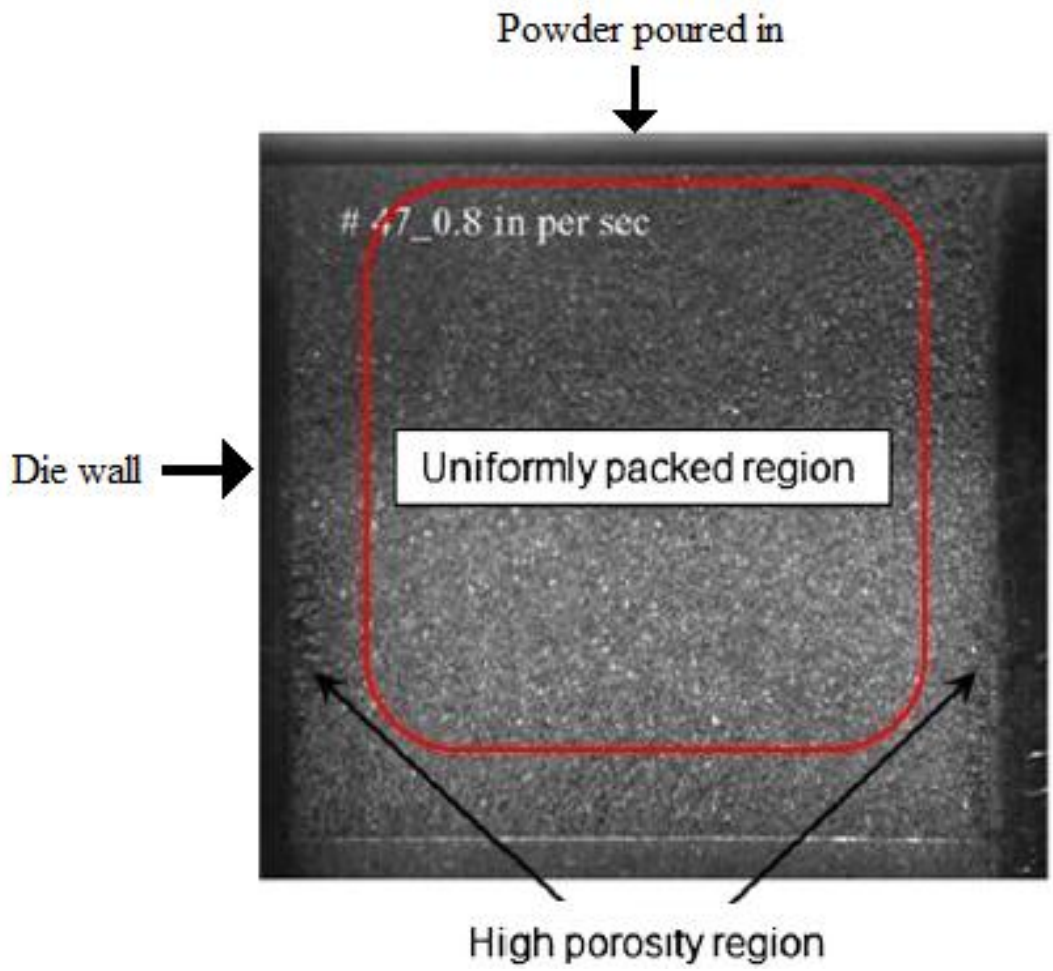

Figure 2.15: High porosity regions appear at the edges of the die where the particles do not flow uniformly due to die wall friction [100]

2.3. Sintering

2.3.1. Basic principles

Sintering involves heat treating a green compact in order to improve its density and mechanical properties [35, 102]. By optimising the sintering temperature, atmosphere, time, heating and cooling rates, the microstructure can be controlled in terms of grain size and density so that a fully dense component is produced [102, 103]. The driving force for sintering is a reduction in the free and interfacial energy of the compact created by the free surface and pores, which can be achieved by decreasing surface curvatures [79, 102].

There are four main stages involved in sintering, which are illustrated in Figure 2.16 [79]. The first stage of sintering involves re-organisation of particles where points of contact between neighbouring particles are made, shown in Figure 2.16a [35, 79, 102]. This is followed by initial creation of necks between the particles by reducing the surface oxide layer via reactions between the furnace atmosphere and the oxygen in the oxide layer, shown in Figure 2.16b [35, 79, 102]. The next step is the growth of these necks, which is driven by a reduction of interfacial energy at the grain boundaries and particle surface as the movement of metal atoms is enhanced and the pores re-arrange themselves, shown in Figure 2.16c [35, 79, 102]. The final stage involves grain growth and elimination of pores at the grain boundaries, shown in Figure 2.16d [35, 79, 102].

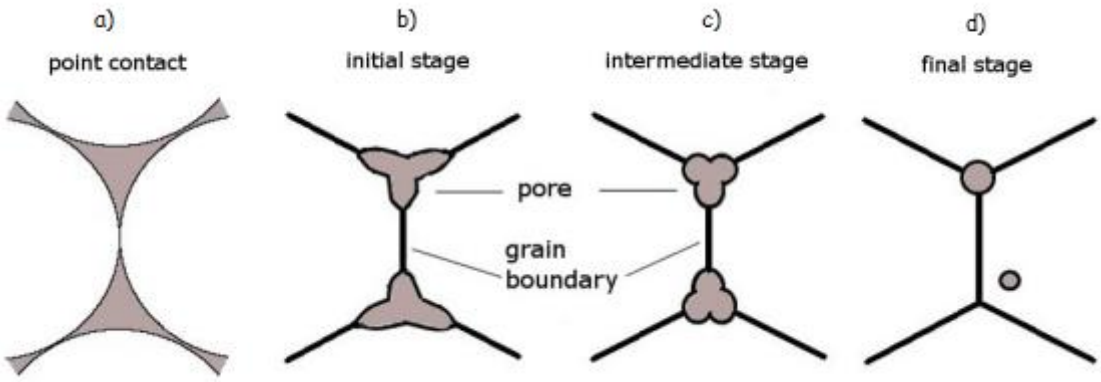

Figure 2.16: A simplified diagram illustrating the four stages of sintering where; a) is point contact; b) is initial stage; c) is intermediate stage and; d) is final stage [79].

There are two major categories of sintering; solid state and liquid phase. The temperature at which these two mechanisms occur is illustrated in Figure 2.17 for an alloy with composition X, where T_1 indicates solid state sintering and T_2 indicates liquid phase sintering [102]. Solid state sintering takes place when the green compact is still solid, whereas liquid phase sintering occurs when the temperature increases above the melting point of one of the alloying additions and a liquid phase is present in the compact [35, 102]. Material variables such as composition, powder size and shape and process variables such as sintering time, atmosphere and temperature all influence sinterability and microstructures of powder compacts [26-28].

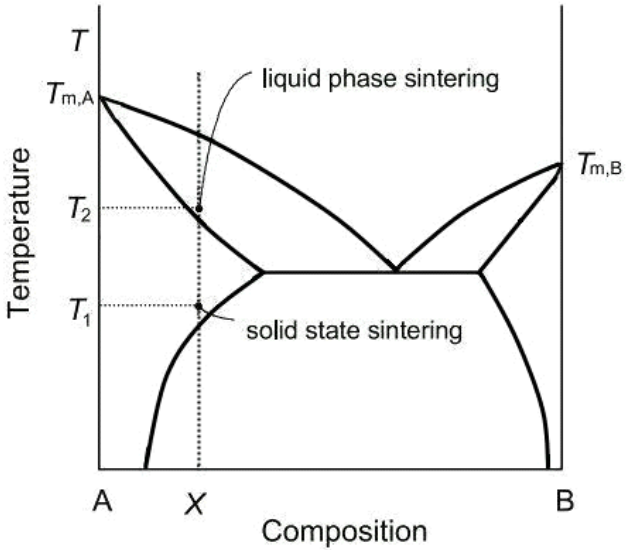

Figure 2.17: A generic binary phase diagram to illustrate when solid state and liquid phase sintering occur [102].

2.3.2. Solid state sintering

Here, diffusion between powder particles in the solid state causes densification. The reduction in free energy between the free surfaces and contact points of particles is the driving force of solid phase sintering [79, 102, 104]. The reduction in surface energy can be achieved by forming low energy solid-solid interfaces, for example grain boundaries, which replace the higher energy solid-vapour interfaces. Other diffusion mechanisms are shown in Figure 2.18 [104, 105]. Bulk pressure, vacancy concentration and vapour pressure induce material transport from the solid particles to particle necks [104, 105].

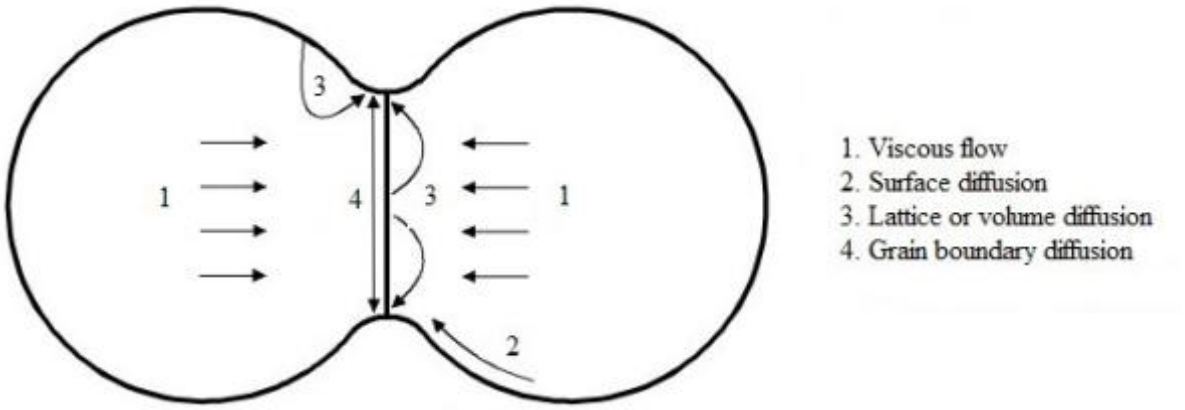

Figure 2.18: The different material transport paths during solid state sintering [105].

Shrinkage occurs as material is removed from the regions of contact between powder particles via grain boundary diffusion and this reduces the distance between particles [79, 104]. However, the distance between particles can also increase as a result of material transport from the particle surface to the particle necks and neck growth occurs due to material being redistributed [79, 102, 104].

There are three main stages in solid state sintering shown in Figure 2.19. The first stage involves formation of necks at the contact points between particles, which grow with increasing sintering time and the interconnected pores have an irregular shape (Figure 2.19a). The intermediate stage involves mass flow of material due to the curvature gradient near the necks, which leads to considerable densification and rounding of the pore structure at the junction of grains (Figure 2.19b). This also causes an increase in grain size. At the final stage, the rate of densification is very slow and the pores become closed off and isolated (Figure 2.19c) [79, 102, 104, 106].

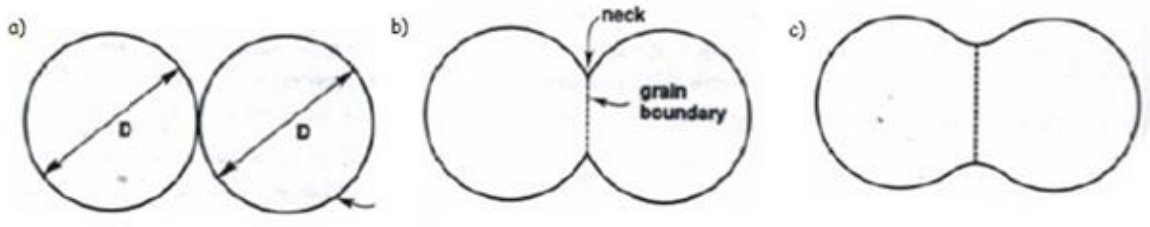

Figure 2.19: Solid state sintering mechanisms [106]

2.3.3. Wetting

Wetting relates to the equilibrium between solid, liquid and vapour phases in sintering, the degree of which can be determined by the wetting angle. The wetting angle is the angle between the solid-liquid interface when a liquid droplet occurs on a solid substrate as shown in Figure 2.20 [102, 107]. This angle depends on the balance between the solid-vapour, liquid-solid and liquid-vapour interfaces, shown in equation (2.4):

$$\gamma_{SV} = \gamma_{SL} + \gamma_{LV} cos\theta \qquad (2.4)$$

where γ is the interfacial energy, subscripts S, L and V are solid, liquid and vapour respectively and θ is the wetting angle. The total free energy of the system must decrease so that the liquid wets the solid. Depending on the contact angle, either swelling or shrinkage will occur. Decreasing θ favours wetting and causes liquid to spread over the solid grains, as shown in Figure 2.21 [102, 107]. This spreading of the liquid encourages capillary forces which attract particles together to increase density and cause shrinkage as sintering progresses. Increasing θ hinders wetting as it causes liquid to retreat from the solid and leads to swelling and liquid being exuded from surface pores, shown in Figure 2.21 [102, 107].

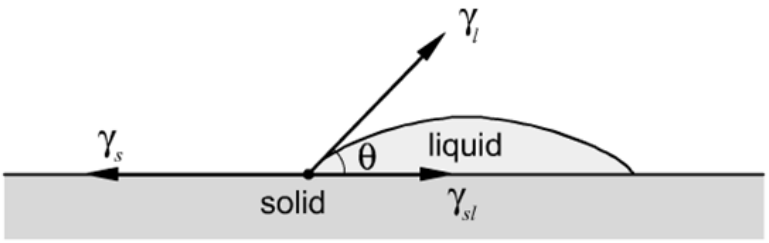

Figure 2.20: An illustration to show wetting angle and interfaces between a solid and liquid [102].

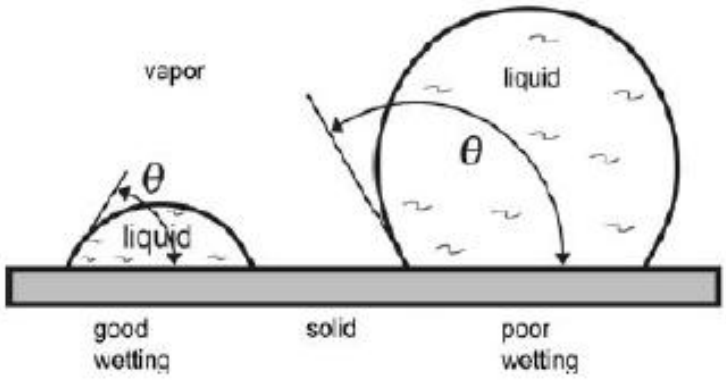

Figure 2.21: Good and poor wetting of liquid on a solid [102].

The likelihood of the liquid wetting the solid depends on surface chemistry. When the liquid has a high attraction to the solid, the wettability is increased. If there are no impurities on the base metal surface, then it is wet by another metal with a high solubility in the base metal [102, 108, 109]. For aluminium alloys, the oxide layer has a negative effect on sintering as it prevents good wetting behaviour. This surface chemistry can be optimised by sintering in an inert or reducing atmosphere. An example of a material with poor wetting characteristics is shown in Figure 2.22 for an Al-8Sn alloy, where tin is exuded from the surface [103].

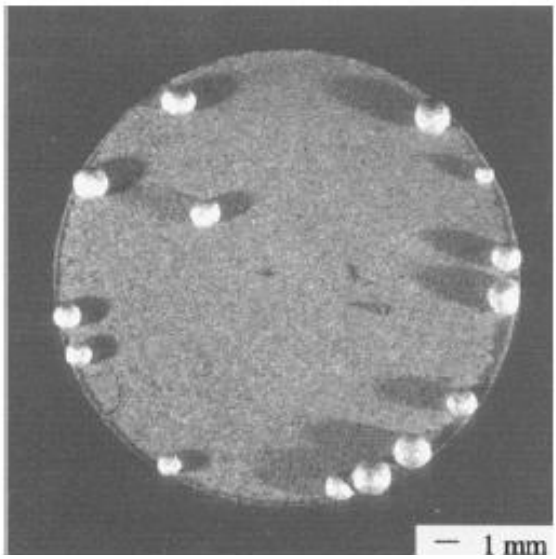

Figure 2.22: Liquid tin exuded on the surface of Al-8Sn after sintering at 620°C [103].

2.3.4. Liquid phase sintering

In liquid phase sintering, the compact densifies by liquid formation, which enhances atomic diffusion and increases the rate of microstructural changes due to a faster rate of material transport through the liquid via capillary action [102, 110]. This is a result of the lower surface energy at solid-liquid interfaces in liquid phase sintering than at solid-vapour interfaces in solid state sintering [79, 110].

Aluminium oxide is always present on the surface of the particles from atomisation [103]. The oxide layer is difficult to overcome in solid state sintering as there is no metal-to-metal contact between neighbouring powder particles, which is essential [79, 111]. The use of liquid phases also improves the sintering of aluminium alloys as the solid particles are wetted and gives a higher diffusion rate of material through the oxide. In order for liquid phase sintering to be effective, the following criteria must be met:

- There should be a metal with a melting point below the main constituents, which aids the development of the liquid phase;
- The solid solubility of the additive in the base material should be lower than the base in the additive. This prevents the additive dissolving in the base and allows more liquid phase for sintering;
- The base materials should have high diffusivity in the liquid so mass transport is increased [112-115].

The amount of liquid in the system has an influence on shrinkage and dimensional changes in the final part. Low liquid volumes retain the shape and dimensions of the sample although the densification may be hindered due to the resistance of the solid phase [105, 116]. Conversely, high liquid volumes can lead to large amounts of shrinkage although some dimensional changes and distortions can occur [117-119].

There are three main stages in liquid phase sintering which are particle re-arrangement, solution re-precipitation and solid-state sintering, shown in Figure 2.23 [110, 120, 121]. As the temperature increases above the solidus temperature of the alloy, the liquid forms and spreads into fine capillaries between the solid particles. Particle re-arrangement occurs when the solid particles are redistributed due to the liquid flow, which is followed by solution-reprecipitation, with elimination of pores and grain growth occurring simultaneously. The final stage consists of very slow sintering rates, similar to solid state sintering, where the system contains rigid solid grains and liquid in between them [110, 120, 121]. These events are described in more detail in subsequent sections.

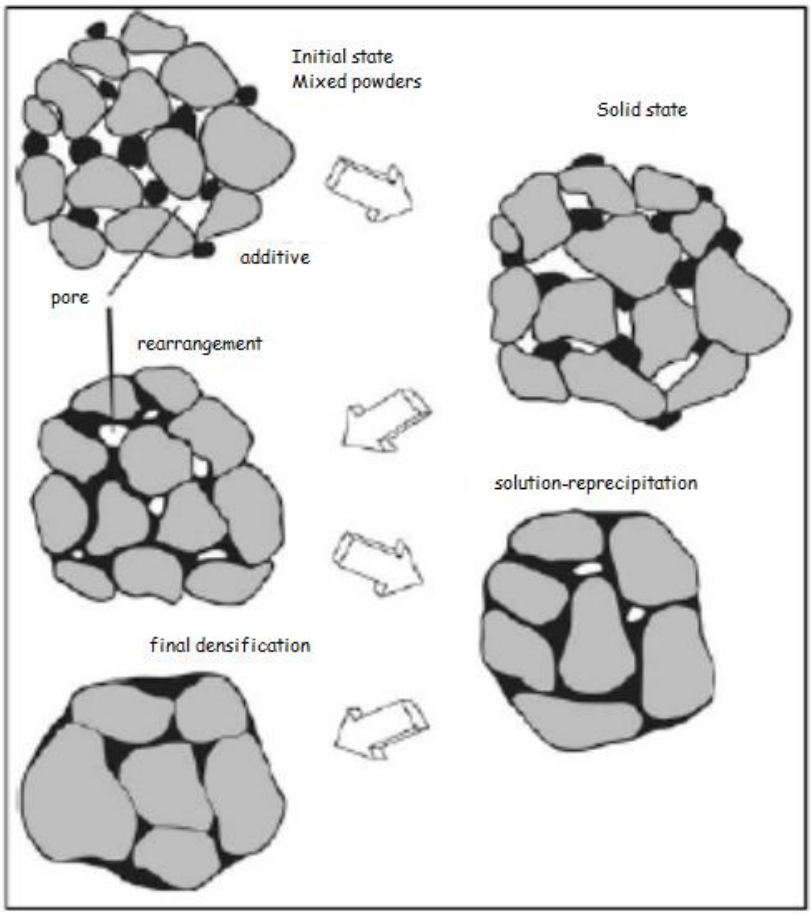

Figure 2.23: The microstructural changes in liquid phase sintering [110]

2.3.4.1. Particle re-arrangement

The liquid that forms in the initial stages of heating flows into porous areas created by the gaps between solid powder particles, which can be moved as a result of this liquid flow due to capillary forces [121-123]. The solid grains dissolve in to the liquid even more as sintering progresses, which allows pores to be filled by the liquid and is an essential process in achieving optimum density as well as grain growth [102, 108, 109]. Rapid shrinkage occurs at this stage, although expansion events possibly occur as well from liquid penetrating through the solid grain boundaries and formation of new contacts at the onset of liquid phase sintering [102, 108, 109].

Having a low contact angle between the solid and liquid phases increases the attraction between the wetted particles, which facilitates particle re-arrangement and shrinkage by capillary forces. Conversely, a high contact angle increases the repulsive forces between particles and leads to swelling. The first stage of particle rearrangement is indicated by the formation of clusters of wetted particles due to random packing of the powders and non-uniform distribution of the liquid [124].

The second stage of particle rearrangement involves particle break-up and liquid flow into grain boundaries due to the initial liquid being under-saturated with solid and not of an equilibrium composition. A low wetting angle is essential for the liquid to break-up the solid particles [110]. The inter-solubility between solid and liquid facilitates particle rearrangement and when the solid-liquid surface energy is lower than the solid-vapour surface energy, viscous flow occurs.

2.3.4.2. Solution re-precipitation

The next stage of liquid phase sintering is determined by the solubility of the solid in the liquid [102, 110]. This involves grain growth, further densification and shape alterations, which all occur simultaneously. The material transport mechanisms consists of Ostwald Ripening, contact flattening and solid-state bonding, illustrated in Figure 2.24 [102, 110, 121].

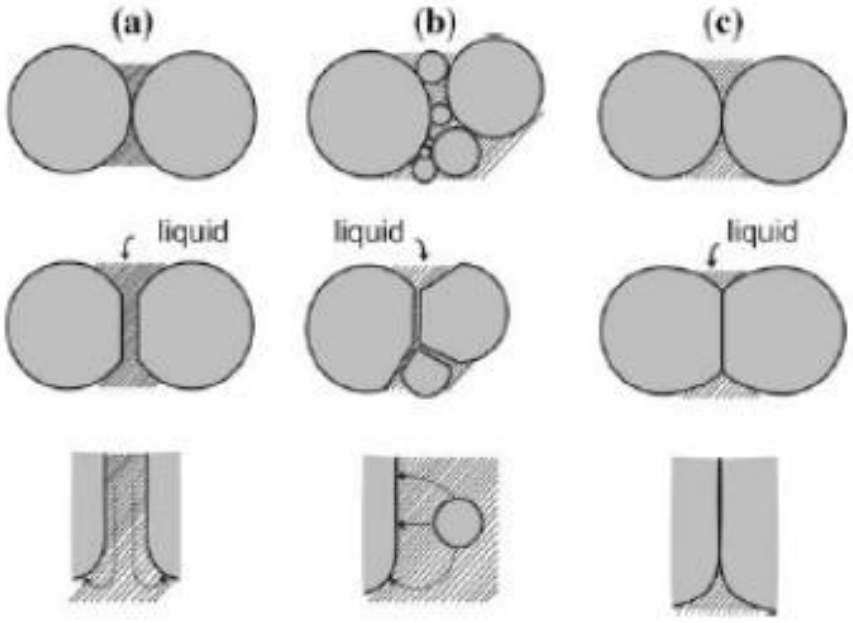

Figure 2.24: The different material transport mechanisms of solution-reprecipitation; a) contact flattening, b) Ostwald ripening and c) solid state bonding [110]

2.3.4.3. Contact flattening

The capillary forces and surface tension of the wetting liquid pulls the grains together [110]. The solid is dissolved into the liquid at the contact point as a result of the concentration gradient, shown in Figure 2.24a [110]. The subsequent diffusion of the solid phase reduces the concentration gradient, which causes the material to re-precipitate to a "lower free-energy area" away from the contact point, such as the surface of the neck regions [110, 125]. This leads to shape changes, as the contact area increases, and densification, due to movement of the particles towards each other [125]. Pore shrinkage occurs simultaneously and the densification rate depends on material transport rate. The densification rate decreases when the rate of solid diffusion decreases.

2.3.4.4. Ostwald Ripening

Ostwald ripening is the process whereby small particles dissolve and larger ones grow, as shown in Figure 2.24b [126]. Smaller particles have larger surface areas and a higher free energy, which means they have a higher solubility in the liquid, creating a concentration gradient between different particle sizes [102]. The concentration gradient and the difference in free energy between finer and coarser particles are the driving force for diffusion of atoms via liquid phase [102]. Therefore the growth of the large grains decreases the net energy of the system and the shape of the large particles changes to allow better packing of the solid [102].

2.3.4.5. Solid state bonding

Diffusion of material via the solid diffusion path leads to growth of contact points between different grains, shown in Figure 2.24c. The diffusion along the wetted grain boundary allows the necks to grow, which results in change of grain shape and densification due to the reduction in distance between the centres of the grains. The neck growth of the grains replaces the region occupied by the solid-liquid interface [102, 110, 126].

2.3.4.6. Pore filling

The driving force for pore filling is the reduction in liquid pressure between the pores and the liquid between the grains. Grain growth and grain shape changes cause densification by pore filling as illustrated in Figure 2.25 [102]. Smaller pores have a greater attraction for wetting liquid due to higher capillary forces. Larger pores, which are surrounded by grains smaller than the diameter of the pore, remain stable due to capillary forces retaining the liquid between the grains in small channels [109]. Pores are removed when the growth of the grains reaches a threshold whereby liquid flow in to the pore is favoured. This threshold depends on pore size, grain size, the liquid meniscus radius and the contact angle between the meniscus, shown in Figure 2.26 [109]. As the grains grow, the meniscus radius also grows, which reduces the capillary gradient. Liquid flows into the pores when the pore size and meniscus radius are equal as this will reduce the liquid pressure [110, 127].

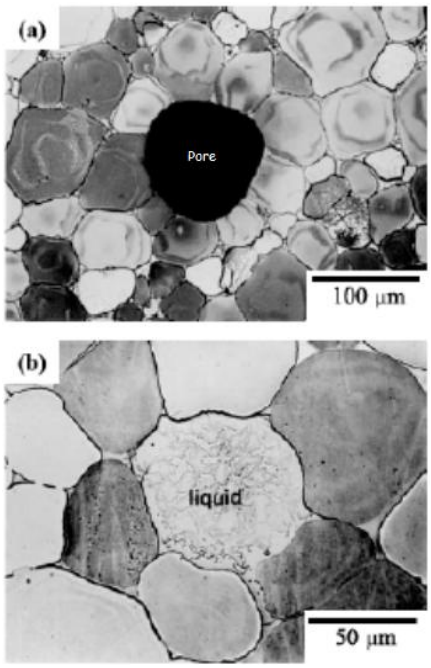

Figure 2.25: Microstructure of Mo-4Ni; a) before and; b) after pore filling [102]

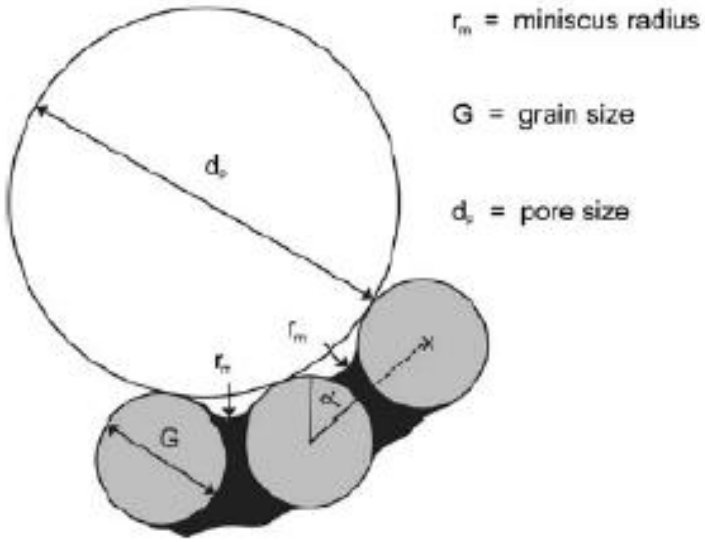

Figure 2.26: A model for pore filling when spherical grains surround a large pore [109]

2.3.4.7. Microstructural coarsening

The final stage of sintering occurs at a lower densification rate due to the microstructure consisting of interconnected solid grains with liquid filling the spaces between them. Therefore the energy configuration between the solid and liquid phases is reduced to a minimum. Densification via diffusion of material is still occurring at a lower rate, although it contributes to grain coarsening. Diffusion, solubility of the solid in the liquid phase, pore characteristics and entrapped gas have a significant influence on densification [110, 124].

If the solid solubility in the liquid is low, then densification is mainly dominated by solid state sintering. Conversely, if solubility of solid in liquid is high, then the solution re-precipitation stage of liquid phase sintering is prolonged. As the contact points between the solid grains flatten, the rate of densification via solution re-precipitation decreases [110, 124].

Trapped gas inside the pores can become pressurised, which is not often anticipated. This will prevent complete pore closure and hinder densification if short sintering cycles are used. For longer heating, pores can grow and join together due to Ostwald Ripening, with large pores growing from smaller pores due to a need to reduce the pore pressure. This causes swelling of the compact rather than shrinkage and thus reduces the density [110, 124].

2.3.5. Transient liquid phase sintering

This process involves forming liquid phase in the initial stages of sintering, which disappears as sintering progresses due to solubility mechanisms and forms a solid solution [128, 129]. From Figure 2.27, the temperature for transient liquid phase sintering, T_2, occurs just above the eutectic temperature but below the solidus line [110].

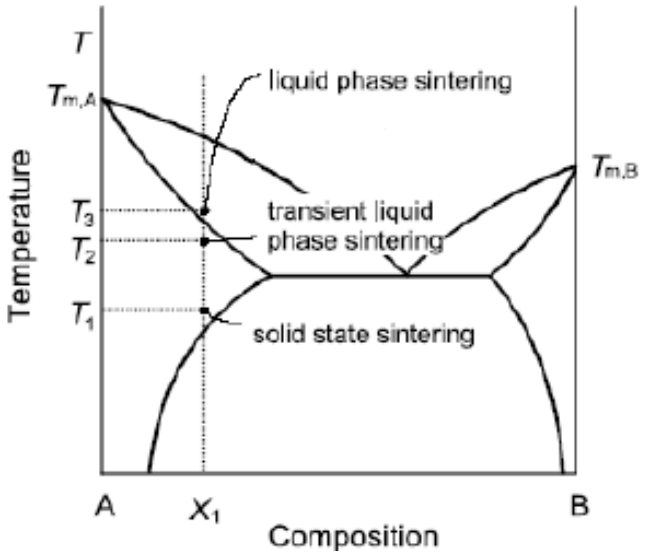

Figure 2.27: A phase diagram to show the different types of sintering at various temperatures for an alloy X_1 [110]

The base material needs to have a high solubility in the alloying material at the sintering temperature. There should also be sufficient formation and duration of the liquid phase, along with rapid re-solidification to achieve high densification and prevent swelling from homogenisation [128]. The liquid spreads through the compact as a result of capillary forces and the material transport mechanism is enhanced, which leads to particle re-arrangement and densification [110]. The formation of liquid in transient liquid phase sintering occurs at a lower temperature than that of liquid phase sintering, which results in rapid densification and possible high densities with homogenous dimensional changes and less coarsening of the microstructure [128].

2.3.6. Supersolidus liquid phase sintering

Pre-alloyed powder particles are heated between the solidus and liquidus temperatures, whereby densification occurs due to viscous flow, which is driven by the capillary forces acting on the semi-solid structure, shown in Figure 2.28 [130]. Liquid forms at contact points and grain boundaries at the sintering temperature, which is shown in Figure 2.28b, followed by densification via capillary forces exerted by the liquid at particle necks, shown in Figure 2.28c. The liquid at the grain boundaries softens the particles and the grains are able to slide during densification [131].

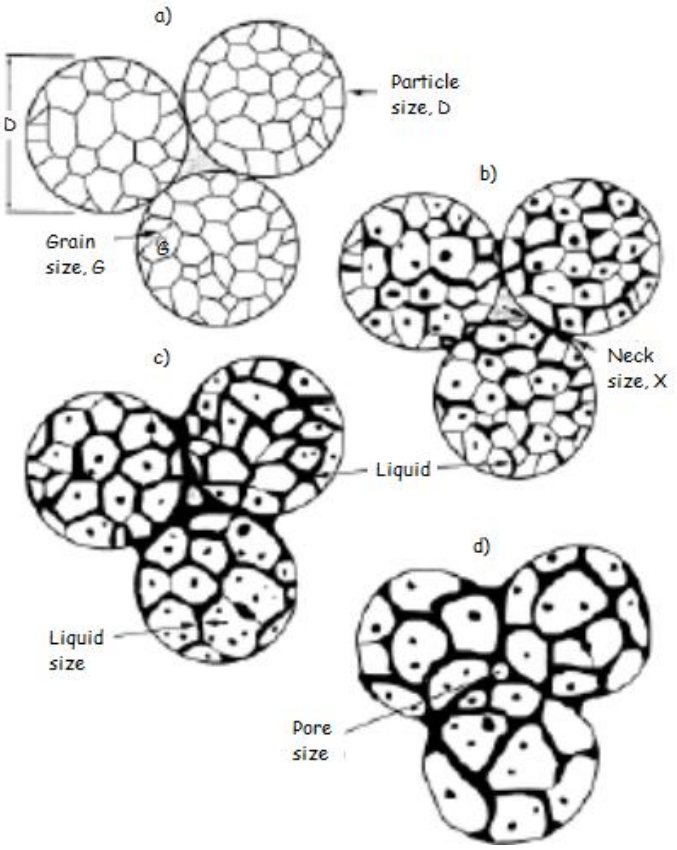

Figure 2.28: Supersolidus liquid phase sintering densification by; a) initial packing of the particles; b) initial liquid formation; c) densification via viscous flow and; d) final sintered microstructure with closed, spherical pores [130].

The densification mechanism depends on the amount of liquid in the system and higher liquid contents are more desirable as the rate of densification increases by particle re-arrangement, contact flattening, grain shape changes and removal of porosity [132]. However, more liquid causes a reduction in the structural stability of the compacts and undesirable shape distortion. Therefore deliberation is needed over the liquid content, which can be optimised by altering sintering temperature, time and composition of the powder [132].

2.3.7. Sintering parameters

2.3.7.1. Particle size

Particle size influences curvatures, contact stresses and capillary forces in liquid phase sintering. Decreasing the particle size increases the driving force for sintering to reduce the interfacial area between the pore and the solid, which would decrease the free energy of the system [110]. The densification rate is improved with smaller particle sizes, which subsequently increases the sintering density for fixed sintering conditions as shown in Figure 2.29 [133]. Furthermore, decreasing the particle size increases the capillary force between particles and solubility of solid in liquid, which facilitates particle rearrangement and solution-reprecipitation [133]. This is due to more particle contacts and necking between the particles being formed with smaller particles, providing better material transport [133].

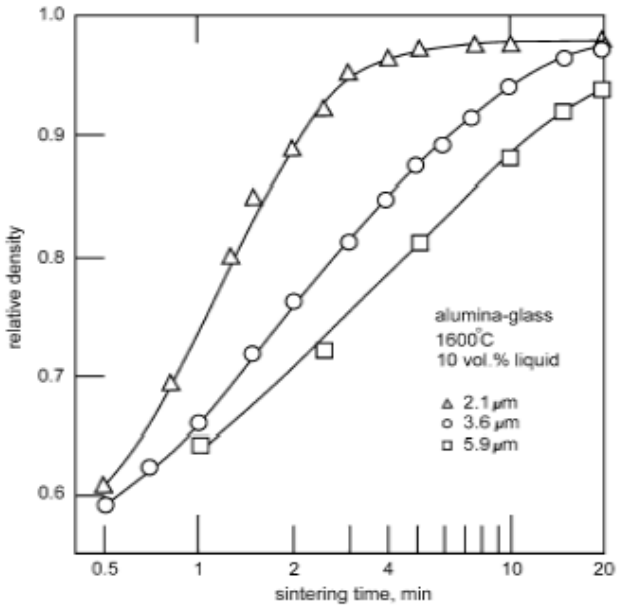

Figure 2.29: Relative density of alumina-glass powders with different particle sizes sintered at 1600°C at various lengths of time [133]

2.3.7.2. Particle shape

With irregular shape, less rearrangement occurs due to higher friction between particles. Despite this, use of a wetting liquid can induce particle rearrangement by creating a torque, which rotates the particles and brings flat surfaces in to contact [134]. Increasing the liquid content increases the torque and thus more particle rearrangement occurs. Spherical particles respond more readily to capillary forces compared to irregular shaped particles, meaning that more uniform microstructures can be formed [134].

As solution-reprecipitation processes dominate, the initial particle shape has little effect. It has been reported that the use of irregular shape particles lead to a higher sintered density of 90% for an Al-4Sn alloy compared to 70% for spherical powders. This was attributed to the surface oxide being broken down due to differences in thermal expansion between the oxide and the aluminium particle [135].

2.3.7.3. Sintering atmospheres

The sintering atmosphere can alter the chemistry of the compact due to reactions between the atmosphere and the material. A protective atmosphere helps prevent adverse reactions, reduces the surface oxide to aid particle contact and remove lubricants [35, 110].

2.3.7.3.1. Pure gases

Hydrogen is used as a reducing atmosphere mainly for stainless steels, tungsten carbides and ceramics [35]. All of the oxygen and moisture needs to be removed from the sintering furnace before hydrogen is applied in order to prevent oxidation. Generally, hydrogen as a sintering atmosphere is limited due to the high cost and handling problems [35].

Inert gases, such as helium or argon, are the most expensive gases to use for sintering and are usually only used for highly reactive materials such as titanium and zirconium alloys [35].

Nitrogen has been proven to improve sinterability of aluminium-based alloys and it is relatively cheap compared to hydrogen, helium and argon. When aluminium is sintered in an atmosphere of nitrogen, it forms AlN, which forms a pressure gradient between the internal material atmosphere and the external atmosphere, which induces pore filling [114, 136]. Therefore, pore filling is a very significant densification mechanism for aluminium sintering.

Nitrogen can also be mixed with small amounts (≤5%) of hydrogen to give a sintering atmosphere with low water vapour and reducing effects. However, this mixture has been detrimental to pore filling and lead to minimal shrinkage and densification of aluminium alloys [114, 136, 137].

2.3.7.3.2. Vacuum sintering

A desired pressure of the furnace is acquired by using a rotary or diffusion pump and maintained throughout sintering. There is no interaction of gas with the material, thus protecting it from oxidation. This is mainly used for materials such as titanium, zirconium, beryllium and tool steels, which react readily with oxygen, moisture and hydrogen. It is a relatively cheap process as the only costs are vacuum operation and oil for the pumps, although the production rate is low and making it a continuous process is difficult [138].

2.3.7.3.3. Dissociated Ammonia

Dissociated ammonia normally contains 25% volume of nitrogen to 75% volume of hydrogen and is a low cost alternative for pure hydrogen. This is produced by evaporating liquid ammonia and subsequent dissociation at temperatures between 900-1000°C using Ni or Fe as a catalyst. The resulting gas is high purity, CO-, CO_2- and O_2- free and is adequately dry to be used in the furnace. It is normally used for sintering of steels, brass, copper and aluminium [139].

2.3.7.4. Sintering time

It is important to allow sufficient time for sintering mechanisms to take place. The majority of densification occurs in the first 20 minutes with longer times aiding further pore elimination. Conversely, having too long a sintering time can lead to microstructural coarsening and decrease the strength of the final sintered material [110]. The mechanism of solution-reprecipitation causes increased grain size due to larger particles growing at the expense of smaller ones and increasing sintering time means there is more time for coarsening to occur [140, 141]. This theory is based around Ostwald ripening and is described in equation (2.5):

$$G^3 = G_0^3 + Kt \tag{2.5}$$

where G is grain size, G_0 is initial grain size, K is temperature-dependent grain growth rate constant and t is length of time that the sintering temperature is maintained [140, 141]. K is sensitive to temperature as other factors such as solubility, diffusivity, surface energy and solid-liquid ratios change with temperature and is shown in equation (2.6):

$$K = \frac{64}{9}\frac{D_S C \Omega \gamma_{SL}}{RT} \tag{2.6}$$

where D_S is solid diffusivity in the liquid, C is solubility of solid in the liquid, Ω is the solid molar volume, γ_{SL} is the surface energy of the solid-liquid surface, R is the gas constant and T is absolute temperature [110].

However, these models assume that the solid has been uniformly dissolved in the liquid and thus takes an average. This means that the rate of growth or shrinkage for a given grain would only be a function of its relative size compared to the mean size; in other words, small grains dissolve and larger grains grow [110, 141]. The local surroundings of the grain are important and can cause large grains to shrink and smaller ones to grow as shown in Figure 2.30 [142]. Along with coalescence and an absence of solution-reprecipitation at pore-solid contacts, these factors make prediction of grain growth behaviour throughout solution-reprecipitation very difficult [110, 141].

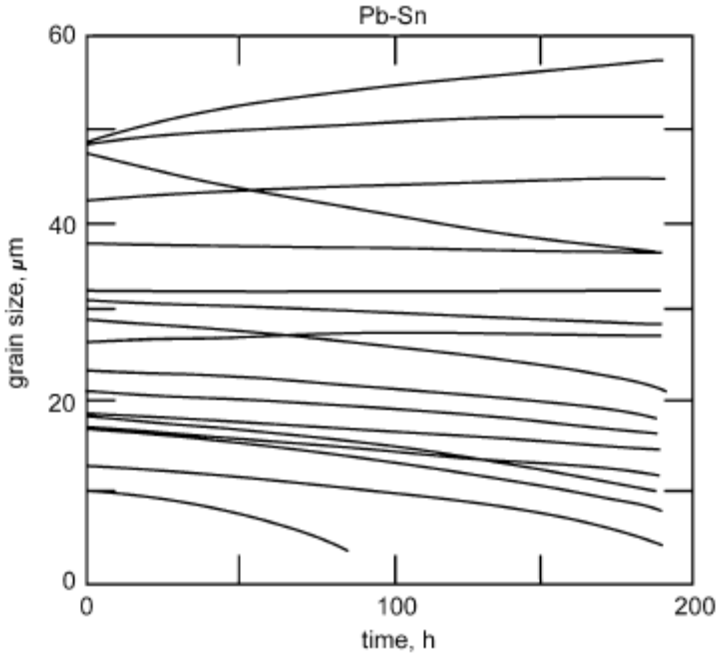

Figure 2.30: A graph showing grain size against sintering time for lead-tin, showing that grain growth depends on local environment of the grains [142].

2.3.7.5. Sintering temperature

The temperature relates to the formation of liquid that is able to wet the particles, thus giving desired densification. It also influences diffusion rates and the solid solubility in the liquid during liquid phase sintering. Increasing the sintering temperature causes an increase in relative densities as it facilitates particle re-arrangement and solution-reprecipitation mechanisms by decreasing liquid viscosity and increasing the solid solubility in the liquid, subsequently increasing the rate of material transport [141, 143, 144]. However, at lower temperatures, densification rate is low due to slow solid diffusion kinetics and low solubility of the solid in the liquid. Therefore achieving an optimum sintering temperature is important to reduce microstructural coarsening and shape distortions, yet increase densification.

2.4. Aluminium P/M

2.4.1. Applications of aluminium P/M

High strength-to-weight ratios, high thermal and electrical conductivity, high corrosion resistance, low thermal expansion and low density are attractive properties for the use of aluminium P/M in automotive and aerospace applications such as pistons for shock absorbers, camshaft bearings, pulleys, rod guides and brake callipers [20]. Aluminium P/M research is still relatively new compared to ferrous P/M, with limited applications [3].

As the automobile industry is the main consumer of powder metallurgy, one important aspect is to reduce mass of car engine components. In order to save weight in automobiles, light weight aluminium powder alloys have been increasingly used in recent times because of its low density and the versatile use of the powders in terms of producing complex geometries with a minimal amount of waste [15-17].

Some examples for the applications of aluminium parts, mainly in automobiles, are in the cam-phaser system in the BMW M3 [18]. Other examples for the use of aluminium powder parts is for the rotor, sprocket pulleys, rod guides, shock absorber pistons, oil pumps and transmission gears [19-21, 145].

The sintering of aluminium P/M components is a key process and the thermodynamically stable oxide layer, which can only be reduced at 600°C with an oxygen partial pressure of $<10^{-50}$atm, is a hindrance to this [103]. Therefore, compaction and liquid phase sintering are important for metal-to-metal contact and diffusion mechanisms. Aluminium P/M components are conventionally sintered in a nitrogen atmosphere to form aluminium nitrides, AlN.

2.4.2. Alloying additions

Pure aluminium has low strength and is not desirable for structural components, therefore the use of alloying additions are required to improve mechanical properties and sinterability.

2.4.2.1. Copper alloying additions

Copper is usually included in aluminium alloys to provide strength by precipitation hardening [146, 147]. In the binary phase diagram of aluminium and copper, a single liquid phase exists where the aluminium is soluble in copper, L, and at 548°C the maximum solid solubility of copper in aluminium is 5.65%, circled in Figure 2.31 [148]. The eutectic composition consists of (Al) and Al_2Cu [103].

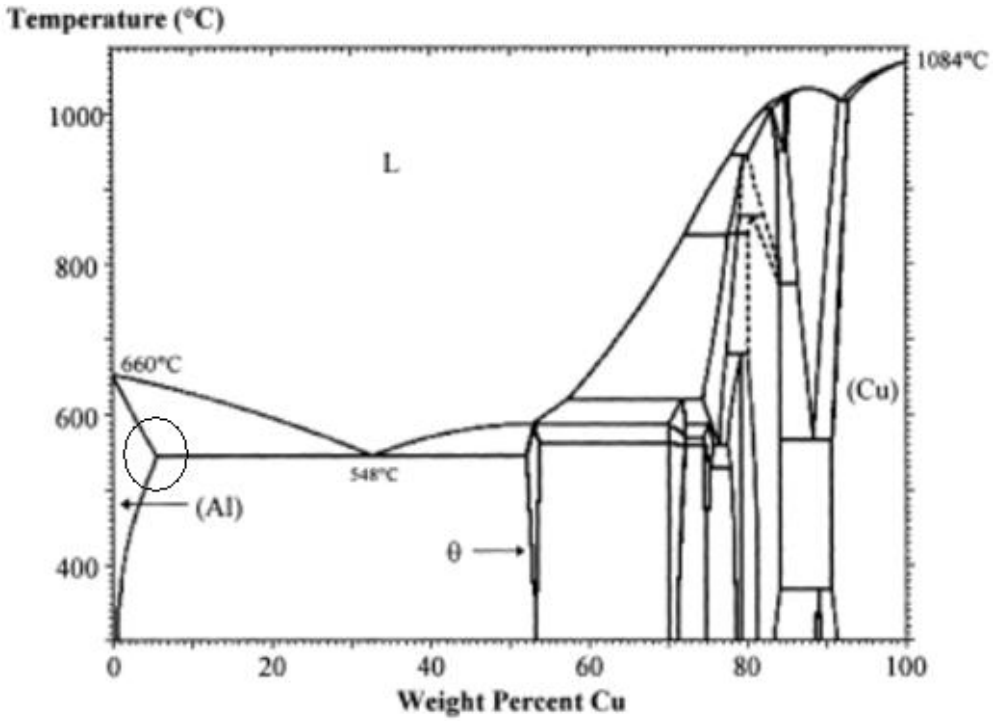

Figure 2.31: The Al-Cu phase diagram [148].

As the temperature rises during sintering, liquid forms at 548°C at the Al-Al_2Cu boundaries. The copper in the liquid moves into solution in the aluminium and is converted into Al_2Cu intermetallics, which are maintained by solid state diffusion from neighbouring copper particles until the copper has been depleted [103]. Al_2Cu normally forms in these alloys and can be used to promote age-hardening mechanisms [146, 149]. However, if they form at grain boundaries in P/M components, they can weaken the material. If the copper content is low, the liquid will be completely absorbed into the aluminium particles [150].

2.4.2.2. Silicon alloying additions

The phase diagram for a binary Al-Si alloy is shown in Figure 2.32 [151]. The eutectic composition is approximately Al-12.6Si at a temperature of 577°C. At equilibrium, the aluminium rich solid solution has 1.65%wt silicon at 577°C and the solid solubility of silicon in aluminium decreases to 0.1%wt below 300°C [152].

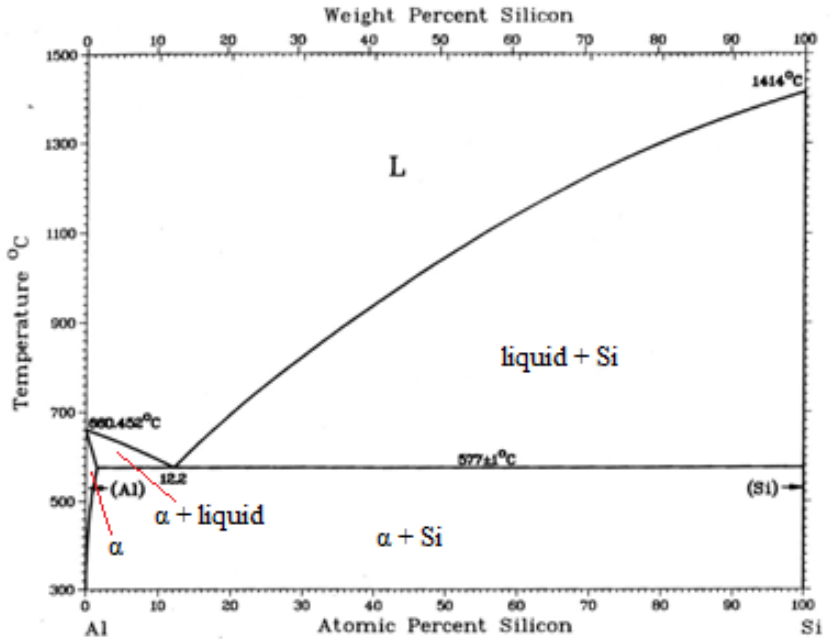

Figure 2.32: Al-Si phase diagram [151].

Al-Si alloys are used in gears and other components requiring high wear resistance. Alloying aluminium with silicon improves wear resistance and strength, increases operating temperatures and lowers the thermal expansion coefficient [146, 149, 153]. Hypereutectic Al-Si alloys have excellent wear resistance, low weight and low thermal expansion and are produced either by casting or via P/M. However, crystallisation of large primary silicon particles in the casting process produces non-uniform microstructures, which is detrimental to the final component [146, 149, 153].

2.4.2.3. Tin alloying additions

The characteristics of a binary aluminium-tin phase system are ideal for liquid phase sintering as the melting point of tin, 232°C, is significantly lower than that of aluminium, 660°C, and there are no intermetallic phases as shown in the phase diagram in Figure 2.33 [103, 154, 155]. Aluminium is wholly soluble in liquid tin and it has a very high diffusivity, particularly when used in an atmosphere of nitrogen [103, 114]. Some research indicates that tin can stop AlN formation in an oxygen free environment as tin moves to the surface of the aluminium in a binary Al-Sn alloy [115, 156, 157]. This leads to poor sintering responses and significant swelling when tin content >2 wt% due to the inability of tin to wet aluminium [115, 158].

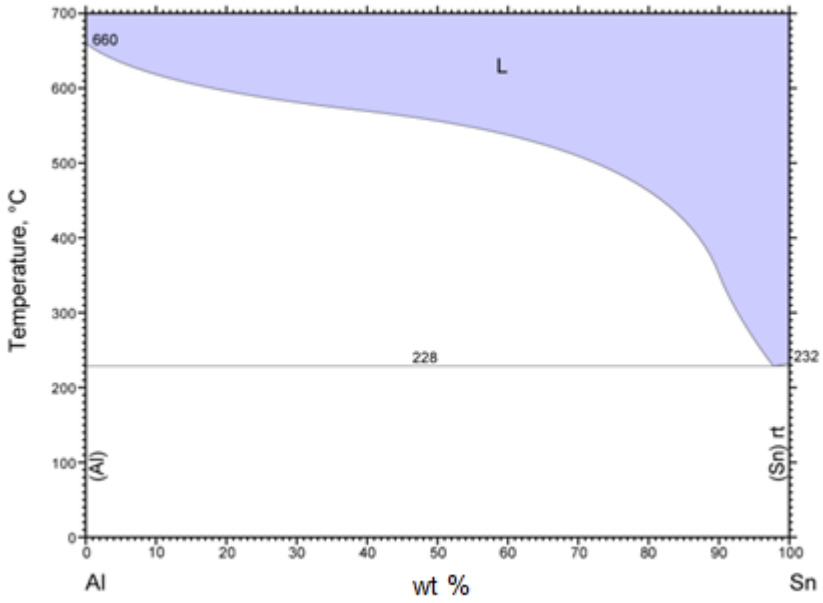

Figure 2.33: The Al-Sn phase diagram [155].

However, trace elements of tin, 0.05wt%, have a beneficial effect on sintering by potentially diffusing in to the vacancies in the aluminium matrix ahead of copper in an Al-4Cu-0.15Mg alloy [159]. Furthermore, an addition of 1.5 wt% of Sn in a Al-1.5Mg alloy improved the sintered density to 99.5% of the theoretical compared to 92.4% without [115]. In the binary alloy, tin stopped AlN formation, whereas in the presence of elemental magnesium, nitridation still occurred but at a reduced rate [115].

Aluminium alloys with a higher tin content up to 20wt% and even 45wt% are primarily used in bearing applications, which are described in more detail in section **2.4.3**.

2.4.3. Aluminium Bearing alloys

2.4.3.1. Introduction

A bearing alloy is essential in applications where metals experience contact with another surface during sliding under pressure and they are designed to provide free movement between the two surfaces in sliding contact [160]. The aim is to maintain the operation of a system for as long as possible without the use of lubrication [161]. These alloys mainly find their use in automotive applications such as diesel engines, where lower fuel consumption and exhaust emissions are required in a high pressure, high temperature environment as well as having a higher fatigue resistance [162, 163].

They mainly contain a hard phase to provide strength and an easily sheared soft phase to allow uniform properties throughout the structure [164]. The matrix can either be soft with hard phases interspersed or vice versa. In a soft matrix, the hard particles may be crushed or pushed down from the surface upon sliding contact and lose their efficiency [161, 165].

2.4.3.2. The history

The initial interest of aluminium alloys for sliding bearings arose in the 1930s as they could withstand high loads, had high thermal conductivity, corrosion and fatigue resistance, without the complications of using Cu-Pb alloys [166, 167]. Such complications resulted from the toxicity of lead and the material being banned by the European Commission for use in cars [164]. Tin was then used as an alloying addition, typically up to 7%, to increase softness. Although the main problem with this alloy comes from the high coefficient of thermal expansion of aluminium, preventing the ability of the alloy to retain its shape at high operating temperatures in modern engines [167].

Traditional manufacture of bearing alloys has involved melting and casting ingots, rolling the ingots out and bonding them to a steel-backing to prevent distortion [165, 166, 168]. Achieving an even distribution of tin throughout the alloy in casting is difficult due to the difference in density between aluminium and tin, causing segregation through gravity during melting [166, 169]. Controlling the growth of the aluminium phase is paramount and can be done by grain refinement at the ingot production stage via rapid solidification [166].

Aluminium bearing alloys with varying amounts of hard phase, silicon, and a soft phase, tin, are cast from high purity materials and either annealed at 350°C for two hours and slowly cooled or heat treated at 500°C for 20 hours and annealed at 175°C for 50 hours [25]. A steel backing is then attached to the bearing alloy, which provides some support although the aluminium oxide layer prevents a close contact between the two surfaces, meaning that severe cold rolling has to be done to facilitate the bonding [167].

Powder metallurgy provides an alternative way of developing bearing alloys. In a set-up similar to atomisation, the steel backing, or substrate, is placed at the bottom of the chamber and the droplets fall on and adhere to the surface, which is shot blasted prior to the process [170]. By using this route, the thickness of the deposited layer can be controlled easily by adjusting the volume of melt delivered in to the system. Once atomisation is complete, the composite is rolled at elevated temperatures in order to suitably bond the steel and bearing alloy [171].

During operation, the bearing alloy will experience friction and wear. Fretting occurs when two materials undergo small amplitude oscillating movements when in contact [172]. Such contact takes place in disks that are fitted to rotating shafts or in riveted and bolted joints. As the components are in constant contact during fretting, the wear debris remains trapped at the interface, leading to seizure [170].

Furthermore, when a fatigue crack develops in the bearing strip, it propagates towards the steel backing and thus increases the risk of seizure [173]. Cracking of the bearing alloy causes aluminium to be exposed and form an alumina layer, which cracks and fragments into debris around the regions of wear [170]. Seizure resistance or compatibility is an important consideration for bearings as there needs to be high resistance to physical welding via friction to the shaft in contact with the bearing [174].

It has been found that the optimum tin content is 20%, which gives the highest seizure resistance. However, thin films of tin surround the aluminium grain boundaries and can decrease the strength of the alloy [164, 167, 175]. This is known as a reticular structure and typically forms when tin content is in excess of 16%, whereas below this, tin forms distinct particles or pools at the corner of the grains [175]. A binary alloy of Al-Sn will not have sufficient strength or fatigue resistance and a binary Al-Si alloy has poor seizure resistance [176]. Therefore, alloying additions can be used to strengthen the alloy by varying the amount of silicon, as well as including copper, magnesium and adjusting the content of tin to improve wear and seizure resistance by providing a solid lubricant [176, 177]. Some alloys that have been developed are described below.

2.4.3.3. Al-4.5Sn-2.7Si-1.5Cu-0.2Cr-0.15Zr cast alloy

This alloy was developed for use in 2.4L diesel engines where the maximum load applied to the bearing alloy was 70MPa [162]. A conventional Al-Sn-Si base was used with additional precipitation hardening elements such as copper and zirconium, which maintain tensile strength at high operating temperatures, and chromium to increase corrosion resistance. This alloy was cast and subjected to a series of heat treatments and, when compared to a conventional Al-12.5Sn-2.7Si-1.8Pb-1Cu-0.2Cr alloy, the tensile strength increased from 142MPa to 185MPa [162].

2.4.3.4. Al-10Sn-4Si-1Cu using the P/M route

This alloy was developed using gas atomisation to spray molten droplets of the bearing material on to the steel substrate, illustrated in Figure 2.34 [170]. The deposited layer reached 1mm thickness and was hot rolled at 200°C in a nitrogen atmosphere to 20%, 40%, 60% or 80% of the original thickness. It was found that porosity does not influence the coefficient of friction when it varies from 0.5% in the 20% original thickness alloy to 10.5% in the 80% original thickness alloy [170]. However, the samples with less porosity experienced a lower wear rate compared to the samples with a higher porosity, although the worn surfaces showed a high concentration of alumina for the 20% original thickness alloy [170].

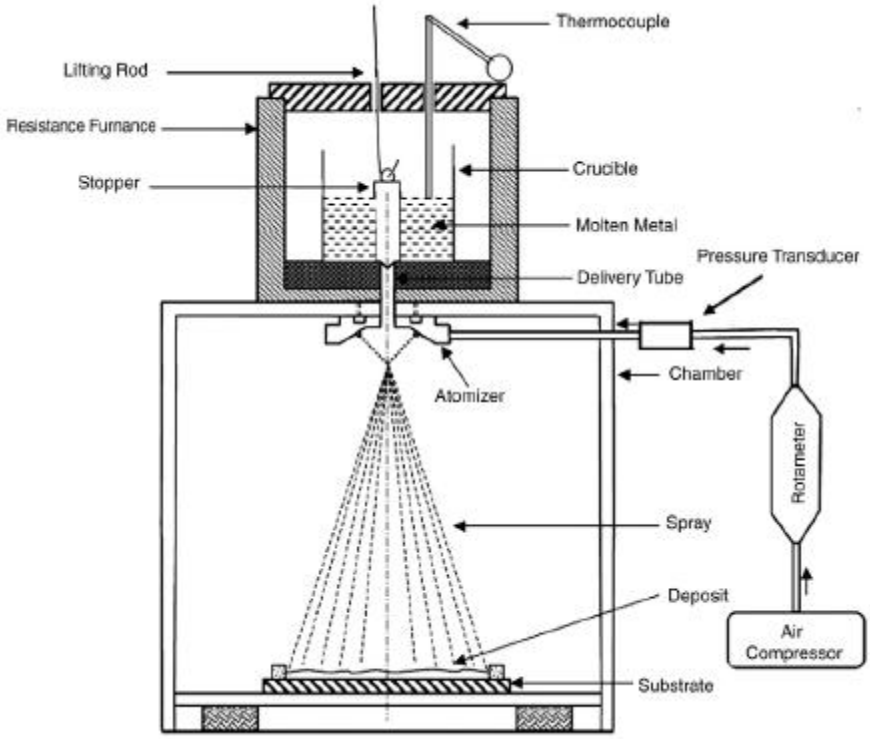

Figure 2.34: The gas atomisation technique for depositing droplets of the molten bearing alloy on to the steel substrate [170]

When compared with a conventional Al-14Sn bearing alloy used in Indian cars, the wear rate and friction coefficient of the 20% thickness sample were lower, which means that less energy is required from the car battery to maintain motion at the wear interface, thus reducing maintenance cost of the part [170].

2.4.3.5. Al-20Sn-7Si-1Cu spray deposition

The spray deposition technique used was similar to that illustrated in Figure 2.34 [165]. The deposited layer and substrate were subsequently heat treated at 300°C for time periods between 1 to 5 hours and cooled to room temperature [165]. During atomisation, the powder particles experience a range of cooling rates depending on the size of the droplets that form. Variation of cooling rates can also be caused by powder composition and with 7wt% silicon, the growth of Al-Si dendritic cells occurs between primary and α-Al dendrites [165]. Residual liquid tin also forms and freezes into isolated pools upon solidification [165]. After annealing, silicon particles formed from the α-aluminium matrix in the pre-alloyed powder and tin-rich phases coarsened and pooled at grain boundaries in all regions of the coating, which caused the micro-hardness to decrease from $150HV_{300g}$ to $50HV_{300g}$ [165].

The Al-20Sn-7Si-1Cu bearing alloy is commercially available and at the time of the thesis research, there has been no literature to suggest that it has been developed for use without being applied to a steel substrate. Therefore, using gas atomised pre-alloyed powders, it might be possible that this alloy can be developed into a monolithic product using the conventional press and sinter route and severe plastic deformation in order to achieve unique properties.

Firstly, there will be an introduction to the ECAP process, describing the fundamental process and parameters, which includes a review of bulk materials processed by ECAP and how ECAP can be used for powder consolidation and advances in the process.

2.5. Equal channel angular processing (ECAP)

2.5.1. Introduction

This process was introduced in the 1970s and the early concept involved applying high strains to metal billets by simple shear. Since the 1990s, ECAP has been found to have potential for producing ultra-fine grains (UFG) in bulk metals [11, 29, 178]. It has also been noted that ECAP has greater potential than other methods for producing UFG products, as the process can be scaled up for industrial applications by multi-pass facilities and the cross-sectional dimension of samples remain constant for net-shape manufacturing as shown in Figure 2.35 for an aluminium alloy [10, 179-181]. ECAP is also a highly attractive technique as it is a simple process to set up [76, 182, 183]. The drawback is that it is a discontinuous process.

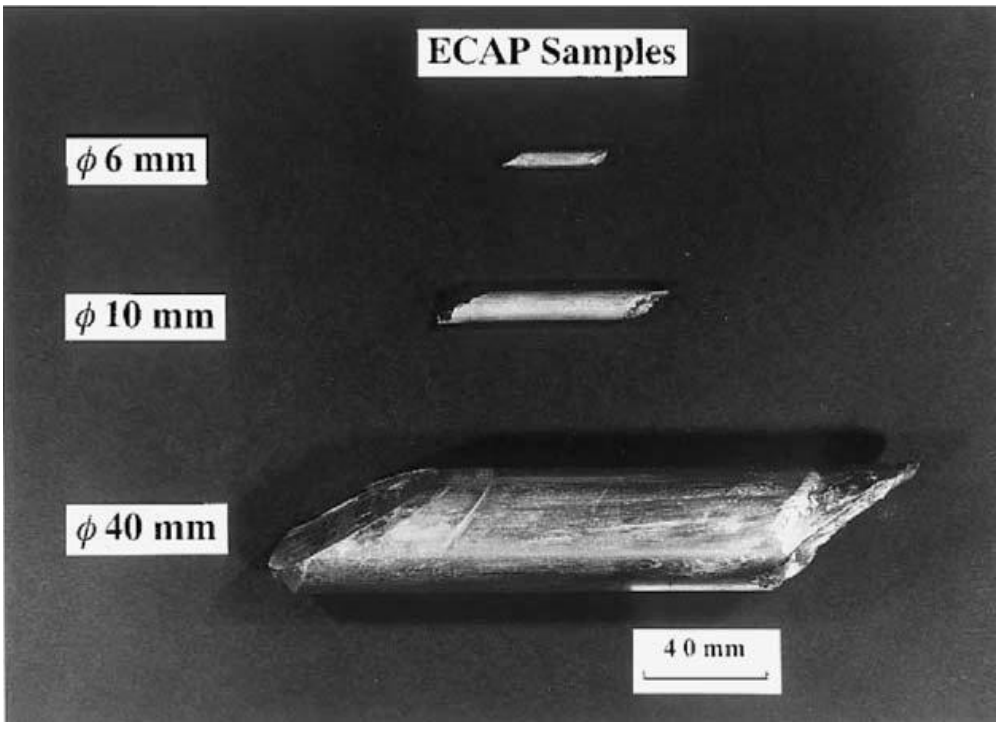

Figure 2.35: Al-1100 alloy after ECAP with diameters of 6, 10 and 40mm [179].

2.5.2. Process

2.5.2.1. Fundamental steps

The conventional, discontinuous process consists of a die with an internal channel that bends at an angle, which can vary from 60° to 160° as shown in Figure 2.36 [10, 12]. The sample, which is either in the shape of a rod or plate, is pushed through the die by a plunger that exerts a downward force. As the sample moves around the channel angle, it experiences simple shear along the shear plane, which causes high plastic strains. Despite experiencing very high plastic strains, the cross-sectional area is retained meaning that the sample can be repeatedly processed. Therefore the plastic strain can be further increased allowing different slip systems to be introduced by rotating the sample between each pass [10]. This is one of the various processing routes in ECAP.

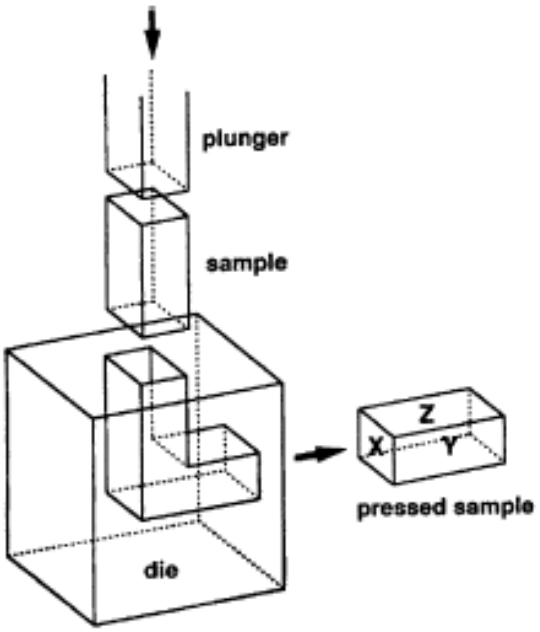

Figure 2.36: Schematic diagram of an ECAP die [10].

2.5.2.2. Mechanisms of severe plastic deformation (SPD) to form ultra-fine grains

When attempting to produce a UFG microstructure, conventional metal-working processes such as extrusion and rolling are unable to refine grain sizes significantly [184]. This is due to corresponding reductions in cross-sectional dimensions of work pieces and the low workability of metallic alloys at ambient and low temperatures, which limit the plastic strain imposed [184]. Therefore, research has focused on severe plastic deformation processing, defined as a metal forming procedure where extremely high plastic strains are imposed at relatively low temperatures without changing the cross-sectional dimensions.

Imposing a high plastic strain to a coarse-grained material is necessary to produce UFG microstructures. In techniques such as rolling, a continuous strain path leads to cellular or fibrous microstructures with low angle grain boundaries (LAGBs) [29]. SPD techniques can change the strain path during deformation and create high angle grain boundaries (HAGBs), which lead to grain refinement via three mechanisms [185]. The first involves elongation of existing grains in the direction of plastic deformation, which increases the high angle boundary area; the second is creation of HAGBs by grain subdivision processes; and the third is the splitting of the elongated grains by localised phenomena such as shear bands [185].

The second mechanism is the most significant and grain subdivision begins at low to medium plastic strains, when grains split up into cells and cell blocks. As the strain increases, the substructure evolves into a lamellar structure, where new HAGBs are created. The accumulation of dislocations in the cell and cell block grain boundaries occurs as the plastic deformation begins, in which, the misorientations increase with increasing strain. A significant fraction of the boundaries evolve into HAGBs in the range of 15-30°. This microstructural mechanism occurs simultaneously with texture evolution, which involves rotation of different parts of a subdivided grain towards varying orientations and generates HAGBs ranging between 20-60° [185].

2.5.2.3. ECAP mechanism of grain refinement

ECAP is characterised by the strain imposed in each pass through the die, which is a fundamental parameter for grain refinement in ECAP. A sample experiences an abrupt strain each time it is passed through an ECAP die, which can be estimated based on various die arrangements shown in Figure 2.37, where the channel angle is Φ and the angle subtended by the angle of curvature at the intersection is Ψ [29, 186]. In Figure 2.37a, $\Psi = 0°$, in Figure 2.37b, $\Psi = (\pi - \Phi)°$ and in Figure 2.37c, an intermediate situation is seen where $0° < \Psi < (\pi - \Phi)°$ [29, 182, 186]. It is assumed that the samples are fully lubricated to neglect frictional effects.

For each condition, a small square billet, abcd, passes through the shear plane and is distorted into a'b'c'd'. For the situations illustrated in Figure 2.37a, Figure 2.37b and Figure 2.37c, the shear strain, γ, can be defined in equations (2.7), (2.8) and (2.9) respectively [29, 182, 186]. Furthermore, a general equation for the equivalent strain after N passes, ε_N, is given by the relationship in equation (2.10) [29, 182, 186-188].

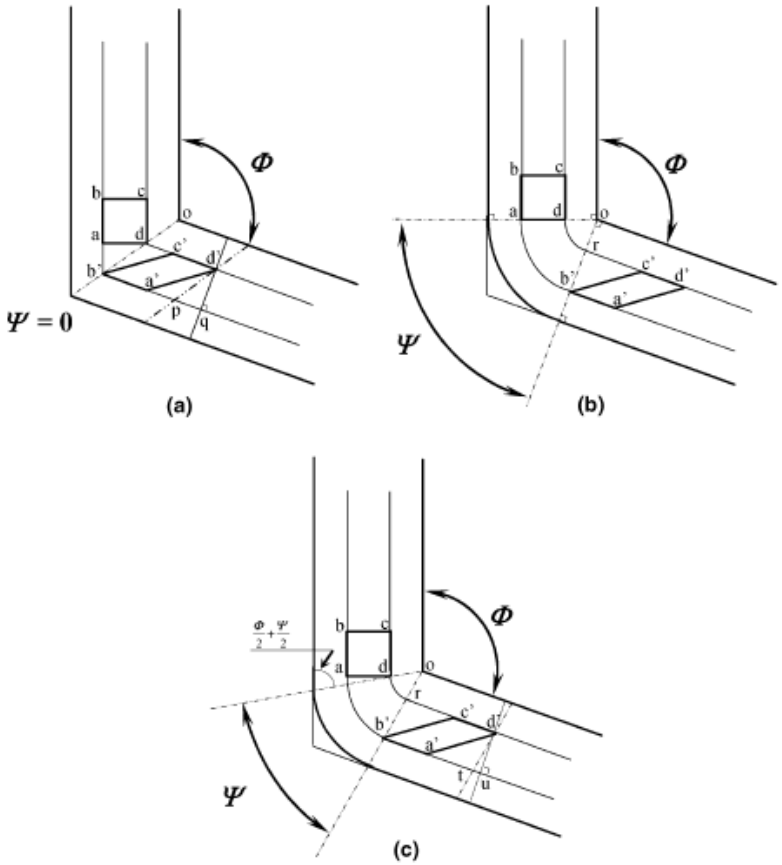

Figure 2.37: ECAP die configurations illustrating the various factors contributing to the strain imposed in each pass, where:

Φ – intersection of the entry and exit channel of the die

Ψ – angle subtended by the angle of curvature at the intersection [186].

$$\gamma = 2cot\left(\frac{\Phi}{2}\right) \tag{2.7}$$

$$\gamma = \Psi \tag{2.8}$$

$$\gamma = 2cot\left(\frac{\Phi}{2} + \frac{\Psi}{2}\right) + \Psi cosec\left(\frac{\Phi}{2} + \frac{\Psi}{2}\right) \tag{2.9}$$

$$\varepsilon_N = \frac{N}{\sqrt{3}}\left[2cot\left(\frac{\Phi}{2} + \frac{\Psi}{2}\right) + \Psi cosec\left(\frac{\Phi}{2} + \frac{\Psi}{2}\right)\right] \tag{2.10}$$

The relationship in equation (2.10) has been investigated using a variety of die angles for Φ and Ψ and the plots are shown in Figure 2.38 [29, 182, 189]. It can be deduced that:

- Ψ has a minor effect on ε_N when Φ is greater than 90°
- Very high strains can be achieved with low values of Ψ and Φ
- When Φ is 90°, as is the case with conventional ECAP dies, the ε_N is approximately 1 for a single pass and is independent of Ψ [29, 182, 189].

Multiple ECAP passes cause sub-grain boundaries to evolve in to HAGBs via absorption of dislocations, which produces an array of ultra-fine grains, separated by HAGBs [29, 182, 189]. The effect of finer grains on the mechanical properties is described in section **2.5.2.4**. The effects of ECAP processing variables are described in section **2.5.4.**

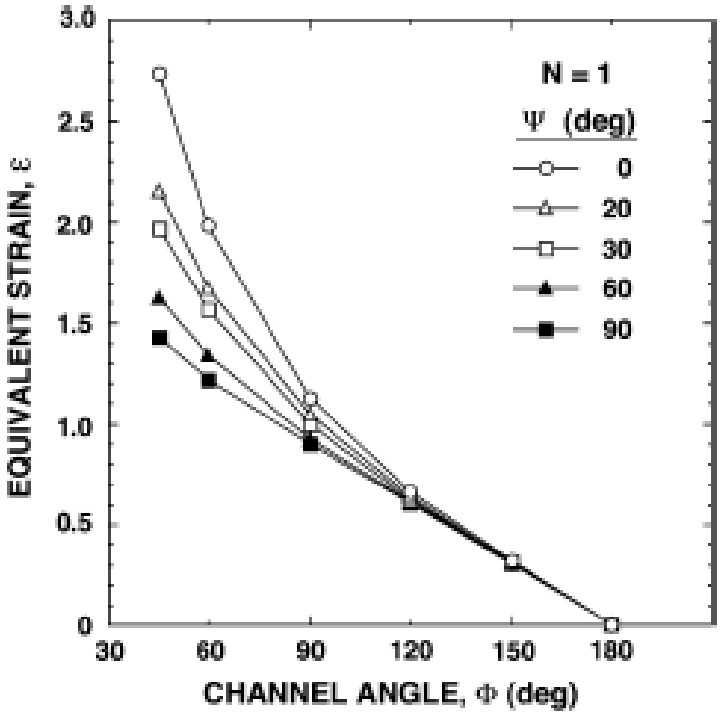

Figure 2.38: The variation of equivalent strain, ε_N, with channel angle, ϕ, and angle of the arc of curvature, Ψ, after a single pass [189].

2.5.2.4. How refining grains improves mechanical properties

Grain boundaries prevent dislocation movement therefore by decreasing the grain size, the amount of grain boundaries increases for a given area on the sample. This means that there are more regions where the dislocations can be stopped [190-192]. Small grains have a higher surface area to volume ratio, giving a greater ratio of grain boundaries to dislocations [190-192]. For many years, the development of ultra-fine grain microstructures has attracted attention in the materials industry [10]. The reason for this interest can be seen directly in the Hall-Petch equation, stating that yield stress, $\sigma_{y,}$ is given by equation (2.11) [29, 193].

$$\sigma_y = \sigma_0 + k_y d^{-1/2} \qquad (2.11)$$

where; σ_0 is the friction stress, k_y is a material dependent constant of yielding and d is grain size [10]. The yield strength increases with decreasing square root of the grain size and tensile strength is increased without reducing the toughness shown in Figure 2.39 [182, 194, 195].

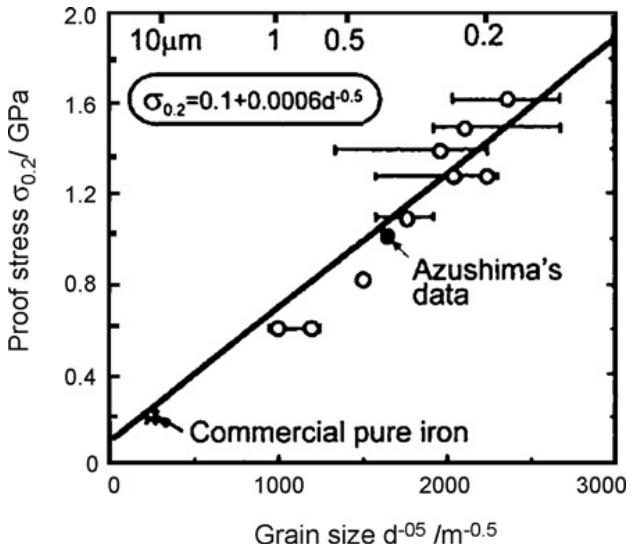

Figure 2.39: Relationship between grain size and proof stress for pure iron [194].

2.5.2.5. Characterising ECAP grain microstructure

2.5.2.5.1. Texture

The grain size and shape changes that happen in ECAP can be characterised using the techniques described in section **2.1.4.** However, the orientation of grains changes due to the shear path and the distribution of grain orientation is known as texture. Texture can influence strength, formability, grain refinement and is most often associated with plastic anisotropy. Plastic anisotropy describes the dependence of the plastic deformation response on the direction of loading [11]. A common method to quantify texture and the evolution of microstructure in ECAP is electron back-scatter diffraction, EBSD.

2.5.2.5.2. Electron back scatter diffraction (EBSD)

The process of EBSD is illustrated in Figure 2.40 [196]. An electron beam contacts a tilted crystalline sample, which causes diffracted electrons to form a pattern on a fluorescent screen. The pattern depends on crystal structure and orientation of the region of the sample from where it was created and EBSD provides absolute crystal orientation with sub-micron resolution [196, 197]. An example of the use of EBSD in an Al-1Mg solid solution material, which has been annealed at 500°C for 1h, is shown in Figure 2.41 [198]. The colours of the grains correspond to their orientation, which is determined by the triangle. The red lines between certain grains indicate the presence of high angle grain boundaries, where the misorientation angle is greater than 15° in Figure 2.41 [198]. EBSD helps examine evolution of grains in samples subject to the different processing routes of ECAP.

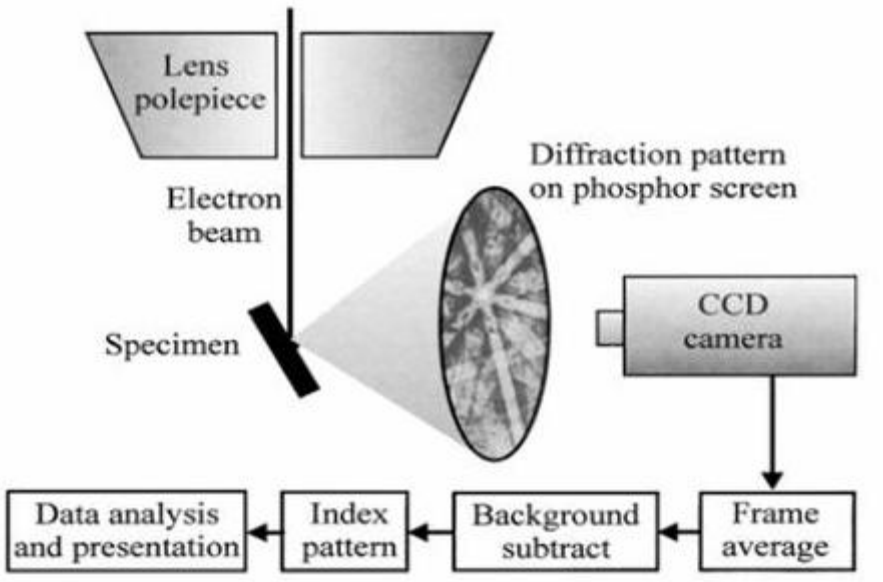

Figure 2.40: The EBSD process [196]

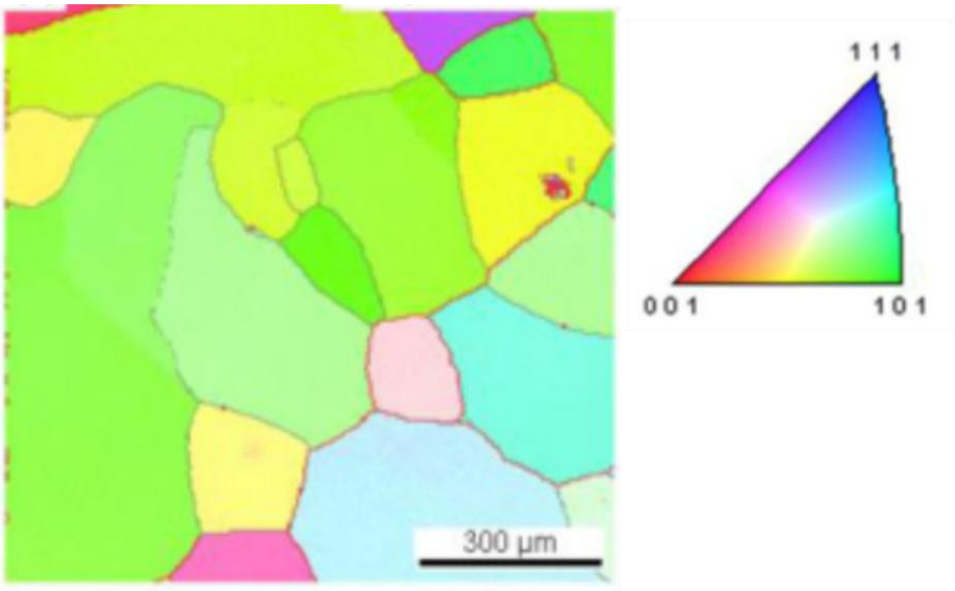

Figure 2.41: EBSD map of an Al-1Mg solid solution alloy that was annealed at 500°C for 1h with the colours corresponding to the orientation of the grains determined by the unit triangle [198].

2.5.3. Processing routes in ECAP

Although this thesis is mainly concerned with single pass processing, it is important to note that different slip systems can be introduced to the sample by multiple passes using one of the following processing routes or a combination of them. The first route involves multiple passes without rotation, called 'route A'. The next involves rotating the sample at 90° in alternate directions between each pass (route B_A). Route B_C consists of rotating the sample 90° in the same sense, which is either clockwise or anti-clockwise, between passes. Finally, the sample is rotated 180° between passes in route C, which is illustrated along with the other processing routes in Figure 2.42 [178, 199].

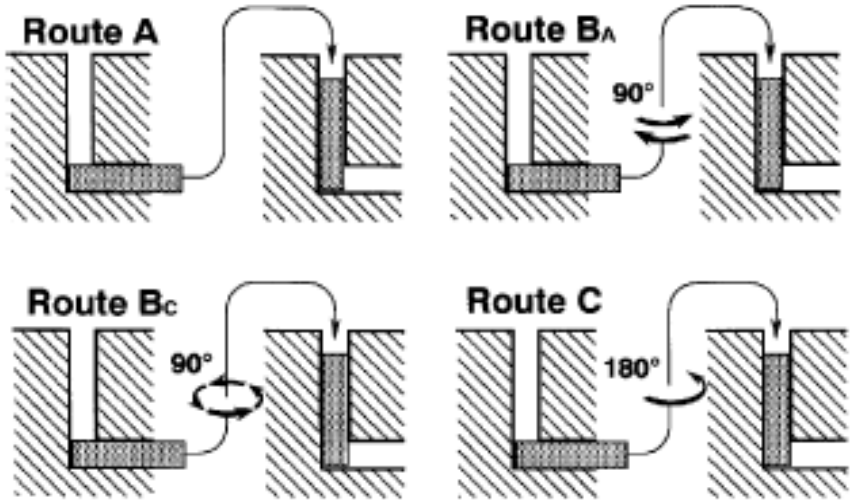

Figure 2.42: Different processing routes for ECAP [199]

2.5.3.1. Slip systems in ECAP

There are two different strain processes associated with the aforementioned processing routes. Route C and B_C are redundant strain processes and routes A and B_A are accumulative strain processes. The slip systems are illustrated in Figure 2.43, where the number above each box indicates the number of passes [29, 200]. With route C, the shear in each pass occurs on the same plane but in the opposite direction and; with route B_C, the slip in the first pass is cancelled by that in the third and likewise for passes 2 and 4 [29, 200]. This means that the strain is restored for every even number of passes. In route A, there are two distinct shear planes and for route B_A, there are four. The strain builds up with each pass through the die for these processing routes [29, 200].

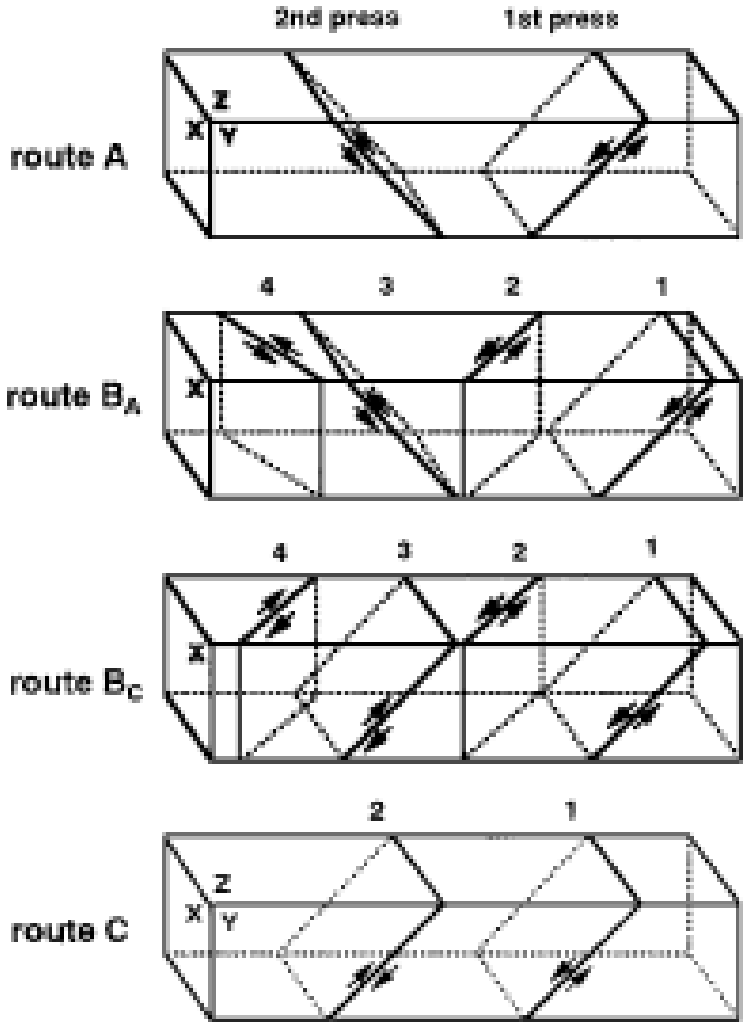

Figure 2.43: Slip systems of the different processing routes in consecutive passes along the X, Y and Z planes [29, 200]. The numbers at the top of each box indicate the number of passes.

The macroscopic distortions on the X, Y and Z planes of the samples when passed up to 8 times through the ECAP die using the different processing routes are illustrated in Figure 2.44 [29, 199]. The cubic elements are restored every two passes in route C and every four passes in route B_C, whereas they become more acute for each pass in routes A and B_A [29, 199].

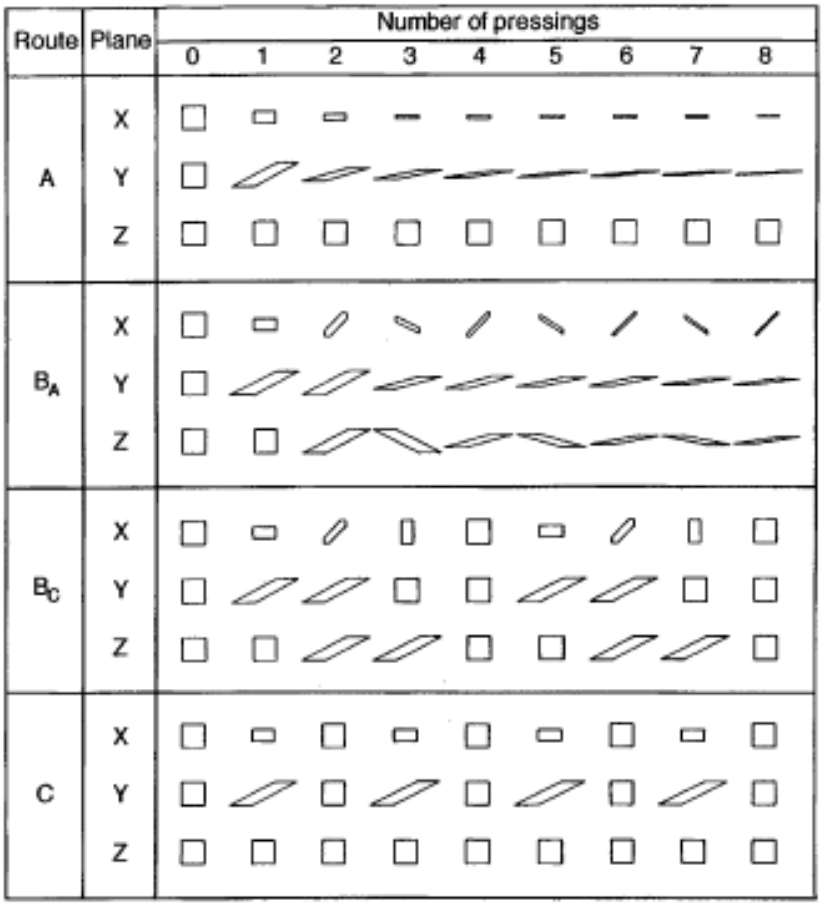

Figure 2.44: Macroscopic distortions of a sample viewed on the X, Y and Z planes for the four processing routes for up to 8 passes [29, 199].

2.5.4. ECAP processing parameters

Several parameters need to be considered for ECAP, which include channel angle, angle of curvature, pressing speed, pressing temperature and back pressure. These are discussed in the following sections with examples of ductile and less ductile alloys.

2.5.4.1. Effect of channel angle

The channel angle plays the most significant role in ECAP as it determines the amount of strain in each pass. One study investigated ECAP dies with varying Φ from 90° to 157.5° to illustrate the different strains imposed in pure aluminium at room temperature using route B_C, shown in Figure 2.45 [201]. The number of passes required to achieve a total imposed strain of ~4 was calculated using equation (2.10) as 4, 6, 9 and 19 for Φ of 90°, 112.5°, 135° and 157.5° respectively [201].

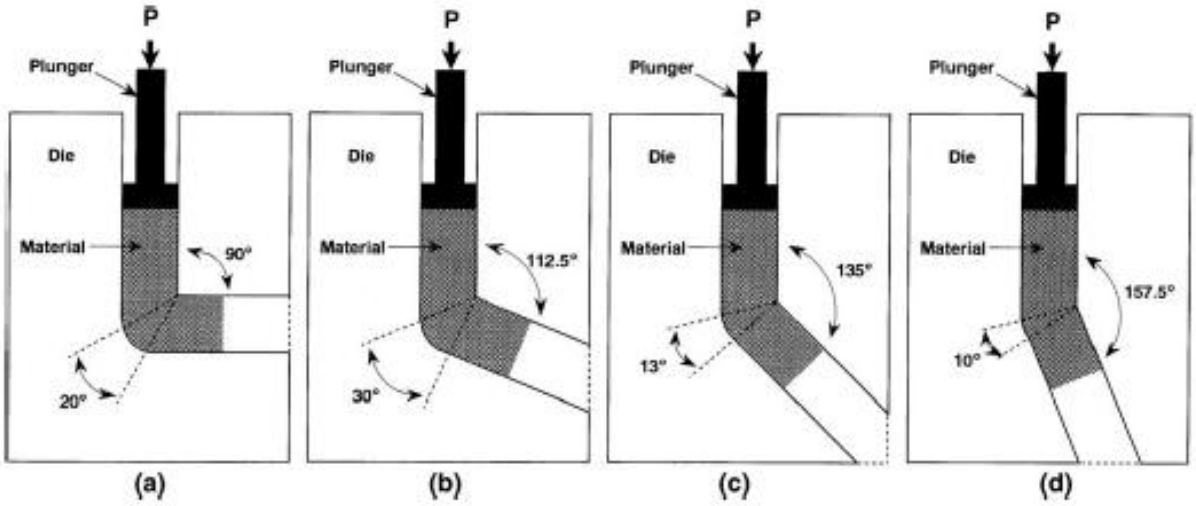

Figure 2.45: ECAP dies with varying Φ to achieve different strains with a) 90°, b) 112.5°, c) 135° and d) 157.5° [201].

The 90° angle produced finer, more equiaxed grains in fewer passes compared to the larger angles and the grain boundaries contained high angles of misorientation in the microstructure of pure aluminium, as shown in Figure 2.46 and Figure 2.47 [29, 201]. When Φ increased, the microstructure was less regular and the boundaries had a lower angle of misorientation [201]. This implies that it is important to impose a high strain with each pass, rather than having a high total accumulative strain and that an ideal ECAP die will have Φ of 90° [29, 201]. Generally, the channel angle used in ECAP is 90° due to the efficiency of imposing high strains in one pass. However, for harder, less ductile materials, such as commercially pure tungsten, or titanium, increasing the die angle is required to prevent cracking and failures in samples [202].

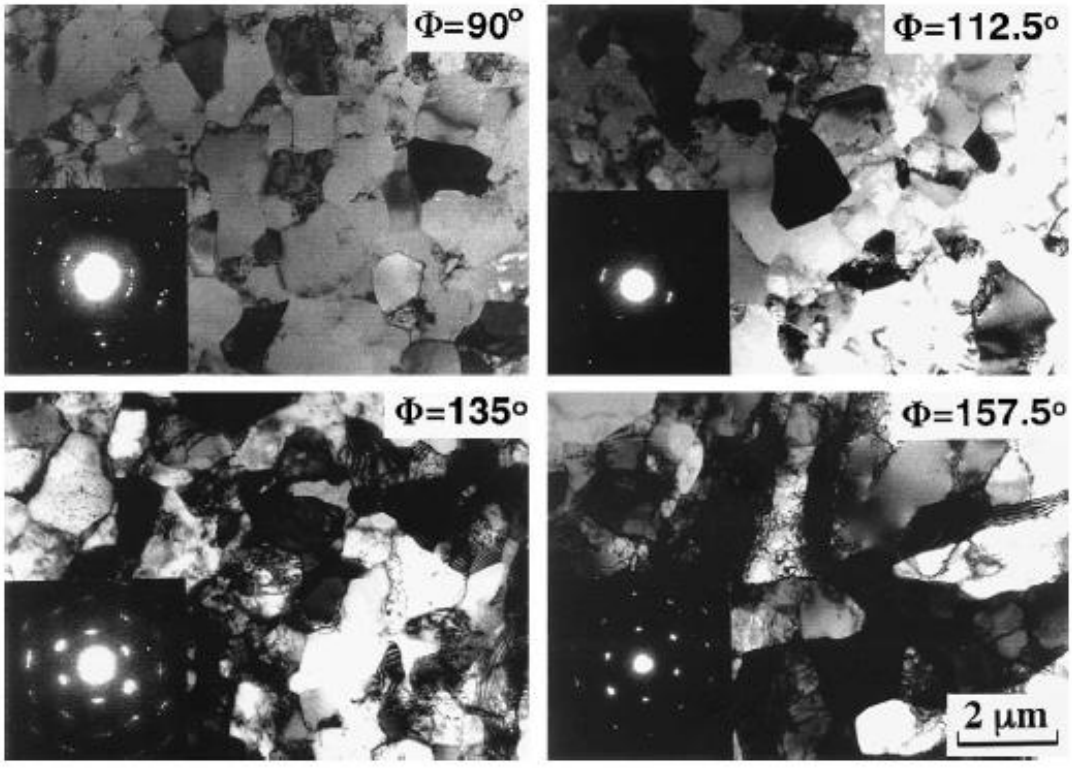

Figure 2.46: Microstructures of pure aluminium under TEM when ECAP through 90°, 112.5°, 135° and 157.5° die angles to a strain of ~4 [29, 201]

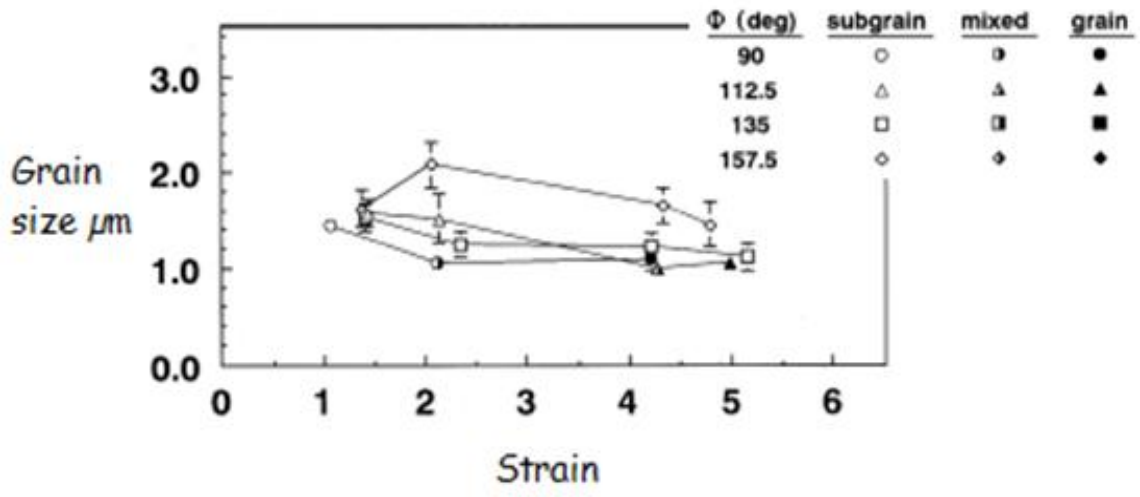

Figure 2.47: The average grain size for pure aluminium ECAP at different strains with Φ ranging from 90° to 157.5° [201].

2.5.4.2. Effect of angle of curvature

The angle of curvature, Ψ, was defined in section **2.5.2.3** in Figure 2.37 [29, 203]. The effect of Ψ to the strain imposed is minimal, according to a study on pure aluminium using two separate dies. One was a split die with a 90° channel angle and 0° angle of curvature using square billets for processing of 10mm x 10mm cross-section. The other die was solid with 90° channel angle and 20° angle of curvature using cylindrical shaped billets of 10mm diameter [204]. After four passes, the effect of Ψ on microhardness was minimal as the values did not vary significantly across the samples [204]. The reason for this small difference between the two dies can be explained by a development of a gap in the outer arc between the sample and the die wall, called the "dead zone", when the sample passes through the intersection [205, 206]. The dead zone represents the region where there is no contact between the billet and the die wall, shown in Figure 2.48 [29, 207, 208]. This is explained in more detail in section **2.5.4.5**.

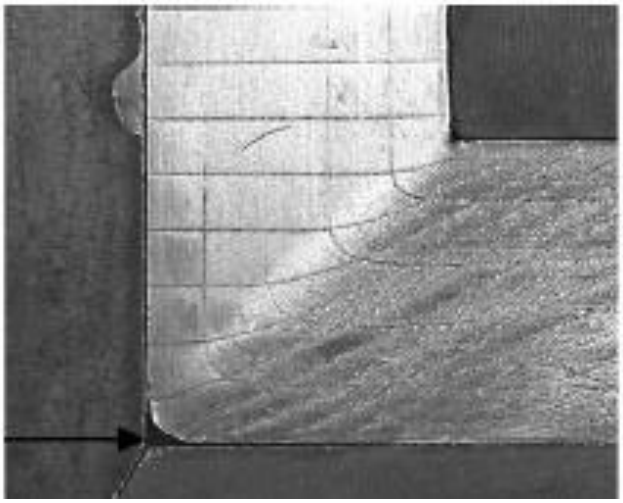

Figure 2.48: The dead zone, where there is no contact between the die wall and sample [209].

2.5.4.3. Effect of pressing speed

In commercial processing, high-capacity hydraulic presses can operate at a range of ram speeds from $\leq$1mms^{-1} to 20mms^{-1}. Varying the pressing speed from 0.02mms^{-1} to 10mms^{-1} does not significantly influence the grain sizes measured in pure aluminium and an Al-1%Mg alloy when processed by route B_C [210]. Furthermore, the yield strength did not differ greatly across different pressing speeds with each pass up to four, as can be seen from Figure 2.49. It was also found after one pass of a titanium billet that only minor differences existed in the microstructure when pressing speeds ranged from 0.2mms^{-1} to 2.8mms^{-1} [29, 92].

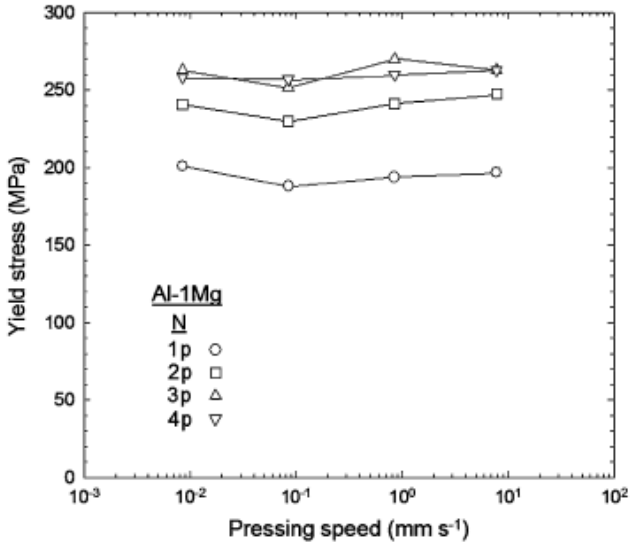

Figure 2.49: Negligible effect of pressing speed on the yield strength achieved. It can be seen that the strength increased with every pass up to four passes [29]

2.5.4.4. Effect of pressing temperature

The pressing temperature is highly variable and can be altered easily. One study investigated a range of pressing temperatures from ambient to 300°C on samples of pure aluminium, Al-3Mg and Al-3Mg-0.2Sc alloys [211]. It was found that the grain size increased with increasing processing temperature of pure aluminium, Al-3%Mg and Al-3%Mg-0.2%Sc alloys from room temperature to 300°C, as illustrated in Figure 2.50 [211]. Another finding was that the fraction of LAGBs increased with increasing temperature. This was attributed to the higher rate of recovery at elevated temperatures, which leads to dislocation annihilation instead of dislocation absorption into the sub-grain walls [211].

However, another finding was that there was a material dependence. For temperatures above 200°C for pure aluminium and above 300°C for the Al-3%Mg alloy, the transition from HAGBs to LAGBs occurred but the Al-3%Mg-0.2%Sc showed HAGBs at all processing temperatures [211]. Similar findings were also seen for commercial 5052 aluminium alloy pressed between temperatures of 50°C-300°C [212]. Although elevating the extrusion temperature causes the material to soften and facilitate the action of ECAP, the optimum grain sizes and microstructures can be achieved when using the lowest possible temperature without cracking occurring in the sample, for example, room temperature for aluminium alloys with the presence of a back pressure [212-214].

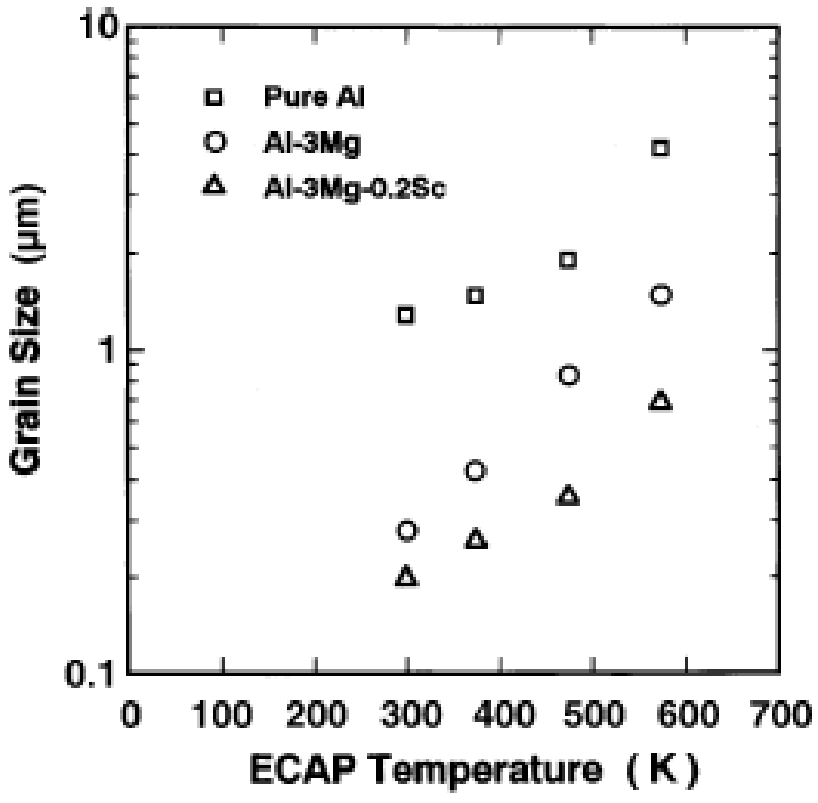

Figure 2.50: Increased grain size with increasing temperature [211]

2.5.4.5. Effect of back pressure

A pressure applied in the opposite direction to the flow of the sample through the die is referred to as back pressure and it can be applied in a couple of ways as shown in Figure 2.51 [29]. The common methods to achieve back pressure is to use another plunger in the exit channel, which gives control over the back pressure applied, or leave a dummy block in the exit channel, such as another sample or copper front stopper [209].

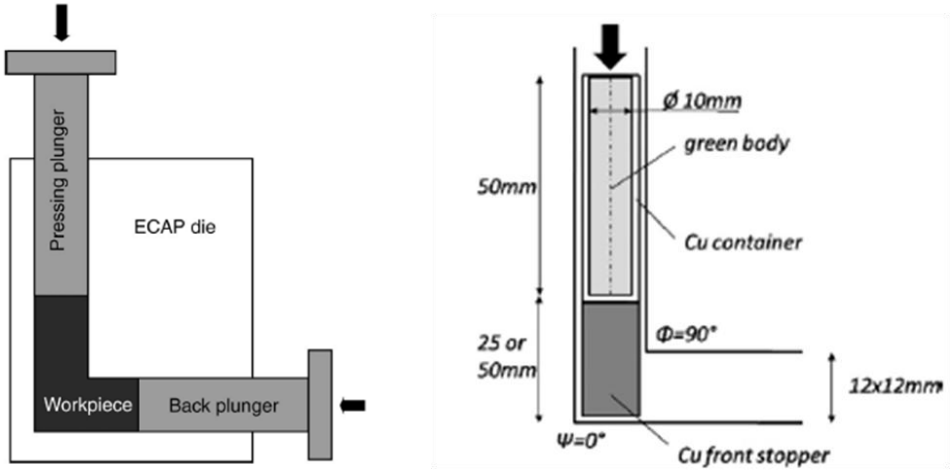

Figure 2.51: An illustration of the back pressure applied in ECAP consolidation via plunger (left) and copper front stopper (right) [215].

Without back pressure, macroscopic cracks appear on the surface of billets, shown in Figure 2.52 [209]. This has been attributed to non-uniform stress-strain distributions during deformation without back-pressure. Several finite element studies on the shear strain in single and multi-pass ECAP experiments reveal that the centre of billets, away from the die walls, experienced the expected deformation and strains from equation (2.10) [208, 216-218]. However, the region of the billet next to the die wall channel angle experienced much lower strains due to frictional effects, as shown in Figure 2.53a and Figure 2.53b [208, 216-218].

Figure 2.52: Cracks appear on the surface of pure magnesium after one pass of ECAP at room temperature through a 120° die [209]

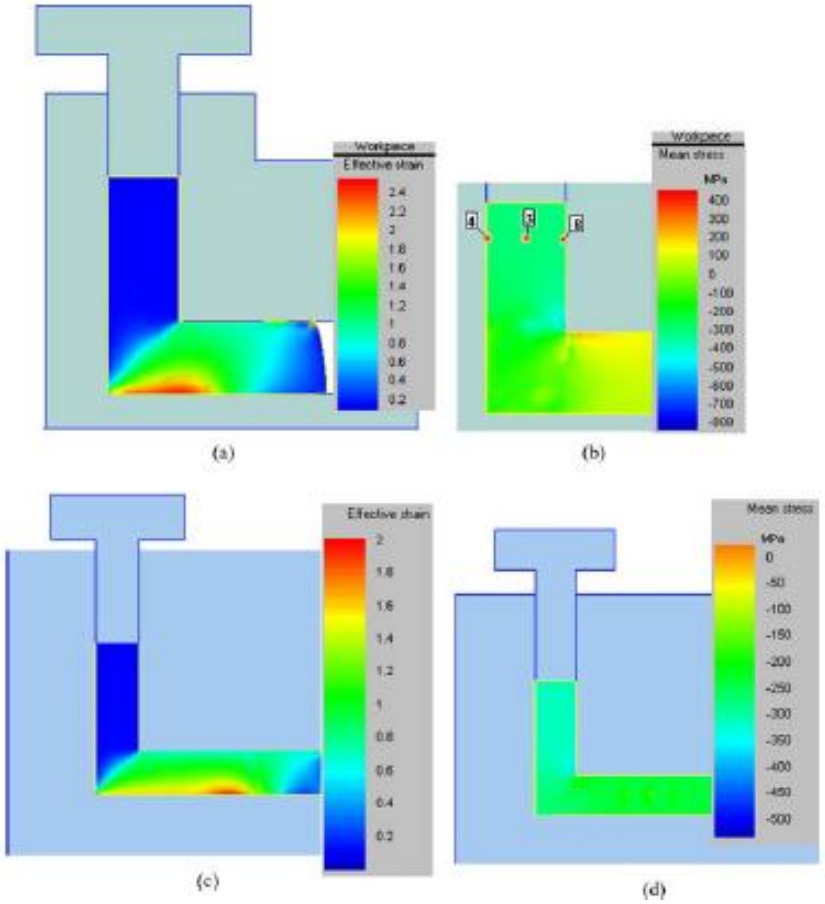

Figure 2.53: Distribution of stress and strain during ECAP; without back-pressure a) and b); and with back pressure c) and d). Effective strain is shown in a) and c), and mean stress is shown in b) and d) [209].

Back pressure helps to homogenise the flow of the metal as it experiences shear and reduces die wall friction. It was mentioned in section **2.5.4.2** that a 'dead zone' exists between the die wall and sample on the outer arc during ECAP, which led to non-uniform grain refinement. When back pressure is introduced, the dead zone is reduced allowing better stress-strain distribution across the sample, shown in Figure 2.53c and Figure 2.53d [29, 209, 219]. This is due to an increase in hydrostatic pressure inside the channel [29, 209, 219]. For pure copper, a back pressure of 300MPa is required to prevent cracking in 16 or more passes [29, 219]. This was also observed for a quenched aluminium 6061 alloy processed at room temperature with and without back pressure. Without a back pressure, the alloy did not form in the first pass. However, with an applied back pressure of 450MPa, the sample could be processed up to four times without signs of cracking [29].

2.5.5. ECAP as a tool for powder consolidation

ECAP has been generally associated with processing of solid metals, examples of which have been given in sections **2.5.4.1** through **2.5.4.5**. However, it can also be used to consolidate metal powders [220]. There are two methods of processing powdered metals through ECAP. One is to compact the powder before inserting it into the ECAP die, for example by cold compaction or by cold isostatic pressing, CIP. In one study, CIP was used to compact Al2025-3Fe-5Ni to a density of 2.271g/cm^3 before ECAP increased it to 2.935 g/cm^3 after one pass without back pressure [221]. The other method involves putting the powders into a can made of a deformable material such as copper, followed by ECAP [222].

In cold compaction, the powder particles are deformed plastically until the compaction pressure is reached. In ECAP, the particles experience high plastic strains as they pass through the channel angle and they are severely deformed. The shearing breaks the oxide layer on aluminium and exposes fresh surfaces of particles and, if back pressure is applied, compressive stress allows good contact between them, which provides excellent bonding at room temperature even after one pass, as shown in Figure 2.54 for pure aluminium particles [223]. There are several studies on the ECAP consolidation of aluminium P/M and its alloys, some of which are described in the following sections.

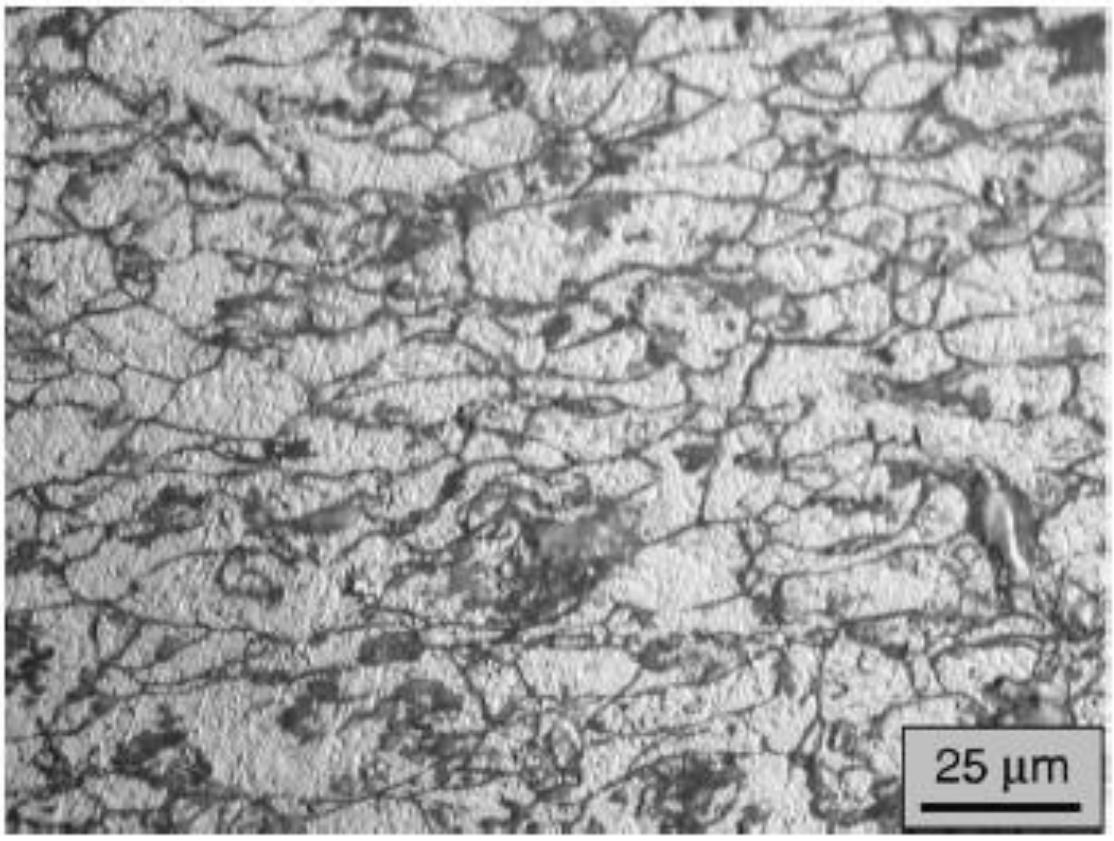

Figure 2.54: Pure aluminium particles that have been consolidated to 100% density after 1 pass of ECAP under back pressure [223].

2.5.5.1. Pure aluminium particles

One study compared ECAP with and without back pressure (BP) and direct extrusion (with a ratio of 11:1) on the consolidation of nitrogen atomised Al particles [215]. The BP was provided either by a copper front stopper or using a hydraulic ram applying pressure of 170MPa, 220MPa or 270MPa. The temperature of ECAP ranged between 250°C-500°C and extrusion temperature was between 350°C-500°C. The powders were pre-compacted using cold isostatic pressing and the starting material was ~1µm size.

Firstly, a significant increase in the pressing load was observed for direct extrusion compared to ECAP with and without BP as shown in Table 2.4 [215]. This meant that ECAP processing could be done at lower pressing temperatures. However, macroscopic cracks appeared after ECAP without BP parallel to the shear plane, which formed due to non-uniform deformation in the cross-section where a gradient of straining exists, as discussed in section **2.5.4.5** [29, 209, 215, 219]. Application of BP in the form of a copper front stopper meant that the hydrostatic pressure in the channel increased, which reduced the dead zone and hence prevented cracks. Nevertheless, the pressing load increased with the presence of a front stopper and even though increasing the ECAP temperature to 400°C decreased the pressing load, macroscopic cracks appeared in the sample again [215]. By using a hydraulic ram, BP can be controlled and it does not increase the frictional force, hence the pressing load is lower compared to using a front stopper.

Table 2.4: Process conditions for direct extrusion and ECAP, where p_{max} is the maximum pressing load needed during compaction, R_m is the ultimate tensile strength and A is ductility [215].

Direct extrusion					
T_{ext} [°C]	350		400	450	500
p_{max} [MPa]	1376		1118	986	797
R_m [MPa]/A [%] at RT	310/9		305/8.7	290/10.9	280/10.4
R_m [MPa]/A [%] at 300 °C	186.7/1.7		181.7/1.5	168.9/2.2	159.9/3.3
ECAP with backpressure applied by front stoppers					
T_{ECAP} [°C]	250				350
Front stopper length [mm]	0		25	50	50
p_{max} [MPa]	670		830	820	410
R_m [MPa]/A [%] at RT	305/1.5		309/1.9	310/2.5	290/2.1
R_m [MPa]/A [%] at 300 °C	188/0.5		165/0.5	155/0.4	–
ECAP with backpressure applied by hydraulic valve					
T_{ECAP} [°C]	250			400	
Backpressure [MPa]	94	167	271	94	167
p_{max} [MPa]	535	510	620	292	296
R_m [MPa]/A [%] at RT	314/2.7	316/1.6	313/1.5	296/2.5	296/5
R_m [MPa]/A [%] at 300 °C	167/0.2	171/0.2	183/0.5	169/0.3	166/0.2

After direct extrusion, the grains were elongated in the extrusion direction with Al_2O_3 particles mainly distributed at the grain boundaries for all extrusion temperatures. At higher temperatures, slightly coarser microstructures were observed and the Al_2O_3 particles were completely distributed at the grain boundaries, which pinned the microstructure and gave stability even after annealing at 350°C for 20h. The microstructure of the ECAP samples was similar to that seen in the high temperature extrusions, whereby the oxides were only located at the grain boundaries. Elongation of the grains occurred along the shear plane as well [215].

Finally, the yield strength achieved for the samples processed by ECAP at 250°C with BP applied by a hydrostatic ram was higher than that achieved by direct extrusion at 350°C. This was attributed to higher deformation energy introduced at lower temperatures causing an increase in dislocation density [215]. However, the lower ductility of the ECAP samples was due to disadvantageous orientation of the grains at an angle of 45° to the loading direction of the tensile test [215].

Applying a back pressure for consolidation requires an increase in pressing forces and the tooling can be damaged rapidly [223-226]. In another study, after one ECAP pass at 100°C using a back pressure of 50MPa, pure aluminium powder was consolidated to full density and the grain size and hardness had improved to 7.2µm and 52.7HV_{50g} respectively [223]. When this is compared to a cast ingot with a post-ECAP grain size of 535µm and 32.3HV_{50g}, it can be seen that ECAP consolidated P/M products offer beneficial end properties [223].

The behaviour of different aluminium particle sizes has been investigated using BP-ECAP at 400°C with BP of 200MPa on a mixture of micro-sized particles, ranging from 30µm-100µm, and nano-sized particles [227]. These mixtures were as follows:

- 100% nano particles (~80nm) – termed Nano100
- 80% volume of nano and 20% micro – termed Nano80
- 50% volume of nano and 50% micro – termed Nano50 [227].

After 4 passes, the Nano100 showed the highest hardness of $220HV_{50g}$ compared to $130HV_{50g}$ for Nano80 and $60HV_{50g}$ for Nano50 [227]. After one pass, the nano-particles slid over each other and did not deform [228]. Therefore, further passes were needed in order to achieve full density and break down the oxide layer [227].

However, the brittleness of the nano-particle compact was high as a result of the oxide content that developed from an amorphous alumina phase on the surface of the particles as shown in Figure 2.55 [227, 228]. Having coarser grains increases the ductility of the material, which can be advantageous depending on the application, although the strength decreases [227].

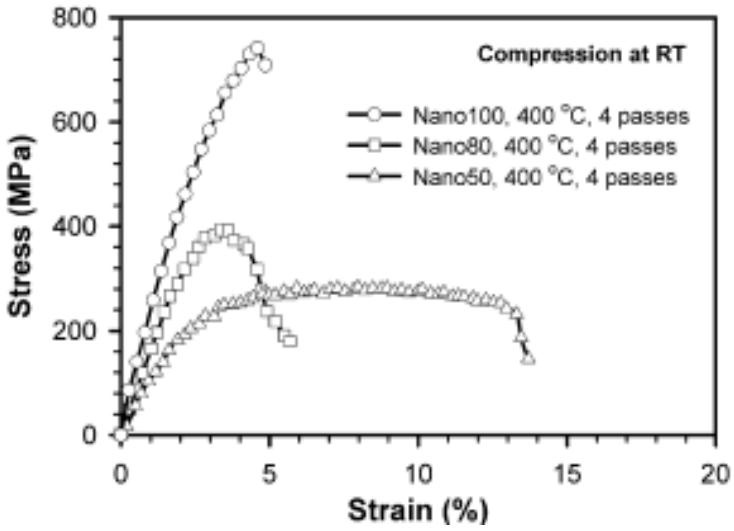

Figure 2.55: Compressive stress-strain curves for the Nano-100, -80 and -50 after four passes of ECAP at 500°C [227].

2.5.5.2. Al2024/Al_2O_3 & Al-Al_2O_3 powder composites

The composition of Al2024 is given in Table 2.5 [229]. In this study, a comparison between the conventional press and sinter route and consolidation via ECAP was made. In the conventional P/M method, the samples were vacuum sintered at 660°C for 2h and furnace cooled. The ECAP die had Φ of 90° and Ψ of 20°, the powders were encapsulated and passed through the die with and without back pressure. The back pressure was applied by having an aluminium block in front of the sample and up to two passes were done using route A [229].

Table 2.5: The composition (wt%) of Al-2024

Element	Cu	Mg	Mn	Fe	Si	Zn	Ti	Cr	Al
wt%	4.4	1.5	0.6	0.5	0.5	0.25	0.15	0.1	Balance

The results of this study have been summarised in Table 2.6. The density after one pass in ECAP was higher for both materials than the conventional press and sinter route, even without back pressure, and increasing the number of passes improved the relative densities further [229]. This can be attributed to the shearing as the sample is pushed through the 90° angle, which exposed fresh particle surfaces and the compressive stress from back pressure led to good particle bonding [223, 229]. The advantage of this mechanism in ECAP is that the particle bonding occurs without the need for high temperatures or time [229].

Table 2.6: Density, grain size and hardness values of Al2024 and Al2024-Al_2O_3 composite after press-sinter and up to two passes of ECAP [229].

Condition	Theoretical density (%)		Average grain size (μm)		Average hardness $HV_{1.0\ kg}$	
	Al-2024	Al-2024/Al_2O_3	Al-2024	Al-2024 composite	Al-2024	Al-2024 composite
Compacted and sintered	85	84.4	26	20	32	37
After I pass of ECAP without back pressure	88	86.2	18	14	40	75
After I pass of ECAP with back pressure	92	90.3	14	12	43	77
After II pass of ECAP (route A) without back pressure	95	92.4	09	08	45	79
After II pass of ECAP (route A) with back pressure	97	95.2	07	06	47	81

For the Al2024-Al_2O_3 composites, the harder alumina was located inside the softer Al2024 particles and may have acted as an obstacle to dislocation movement. This would increase the yield strength by dispersion hardening [229]. The increase in hardness after ECAP is associated with the improved density as well as the grain refinement. Pores act as initiators for crack propagation, therefore increasing the density is paramount.

ECAP at 200°C was also successfully used on Al-5%Al_2O_3 particles using a similar die and using encapsulation [230]. The starting particle shape of the Al and Al_2O_3 particles was irregular, causing bridges and high friction between particles and this raised difficulties in consolidation. After one ECAP pass, there were large micropores around the agglomerated alumina particles, which were not eliminated until the third pass after route B_C was applied, shown in Figure 2.56a and Figure 2.56c respectively [230]. After the third pass, the alumina particles had good bonding with the aluminium matrix. For comparison, samples were pressed at 200MPa, sintered at 540°C for 1h and extruded in one step at a ratio of 20:1, shown in Figure 2.56d [230]. It was observed that the alumina particles were larger after extrusion than for 3 passes of ECAP, which was due to the breakup of alumina clusters via ECAP [230].

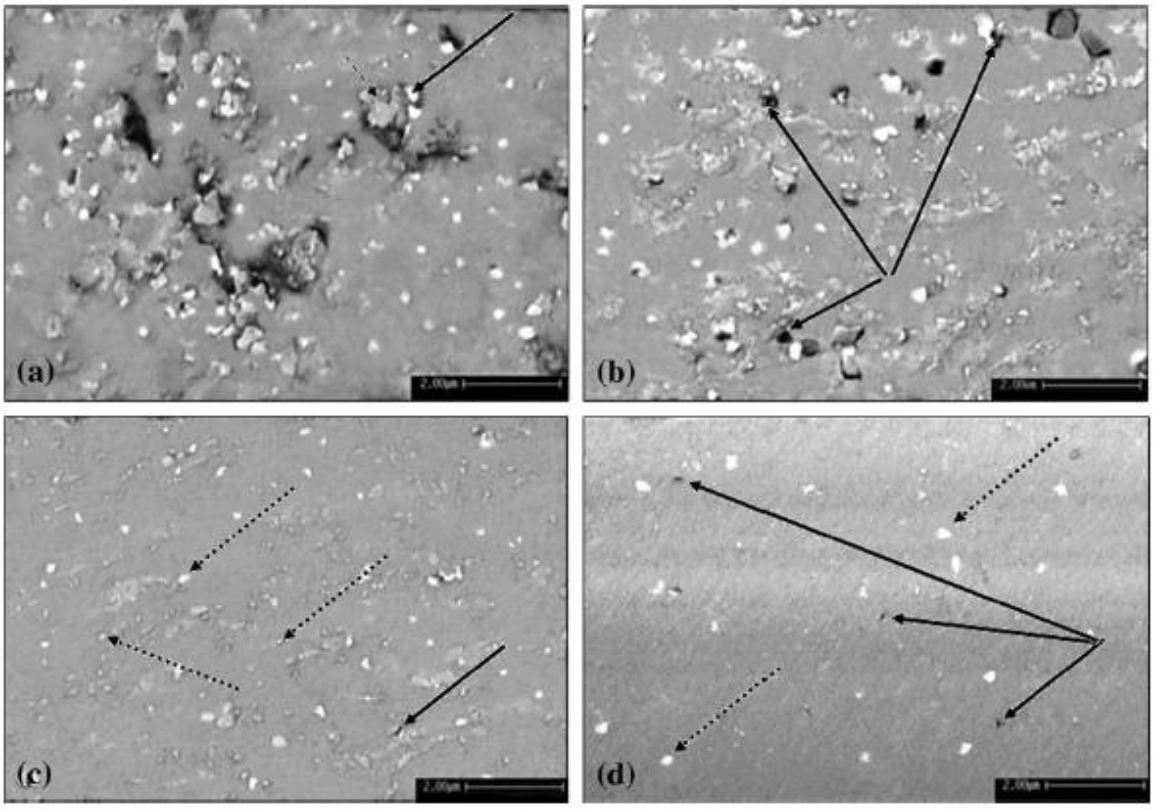

Figure 2.56: SEM micrographs of Al-5%alumina composite after a) one pass, b) two passes and c) three passes. The micrograph from extrusion is shown in d). The bold arrows point out loose alumina and the dotted arrows show loose aluminium powder [230].

After three ECAP passes, the grains were almost equiaxed and the size was reduced more than the extrusion processing to 7µm and 17.3µm respectively, shown in Figure 2.57a and Figure 2.57b respectively [230]. This was due to the repetitive ECAP passes accumulating dislocations, which caused grain refinement. Density also increased with the number of ECAP passes to 99.3% of the theoretical density, which is a result of the change in pore geometry. This was attributed to the shear mode of plastic deformation in ECAP, which favours pore closure under hydrostatic pressure [230-232]. Similarly, an increase in hardness was observed as a result of the accumulative strain and increased dislocation density resulting from smaller grain sizes, shown in Table 2.7 [230].

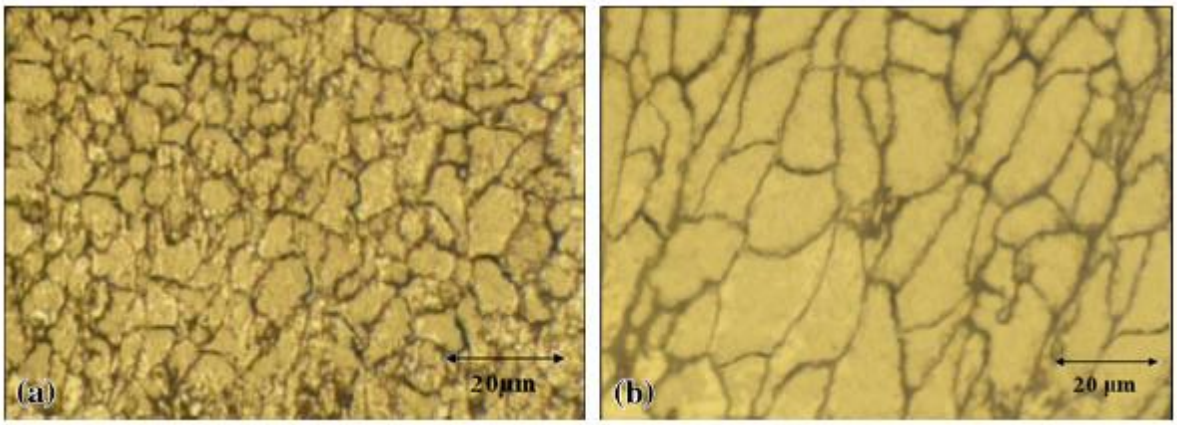

Figure 2.57: Etched optical micrographs of Al-5%Al2O3 after a) 3 passes of ECAP and b) extrusion [230].

Table 2.7: Microhardness of ECAP and extruded pure aluminium and Al-5%Al2O3

Consolidation method	Pure Al	Al-5 vol.% Al_2O_3
First pass ECAP	49.5	106.1
Second pass ECAP	61.6	134.9
Third pass ECAP	...	143.6
Extrusion	50.2	85.6

2.5.5.3. Developments in ECAP for powder consolidation

2.5.5.3.1. Torsional ECAP (T-ECAP)

Here, the sample is pushed through the 90° channel to apply shear strain followed by torsional strain in the exit channel where the die rotates about its axis, shown in Figure 2.58 [220, 233]. It can be seen that as the sample enters the rotating part of the die, the area decreases and also extrudes the sample, which creates a shear band and causes the shapes of the pore to change and close as illustrated in Figure 2.59 [220, 233]. In tests on consolidation of aluminium particles in copper tubes, it was found that T-ECAP improved the relative density of the samples to 96% after the first pass compared to 86% in conventional ECAP [220]. Microhardness results also showed an increase after one pass for T-ECAP samples to $65HV_{100g}$ compared to $55HV_{100g}$ in conventional ECAP [220]. However, it should be noted that the powder was loose in the copper can before processing and it is possible that the copper absorbs some of the shear forces from the ECAP process and deforms before the powder begins to consolidate [220].

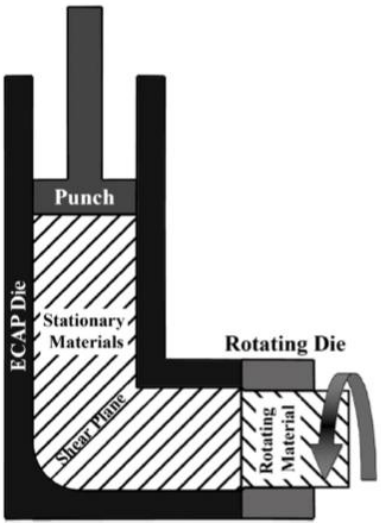

Figure 2.58: An illustration of the T-ECAP die [220].

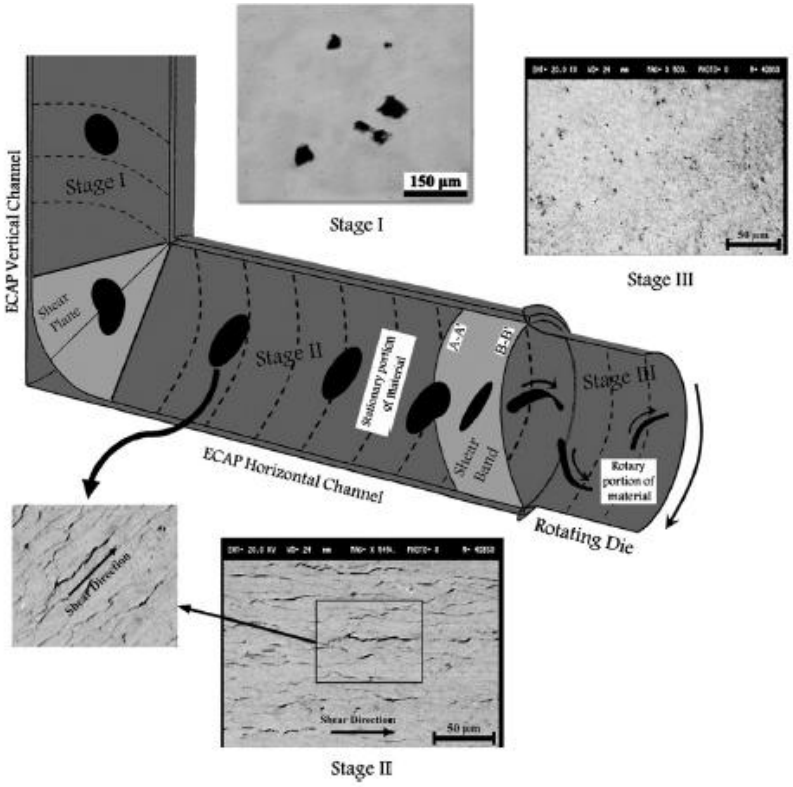

Figure 2.59: An illustration showing the porosity changes during T-ECAP [220].

2.5.5.4. Forward extrusion-ECAP (FE-ECAP)

This involves combining ECAP with forward extrusion and is illustrated in Figure 2.60 [234]. Air atomised pure aluminium powder wrapped in foil and a pure Al ingot were passed through the FE-ECAP die at 200°C. The entry channel diameter was 13mm, which reduced to 6mm after the exit channel in the ECAP section and corresponded to an area reduction of 80%. For comparison, both these materials were passed through a conventional extrusion die with a ratio of 10 at 200°C. A profile of the applied load to the FE-ECAP die during pressing is shown in Figure 2.61 [234]. The sharp rise in the extrusion stage corresponds to approximately 527MPa, which acts as BP for the ECAP process.

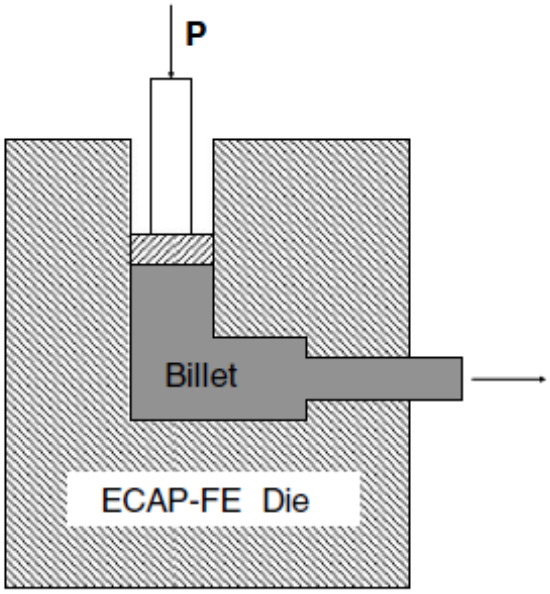

Figure 2.60: The FE-ECAP process [234]

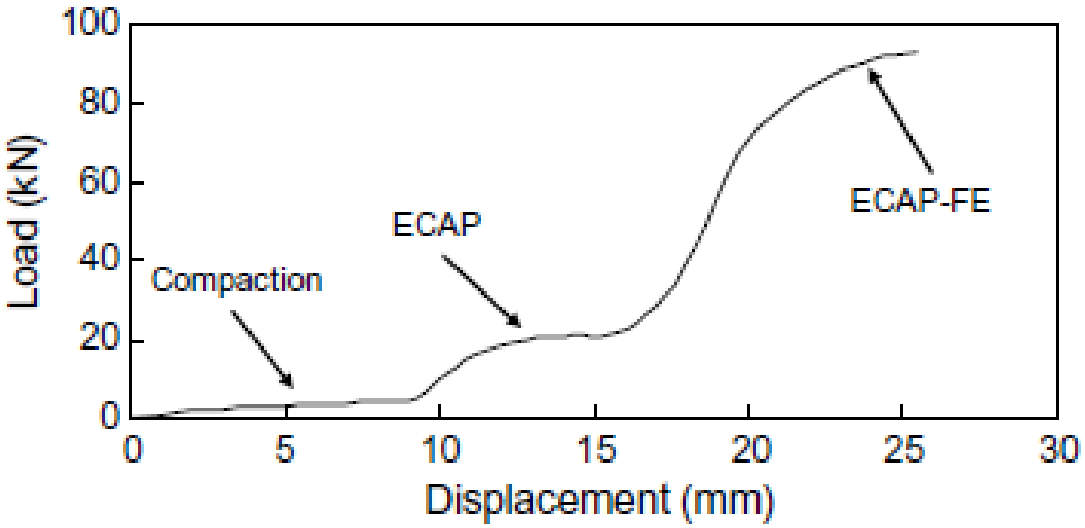

Figure 2.61: The applied load to the FE-ECAP die during pressing [234].

Microstructure analysis at the centre of the FE-ECAP P/M sample revealed relatively equiaxed grains in the transverse section, with grain sizes of 21.5µm, and elongated grains in the longitudinal section, with a width of 11.5µm, shown in Figure 2.62, which is typical of a sample processed by extrusion [234]. Excellent bonding between particles was seen and full density was achieved as shown in Table 2.8 [234]. This is due to high shear strains, which break the surface oxide film of the particle to expose a fresh surface and also changes the shape of pores from spherical to elliptical, aiding pore closure with the presence of BP. Furthermore, the increase in dislocation density and strain hardening increases the strength of material as it goes through the ECAP die and as this process can provide a back-pressure, there is no need to use a separate hydraulic ram.

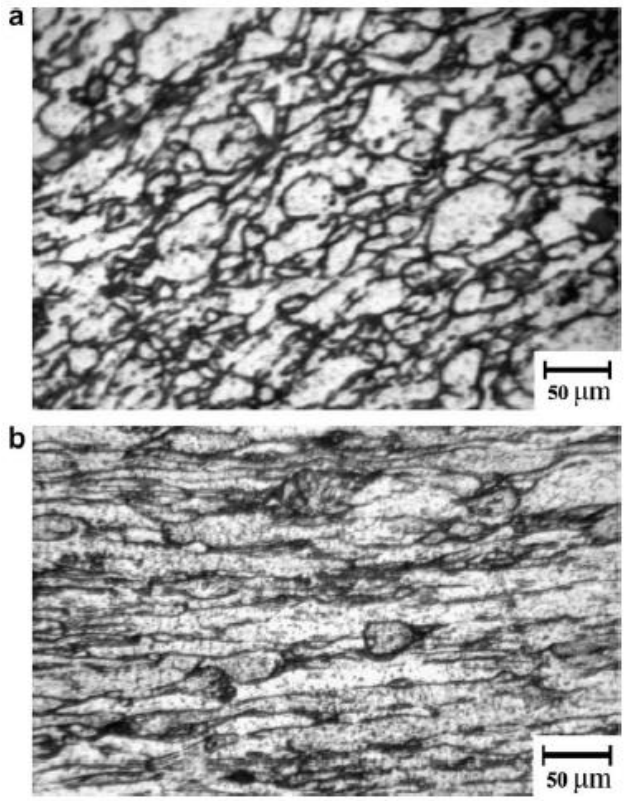

Figure 2.62: Optical micrographs of the a) transverse and b) longitudinal section of the pure Al powder consolidated by FE-ECAP [234].

Table 2.8: The experimental data for the properties of the ingot, FE, FE-ECAP and BP-ECAP samples from a separate study [223, 234]

Properties	Materials			
	Ingot sample	FE sample	ECAP–FE sample	BP–ECAP sample
Average grain size (μm)	150	30 (perpendicular section)	21.5 (perpendicular section) 11.5 (parallel section)	7.2
Density (gr/cm^3)	2.70	2.68	2.70	2.70
Vickers Hardness (HV)	31	48	81	52.7
0.2% Proof stress (MPa)	48	110	142	135
UTS (MPa)	88	137	152	160
Strain to fracture (%)	20.5	5.8	12.8	11

3. EXPERIMENTAL METHOD

3.1. Starting Materials

3.1.1. Pure aluminium powder

Commercially pure aluminium (99.9wt%) air atomised powders were supplied by the Aluminium Powder Company, AlPoCo. Sieves with different sized holes were stacked on top of each other and the particles were sieved to three sizes using a Retsch AS200 basic sieve-shaker, which operated at a frequency of 50 Hz and amplitude of 2.4mm for a period of 15 minutes as shown in Figure 3.1. The different size ranges are summarised in Table 3.1.

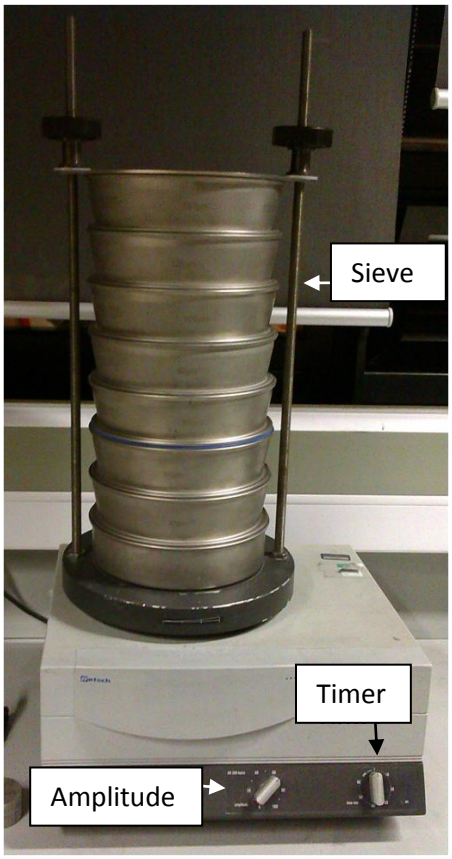

Figure 3.1: The Retsch AS200 sieve shaker with sieves stacked.

Table 3.1: Composition and size distribution of the pure aluminium powder as-supplied by AlPoCo.

Alloy	Composition (wt%)	Particle size
Coarse pure aluminium powder particles	99.9% Aluminium	>150µm
Medium pure aluminium powder particles	99.9 % Aluminium	>76µm <105µm
Fine pure aluminium powder particles	99.9% Aluminium	<45µm

3.1.2. Al-20Sn-7Si-1Cu bearing alloy (wt%)

Pre-alloyed Al-20Sn-7Si-1Cu nitrogen gas atomised powders were supplied by AlPoCo.

3.2. Cold compaction process

In order to compact the samples, a cylindrical shaped H13 tool steel die was used with an inner diameter of 12.5mm and a length of 50mm as illustrated in Figure 3.2. This allowed compacts of 20mm length to be produced.

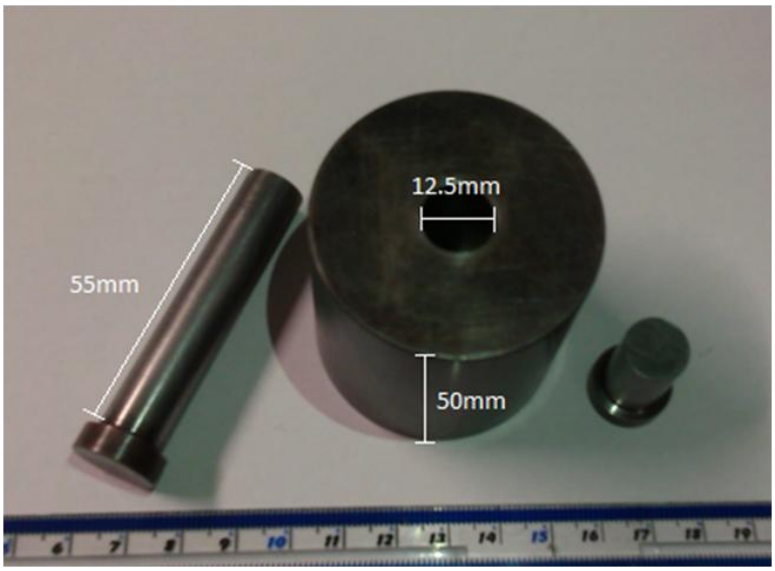

Figure 3.2: The H13 tool steel cold compaction die set.

A pre-determined mass of powder was poured into the die for each composition, shown in Table 3.2. KenoLube P11, a lubricant consisting of 2% Zn supplied by Höganäs Sweden was applied to the die wall. The die was then tapped so that the powder filled the die effectively. A double acting hydraulic press supplied by Eco Hydraulic Presses with a capacity of 300kN was used to press the powder as shown in Figure 3.3. A variety of pressures were applied in order to obtain a compressibility curve to determine the optimum pressing force, which ranged from 100-500MPa. Higher pressing forces caused tool wear therefore for the remainder of sample production, a pressure of 400MPa was used.

Table 3.2: Masses of powders used for cold compaction

Powder particles	Mass of powder (g)
Pure aluminium (<45μm)	5.2
Pure aluminium (75-105μm)	6
Pure aluminium (>150μm)	5
Al-20Sn-7Si-1Cu	7

Figure 3.3: The double acting hydraulic press supplied by Eco Hydraulic Presses.

3.3. Sintering conditions

Once the green compacts had been produced, they were either put straight into the ECAP die or sintered prior to deformation. The heating rate was kept constant at 10°C/min and the samples were furnace cooled. The tube furnace used was supplied by Elite Thermal Systems Ltd and is shown in Figure 3.4.

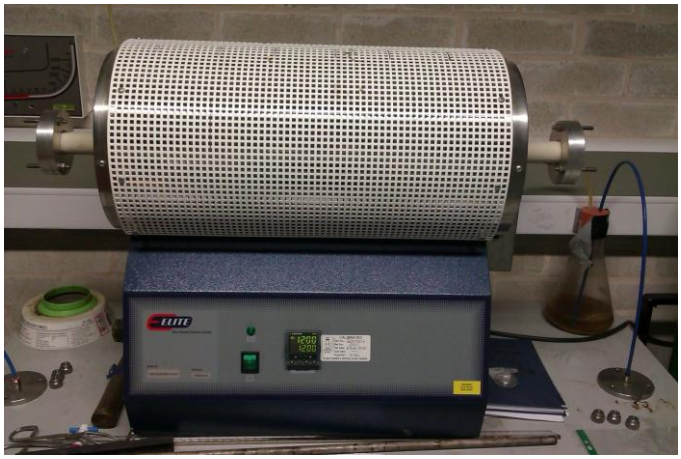

Figure 3.4: The tube furnace supplied by Elite Thermal Systems Ltd.

3.3.1. Pure aluminium sintering

The pure aluminium samples were sintered at 620°C for one hour in an atmosphere of oxygen free nitrogen and furnace cooled to room temperature [111, 115, 235, 236].

3.3.2. Aluminium bearing alloys sintering

The conditions for sintering the aluminium bearing alloys are summarised in Table 3.3. These samples were used for ECAP as well as being used for comparative analysis.

Table 3.3: Sintering conditions for bearing alloys

Material	Sintering condition
Al-20Sn-7Si-1Cu	300°C 1h, 500°C 1h & 10h and 550°C 1h oxygen free nitrogen atmosphere, furnace cooled to RT

3.4. Equal Channel Angular Pressing

3.4.1. ECAP Die

An H13 grade tool steel split die arrangement was used for ECAP illustrated in Figure 3.5. The die had nine 5mm screwholes so that the two halves could be secured together tightly in order to prevent any flash. The channel angle, Φ, was 90°, outer angle of curvature, Ψ, was 30°, channel diameter of 12.7mm and the entry and exit channels had a length of 55mm.

The lubricant used on the ECAP die wall was a mixture of 10% graphite powder, supplied by Höganäs Sweden, and ethanol. The ethanol dried off once the solution was sprayed on to the die and left behind a layer of graphite powder evenly dispersed on the channel wall.

The ECAP die, once closed, was then inserted into a large mild steel support for stability, which is shown in Figure 3.6. The force required to push the ECAP die into the steel support was 40kN, which meant that there was a compressive force on the ECAP die pushing the die halves together to reduce the risk of flash further.

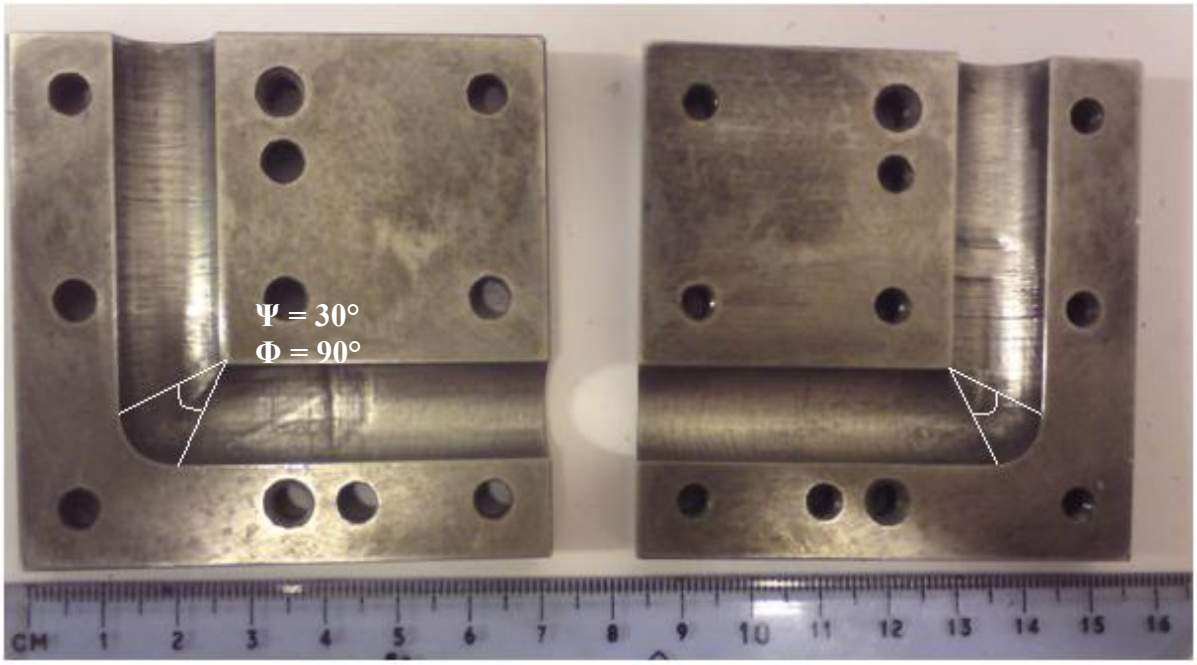

Figure 3.5: The H13 tool steel split die arrangement with a channel angle, Φ, of 90°, outer angle of curvature, Ψ, of 30°, channel diameter of 12.7mm and entry and exit channel lengths of 55mm.

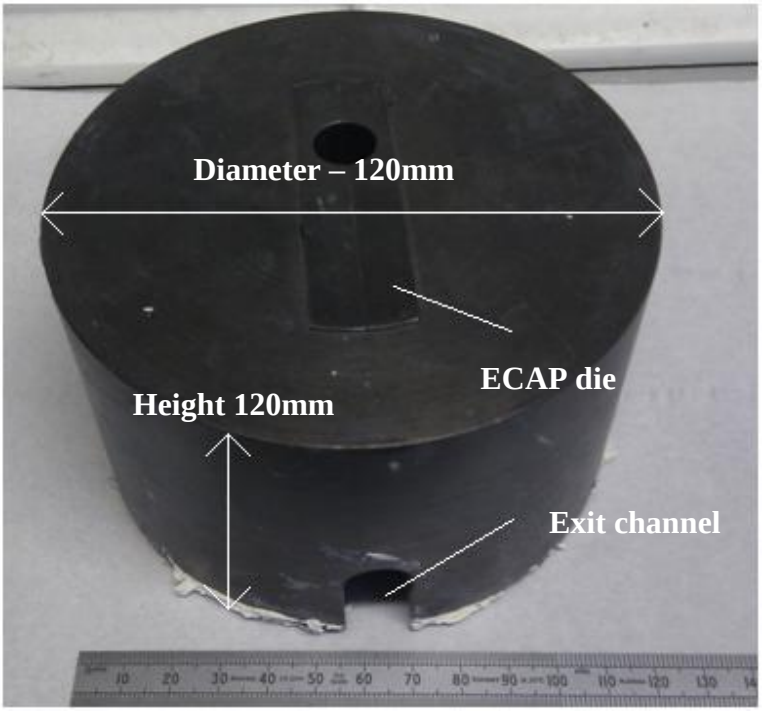

Figure 3.6: The ECAP die in the ring support with outer diameter of 120mm and length of 120mm.

3.4.2. ECAP conditions and sample extraction

ECAP was performed at room temperature and the hydraulic press operated at a speed of 300mm/min. Once the sample had been subjected to ECAP, it was either extracted from the die by being pushed out via another sample through the die or the ECAP die was taken out of the mild steel support, unscrewed and opened. The former meant that samples could be discontinuously passed through the die without having to take it apart and hence saved time compared to the latter. This also meant the samples left in the exit channel of the die provided some back pressure in order that the consolidation of the samples was improved slightly.

3.5. Material characterisation

3.5.1. Apparent density of powder

A container of 25cm^3 volume with mass of 40.935g was used. The powder was poured into the container until it overflowed the sides. The powder was then levelled off using a flat knife and the combined mass was measured. The mass of the powder was worked out by subtracting the mass of the container from the combined mass and the apparent density was worked out as shown in equation (3.1).

$$\rho = mass/volume \qquad (3.1)$$

3.5.2. Density measurements post processing

After cold compaction, sintering and ECAP, the density of the sample was measured using Archimedes' principle, where the mass of the sample was determined when it was dry and in air. Following this, the samples were impregnated with water under vacuum and the mass was measured when in air and when submersed in water. Using equation (3.2) the density of the compacted, sintered and ECAP samples was calculated.

$$\rho_C = \left(\frac{m_d}{m_w - m_i}\right) . \rho_w \qquad (3.2)$$

where m_d is the mass of the dry sample in air, m_w is the mass of the water impregnated sample in air, m_i is the mass of the water impregnated sample immersed in water and ρ_w is the density of water at room temperature, which is 0.997g/cm^3 [237].

3.5.3. Sample preparation

3.5.3.1. Sectioning

Prior to microstructure analysis, the green, sintered and ECAP samples were cut parallel to the extrusion direction, named the 'longitudinal section', and perpendicular to the extrusion direction, named the 'transverse section'. All sectioning was done using a diamond edged blade, supplied by National Diamond Laboratories, with a 4 inch outer diameter, 0.012 inch thickness and 0.5 inch hole through the centre that was attached to Beuhler's Ltd Low Speed Cutter at a speed of 200rpm, shown in Figure 3.7.

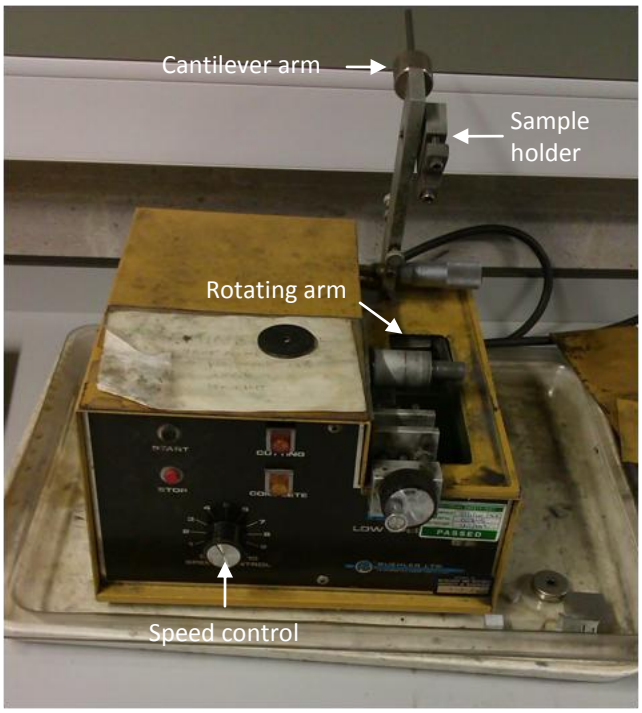

Figure 3.7: The Low Speed Cutter used to section the samples, supplied by Beuhler Ltd.

3.5.3.2. Mounting

All of the samples were cold mounted using DuroCit powder and liquid supplied by Struers. Two parts of powder to one part of liquid was mixed together and poured into a sample cup having a diameter of 32mm, with the sectioned sample face down at the bottom of the cup. Once fully set after 20 minutes, the mounted sample was ready for grinding and polishing.

3.5.3.3. Grinding

Buehler silicon carbide wet and dry grinding discs were used to grind the samples until they were flat and suitable for polishing. The following grades were used from the coarser 120, 240, 400, 800, 1200, 2500 and finest 4000 and water was used for wet grinding.

3.5.3.4. Polishing

Once the grinding stages had been completed, the samples were polished using a 6µm MDMOL polishing cloth using DiaDuo 6µm lubricant and final polishing using a 1µm MDCHEM polishing cloth using OP-S colloidal silica. The 1µm polishing cloth was moistened with water prior to the application of colloidal silica and all the polishing discs and lubricants were supplied by Struers. The motorised polishing wheel used was a Struers LaboPol-5 operating at a rotating speed of 300rpm and is illustrated in Figure 3.8.

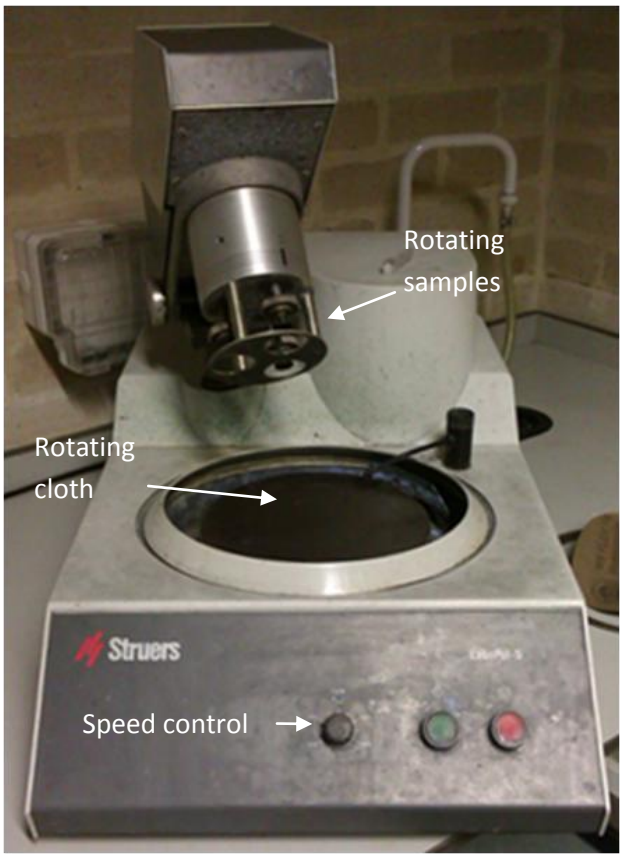

Figure 3.8: The Struers LaboPol-5 polishing machine.

Between polishing stages, the faces of the samples were washed and cleaned using dampened cotton wool with Teepol and warm water to remove any debris. Then ethanol was sprayed on to the surface and a hot air dryer was used to evaporate the ethanol so that the sample could be investigated under the light microscope and SEM.

3.5.3.5. Etching

In order to reveal the microstructure and grain size, shape and morphology of the samples at the green, sintered and ECAP stage, either Keller's etchant or Kroll's reagent were used, which are listed in Table 3.4 [238]. The polished samples were immersed in the etchant at room temperature until the surface from the final stages of polishing turned dull, which was approximately 10 seconds. Once this happened, the sample was immediately washed using warm water, the surface was sprayed with ethanol, hot air dried and ready for analysis.

Table 3.4: Keller's etchant and Kroll's reagant solutions [238]

Keller's etchant	Kroll's reagent
190ml distilled water	2ml hydrofluoric acid
5ml nitric acid	198ml distilled water
3ml hydrochloric acid	
2ml hydrofluoric acid	

3.5.4. Aluminium grain & silicon size analysis

The samples were investigated using an optical microscope from Zeiss, the model of which was the Axioskop 2. Magnifications of 5x, 10x, 20x and 50x optical magnification were used and images were taken using Axiovision 4.6.3 software. Other images came from an SEM supplied by Joel, the model of which was the 6060, using 20kV accelerating voltage with secondary electron imaging (SEI) and back-scatter electron imaging (BSEI) modes. Magnification ranged between 100x to 1500x.

These images were then analysed using JMicrovision v1.27 and individual grains were characterised by scaling the image according to the scale bar and setting the parameters for measurement. These were the equivalent diameter of circle, length and width. A total of 10 optical images were taken at random locations throughout the various regions of the samples, unless otherwise stated in the results section, and grains were drawn around for each sample at the green, sintered and ECAP stages. Histograms were also made of these parameters to analyse the mode of distribution of grain sizes and silicon sizes.

EDX compositional analysis was done on random areas of samples using the SEM 6060. Both point and area analyses were used in determining the chemical distribution of the samples and the silicon maps obtained were used to quantify silicon sizes.

3.5.5. Hardness testing

Vickers' hardness testing was done using an Indentec semi-automatic hardness tester shown in Figure 3.9. Ten indents were made on each sample with an applied load of 2.5kg for seven seconds and an average hardness was determined.

Figure 3.9: The Indentec hardness tester.

4. RESULTS & DISCUSSION

4.1. Pure aluminium powder

4.1.1. Starting powder

4.1.1.1. Size and morphology

The starting pure aluminium particles for the coarse (≥150µm), medium (75-105µm) and fine (≤45µm) size ranges are shown in Figure 4.1, Figure 4.2 and Figure 4.3 respectively via optical imaging and Scanning Electron Microscopy. The morphology of all powders was mainly irregular, although the ≤45µm size exhibited slightly more regular shapes. The coarse particles had an average equivalent circular diameter, ECD, of 430.41 ± 202.52µm, the medium particles of 103.27 ± 23.35µm and the fine particles of 28.48 ± 10.74µm. A summary of the average length, width and ECD of the powder particles is shown in Table 4.1. Typical histograms for the length, width and ECD of the medium sized pure aluminium particles are shown in Figure 4.4. The typical histograms for length, width and ECD of the fine and coarse starting powders are shown in Appendix 6-1 and Appendix 6-2.

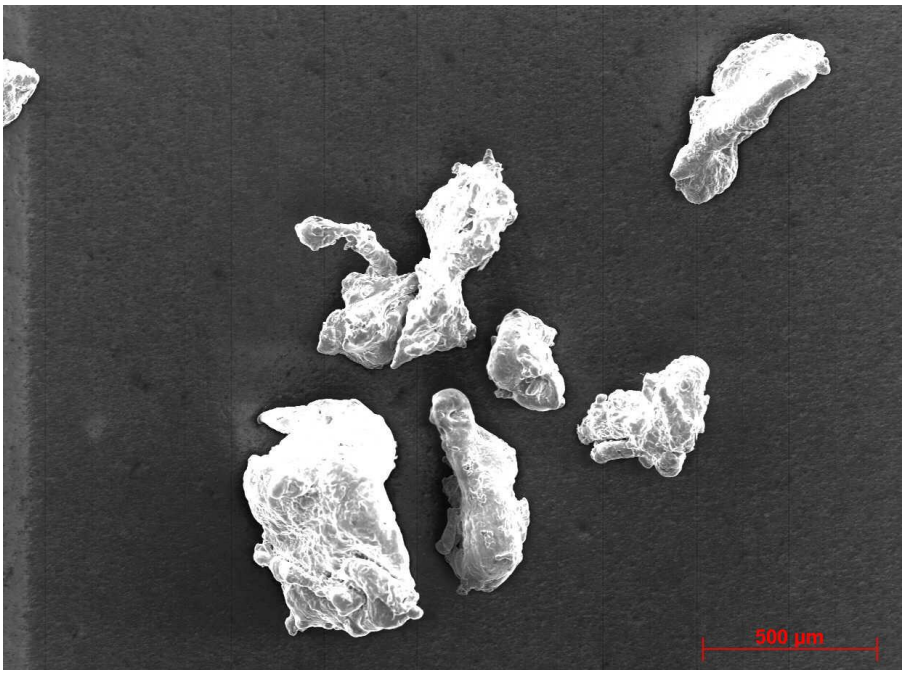

Figure 4.1: Optical image of pure aluminium powder particles that remained on top of the 150µm sieve.

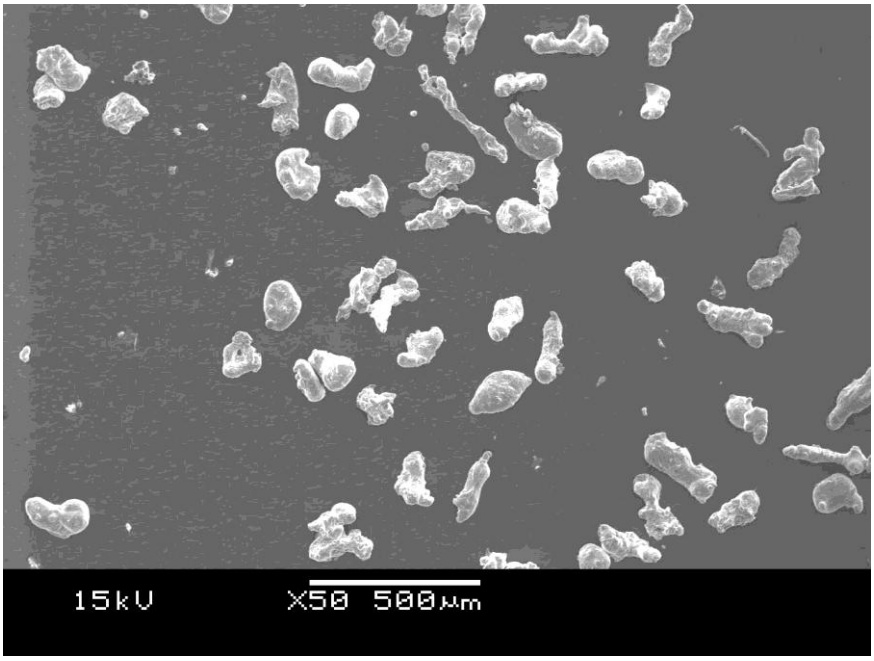

Figure 4.2: SEM image of pure aluminium powders that were sieved between the range of 75-105µm.

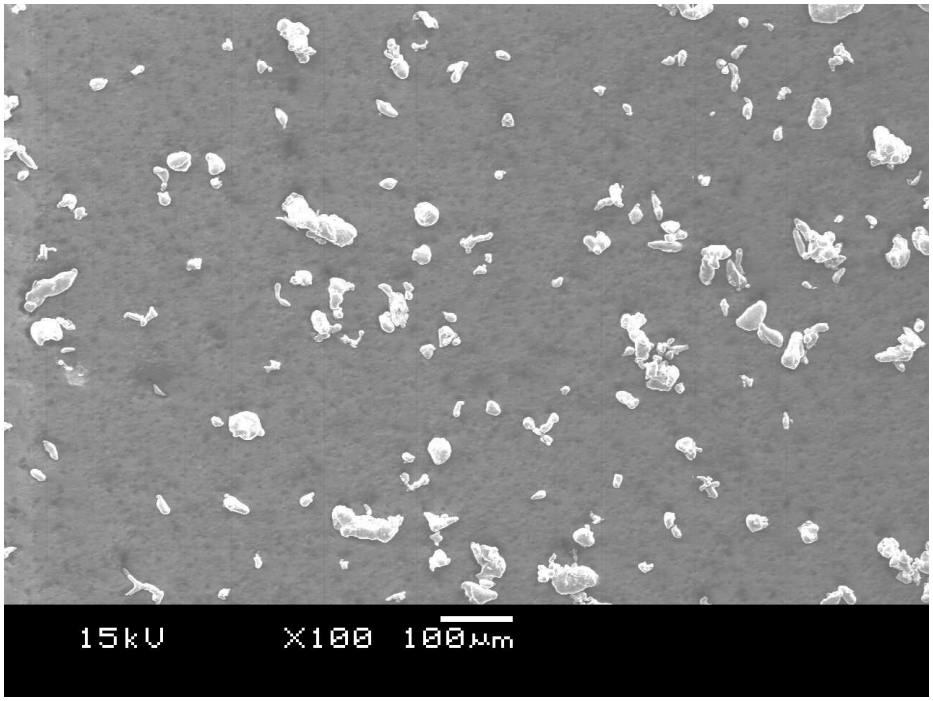

Figure 4.3: SEM image of the fine pure aluminium powder particles sieved using the <45µm sieve.

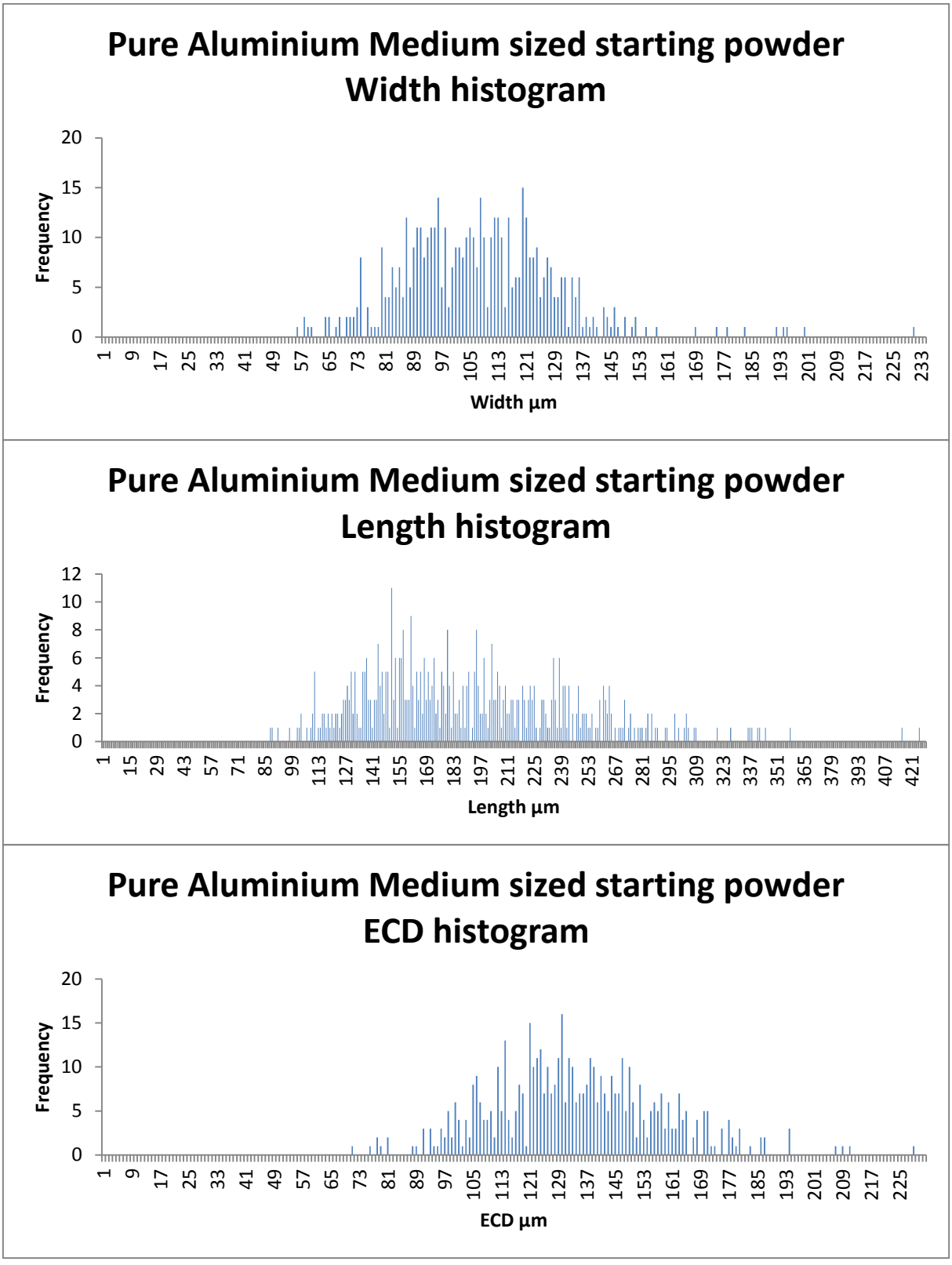

Figure 4.4: Histograms for the length, width and ECD of medium sized pure aluminium particles

Table 4.1: The starting particle sizes for pure Aluminium powder

Powder particle size range	Length µm	Width µm	Aspect ratio	ECD µm
Coarse	715.48 ± 416.29	342.76 ± 161.5	0.48	430.41 ± 202.52
Medium	120.45 ± 53.47	98 ± 22.11	0.56	103.27 ± 23.35
Fine	37.43 ± 16.57	23.33 ± 9.65	0.62	28.48 ± 10.74

4.1.1.2. Apparent Density

The apparent density of the pure aluminium powders is shown in Table 4.2. The relative apparent densities for the coarse, medium and fine powders are 37.12 ± 0.77%, 48.27 ± 0.24% and 34.06 ± 0.48% respectively.

Table 4.2: The apparent density of the pure aluminium powder

Powder particle size range	Apparent density (g/cm^3)	Relative apparent density (%)
Coarse	1.00 ± 0.52	37.12 ± 0.77
Medium	1.30 ± 0.16	48.27 ± 0.24
Fine	0.92 ± 0.32	34.06 ± 0.48

4.1.2. Cold compacted specimens

4.1.2.1. Density & compressibility curve

The compressibility curve of all of the cold compacted size ranges are illustrated graphically in Figure 4.5. The density of the medium sized particles increased from the apparent density of 1.3g/cm^3 to 2.64g/cm^3 at 400MPa and the curve begins to plateau as higher pressing forces are applied.

The compaction pressure did not exceed 400MPa due to a risk of tool wear. Therefore the coarse and fine particles were also compacted at 400MPa and the densities of these are compared in Table 4.3. The coarse and medium particle size range both had densities of 2.64g/cm^3 and the fine particles had a density of 2.59g/cm^3.

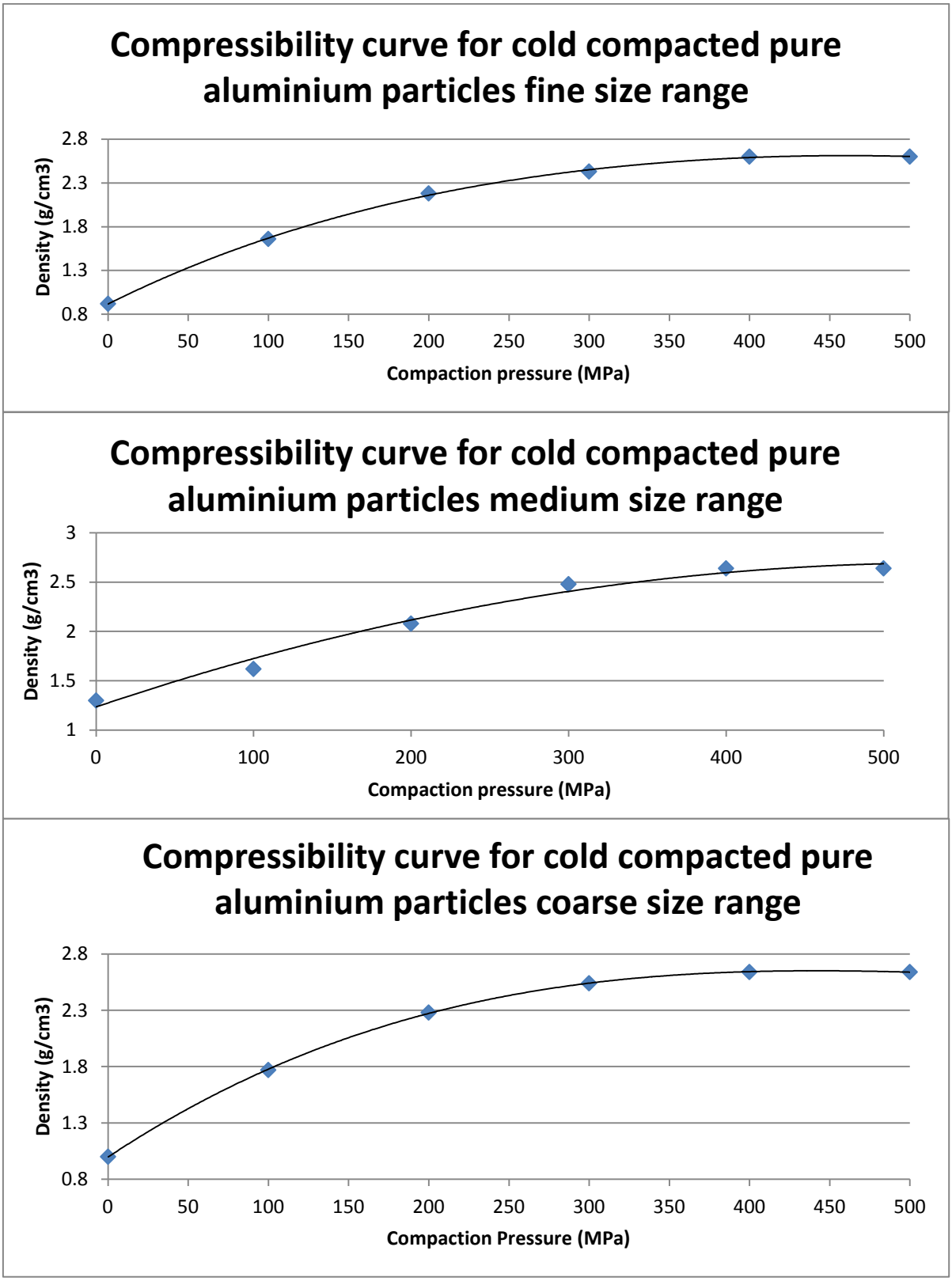

Figure 4.5: The compressibility curves with trend line for the fine, medium and coarse sized aluminium powders.

Table 4.3: Green densities of the coarse, medium and fine aluminium cold compacted at 400MPa

Powder particle size range	Density (g/cm^3)	Density (%)
Coarse	2.64 ± 0.01	97.78 ± 0.24
Medium	2.64 ± 0.024	97.78 ± 0.89
Fine	2.59 ± 0.008	96.40 ± 0.18

4.1.2.2. Microstructure of cold compacted samples

Unetched optical images of the cold compacted pure aluminium coarse, medium and fine size range in the longitudinal section are shown in Figure 4.6 to show the level and characteristics of porosity. The transverse sections are shown in Figure 4.7. The images reveal a region of higher porosity at the edge of the samples that gradually reduces towards the centre of the sample. Closer inspection of the pores reveals that they occur at the junction of neighbouring powder particles as indicated by the black arrows in Figure 4.8.

Etched optical images of the cold compacted aluminium samples are shown in Figure 4.9. The data for the length, width and equivalent circular diameter of particles are shown in Table 4.4. The coarse particle ECD ranged from 140.77µm to 164.67µm in the transverse and longitudinal sections respectively, medium particles from 40.66µm to 52.39µm and fine particles from 28.41µm to 33.82µm. The spread of data measured for the medium sized particles in the longitudinal and transverse sections are shown in the length, width and ECD histograms in Figure 4.10 and Figure 4.11 respectively. This trend is seen in all samples in the pure aluminium cold compacted particles, which is shown in Appendix 6-3 to Appendix 6-6.

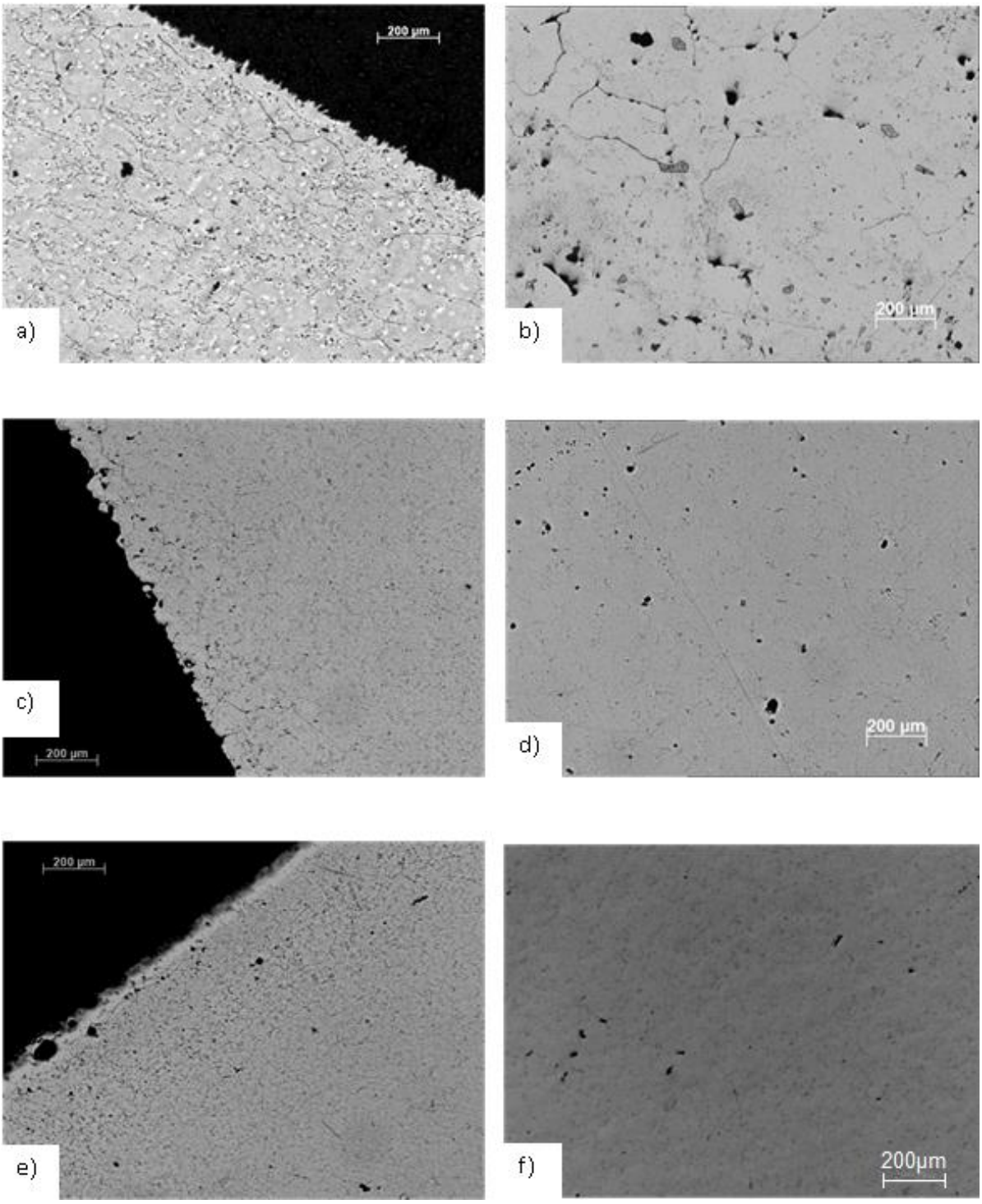

Figure 4.6: Unetched optical images showing porosity for longitudinal sections of cold compacted coarse powder particles at the a) edge and b) core of the sample, medium c) edge and d) core and fine e) edge and f) core.

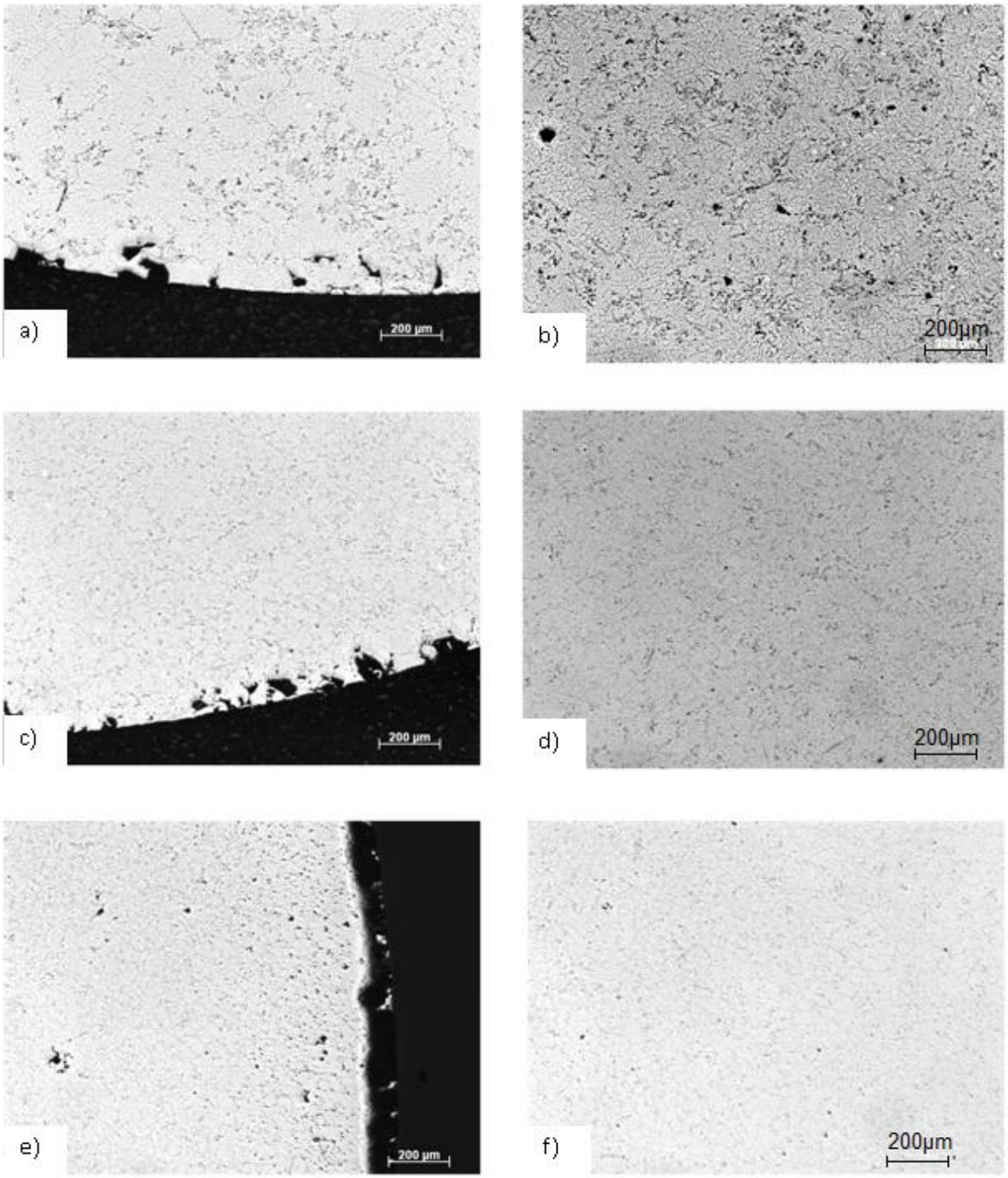

Figure 4.7: Unetched optical images showing porosity for transverse sections of cold compacted coarse powder particles at the a) edge and b) core of the sample, medium c) edge and d) core and fine e) edge and f) core.

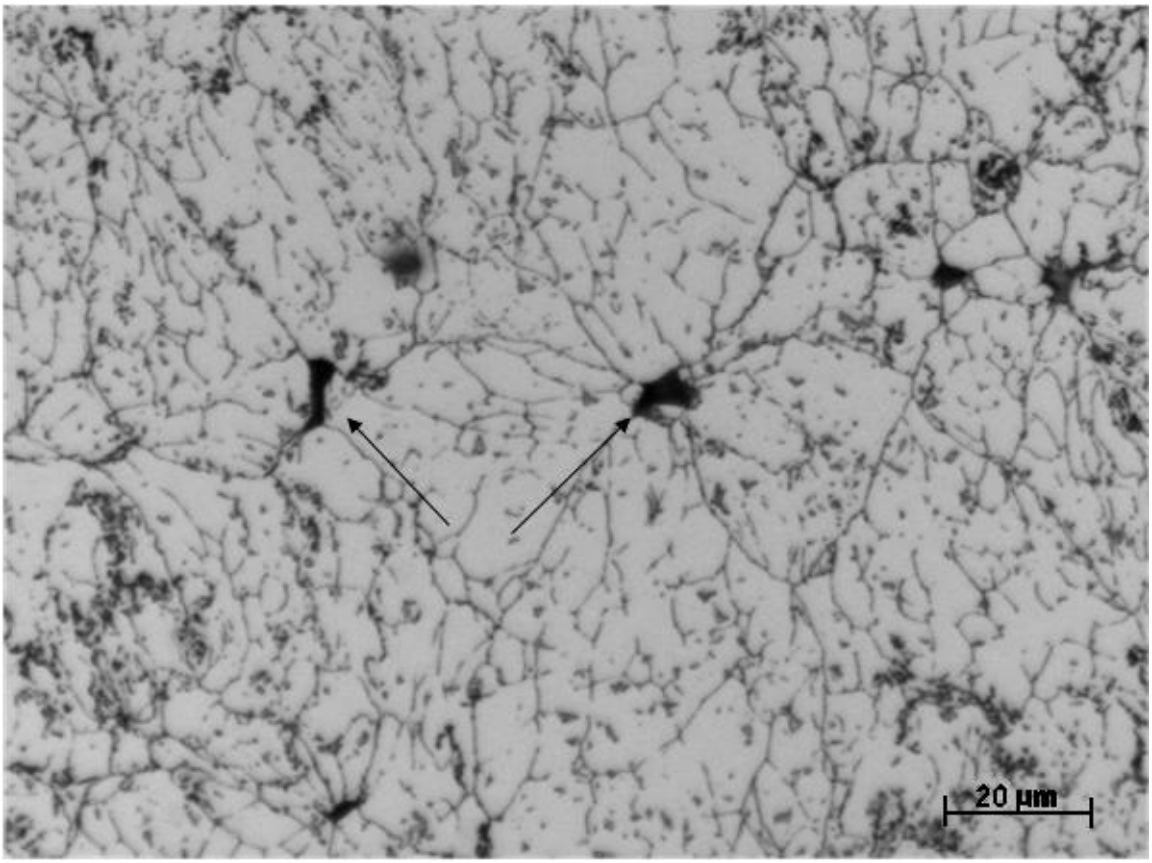

Figure 4.8: Etched optical image of the longitudinal section of the cold compacted pure aluminium medium particle size range reveals that porosity occurs at the junction of neighbouring powder particles, indicated by the black arrows. This image is taken from the core of the sample.

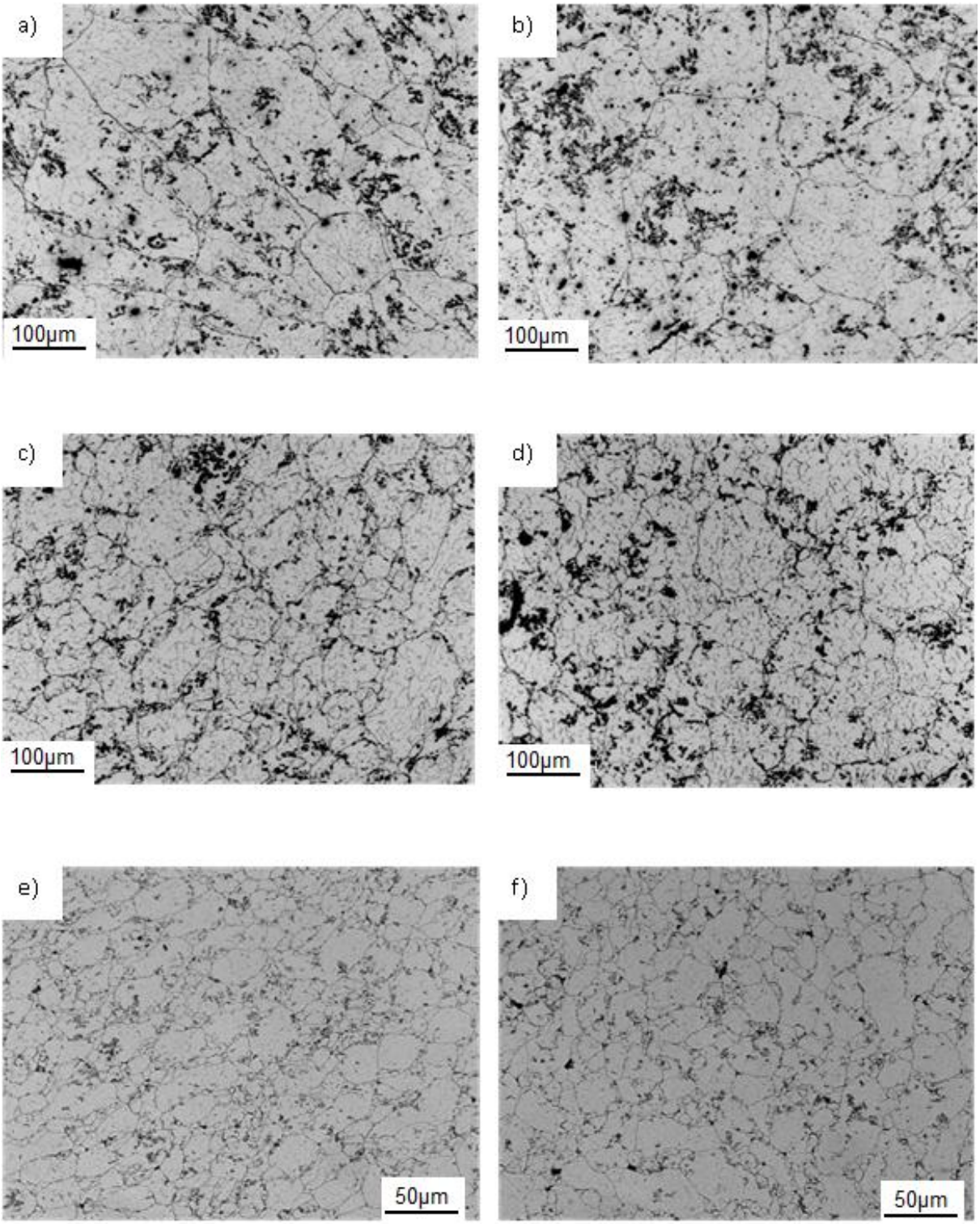

Figure 4.9: Etched optical images of the cold compacted pure aluminium coarse a) longitudinal and b) transverse section, medium c) longitudinal and d) transverse sections and fine e) longitudinal and f) transverse sections. These images are taken from the core of the samples.

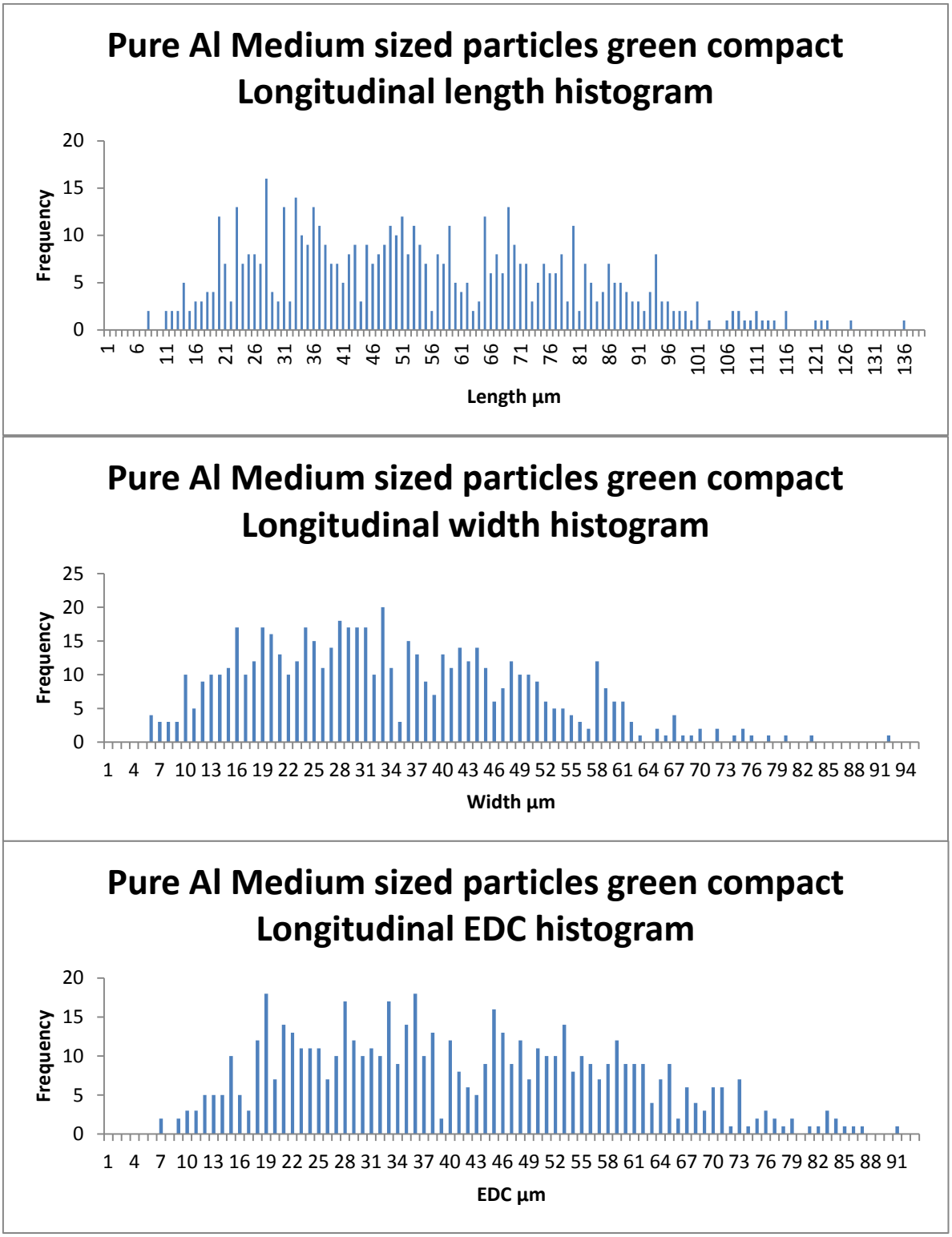

Figure 4.10: Length, width and ECD histograms of the medium sized particles longitudinal section data.

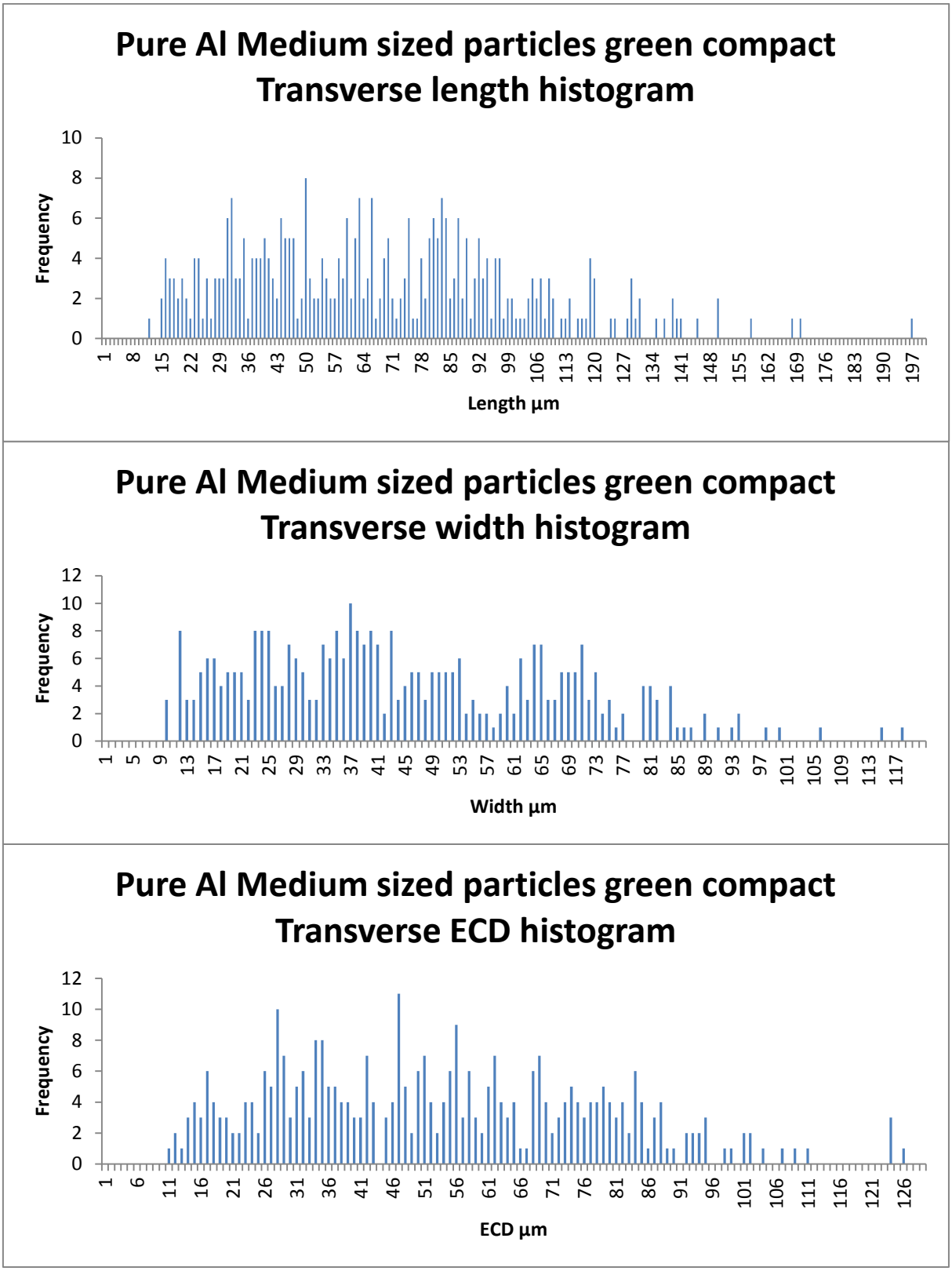

Figure 4.11: Length, width and ECD histograms of the medium sized particles transverse section data.

Table 4.4: The length, width, aspect ratio and equivalent circular diameter of particles within the longitudinal and transverse sections of cold compacted samples using the coarse, medium and fine sized Al powder particles

Sample	Length µm		Width µm		Aspect ratio		ECD µm	
	Longitudinal	Transverse	Longitudinal	Transverse	Longitudinal	Transverse	Longitudinal	Transverse
Coarse	215.98 ± 123.59	225.75 ± 114.24	106.26 ± 51.7	139.85 ± 71.89	0.49	0.62	140.77 ± 67.18	164.67 ± 78.17
Medium	53.72 ± 25.07	67.58 ± 33.35	33.29 ± 15.63	44.66 ± 22.11	0.62	0.66	40.66 ± 17.88	52.59 ± 24.55
Fine	44.67 ± 22.49	35.69 ± 19.31	27.08 ± 13.05	23.64 ± 11.45	0.61	0.66	31.82 ± 15.53	28.41 ± 13.6

4.1.2.3. Hardness of cold compacted samples

The hardness of the cold compacted pure aluminium powder in the transverse and longitudinal sections is shown in Table 4.5. The compacted coarse powder had a hardness ranging from 39.82 to 39.75$HV_{2.5kg}$ on the longitudinal and transverse sections respectively. The hardness increased to between 43.88 and 44.04$HV_{2.5kg}$ on the longitudinal and transverse sections respectively for the medium sized powder particles and increased further to between 45.91 and 45.94$HV_{2.5kg}$ for the fine sized particles on the longitudinal and transverse sections respectively.

Table 4.5: The Vickers hardness of the cold compacted transverse and longitudinal sections of all the powder particle size ranges

Sample	Longitudinal $HV_{2.5kg}$	Transverse $HV_{2.5kg}$
Coarse green compact	39.82 ± 0.73	39.75 ± 1.02
Medium green compact	43.88 ± 0.74	44.04 ± 0.57
Fine green compact	45.91 ± 0.59	45.94 ± 0.31

4.1.3. Sintering response

Although it is economically cheaper to produce coarser powders in the atomisation process, medium and fine particle size ranges were also used to compare the effects of sintering on particle size.

4.1.3.1. Sintered density

The densities of the compacts before and after sintering are shown in Table 4.6. The sintered density achieved for the coarse and fine size range was 2.59g/cm^3, which is 95.76% of the theoretical density of 2.7g/cm^3 for aluminium compared to 2.64g/cm^3 for the medium sintered density (97.29% of theoretical).

Table 4.6: Comparison of density before and after sintering for the different sized Al powder

Condition	Density (g/cm^3)	Density (% theoretical)
Coarse green compact	2.64 ± 0.01	97.93 ± 0.24
Coarse green → sintered 620°C 1h	2.59 ± 0.01	95.76 ± 0.45
Medium green compact	2.64 ± 0.024	97.78 ± 0.89
Medium green → sintered 620°C 1h	2.63 ± 0.01	97.29 ± 0.51
Fine green compact	2.59 ± 0.008	96.40 ± 0.18
Fine green → sintered 620°C 1h	2.59 ± 0.004	95.78 ± 0.78

4.1.3.2. Microstructure of sintered samples

Unetched optical images of the longitudinal and transverse sections of the fine, medium and coarse sintered samples are shown from Figure 4.12 to Figure 4.17, which illustrate porosity at the edge and centre of the samples.

Etched optical images can be seen from Figure 4.18 to Figure 4.20 for the fine, medium and coarse sized sintered powder compacts respectively. The data for length, width and ECD for these grains is shown in Table 4.7, which compares the cold compacted samples with those that were sintered. The particle sizes remained relatively the same after sintering compared to those measured after cold compaction. The ECD of the coarse sintered pure aluminium particles was 143.33 ± 98.11µm and 160.77 ± 86.51µm in the longitudinal and transverse section respectively. For the medium sintered particles, the ECD was 45.74 ± 19.5µm and 50.2 ± 27.47µm in the longitudinal and transverse section respectively. For the fine sintered particles, the ECD was 24.54 ± 8.53µm and 23.99 ± 10.09µm in the longitudinal and transverse sections respectively. The spread of the longitudinal and transverse data for length, width and ECD measurements are shown in the histograms from Figure 4.21 to Figure 4.26 for all the samples.

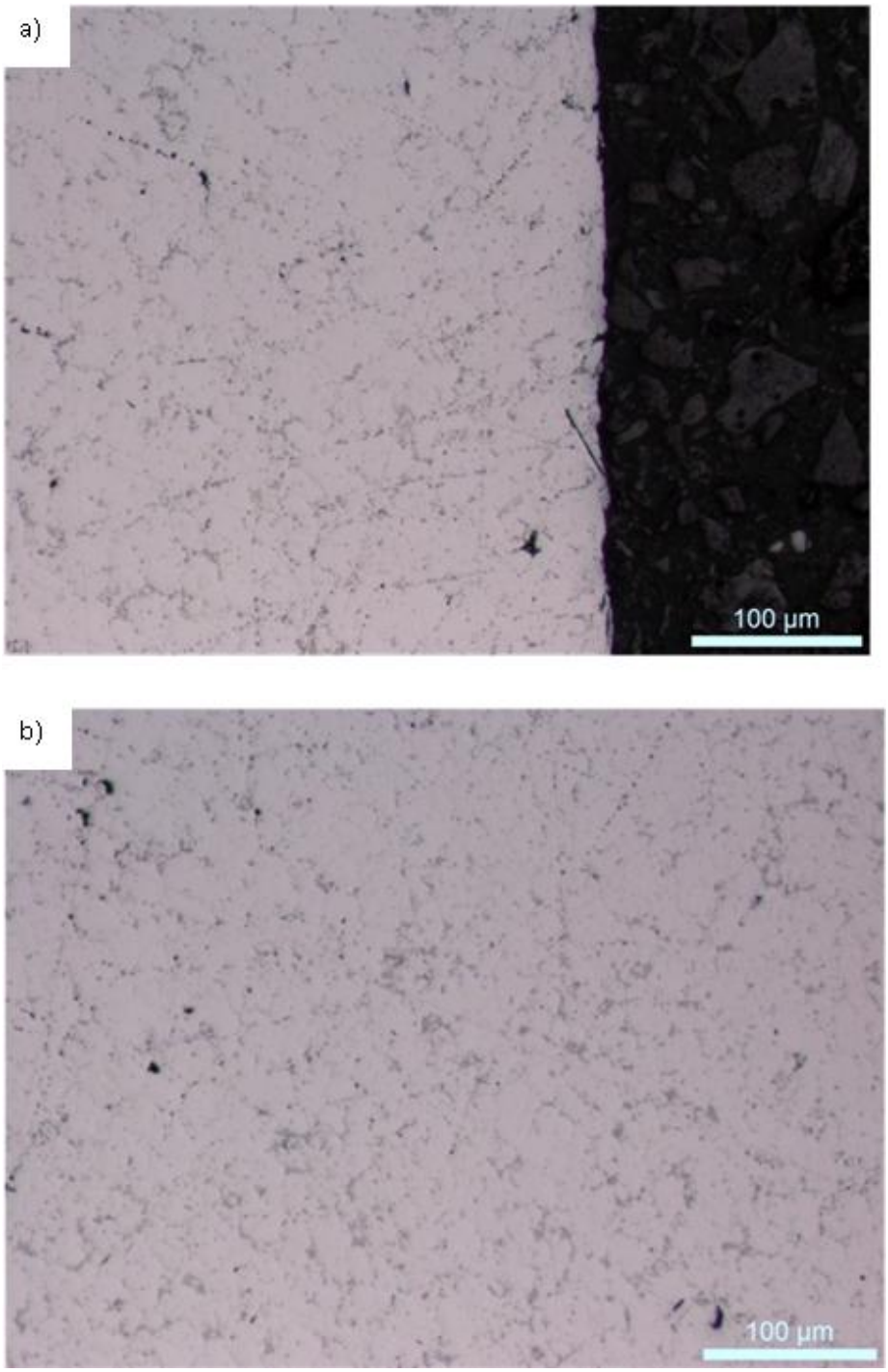

Figure 4.12: Unetched optical images of the a) edge and b) core longitudinal section of the fine sized sintered particles.

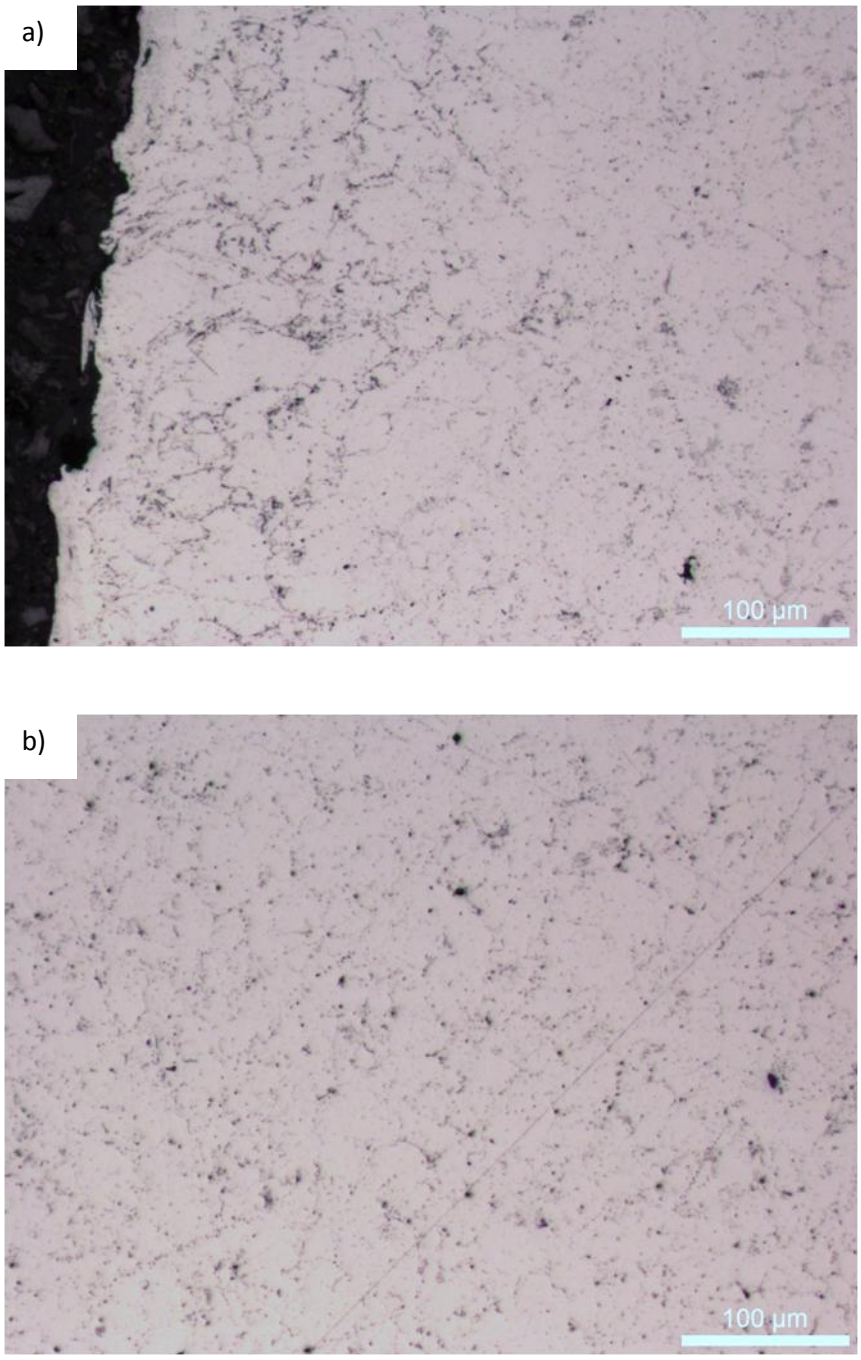

Figure 4.13: Unetched optical images of the a) edge and b) core transverse section of the fine sized sintered particles.

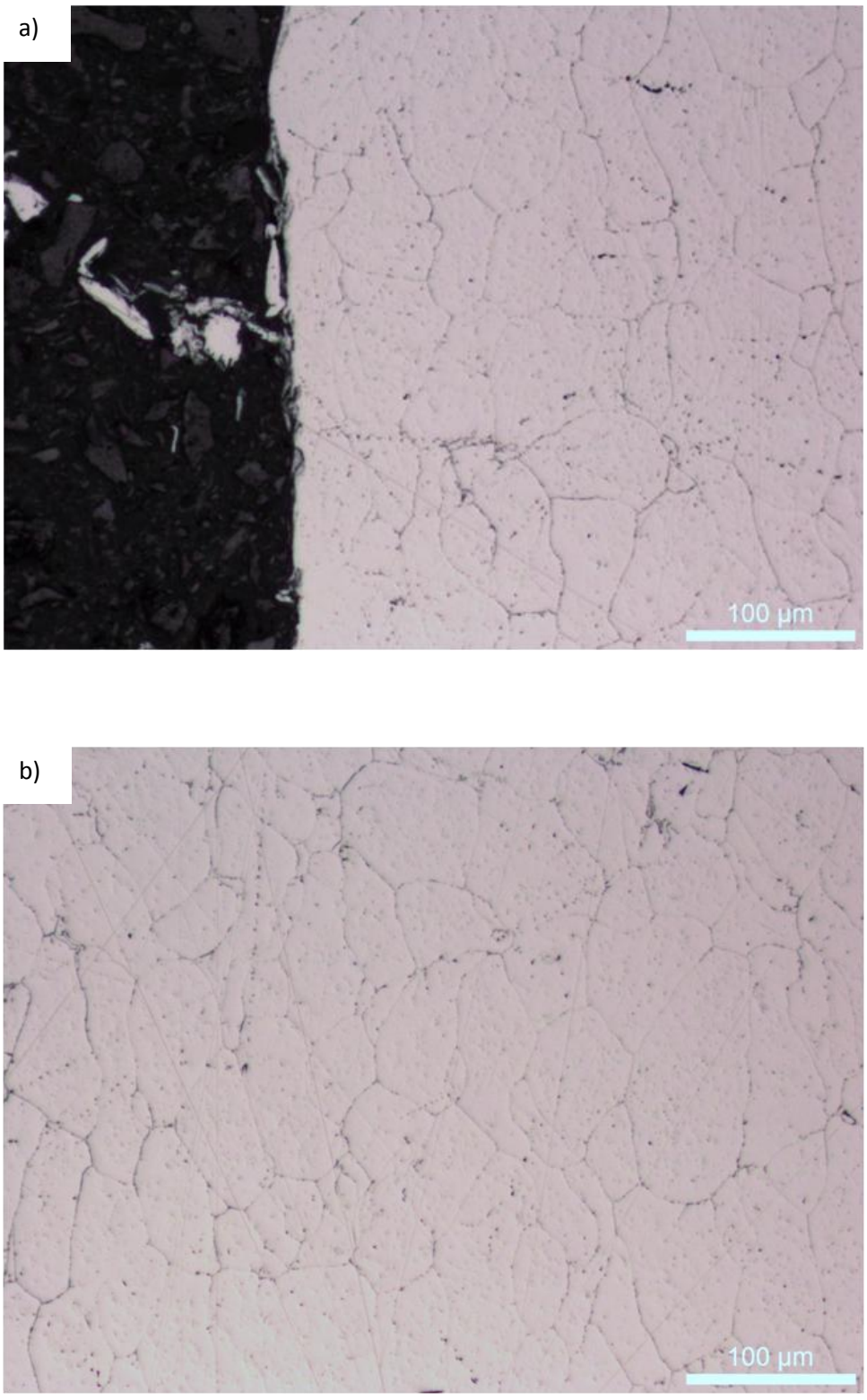

Figure 4.14: Unetched optical images of the a) edge and b) core longitudinal section of the medium sintered samples.

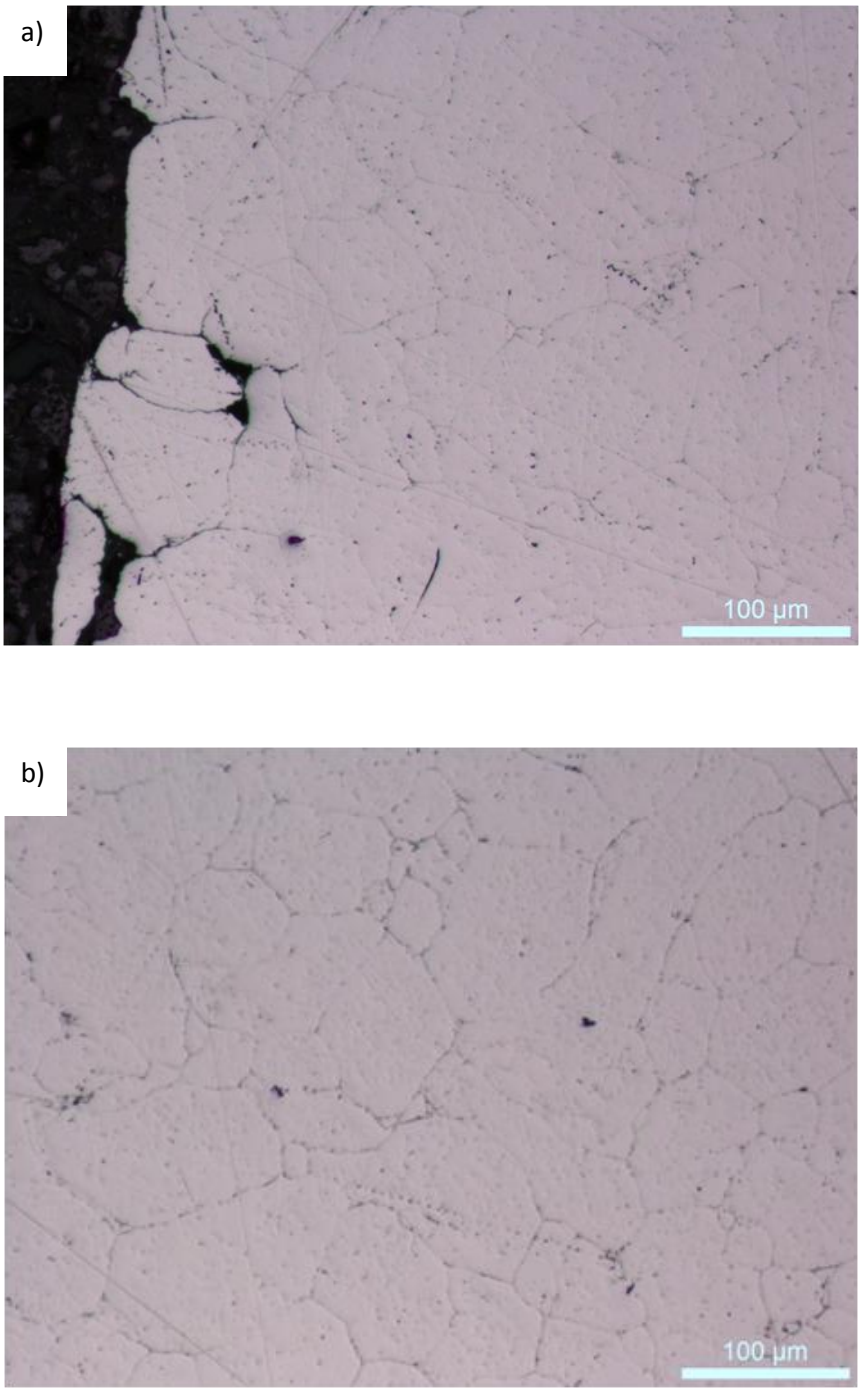

Figure 4.15: Unetched optical images of the a) edge and b) core transverse section of the medium sized sintered particles.

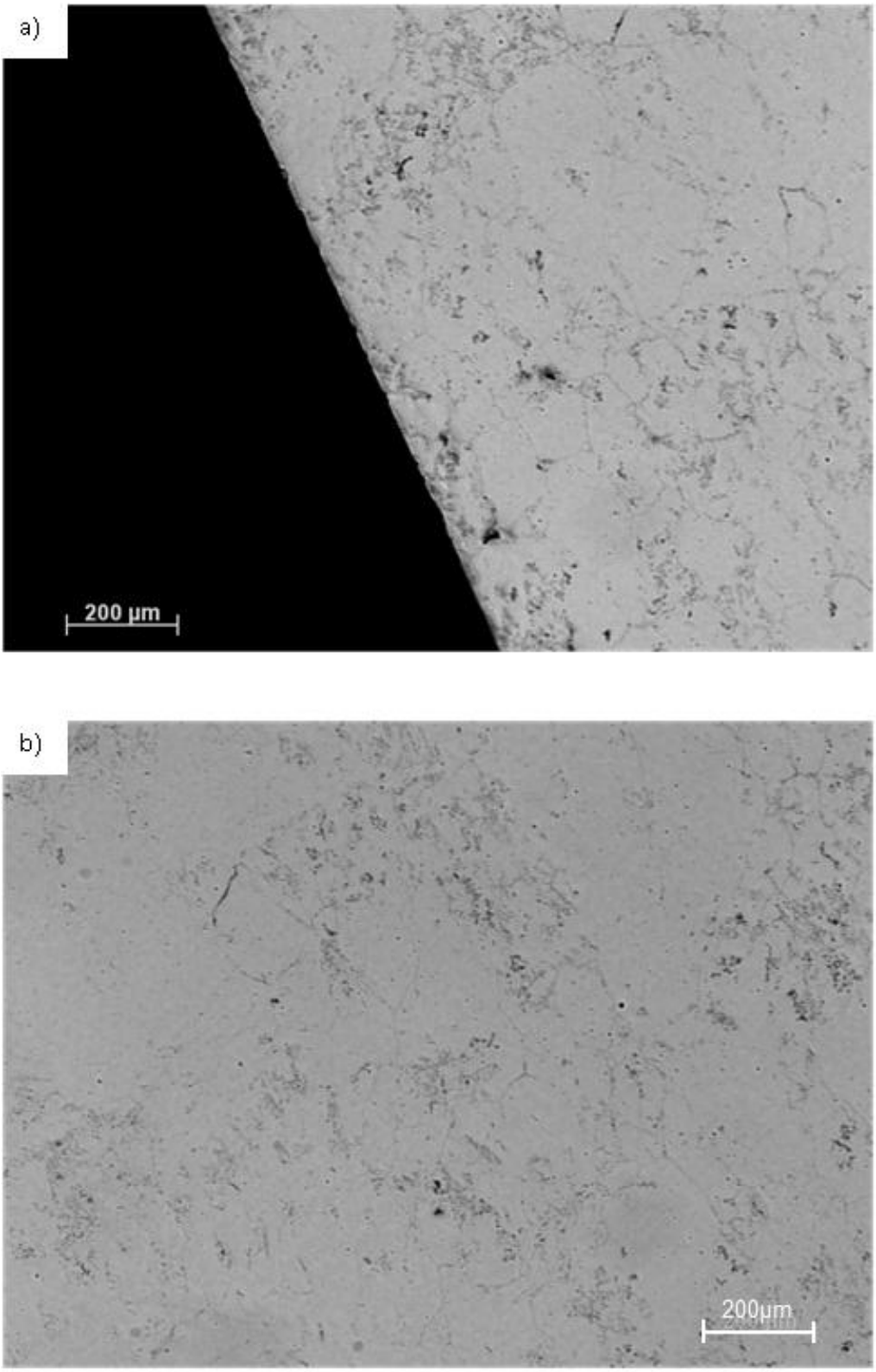

Figure 4.16: Unetched optical images of the a) edge and b) core of the longitudinal section of the coarse sized sintered powder compacts.

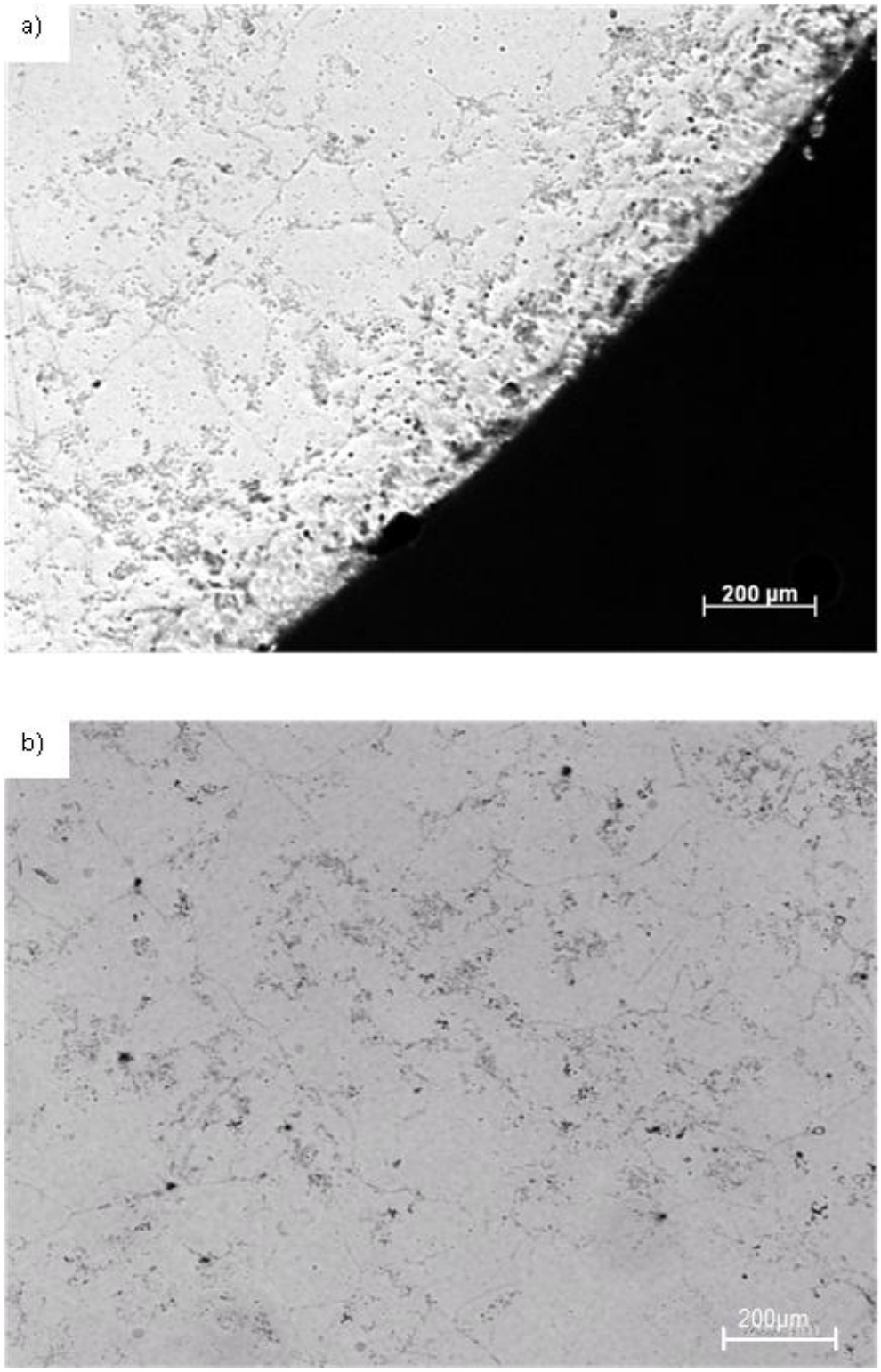

Figure 4.17: Unetched optical images of the a) edge and b) core of the transverse section of the coarse sized sintered powder compacts.

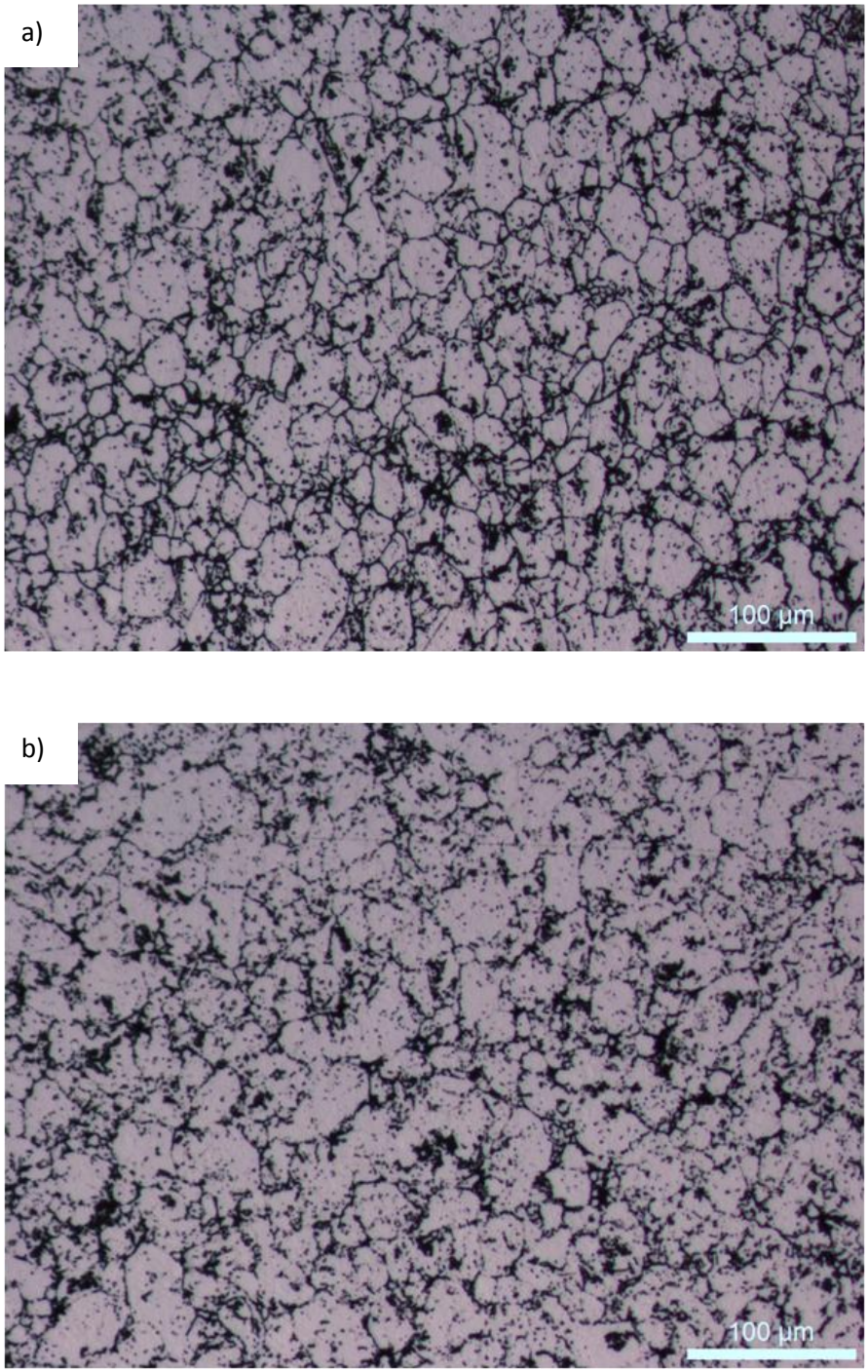

Figure 4.18: Etched optical images of a) longitudinal and b) transverse sections of fine sized pure aluminium compacts sintered at 620°C for 1 hour from the core of the sample.

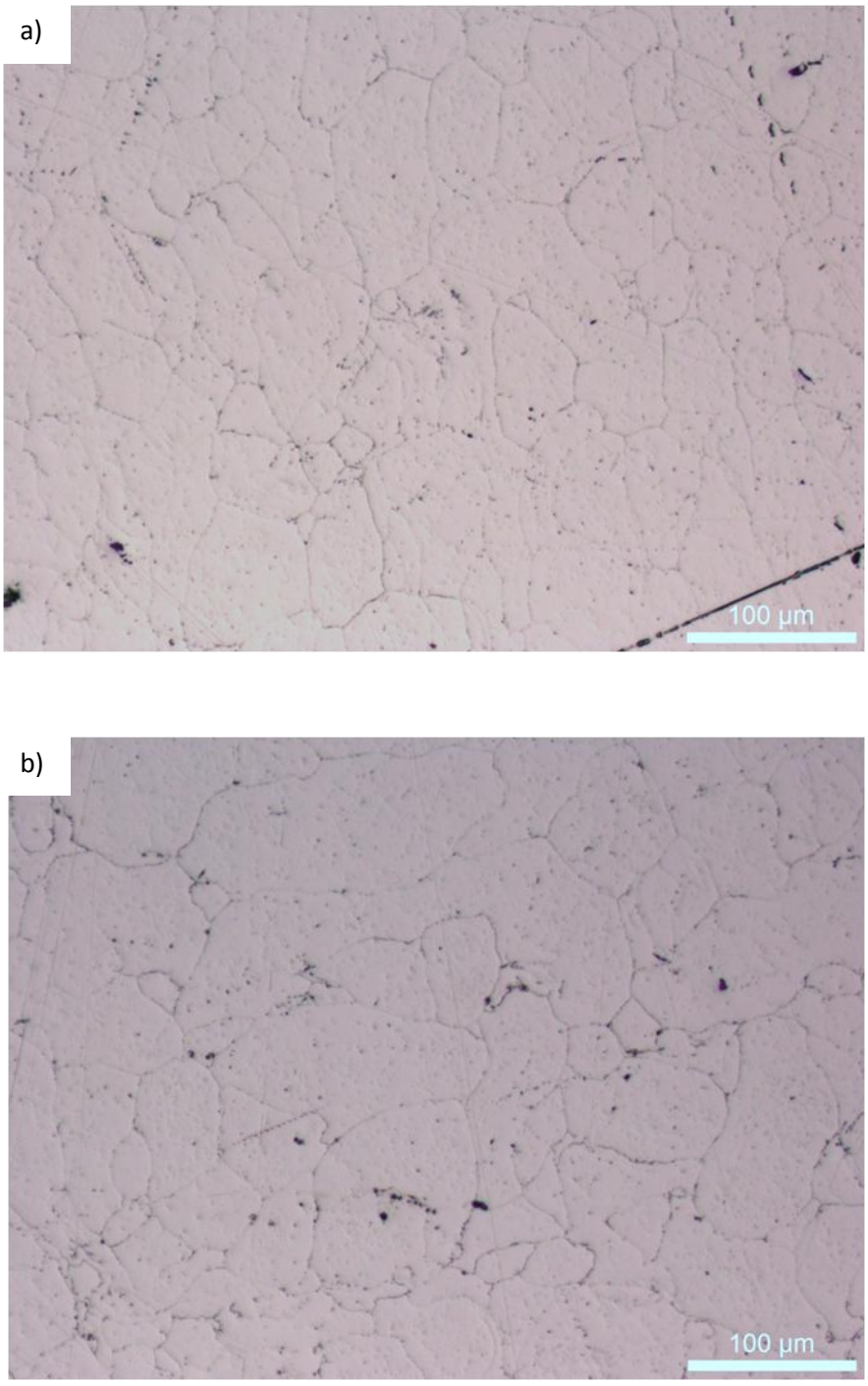

Figure 4.19: Etched optical images of a) longitudinal and b) transverse sections of medium sized pure aluminium compacts sintered at 620°C for 1 hour from the core of the sample.

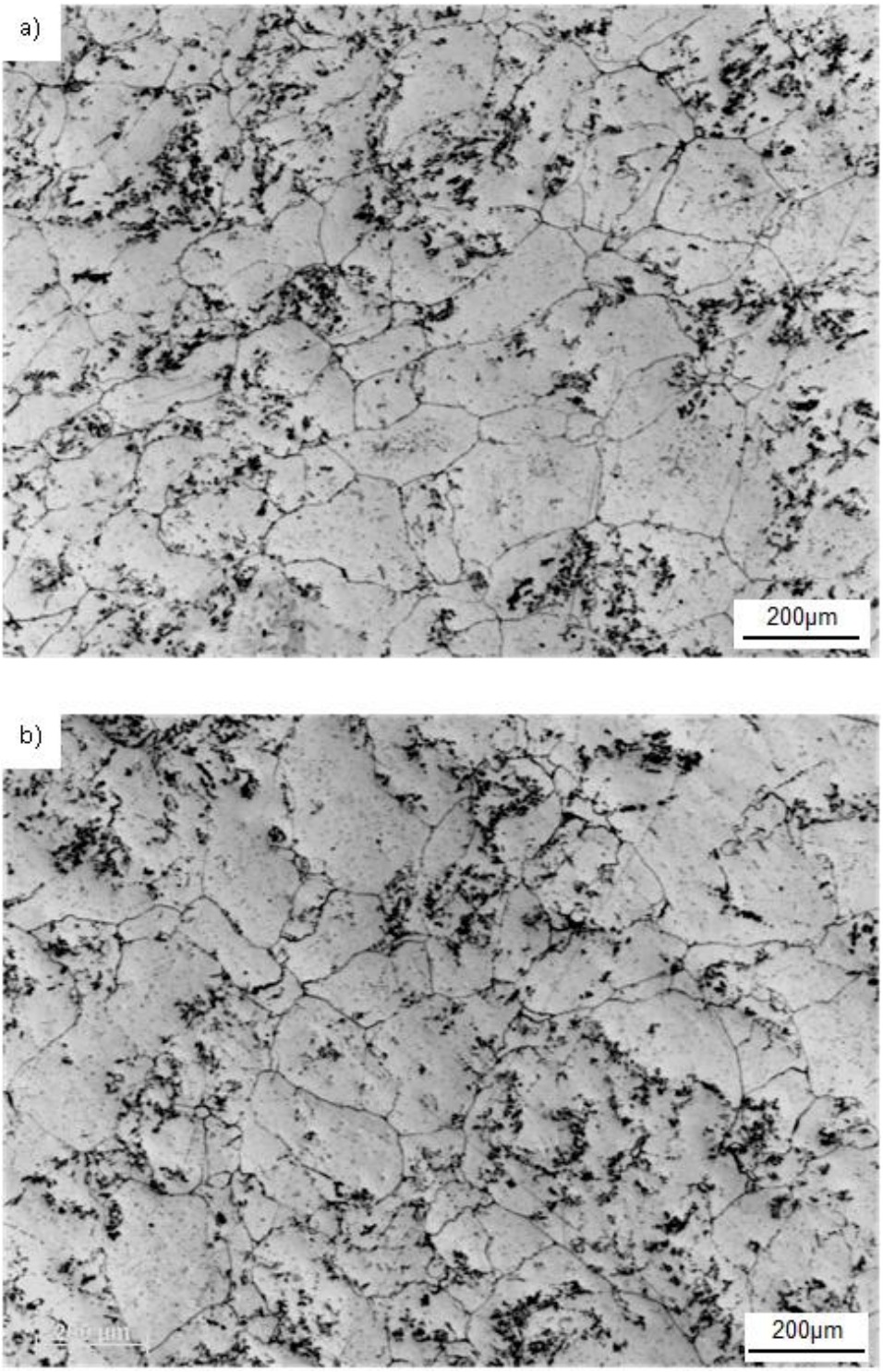

Figure 4.20: Etched optical images of a) longitudinal and b) transverse sections of coarse sized pure aluminium compacts sintered at 620°C for 1 hour from the core of the sample.

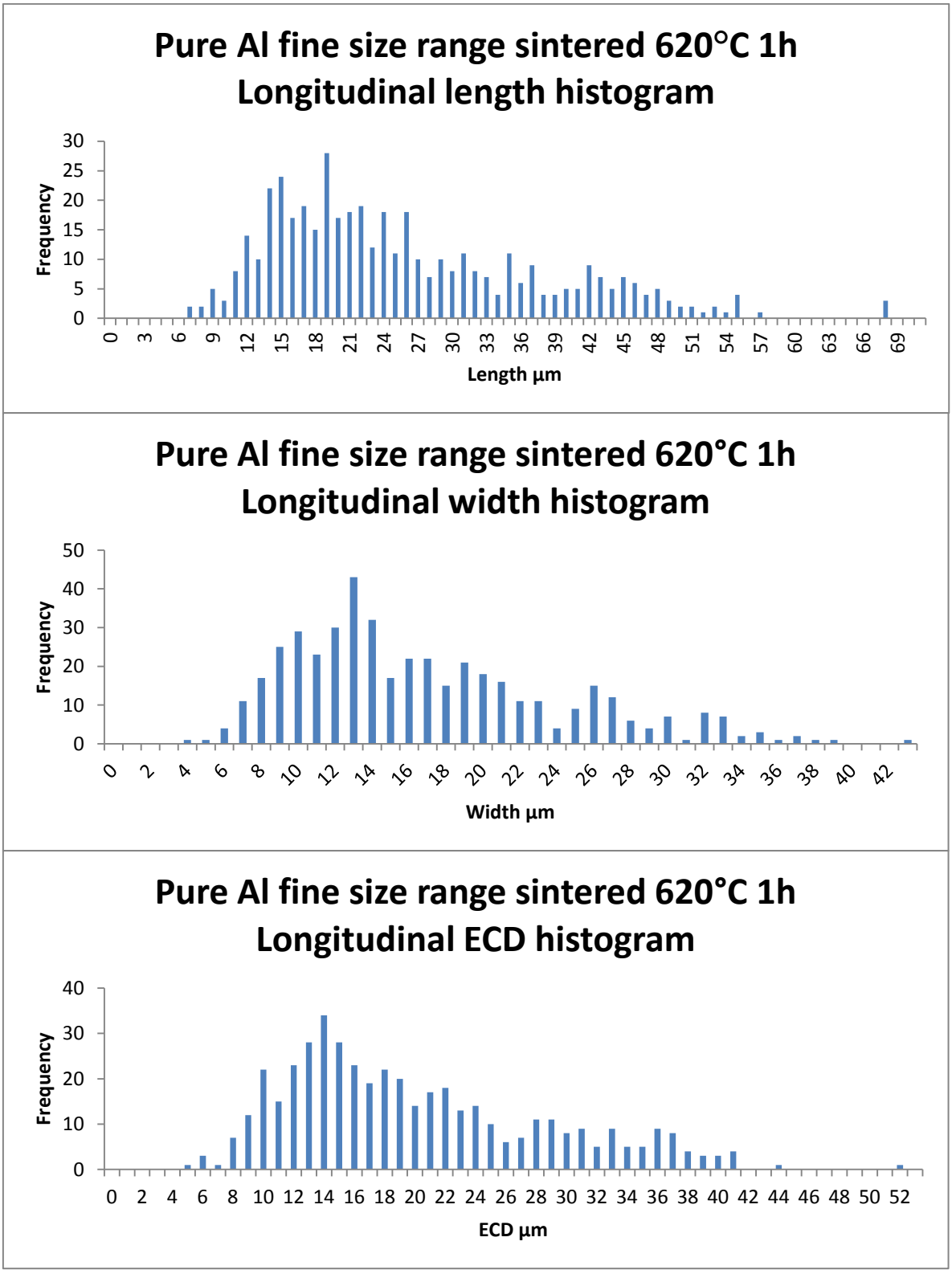

Figure 4.21: Histograms showing the spread of data for length, width and ECD of fine press and sintered samples in the longitudinal section

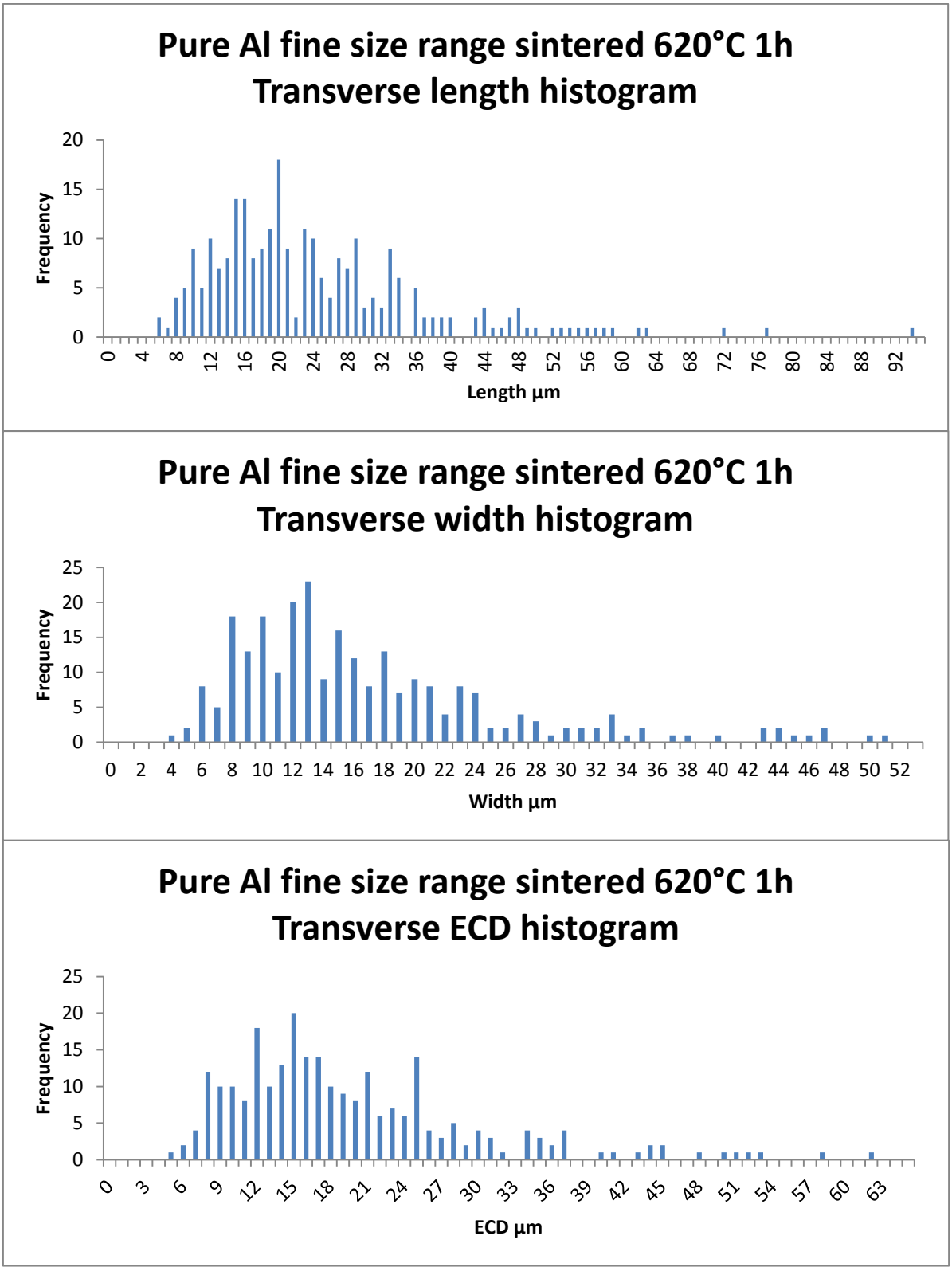

Figure 4.22: Histograms showing the spread of data for length, width and ECD of fine press and sintered samples in the transverse section

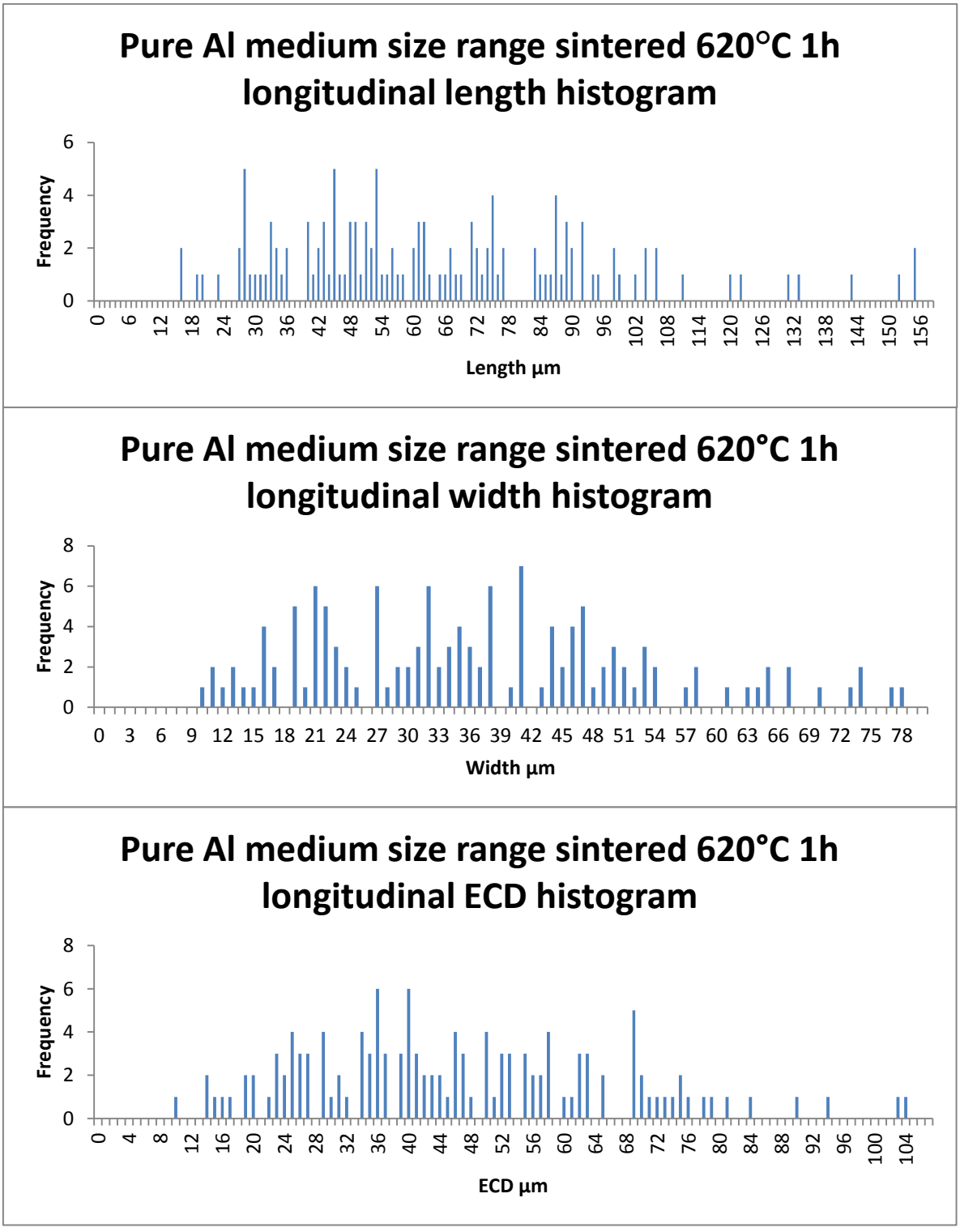

Figure 4.23: Histograms showing the spread of data for length, width and ECD of medium press and sintered samples in the longitudinal section.

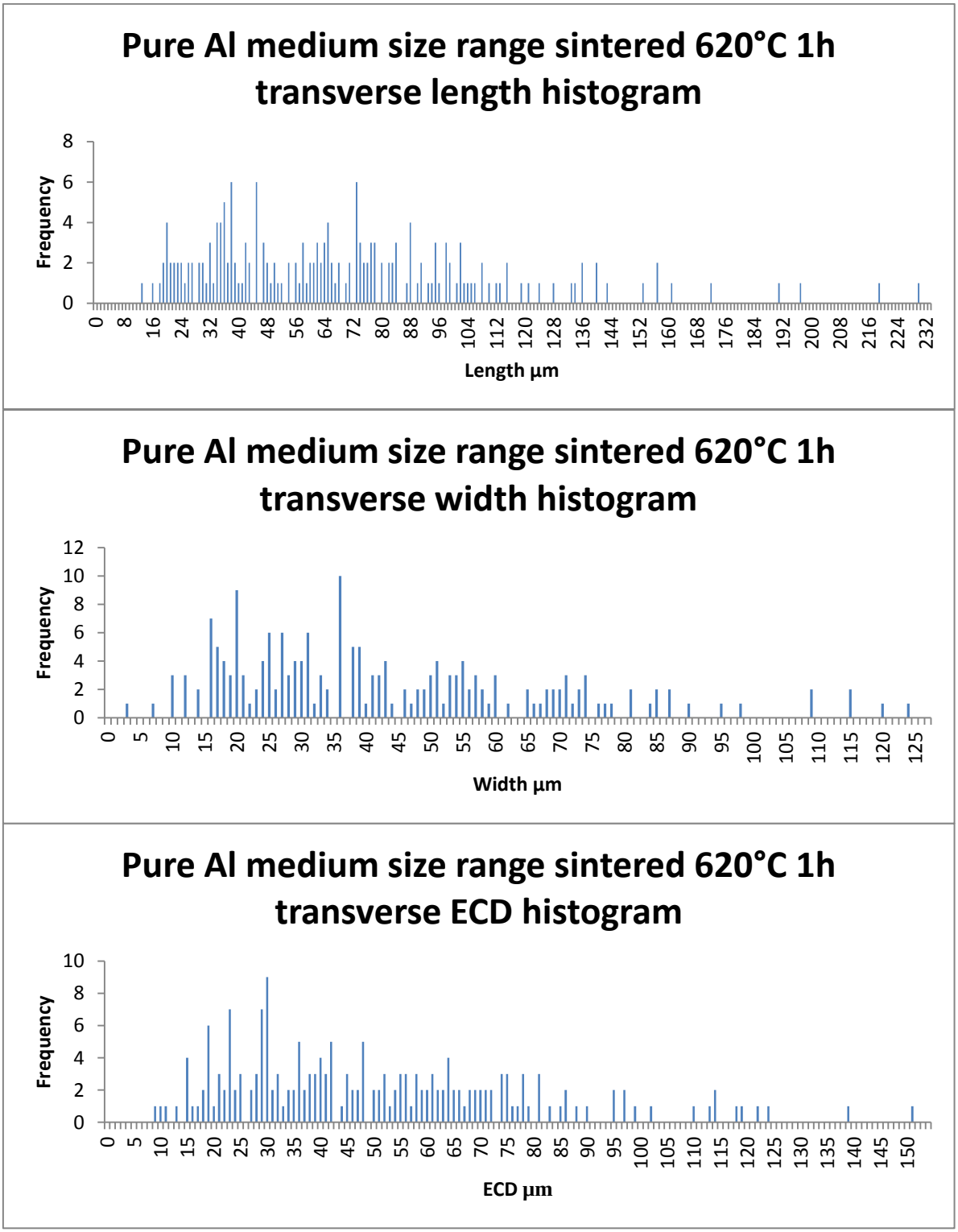

Figure 4.24: Histograms showing the spread of data for length, width and ECD of medium press and sintered samples in the transverse section.

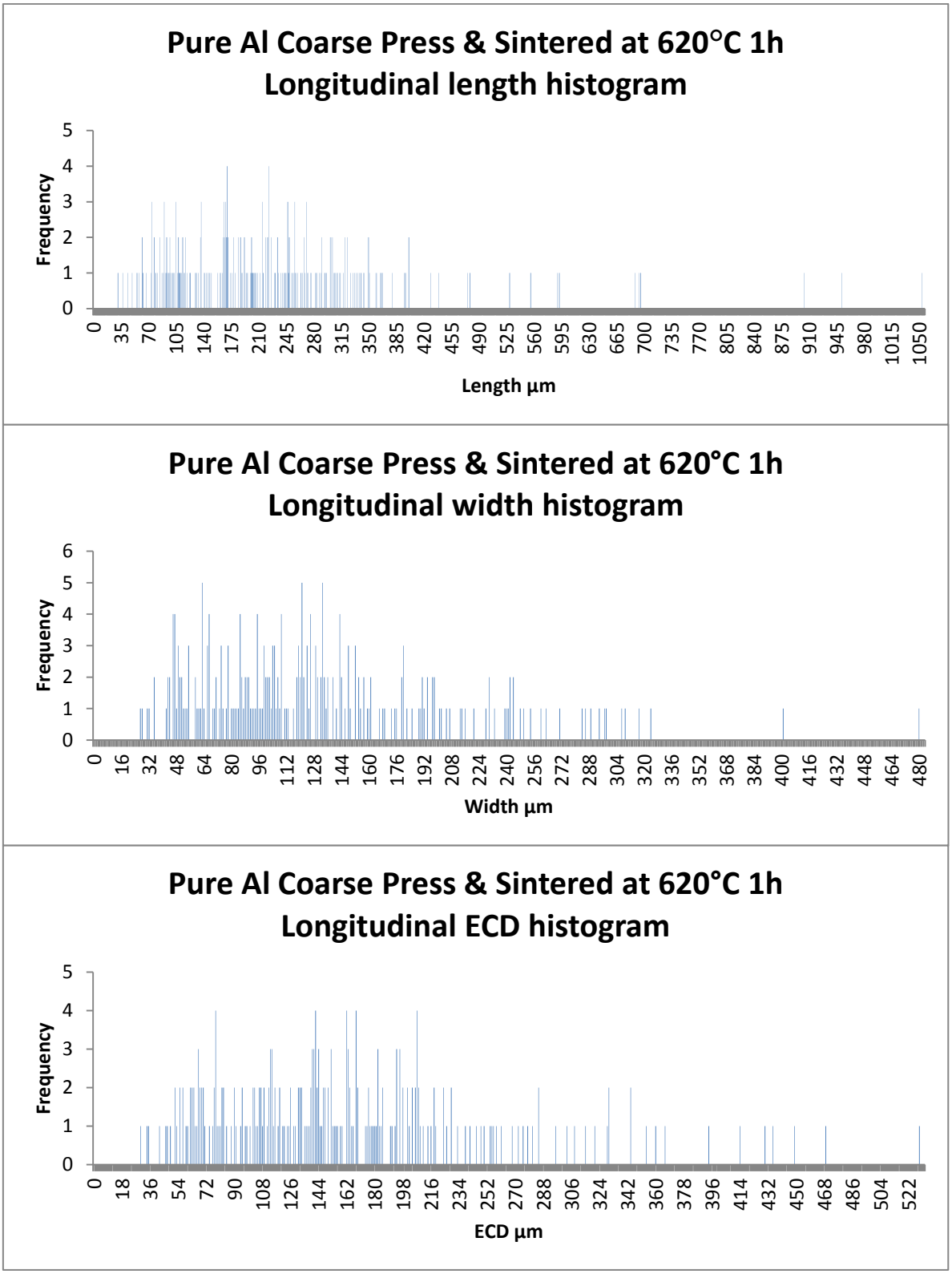

Figure 4.25: Histograms showing the spread of data for length, width and ECD of coarse press and sintered samples in the longitudinal section.

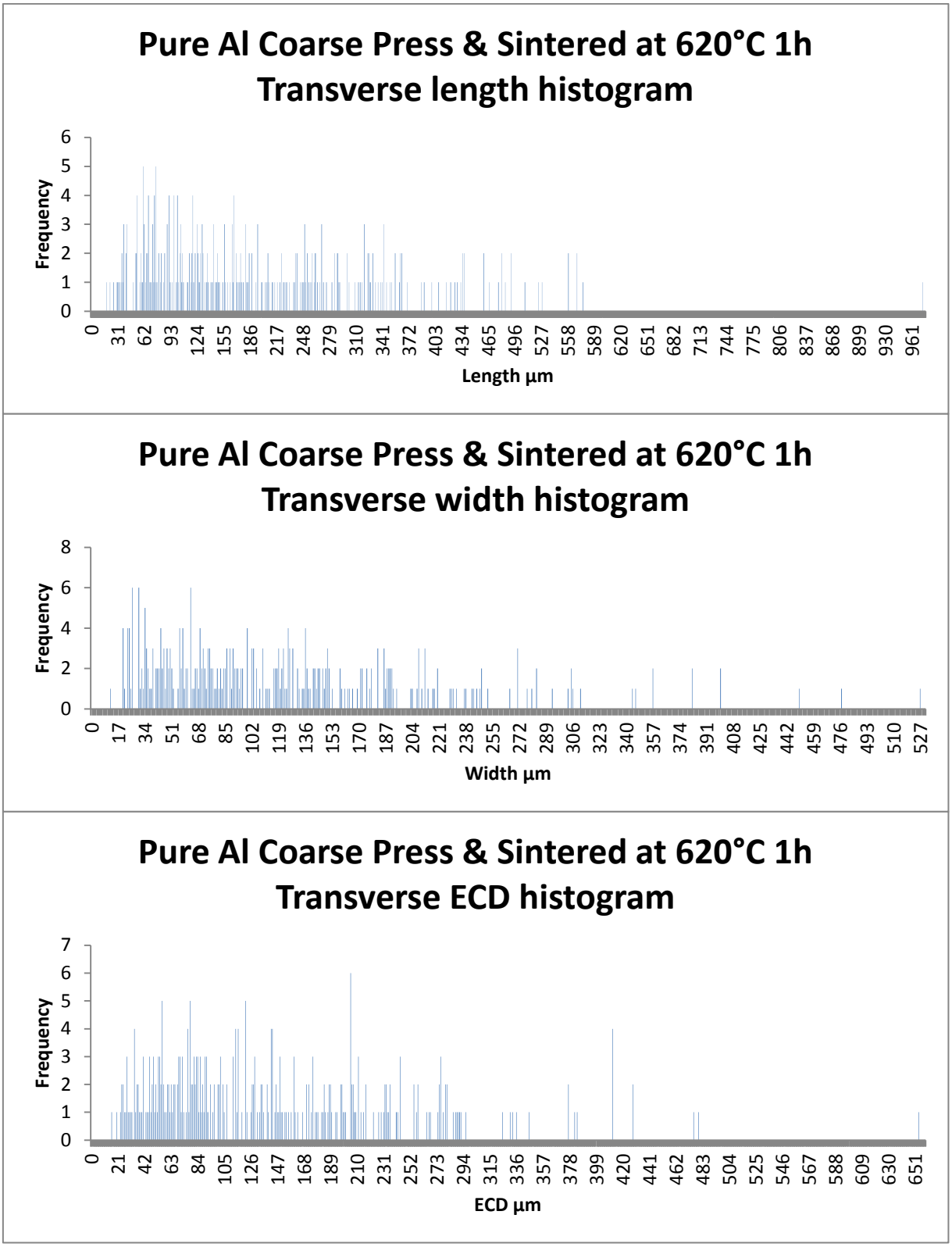

Figure 4.26: Histograms showing the spread of data for length, width and ECD of coarse press and sintered samples in the transverse section.

Table 4.7: The length, width and ECD of all the particles from the compacted and sintered powders.

Sample	Length µm		Width µm		Aspect ratio		ECD µm	
	Longitudinal	Transverse	Longitudinal	Transverse	Longitudinal	Transverse	Longitudinal	Transverse
Coarse green	215.98 ± 123.59	225.75 ± 114.24	106.26 ± 51.7	139.85 ± 71.89	0.49	0.62	140.77 ± 67.18	164.67 ± 78.17
Coarse sintered	195.12 ± 134.94	231.34 ± 145.81	122.13 ± 87.72	129.49 ± 72.06	0.56	0.63	143.33 ± 98.11	160.77 ± 86.51
Medium green	53.72 ± 25.07	67.58 ± 33.35	33.29 ± 15.63	44.66 ± 22.11	0.62	0.66	40.66 ± 17.88	52.59 ± 24.55
Medium sintered	64.32 ± 29.84	68.98 ± 39.93	36.51 ± 16.04	42.52 ± 24.49	0.57	0.62	45.74 ± 19.5	50.2 ± 27.47
Fine green	44.67 ± 22.49	35.69 ± 19.31	27.08 ± 13.05	23.64 ± 11.45	0.61	0.66	31.82 ± 15.53	28.41 ± 13.6
Fine sintered	30.32 ± 11.7	29.04 ± 13.24	21.44 ± 7.24	21.46 ± 9.18	0.71	0.74	24.54 ± 8.53	23.99 ± 10.09

4.1.3.3. Hardness of sintered samples

The Vickers hardness of the pure aluminium particles before and after sintering is summarised in Table 4.8. The hardness after sintering decreased for all sintered samples. In the coarse sample, the hardness reduced from 39.82 ± 0.73$HV_{2.5kg}$ and 39.75 ± 1.02$HV_{2.5kg}$ in the longitudinal and transverse sections respectively before sintering to 20.11 ± 0.44$HV_{2.5kg}$ and 21.47 ± 1.37$HV_{2.5kg}$ in the longitudinal and transverse sections respectively after sintering. For the medium samples, hardness reduced from 43.88 ± 0.74$HV_{2.5kg}$ and 44.04 ± 0.57$HV_{2.5kg}$ in the longitudinal and transverse sections respectively before sintering to 23..42 ± 1.33$HV_{2.5kg}$ and 24.21 ± 0.54$HV_{2.5kg}$ in the longitudinal and transverse sections after sintering. For the fine samples, hardness reduced from 45.91 ± 0.59$HV_{2.5kg}$ and 45.94 ± 0.31$HV_{2.5kg}$ in the longitudinal and transverse sections respectively before sintering to 27.36 ± 0.75$HV_{2.5kg}$ and 27.36 ± 0.5$HV_{2.5kg}$ in the longitudinal and transverse sections respectively after sintering. The hardness of the post-sintered samples was highest in the fine particles and lowest in the coarse particles.

Table 4.8: The Vickers hardness values of cold compacted and sintered aluminium compacts

Sample	Longitudinal $HV_{2.5kg}$	Transverse $HV_{2.5kg}$
Coarse green	39.82 ± 0.73	39.75 ± 1.02
Coarse sintered	20.11 ± 0.44	21.47 ± 1.37
Medium green	43.88 ± 0.74	44.04 ± 0.57
Medium sintered	23..42 ± 1.33	24.21 ± 0.54
Fine green	45.91 ± 0.59	45.94 ± 0.31
Fine sintered	27.36 ± 0.75	27.36 ± 0.5

4.1.4. ECAP response

4.1.4.1. Density after ECAP

The density of the cold compacted, sintered and ECAP samples for all size ranges is shown in Table 4.9. After ECAP, the average density improved for all samples and peaked at $2.67 \pm 0.01 g/cm^3$ for the coarse pre-compacted and pre-sintered samples. The average ECAP density was slightly lower for the medium pre-compacted and pre-sintered samples at $2.65 \pm 0.03 g/cm^3$. For the fine aluminium particles, the average ECAP density was slightly lower still at $2.64 \pm 0.01 g/cm^3$ and 2.63 ± 0.01 for the samples pre-sintered and pre-compacted respectively.

Table 4.9: Comparison of densities for all pure aluminium test conditions

Powder particle size and condition	Density (g/cm^3)	Density (%)
Coarse green	2.64 ± 0.01	97.78 ± 0.24
Coarse sintered	2.59 ± 0.01	95.76 ± 0.18
Coarse green → sintered → ECAP	2.67 ± 0.01	98.97 ± 0.45
Coarse green → ECAP	2.67 ± 0.01	99.06 ± 0.75
Medium green	2.64 ± 0.024	97.78 ± 0.89
Medium sintered	2.63 ± 0.01	97.29 ± 0.51
Medium green → ECAP	2.65 ± 0.01	98.0 ± 0.11
Fine green	2.59 ± 0.00	96.40 ± 0.18
Fine sintered	2.59 ± 0.004	95.78 ± 0.78
Fine green → ECAP	2.63 ± 0.01	97.28 ± 0.28

4.1.4.2. Microstructure of ECAP samples

Unetched optical images of the longitudinal and transverse (edge and centre) of the coarse pre-sintered samples and all the pre-compacted size ranges after ECAP are shown in Figure 4.27 and Figure 4.28 respectively. The pores appear to have an elliptical shape throughout the longitudinal cross section and a rounder shape in the transverse section.

Etched optical images of all the aforementioned ECAP samples and size ranges can be seen in Figure 4.29. The longitudinal sections are shown in images a), c), e) and g) and the transverse sections are shown in b), d), f) and h). Elongation of the pure aluminium particles can be seen in the longitudinal sections for all particle size ranges and the coarse sintered specimens following one pass of ECAP. In the transverse sections, the grains have a more rounded, equiaxed shape for all conditions.

The data for length, width and equivalent circular diameter is presented in Table 4.10 and the histograms for the length, width and ECD of the samples are shown in Appendix 6-7 to Appendix 6-14. The transverse ECD of the coarse particles reduced from 164.67 ± 78.17µm after compaction to 136.67 ± 47.14µm after ECAP. For the coarse sintered samples, the transverse ECD reduced from 160.77 ± 86.51µm after cold compaction to 118.57 ± 56.22µm after ECAP. The transverse ECD of the medium sized powders reduced from 52.59 ± 24.55µm after cold compaction to 51.03 ± 18.15µm after ECAP. The transverse ECD of the fine sized powders reduced from 28.41 ± 13.6µm to 21.22 ± 8.39µm.

In the longitudinal section, the length of the grains increased for all ECAP samples with a large reduction in width. This corresponded to a reduction in aspect ratio for all ECAP samples, indicating elongation of the grains. In the transverse section, the aspect ratios stayed relatively the same before and after ECAP and were closer to 1, indicating more equiaxed grains compared to in the longitudinal section.

The aspect ratio for the coarse green and coarse sintered samples was 0.49 and 0.56 respectively in the longitudinal section, which reduced to 0.17 and 0.11 after ECAP of these samples respectively. In the transverse section of these ECAP samples, the aspect ratio stayed relatively the same at 0.62 and 0.63 for the green and sintered coarse samples respectively to 0.72 and 0.69 for these samples after ECAP. The aspect ratio of the medium samples in the longitudinal section changed from 0.62 after cold compaction to 0.21 after ECAP and in the transverse section stayed relatively the same at 0.66 and 0.71 before and after ECAP respectively. For the fine particles, the aspect ratio in the longitudinal section reduced from 0.61 to 0.19 before and after ECAP respectively, whereas in the transverse section, aspect ratio stayed relatively the same at 0.66 and 0.75 before and after ECAP respectively.

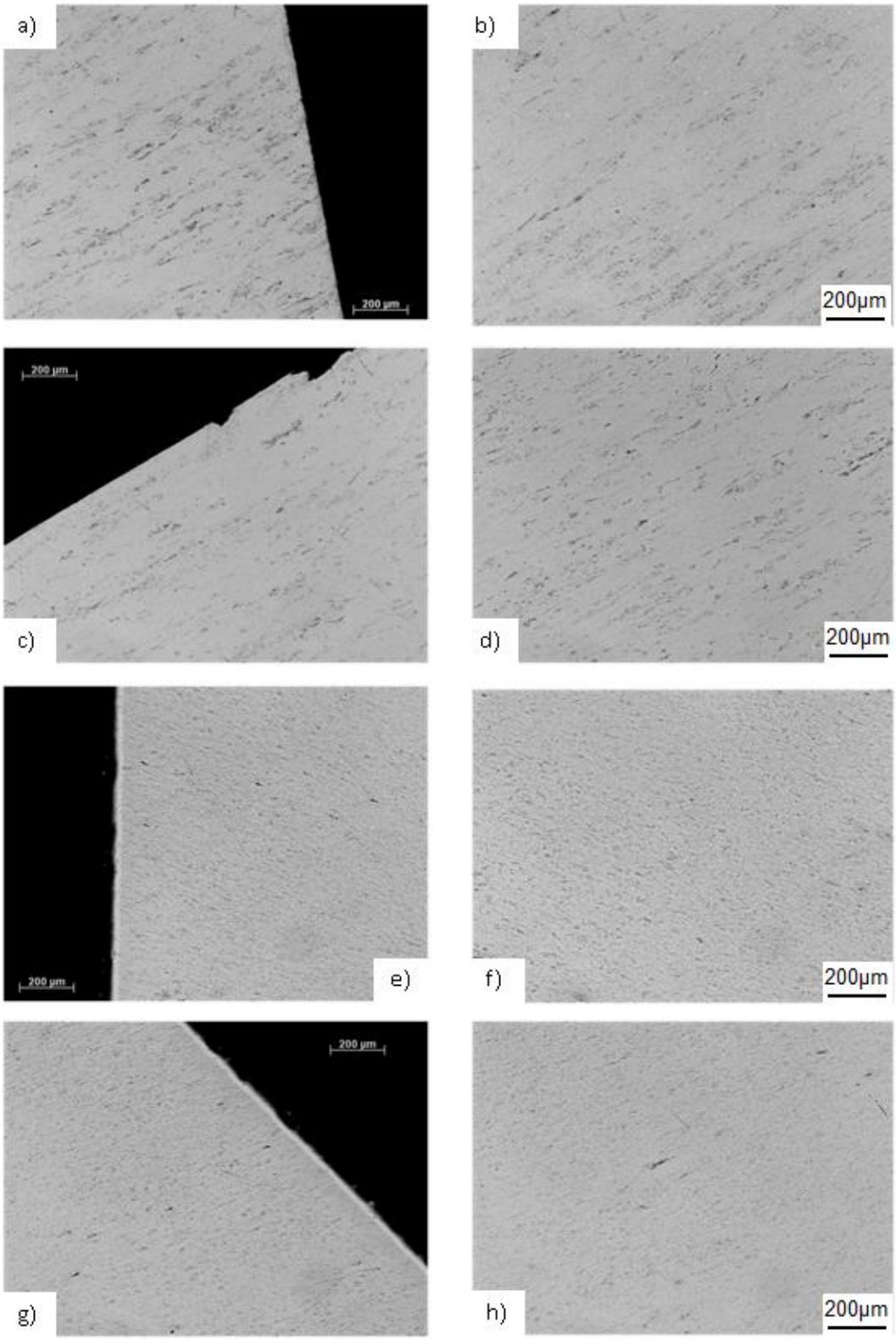

Figure 4.27: Images of porosity for; coarse sintered --> ECAP edge a) and core b); coarse green --> ECAP edge c) and core d); medium green --> ECAP edge e) and core f) and; fine green --> ECAP edge g) and core h) longitudinal sections.

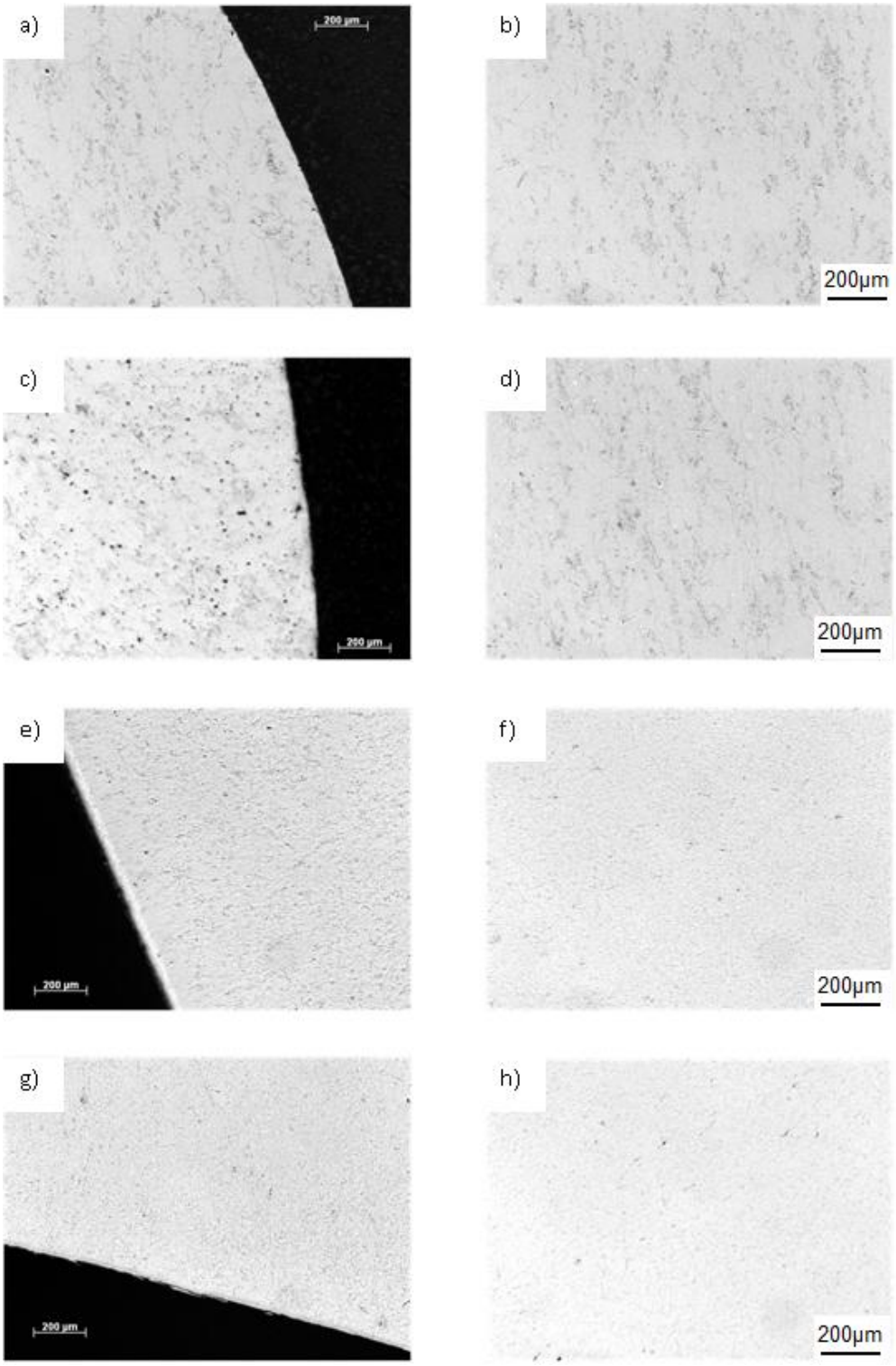

Figure 4.28: Images of porosity for; coarse sintered --> ECAP edge a) and core b); coarse green --> ECAP edge c) and core d); medium green --> ECAP edge e) and core f) and; fine green --> ECAP edge g) and core h) transverse sections.

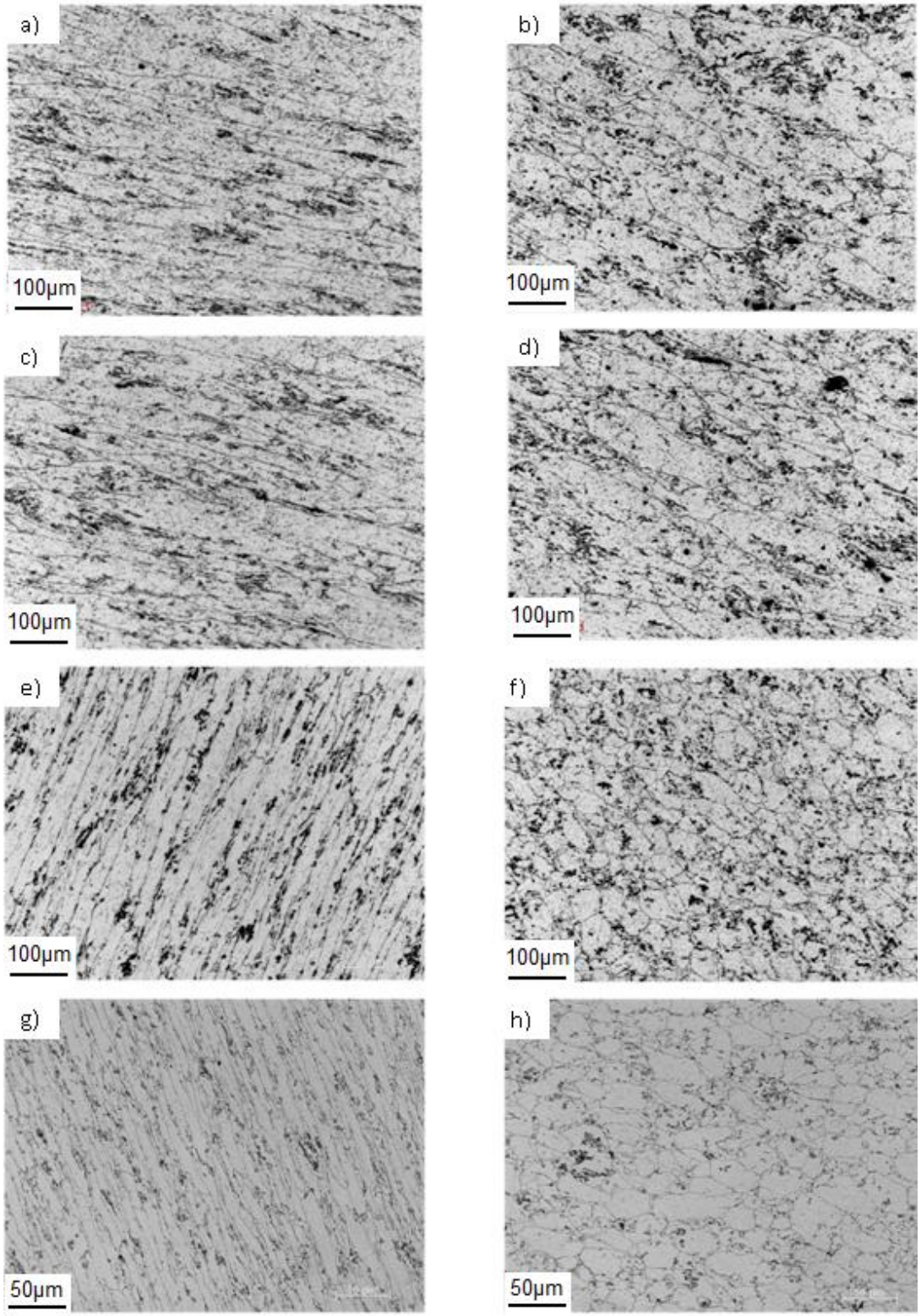

Figure 4.29: Etched ECAP optical images of; coarse sintered a) longitudinal and b) transverse; coarse green c) longitudinal and d) transverse; medium green e) longitudinal and f) transverse and; fine green ECAP g) longitudinal and h) transverse pure aluminium samples. The dark spots are pores and effects of overetching.

Table 4.10: The data for length, width and ECD of the grains after one pass of ECAP for all of the pure aluminium powder samples

Sample	Length µm		Width µm		Aspect ratio		ECD µm	
	Longitudinal	Transverse	Longitudinal	Transverse	Longitudinal	Transverse	Longitudinal	Transverse
Coarse green	215.98 ± 123.59	225.75 ± 114.24	106.26 ± 51.7	139.85 ± 71.89	0.49	0.62	140.77 ± 67.18	164.67 ± 78.17
Coarse sintered	195.12 ± 134.94	231.34 ± 145.81	122.13 ± 87.72	129.49 ± 72.06	0.56	0.63	143.33 ± 98.11	160.77 ± 86.51
Coarse green → sintered → ECAP	358.81 ± 138.27	237.79 ± 130.36	62.49 ± 24.47	170.82 ± 85	0.17	0.72	140.29 ± 49.27	118.57 ± 56.22
Coarse green → ECAP	612.78 ± 290.79	260.54 ± 107.34	65.32 ± 26.65	180.93 ± 98.31	0.11	0.69	176.65 ± 69	136.67 ± 47.14
Medium green	53.72 ± 25.07	67.58 ± 33.35	33.29 ± 15.63	44.66 ± 22.11	0.62	0.66	40.66 ± 17.88	52.59 ± 24.55
Medium green → ECAP	146.33 ± 57.91	80.59 ± 40.44	30.18 ± 9.37	56.86 ± 12.87	0.21	0.71	61.31 ± 17.69	51.03 ± 18.15
Fine green	44.67 ± 22.49	35.69 ± 19.31	27.08 ± 13.05	23.64 ± 11.45	0.61	0.66	31.82 ± 15.53	28.41 ± 13.6
Fine green → ECAP	70.27 ± 32.5	33.1 ± 16.58	13.14 ± 4.69	24.71 ± 6.76	0.19	0.75	28.5 ± 10.34	21.22 ± 8.39

4.1.4.3. Hardness of the ECAP samples

The Vickers hardness values for all of the samples processed by one pass of ECAP are summarised in Table 4.11. After ECAP, the hardness improved for all size ranges. The hardness of the coarse particles increased from 39.82 ± 0.73$HV_{2.5kg}$ to 49.34 ± 0.92$HV_{2.5kg}$ in the pre-compacted and ECAP samples respectively. The hardness of the pre-sintered coarse particles increased from 20.11 ± 0.44$HV_{2.5kg}$ to 47.80 ± 1.60$HV_{2.5kg}$ after ECAP. The hardness of the medium sized particles increased from 43.88 ± 0.74$HV_{2.5kg}$ after cold compaction to 54.53 ± 1.15$HV_{2.5kg}$ after ECAP. The hardness of the fine sized particles increased from 45.91 ± 0.59$HV_{2.5kg}$ after cold compaction to 55.58 ± 2.62$HV_{2.5kg}$ after ECAP.

Table 4.11: The Vickers hardness values for all of the samples.

Sample	Longitudinal $HV_{2.5kg}$	Transverse $HV_{2.5kg}$
Coarse green	39.82 ± 0.73	39.75 ± 1.02
Coarse sintered	20.11 ± 0.44	21.47 ± 1.37
Coarse green → sintered → ECAP	47.80 ± 1.60	45.39 ± 1.00
Coarse green → ECAP	49.34 ± 0.92	49.14 ± 1.28
Medium green	43.88 ± 0.74	44.04 ± 0.57
Medium sintered	23.42 ± 1.33	24.21 ± 0.54
Medium green → ECAP	54.53 ± 1.15	53.94 ± 1.94
Fine green	45.91 ± 0.59	45.94 ± 0.31
Fine sintered	27.36 ± 0.75	27.36 ± 0.5
Fine green → ECAP	55.58 ± 2.62	56.73 ± 2.11

4.2. Pure Aluminium particles Discussion

4.2.1. Starting powder

From section **4.1.1**, a majority of the coarser starting powder particles had an irregular shape and as the size decreased, particle morphology appeared to be more rounded from the SEM images in Figure 4.1, Figure 4.2 and Figure 4.3 respectively. Cooling rates have a significant influence on particle morphology in the chamber [4, 45, 50]. As the particles fall through the atomisation chamber, they lose heat via several mechanisms, which are: radiation; heat flow via the gas that is in contact with the melt; and particle collisions [49, 239]. Larger particles have a smaller surface area, which means that the cooling rates are lower. Therefore the droplet is in a liquid state for longer and the shape is influenced by air turbulence as it falls in the chamber. Conversely, finer particles have a higher surface area and solidify much more rapidly meaning that the shape is not influenced by air turbulence during free-fall [2, 49, 240].

Surface tension forces also affect the particle shape, and can lead to spheroidisation of droplets that were initially irregular, if they have not solidified already, due to a reduction in surface energy [49, 241]. The cooling rate affects the time available for the spheroidisation process. Longer solidification times mean that the time required for spheroidisation is greater as the droplets are liquid for longer. If the time for droplet spheroidisation is longer than the time for solidification, then the particles will have an irregular shape and vice versa for spherical particles [49, 241].

4.2.2. Apparent density

From Table 4.2, the highest apparent density was achieved for the medium sized powder particles at 48.27 ± 1.3%, compared to 37.12 ± 0.52% for the coarse sized particles and 34.06 ± 0.32% for the fine sized particles. Apparent density is a reflection of how well the particles flow past each other as they are poured in to the container. The volume that can be occupied by the mass of powder affects the ability of industrial presses to mass produce compacts and is related to the characteristics of the particle, where shape, size and distribution have a large influence on the efficiency of die filling [4, 62, 66, 68].

4.2.2.1. Coarse, ">150µm", sized particles

The coarse sized particles had a lower apparent density compared to the medium sized particles due to the size and shape differences of the particles. From Table 4.1, the average ECD of the coarse particles was 430 ± 202.53µm compared to 133.27 ± 23.35µm for the medium sized particles. The irregular morphology of the larger particles leads to bridging between neighbouring particles when they are poured in to the container, which creates voids. The larger the particles, the larger the bridges and this in turn creates larger voids which cannot be filled by the other coarse particles, hence a lower apparent density is seen as a result of poor packing [4, 62].

4.2.2.2. Fine, "<45µm", sized particles

The fine sized particle range had the lowest apparent density due to high friction between the particles, despite the morphology of the finer particles being more regular. From Table 4.1, the average ECD of the fine sized particles was 28.48 ± 10.74µm, which was considerably finer than the medium sized particles. Finer particles have a higher specific surface, which means that they have a larger area of contact with neighbouring particles [4]. The larger area of contact means that the frictional forces of the powder particles increases, which subsequently prevents adequate flow and filling of dies under gravity, hence a low apparent density [35, 62, 69].

4.2.2.3. Medium, ">76µm <105µm", sized particles

The medium sized particle range had the highest apparent density. The reason for this may be attributed to the particle size distribution, which can be seen in the histograms in Figure 4.4. The minimum ECD from the histogram was 70µm which is less than the minimum sieve size used to collect the powders from and some ECD measurements were far greater than the 105µm apertures in the sieve, with the maximum being 230µm. This implies that there is a wide range of particle sizes present in the medium sized particle batch and it is likely that the smaller particles would fit in the voids that would be created by larger particles, which increased the apparent density [4, 62, 68].

4.2.3. Cold compacted powders

4.2.3.1. Density

From Figure 4.5, the density of the medium sized powder particles increased with compaction pressure, from 2.39 ± 0.025g/cm^3 at 50MPa to 2.64 ± 0.024g/cm^3 at 400MPa, and began to plateau. This trend was expected due to higher compaction forces deforming the powder particles so they fill the voids created from die fill [77, 89]. A plateau began as the aluminium particles could no longer move past each other or deform into the available space with higher pressing forces [17, 87, 242]. Increasing the compaction pressure above 400MPa lead to marginal increases in density although the risk of tool wear was also higher, thus adding to the cost of manufacture if parts have to be replaced more frequently [77, 81, 242, 243].

It has been reported that densification occurs in a few stages, shown in Figure 4.30 [17, 42, 87, 88]. At the beginning of the compaction process, the primary mechanism for densification is the movement and re-arrangement of the powder particles as they slide and rotate past each other in to the optimum position [8, 76, 87, 90]. When the powders are loosely settled upon die filling, there is an interconnected porous network. As densification proceeds, more contact points are created between the powder particles, which subsequently causes isolated porous networks in the compact and breaks down the bridges that were formed in die filling [8, 70, 71, 76, 90]. The asperities on the surface of the particles merge together and form bonding surfaces between neighbouring particles, which develops several cold welding spots due to the strong shearing along the contact surfaces [8, 76, 87, 90].

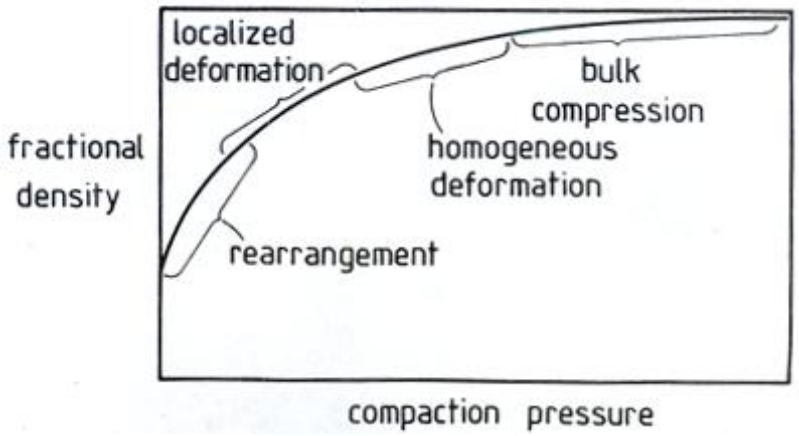

Figure 4.30: The different stages of compaction [42].

In the second stage of compaction, densification mainly occurs by the localised elastic deformation of particles [76, 87, 90]. The asperities of the particles in contact with each other become deformed due to pressure and the deformation begins to spread through the contact region, with the displaced material facilitating neck growth to isolate the network of pores [71, 76]. As densification increases, the deformation at the contact points exceeds the yield strength of the material, causing local plastic deformation at these regions. The material starts to flow into the voids between the particles, which leads to further densification in the homogenous deformation stage. Strain hardening occurs due to the plastic deformation of particles, which increases the resistance to further deformation [71, 76, 88]. The final stage generally occurs at very high pressures where plastic deformation cannot proceed due to a lack of porosity and the compact behaves like a fully dense body [71, 76, 88].

The deformation of the particles can be seen in the etched optical images from Figure 4.8 and Figure 4.9 when compared to the starting powder particles from Figure 4.1, Figure 4.2 and Figure 4.3. The location of the pores at the junctions of neighbouring particles was expected as a result of the aforementioned densification mechanism [93]. Using higher compaction pressure also leads to higher ejection forces and frictional effects on the material, which causes cracking of the sample and is undesirable [71, 76, 88].

It is ideal to increase the green density as much as possible in order to optimise the final mechanical properties; therefore the cold uni-axial compaction pressure remained at 400MPa for all samples throughout. From Table 4.3, the coarse particles reached the same density as the medium particles at 2.64 ± 0.01g/cm^3 and the fine particles slightly lower at 2.59 ± 0.001g/cm^3. The lower green density for the fine powder particle size range can be attributed to the high friction forces between the particles, which prevented adequate flow during the first stage of densification [8, 17, 65, 87-90]. This meant that there was very little movement of particles into the available space left by the voids from die filling. Therefore, the second stage of densification, where the particles plastically deform, happened much sooner, which increased the amount of contact points between particles and closed off some porous networks [17, 65, 87-93].

4.2.3.2. Microstructure

4.2.3.2.1. Porosity variation

From Figure 4.6, a region of high porosity existed at the edge of the samples compared to the relatively low porosity at the centre. This region of increased porosity can be created by the way in which the powder particles settle prior to compaction. From die filling, an area of uniformly packed particles exists in the centre, whereas a more porous region occurs next to the die wall [100]. Even after tapping the die to try and homogenise the distribution of particles, this outer shell of porosity remains in the green compacts as a result of the higher friction at the die wall, despite applying die wall lubricant in the form of Kenolube [72, 73, 83]. This prevented adequate flow from die fill and the non-uniform transmission of pressure.

For the fine aluminium particles, the region of higher porosity at the edge extended slightly further in to the centre of the sample and is slightly more pronounced compared to the coarse and medium sized particle ranges. This can be explained by the higher friction in smaller particles as result of the increased surface area in contact with the die wall preventing adequate movement of the particles as well as smaller particles being harder and more resistant to plastic deformation, thus affecting the transmission of force.

4.2.3.2.2. Grain size

From Table 4.4, it can be seen that the particle sizes decreased after cold compaction when compared to the starting powder for the coarse and medium sized particle ranges. This reduction in particle size was expected as a result of the compaction process and the densification mechanisms. In the second stage of densification, after the particles have re-arranged to their optimum position, they undergo plastic deformation when in contact with other particles, which causes an associated reduction in grain size [76, 87, 90].

The fine sized particles did not show much change from the starting ECD of 28.48 ± 10.74µm to 28.41 ± 13.6µm in the transverse section and 31.82 ± 15.53µm in the longitudinal section of the cold compacted sample. Smaller grains have a higher hardness and are more resistant to deformation, therefore less plastic deformation occurred in the latter stages of densification, hence no significant change is seen in the grain size for the cold compacted fine aluminium particles [10, 182].

4.2.3.2.3. Hardness

The hardness values for the different size ranges followed the trend from the Hall-Petch equation, where the finer particle size range had the higher hardness of 45.94 ± 0.31 compared to 44.04 ± 0.57 and 39.75 ± 1.02 for the medium and coarse particles respectively. In the second stage of densification, the particles were subjected to plastic deformation and the work hardening effect contributed to the hardness of the compacts [77, 89].

Smaller particles have a higher hardness as they restrict the movement of dislocations. These dislocations move across slip planes until they reach a grain boundary, which prevents them moving any further [190, 191]. The hardness of a material is determined by its ability to stop dislocation movement and decreasing grain sizes increases the amount of grain boundaries. As can be seen from Figure 4.18, the fine particles have a higher amount of grain boundaries for a given area compared to the medium and coarse etched optical images and thus preventing dislocation movement and increasing the hardness [190, 191].

4.2.3.2.4. Heckel relationship

This can be used to calculate the yield strength of a material using the density achieved at various compaction pressures, which was shown in equation (2.2) [94, 95]. Graphs of $ln\frac{1}{1-D}$ against P are shown in Figure 4.31 for all the size ranges of pure aluminium powder and the gradient of the graph is the value for the constant k_H. As k_H is related to the yield stress by equation (2.3), this can be re-arranged so that the yield stress, σ_y, is on its own to give equation (4.1) [79, 95].

$$\sigma_y = \frac{1}{3k_H} \tag{4.1}$$

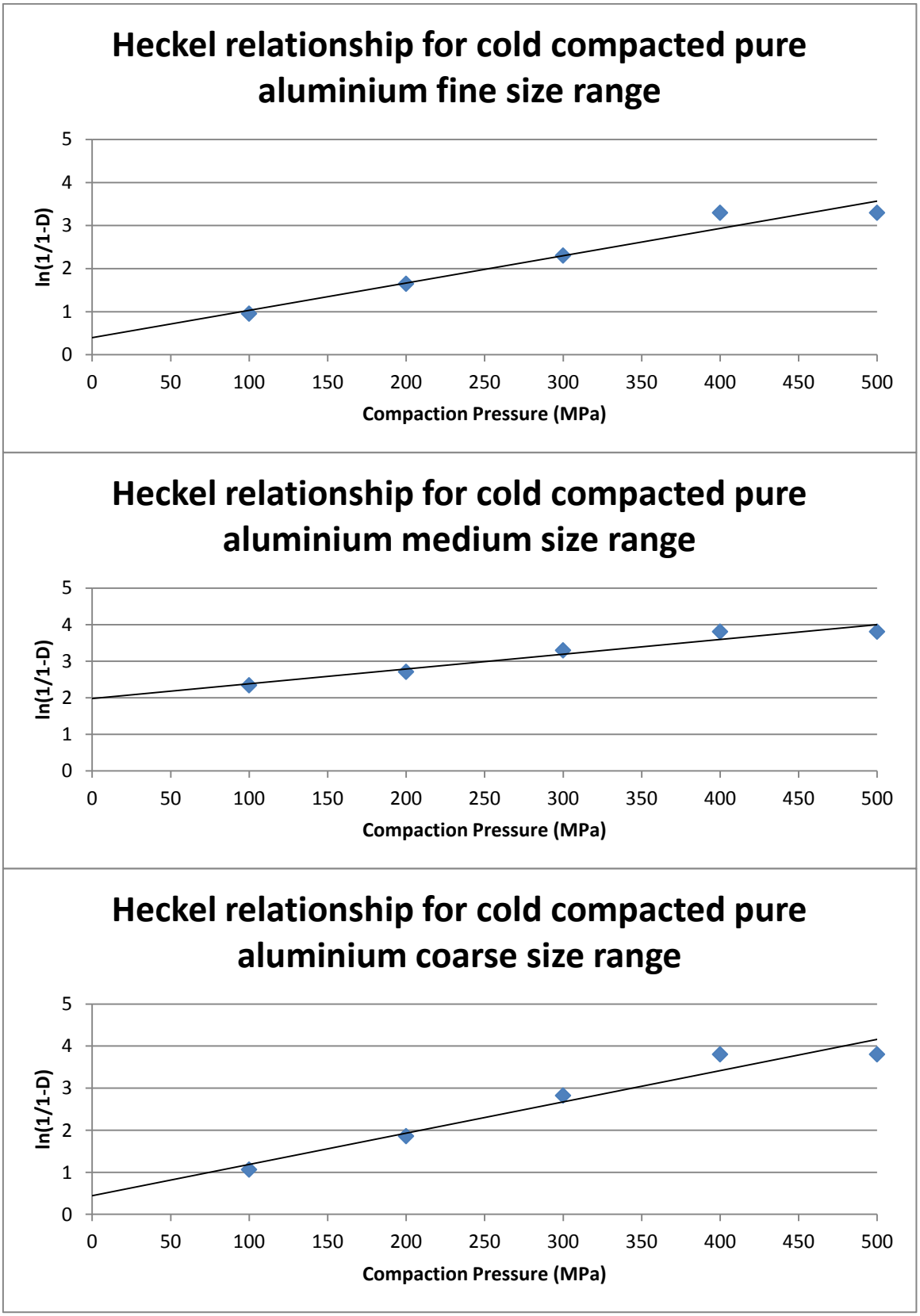

Figure 4.31: Heckel relationship for cold compacted pure aluminium medium sized particle range.

The yield strength of the aluminium powders is summarised in Table 4.12. The optimum yield strength of 66.15MPa was reached by the medium size range, which is comparable to a wrought 1000 series aluminium alloy [192, 244-246]. The lower values for the fine and coarse particle sizes are due to the gradient of the slope being slightly steeper than the medium size range. From the Hall-Petch equation, smaller particles are harder to deform, thus there is a resistance to plastic deformation during compaction and affects the densification behaviour, thus increasing the gradient of the graph. Larger particles on the other hand are softer and easier to deform, which decreases the yield strength from the Heckel plots.

Table 4.12: The approximate yield strengths of the different pure aluminium size ranges

Powder particle size range	Approximate Yield strength (MPa)
Fine	52.64
Medium	66.15
Coarse	44.88

4.2.4. Sintering response

4.2.4.1. Density

The density of the sintered powders did not show any improvement from cold compaction for any of the pure aluminium size ranges as shown in Table 4.6. The lack of densification can be explained by the stable oxide layer on the surface of the aluminium particles preventing adequate contact between neighbouring particles [103, 111, 247]. This behaviour has also been observed in an aluminium compact that underwent solid state sintering at 625°C for 2.5 hours and 620°C for 1h [21, 248].

4.2.4.2. Microstructure

The ECD of the sintered particles did not differ greatly when compared to the grain sizes from the cold compaction, shown in Table 4.7. Optical images revealed a very similar microstructure in the green compacts (Figure 4.9) compared to sintered samples (Figure 4.18 to Figure 4.20). This can be explained by the surface oxide layer preventing any metallurgical bonding between neighbouring particles and so the effects of solid state sintering on the grain size are not significant. Previous studies had shown that for sintering at 625°C for 2.5 hours on commercially air atomised pure aluminium particles, there was an insignificant effect on the grain size [248].

However, the porosity variation seen in the cold compacted samples from the edge to the centre appeared to have changed as a result of the sintering, as shown in Figure 4.6 and Figure 4.16 respectively. It is possible that there was some material transport towards the edge of the sample where there is more porosity and therefore homogenised the pore distribution in order to reduce the free surface energy [248, 249]. The interfacial energy between solid and vapour is much higher than solid-solid. As the material is more porous in the skin region, there is more solid-vapour interface between particles and pores. Thus, there is a drive to reduce the interfacial energy at this region to create more solid-solid interfaces [248, 249].

4.2.4.3. Hardness

Table 4.8 showed that the Vickers hardness of the sintered pure aluminium particles reduced to approximately half of the hardness for the cold compacted samples. This is likely to be a result of the change in stored energy as the sample is heated from room temperature. During deformation and work hardening from compaction, the powders absorb high amounts of strain energy as dislocations form and become entangled, which increased the hardness [190-192]. When temperature is applied during sintering, the thermal energy allows the atoms to move via the driving force of the strain energy [245, 250-252]. The entangled dislocations then become re-arranged into low-angle grain boundaries that are relatively free of dislocations, indicating recovery [245, 250-252]. The changes seen in the hardness are likely to be caused by re-crystallisation, where new, non-deformed grains nucleate and grow into the rest of the compact, reducing the dislocation density to the original value and reducing the hardness [245, 250-252].

4.2.5. ECAP samples

4.2.5.1. Density

From Table 4.9, after one pass of ECAP, all compacts showed an increase in density although the sintered coarse particles size range showed the highest increase in density from 2.59g/cm^3 ± 0.01 after sintering to 2.67g/cm^3 ± 0.01 after ECAP. Densification is caused by high shear strains to the material as it passes through the 90° channel. The severe plastic deformation of the aluminium particles ruptures the oxide layer thus exposing fresh surfaces, which bond together via back pressure from the samples in the die, as mentioned in section **2.5.5** [220, 221, 253-255]. In cold compaction, plastic deformation of the powder particles at contact points causes the particles to begin closing off the porous network until the compaction pressure is reached [8, 70, 71, 76, 90]. When severe plastic deformation occurs, the isolated porous networks are almost eliminated as the particles spread in to them, which subsequently leads to an increase in density [220, 221, 253-255].

The coarse particles reached a higher ECAP density compared to the other size ranges. From the Hall-Petch equation, larger particles are softer and are able to deform more easily compared to the fine and medium particles [10, 29, 182, 190, 191, 193]. When comparing the Vickers hardness after cold compaction, the coarse particles had lower values compared to that of the other size ranges, seen in Table 4.5. After sintering, the coarse particles were even softer, hence severe plastic deformation had a greater effect during ECAP and this increased the density as can be seen in Table 4.11.

4.2.5.2. Microstructure

The grains on the transverse and longitudinal sections of the cold compacted samples were generally equiaxed, with a relatively small difference between the width and the length of the measured particles from Table 4.4. After ECAP, this difference drastically changed in the longitudinal section, which is parallel to the shear plane, as can be seen in Table 4.10. The severe plastic deformation from ECAP significantly elongated the grains in the longitudinal section for all samples illustrated in Figure 4.29 a), c), e) and g). As was mentioned in section **2.5.5**, the particles experience high plastic strains as they pass through the channel angle. This exposes fresh surfaces and, with back pressure from samples left in the exit channel providing the compressive force required for good contact between the particles, there is excellent bonding between particles.

The transverse sections perpendicular to the shear plane showed relatively equiaxed grains compared to the longitudinal sections seen in Figure 4.29 b), d), f) and h). The ECD of the grain sizes in the transverse section are shown for all samples in Table 4.13. The average ECD grain size measurement in the transverse section decreased with one pass of ECAP for all particle size ranges, which is expected due to the severe plastic deformation refining the grains after one pass.

Table 4.13: A summary of the transverse ECD grain sizes for all of the pure aluminium samples.

Sample	ECD µm
Coarse starting	430.41 ± 202.52
Coarse green	164.67 ± 78.17
Coarse sintered	160.77 ± 86.51
Coarse green → ECAP	136.47 ± 47.14
Coarse green → sintered → ECAP	118.57 ± 56.22
Medium starting	103.27 ± 23.35
Medium green	52.59 ± 24.55
Medium green → ECAP	51.03 ± 18.15
Fine starting	28.48 ± 10.74
Fine green	28.41 ± 13.6
Fine green → ECAP	21.22 ± 8.39

The coarse particles showed the largest refinement after ECAP, which can be linked to the hardness of these particles after cold compaction in Table 4.5. Larger grains are easier to deform when considering the Hall-Petch relationship, therefore the effect of ECAP on the grain sizes of larger particles is much greater [10, 29, 182, 190, 191, 193]. For the medium and fine sized particle range, the decrease in grain size is very small even after ECAP, which is due to smaller grain sizes having higher hardness and therefore have a higher resistance to plastic deformation.

4.2.5.3. Hardness

The Vickers hardness increased in all samples after one pass of ECAP, as seen in Table 4.11. One aforementioned factor is the reduction in grain size that can contribute to strengthening via restriction of the movement of dislocations. The other factor is the slight increase in density after ECAP, causing a reduction in porosity, therefore decreasing the number of sites whereby cracks can be initiated from to weaken the material.

4.2.6. Summary

In the literature review, research on the ECAP of pure aluminium had been reported including the use of bimodal distribution of nano-powders with micron sized particles. However, nano-particles are more expensive to produce than coarser micron sized particles and the important finding from this section of the thesis is that ECAP is able to improve hardness and, to some degree, density, regardless of the size of the particles used. Therefore to keep the costs down, coarser particles can be used and be processed by ECAP in order to improve hardness of net shape parts.

4.3. Al-20Sn-7Si-1Cu bearing alloy

4.3.1. Starting powder

4.3.1.1. Size and morphology

The starting powder of the gas atomised Al-20Sn-7Si-1Cu particles is shown in the back scattered SEM image in Figure 4.32. The particles were mainly spherical in shape and the average particle diameter by mass (D_{50}) was 21.70µm as supplied by AlPoCo, which is shown in the sieve analysis in Table 4.14. The compositional analysis by AlPoCo is shown in Table 4.15. The apparent density was 1.49g/cm^3 ± 0.47g/cm^3, which is 34% of the theoretical (3.08g/cm^3), the calculation of which is shown in Appendix 6-15.

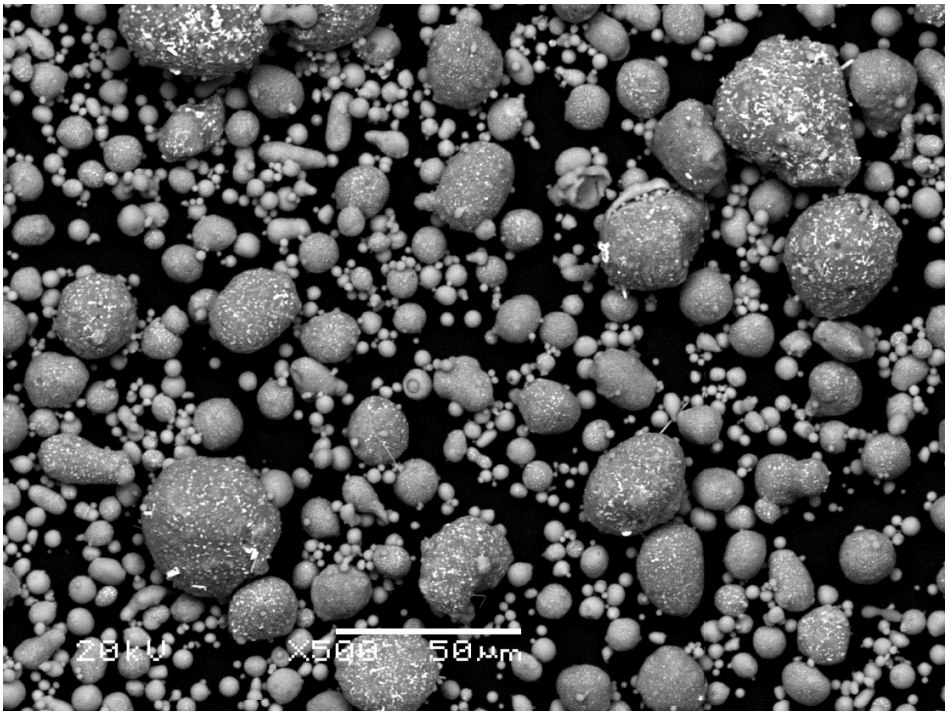

Figure 4.32: A back scattered SEM image of the starting Al-20Sn-7Si-1Cu particles where each particle had the composition as specified in Table 4.15.

Table 4.14: Particle size fraction for the as-supplied AlPoCo powder.

Size Fraction	Average Size µm
D_{10}	6.46
D_{50}	21.70
D_{100}	54.36

Table 4.15: Certificate of Analysis (COA) of the as-supplied AlPoCo powder.

	Sn (%)	Si (%)	Cu (%)	Al (%)
Specification	19-21	6-7	0.75-1.25	Balance
COA analysis	22.2	7.52	1.13	Balance

4.3.1.2. Hardness

The microhardness of the particle sizes between 60-80µm was measured as $77.7HV_{0.15kg} \pm 1.71$.

4.3.2. Cold compacted specimens

4.3.2.1. Density and compressibility curve

The compressibility curve for the cold compacted Al-20Sn-7Si-1Cu powders is shown in Table 4.16 and Figure 4.33 for compaction pressures ranging from 100MPa to 500MPa. A compaction pressure of 400MPa was used for all other pressings to reduce tool wear. The density began to plateau with increasing compaction pressure from $2.19 \pm 0.00 g/cm^3$ at 100MPa to $2.76 \pm 0.01 g/cm^3$ at 500MPa. The density at 400MPa was $2.67 \pm 0.04 g/cm^3$, which is $86.76 \pm 1.16\%$ of the theoretical density.

Table 4.16: The densities obtained at different compaction pressures for the Al-20Sn-7Si-1Cu alloy

Compaction Pressure MPa	Green density g/cm^3	Green density %
100	2.19 ± 0.00	71.18 ± 0.14
200	2.38 ± 0.11	77.37 ± 3.59
300	2.53 ± 0.01	82.15 ± 0.19
400	2.67 ± 0.04	86.76 ± 1.16
500	2.76 ± 0.01	89.51 ± 0.30

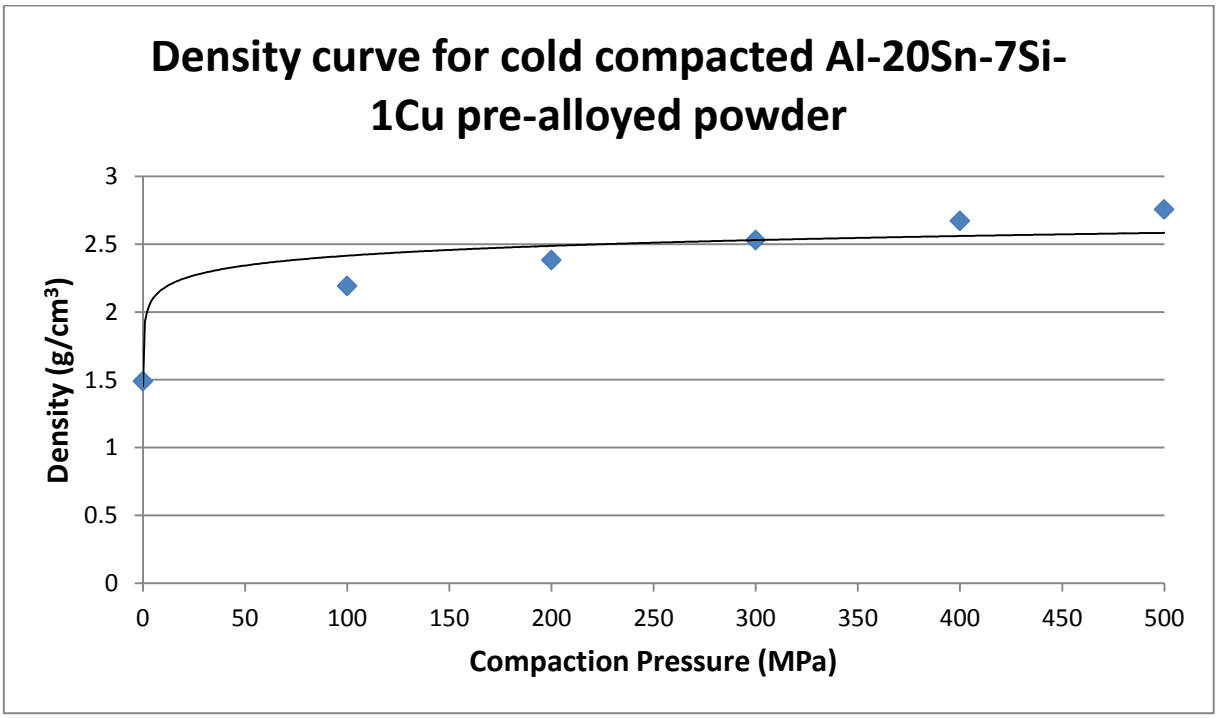

Figure 4.33: The compressibility curve for the Al-20Sn-7Si-1Cu cold compacted samples

4.3.2.2. Microstructure of the cold compacted samples

Macro images were taken of the two sections of the as-pressed material and these are shown in Figure 4.34. An outer region or skin surrounding the core of the sample is seen on the surface of both sections. The optical micrographs of the skin and core region of the longitudinal section of the cold compacted Al-20Sn-7Si-1Cu are shown in Figure 4.35. The region close to the edge in the skin region appears more porous than that in the centre of the sample. The transverse section also shows a similar trend with the skin region showing a more porous microstructure shown in Figure 4.36.

.

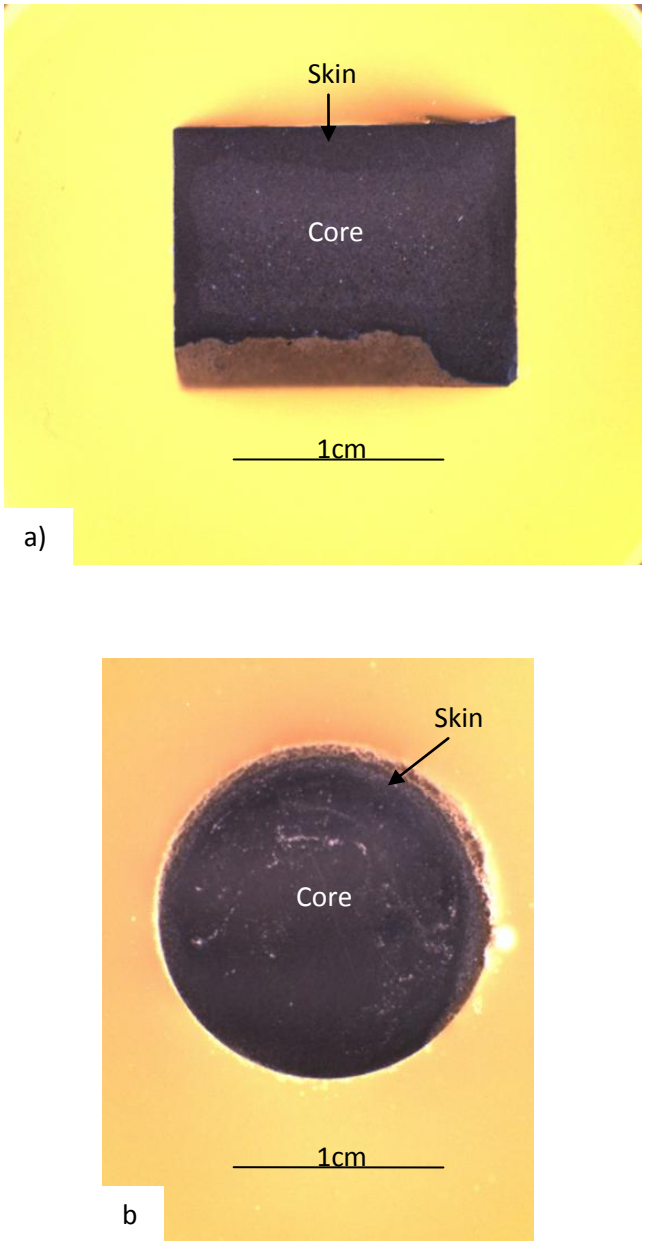

Figure 4.34: Macro images of the as-pressed Al-20Sn-7Si-1Cu a) longitudinal and b) transverse sections

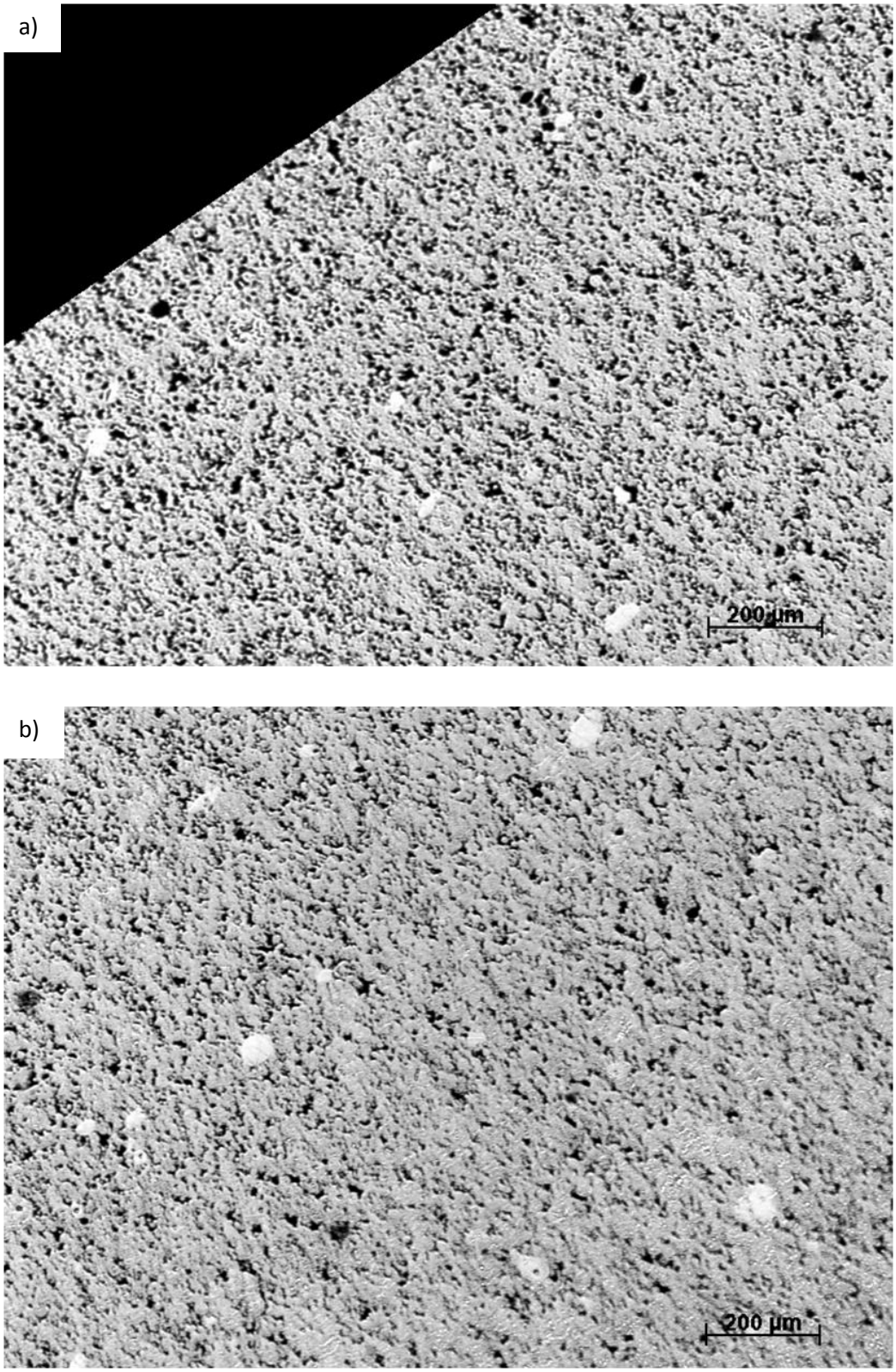

Figure 4.35: Unetched optical images of the longitudinal a) edge and b) core regions of the Al-20Sn-7Si-1Cu green compacts.

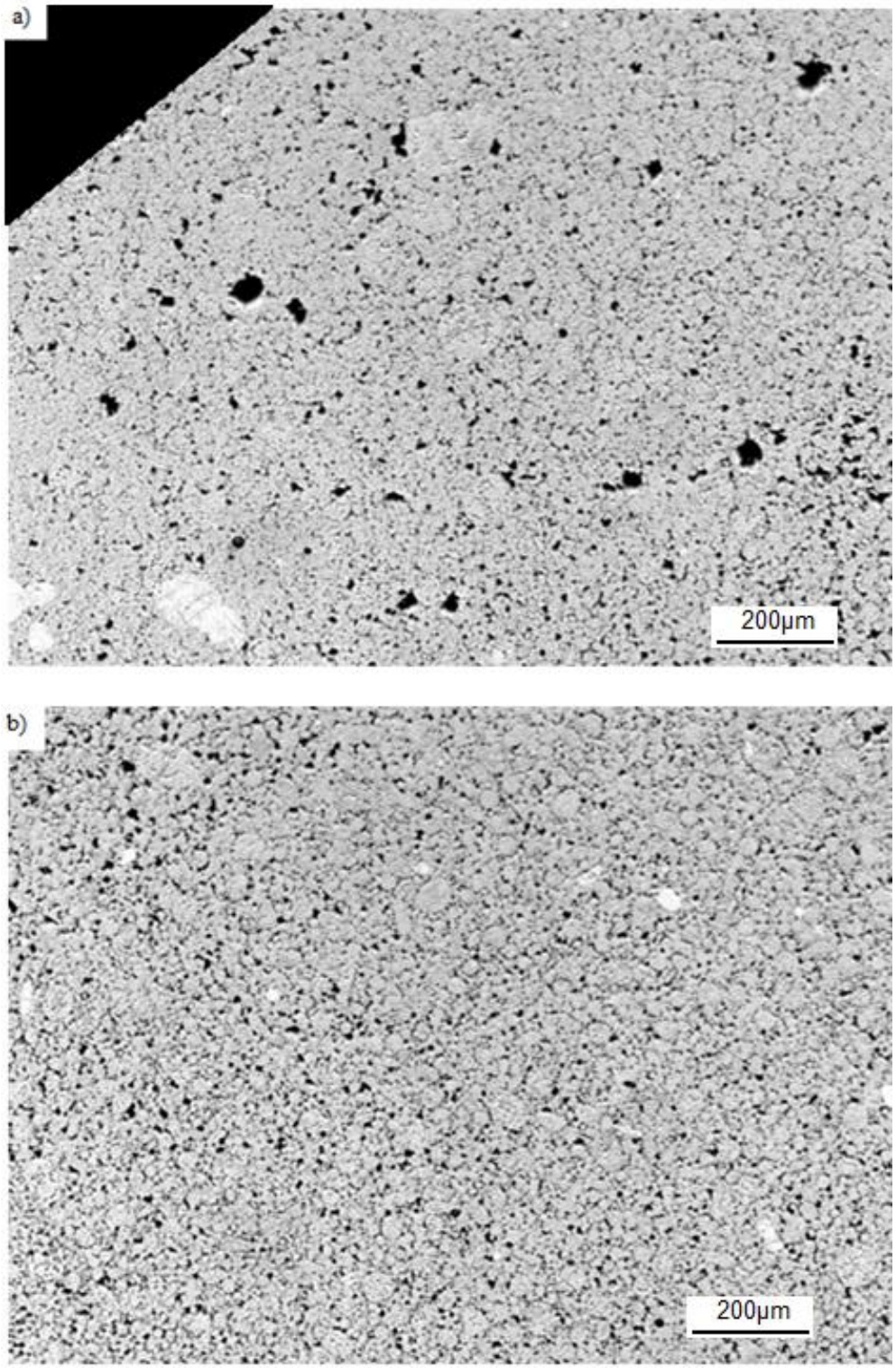

Figure 4.36: Unetched optical images of the transverse a) edge and b) core regions of the Al-20Sn-7Si-1Cu green compacts.

The etched optical images of the cold compacted longitudinal and transverse sections are shown in Figure 4.37. The data for the length, width and equivalent circular diameter of discrete particles are shown in Table 4.17. The ECD of the particles ranged from 12.43 ± 7.25µm in the longitudinal section to 13.9 ± 8.65µm in the transverse section.

A back-scattered SEM image and EDX analysis is shown in Figure 4.38. The dark grey regions represent aluminium; the bright phases are tin, which appear in localised pools from the atomised powder; and silicon and copper are dissolved throughout the matrix. The spread of data measured for the longitudinal and transverse sections can be seen in the length, width and ECD histograms in Figure 4.39 and Figure 4.40 respectively.

Table 4.17: The length, width and ECD for the cold compacted Al-20Sn-7Si-1Cu samples

Sample	Length µm		Width µm		Aspect ratio		ECD µm	
	Longiudinal	Transverse	Longiudinal	Transverse	Longiudinal	Transverse	Longiudinal	Transverse
Green compact	14.65 ± 8.7	16.49 ± 10.86	11.3 ± 6.75	12.42 ± 7.96	0.77	0.75	12.43 ± 7.25	13.9 ± 8.65

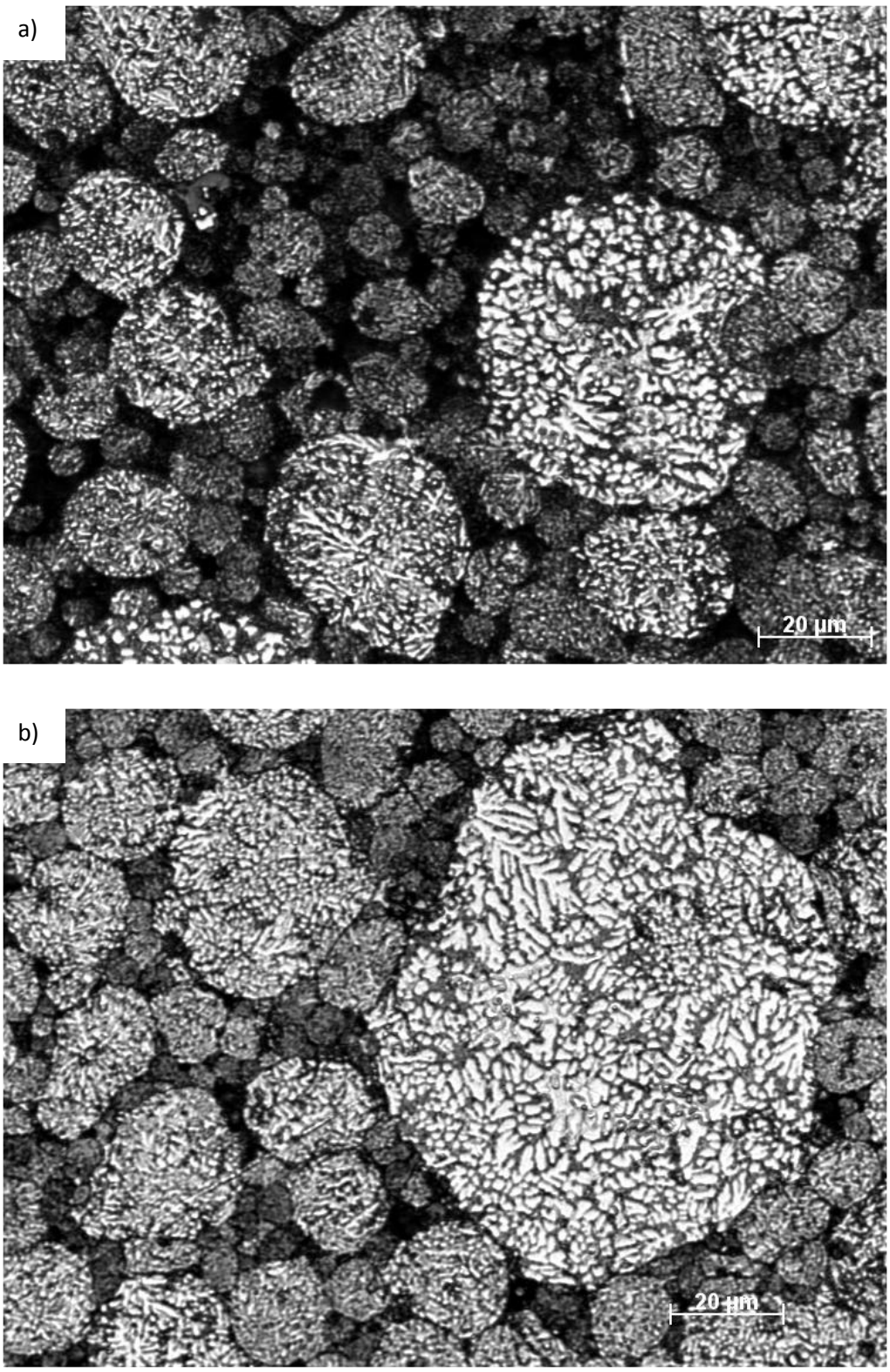

Figure 4.37: Etched optical images of the cold compacted Al-20Sn-7Si-1Cu in the a) longitudinal and b) transverse section.

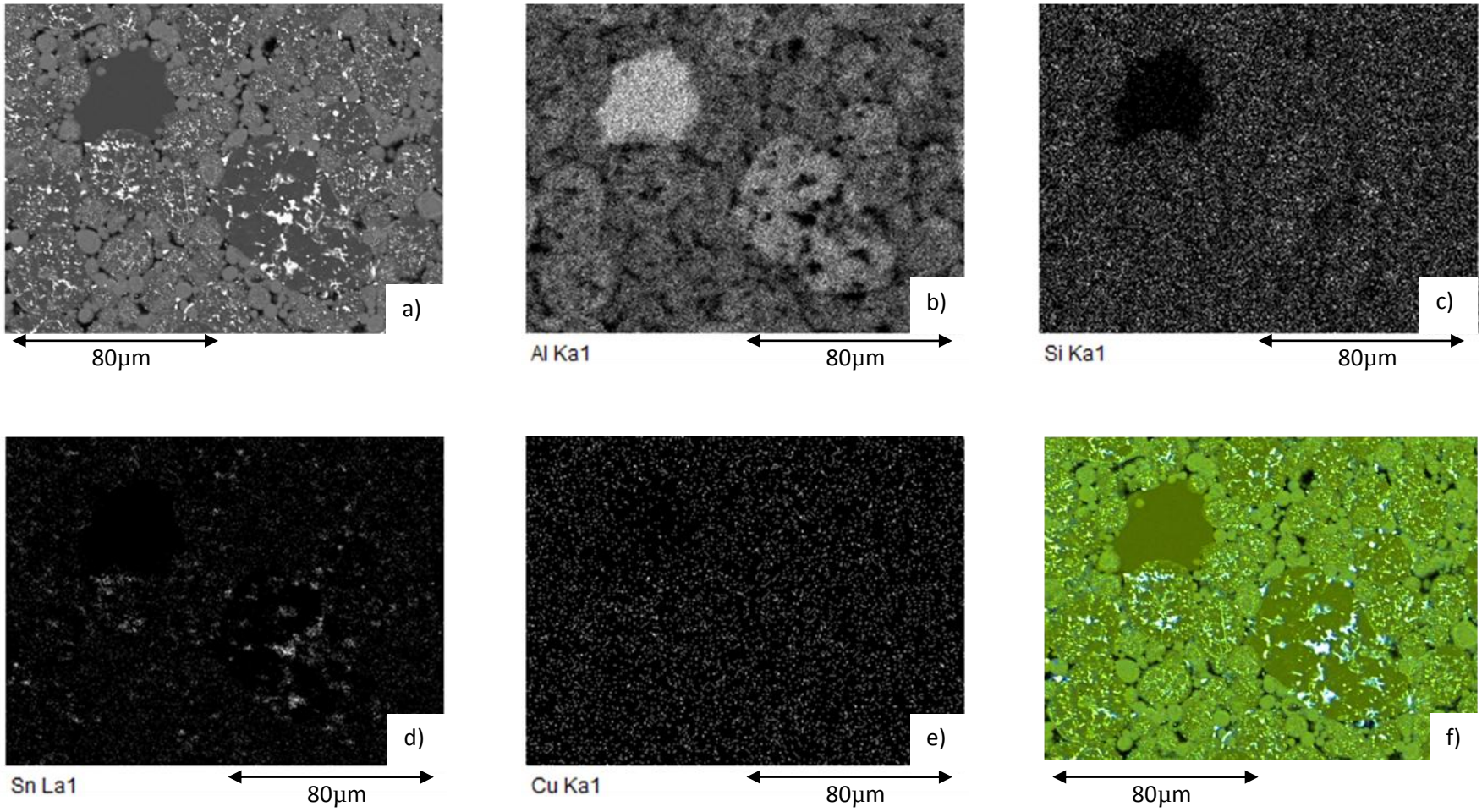

Figure 4.38: EDX of the green compact; a) SEM; b) Al map; c) Si map; d) Sn map; e) Cu map; f) Coloured map where dark green represents Al, lighter green represents Si and blue/white represents Sn.

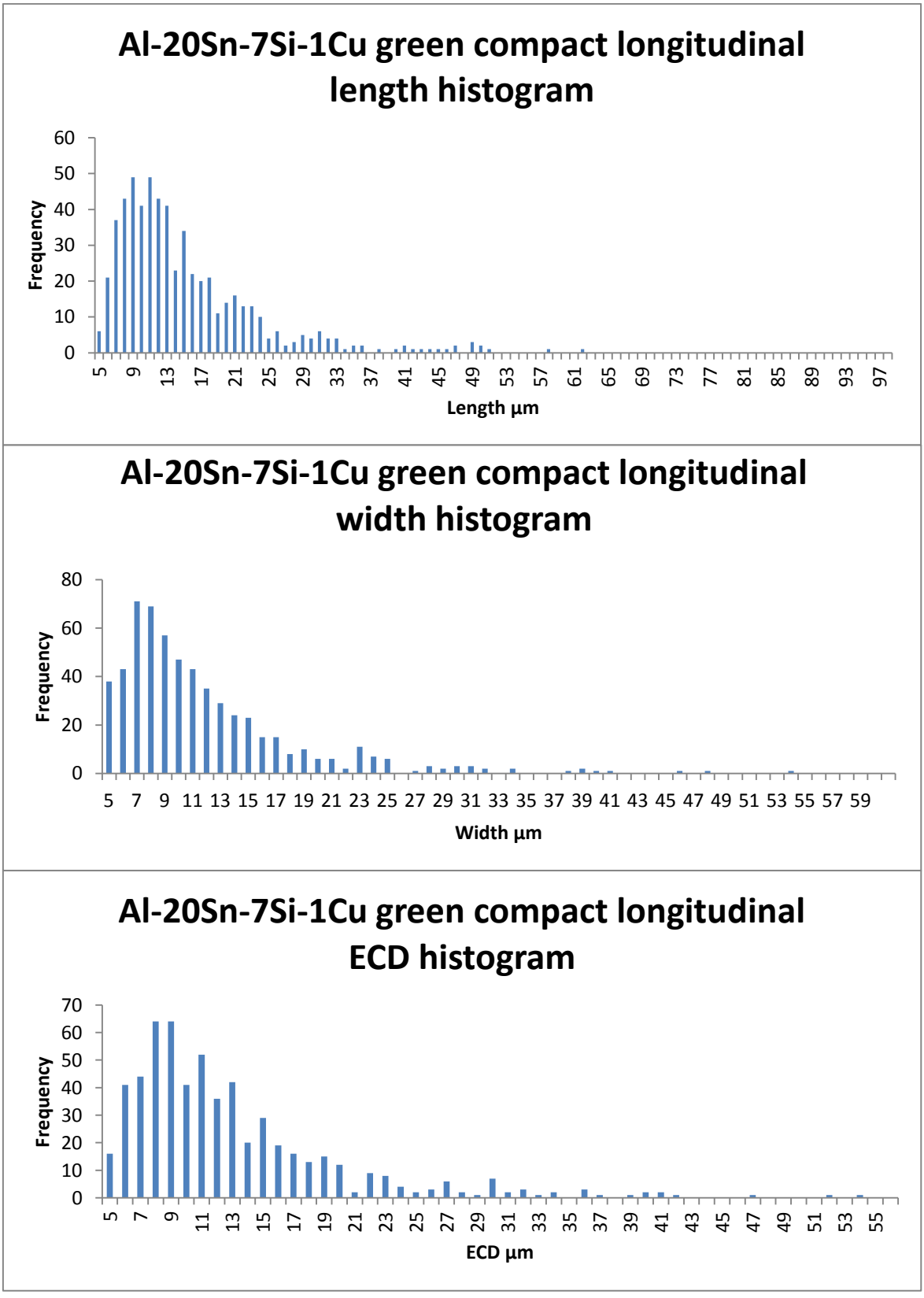

Figure 4.39: Histograms for the longitudinal section of as-pressed Al-20Sn-7Si-1Cu powders.

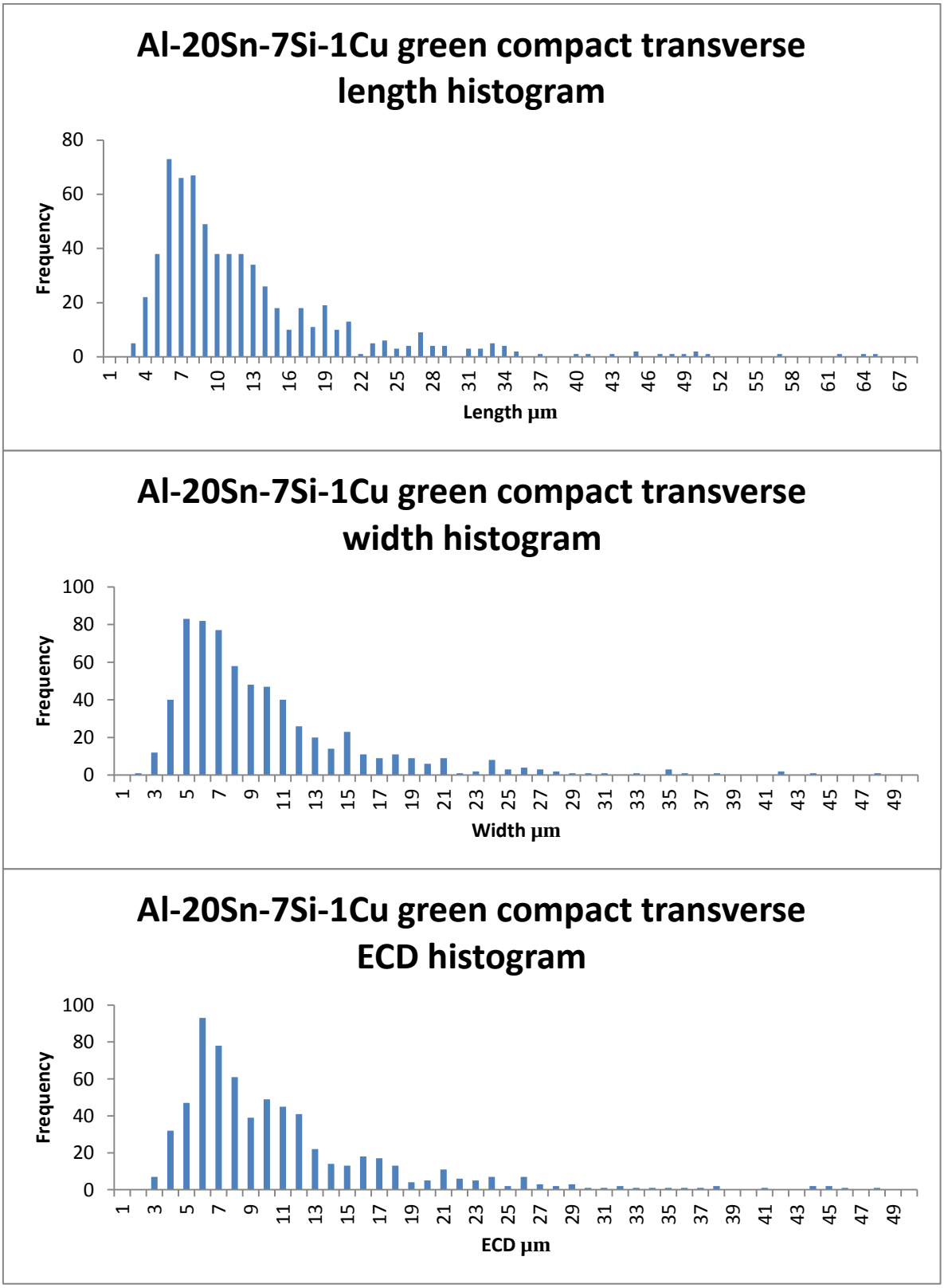

Figure 4.40: Histograms for the transverse section of as-pressed Al-20Sn-7Si-1Cu powders.

4.3.2.3. Hardness of cold compacted samples

The Vickers hardness of the cold compacted Al-20Sn-7Si-1Cu powder is shown in Table 4.18 and it ranged from 60.19 ± 2.27$HV_{2.5kg}$ to 62.2 ± 1.95$HV_{2.5kg}$ in the longitudinal and transverse sections respectively.

Table 4.18: The Vickers Hardness values for the Al-20Sn-7Si-1Cu cold compacted samples

Sample	**$HV_{2.5kg}$**	
	Longitudinal	Transverse
Green compact	60.19 ± 2.27	62.2 ± 1.95

4.3.3. Sintering response

Different temperatures were tested at one hour in order to have a compact with suitable strength to withstand ECAP. This is because the samples crumbled when they were not sintered prior to ECAP. At 300°C 1h in an atmosphere of nitrogen, the samples were very fragile and did not have sufficient strength as they crumbled when attempting ECAP. At 500°C for 1h in an atmosphere of nitrogen, the samples developed sufficient strength to be passed through ECAP without fragmenting. Therefore the sintering temperature remained at 500°C for a minimum of one hour, with 10h also used to test the effect of longer sintering times on the microstructure of this alloy. A temperature of 550°C for one hour was also studied. Tin exuded out of the sample as shown in Figure 4.41 and also held together after ECAP. The sample sintered at 500°C for 1h is shown in Figure 4.42.

Figure 4.41: Tin sweating out of the sintered samples at 550C for 1h in nitrogen atmosphere

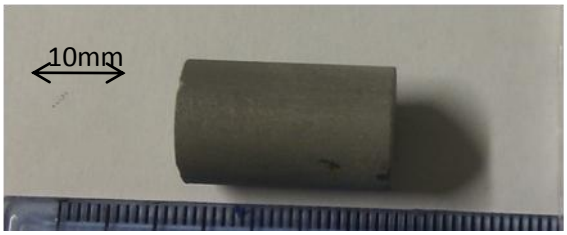

Figure 4.42: The Al-20Sn-7Si-1Cu sample sintered at 500°C 1h in a Nitrogen atmosphere

4.3.3.1. Sintered density

The density of the sintered samples is summarised in Table 4.19. After sintering for 500°C 1h, the density remained the same as the cold compacted density at 2.67 ± 0.01g/cm^3. After sintering at 500°C for 10h, the density decreased marginally to 2.66 ± 0.01g/cm^3 and decreased further to 2.60 ± 0.01g/cm^3 for the sample sintered at 550°C for 1h.

Table 4.19: The density of the sintered Al-20Sn-7Si-1Cu samples

Sintering condition	Density g/cm^3	Density %
500°C 1h	2.67 ± 0.01	86.53 ± 0.28
500°C 10h	2.66 ± 0.01	86.44 ± 0.09
550°C 1h	2.60 ± 0.01	84.51 ± 0.13

4.3.3.2. Sintered microstructure

Macroscopic images were taken of the longitudinal and transverse sections of the sintered samples, which are shown in Figure 4.43 to Figure 4.45 for the samples sintered at 500°C for 1h, 10h and 550°C for 1h respectively. There is a smaller skin region compared to the green compact for all sintered samples. Unetched optical images of the samples sintered at 500°C for 1h & 10h and 550°C are shown in Figure 4.46 to Figure 4.48 respectively, with a higher magnification of the skin region.

Etched optical micrographs of the longitudinal and transverse sections of all sintered samples are shown from Figure 4.49 to Figure 4.51 to attain aluminium grain size measurements. The length, width and ECD of the aluminium grains are shown in Table 4.20. The aluminium ECD after sintering at 500°C 1h was 9.83 ± 5.95µm and 12.77 ± 8.07µm for the longitudinal and transverse section respectively. The ECD of the sample sintered at 500°C for 10 was 13.48 ± 6.47µm and 15.32 ± 6.68µm for the longitudinal and transverse sections respectively and for the sample sintered at 550°C for 1h, the ECD was 15 ± 8.62µm and 16.26 ± 8.38µm in the longitudinal and transverse sections respectively.

The histograms of the length, width and ECD of the aluminium grains in the longitudinal and transverse sections of the sample sintered at 500°C for 1h are shown in Figure 4.52 and Figure 4.53 respectively. The corresponding histograms for the samples sintered at 500°C for 10h and 550°C for 1h are shown in Appendix 6-16 to Appendix 6-19.

SEM images, including EDX, of the samples sintered at 500°C 1h & 10h and at 550°C for 1h are shown from Figure 4.54 to Figure 4.59 for the longitudinal and transverse sections. On the EDX images, the light white phase is tin, the dark grey phase is aluminium and the lighter grey regions are copper for all sintered samples. Tin moved out of the pre-alloyed particles and settled around the aluminium grains and silicon particles formed during heat treatment. These characteristics appeared in all sintered samples.

The silicon maps from the EDX were used to attain the length, width and ECD data for the silicon particles, which is shown in Table 4.21. The ECD of the silicon particles after sintering at 500°C for 1h was 3.51 ± 1.1µm and 3.86 ± 1.14µm in the longitudinal and transverse sections respectively. This increased to 4.5 ± 1.15µm and 4.3 ± 1.41µm in the longitudinal and transverse sections respectively for sintering at 500°C at 10h and further increased to 4.89 ± 1.96µm and 5.52 ± 2.19µm in the longitudinal and transverse sections respectively for sintering at 550°C for 1h.

Histograms for the length, width and ECD of the silicon particles are shown in Figure 4.60 and Figure 4.61 for the samples sintered at 500°C 1h. The corresponding histograms for the samples sintered at 500°C for 10h and 550°C for 1h are shown from Appendix 6-20 to Appendix 6-23.

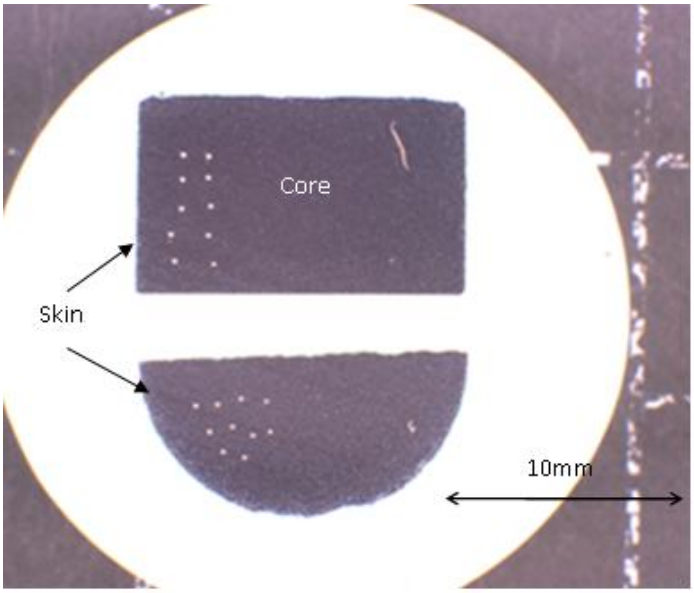

Figure 4.43: The macroscopic image of the longitudinal (top) and transverse (bottom) sample sintered at 500°C 1h in a nitrogen atmosphere. The white dots on the sample are hardness indents.

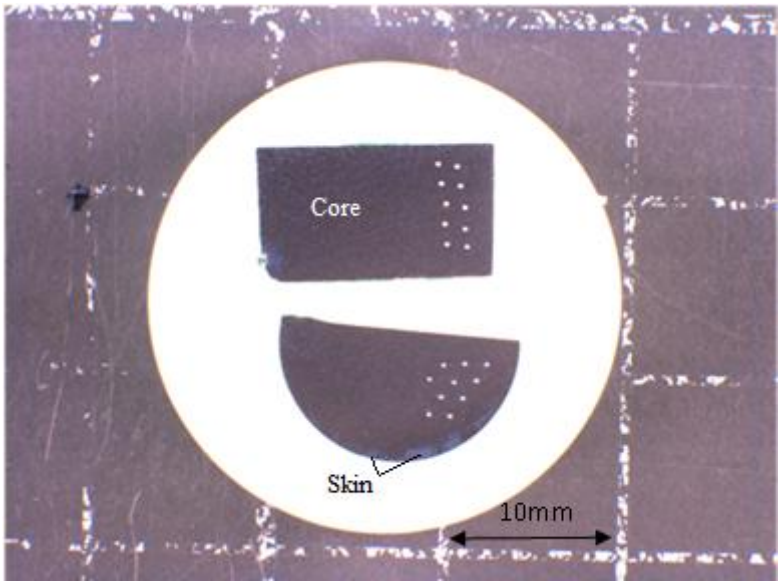

Figure 4.44: The macroscopic image of the longitudinal (top) and transverse (bottom) sample sintered at 500°C 10h in a nitrogen atmosphere. The white dots on the sample are hardness indents.

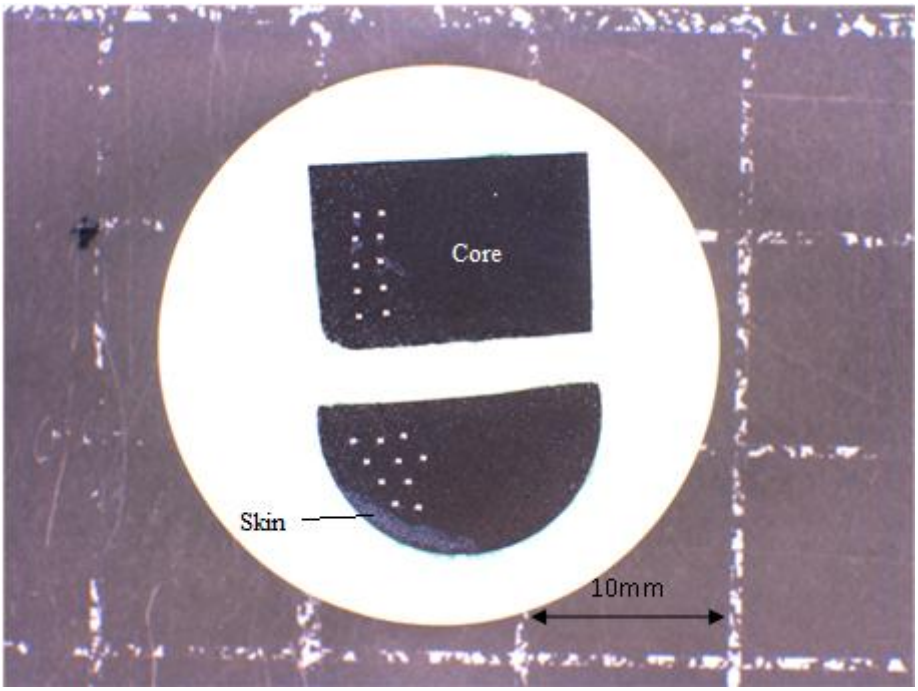

Figure 4.45: The macroscopic image of the longitudinal (top) and transverse (bottom) sample sintered at 550°C 1h in a nitrogen atmosphere. The white dots on the sample are hardness indents.

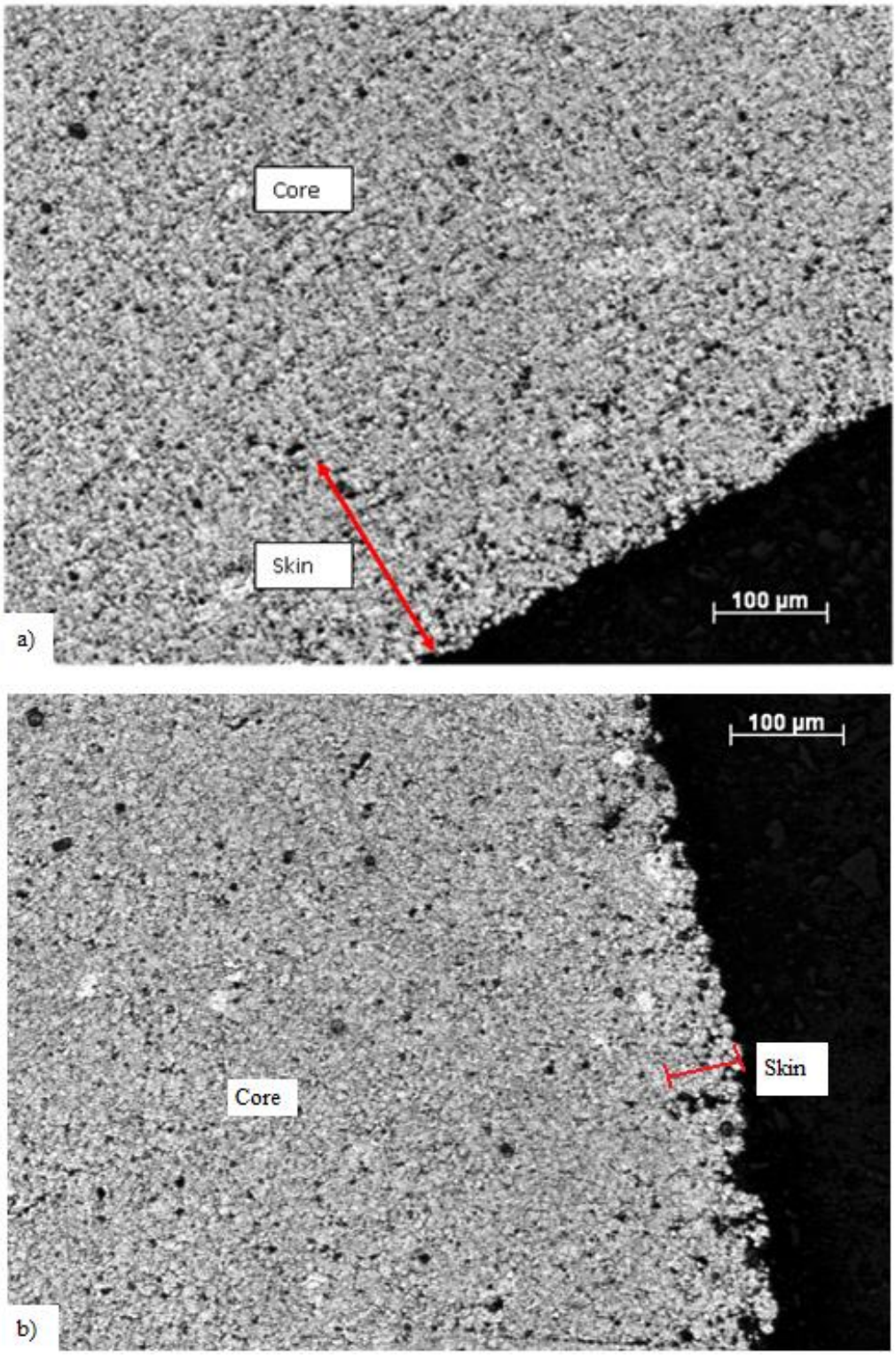

Figure 4.46: Optical micrograph showing the skin and the core of the longitudinal section of a sample sintered at 500°C 1h in an atmosphere of nitrogen.

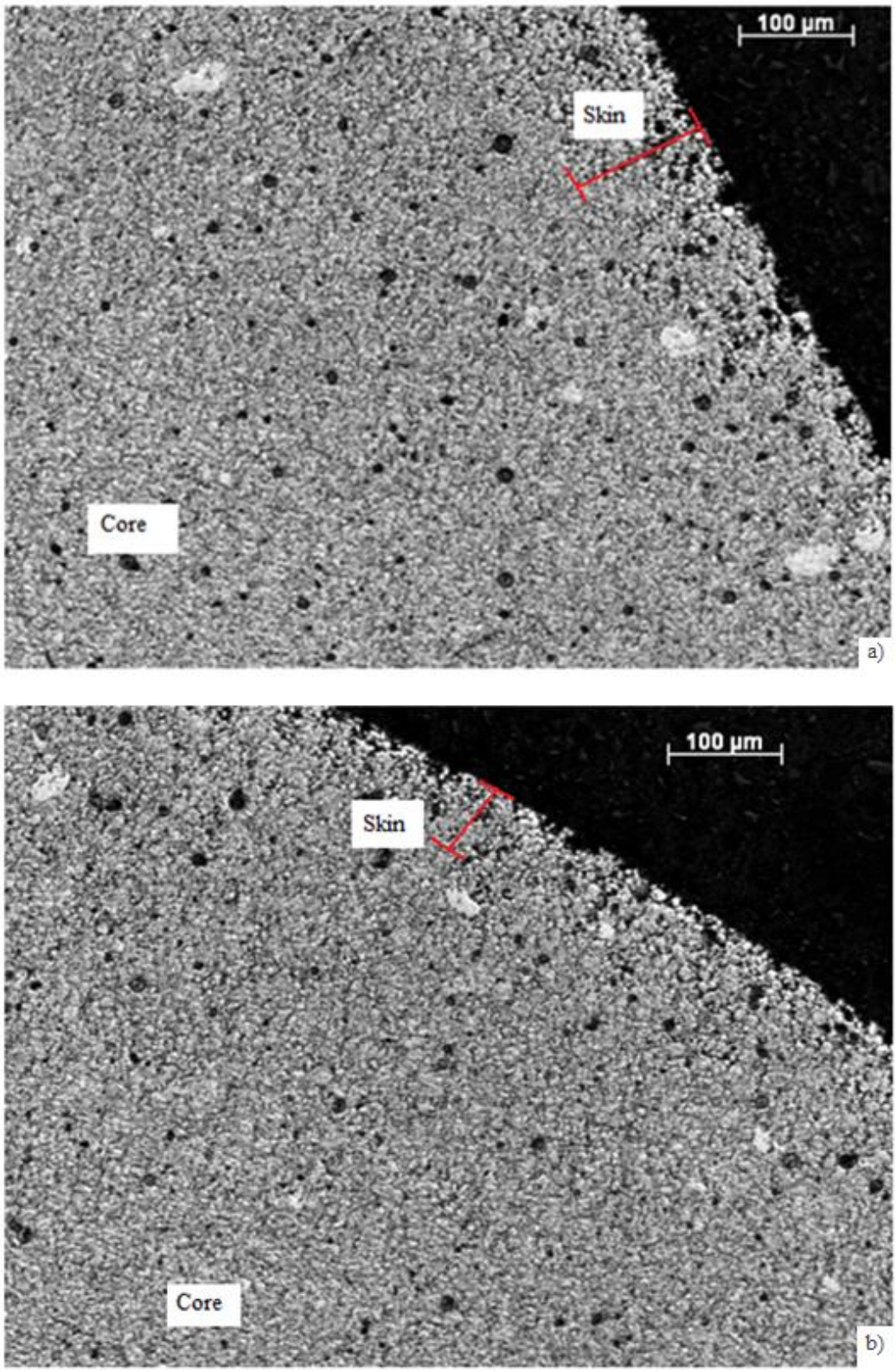

Figure 4.47: Optical micrograph showing the skin and the core of the a) longitudinal and b) transverse section of a sample sintered at 500°C 10h in an atmosphere of nitrogen.

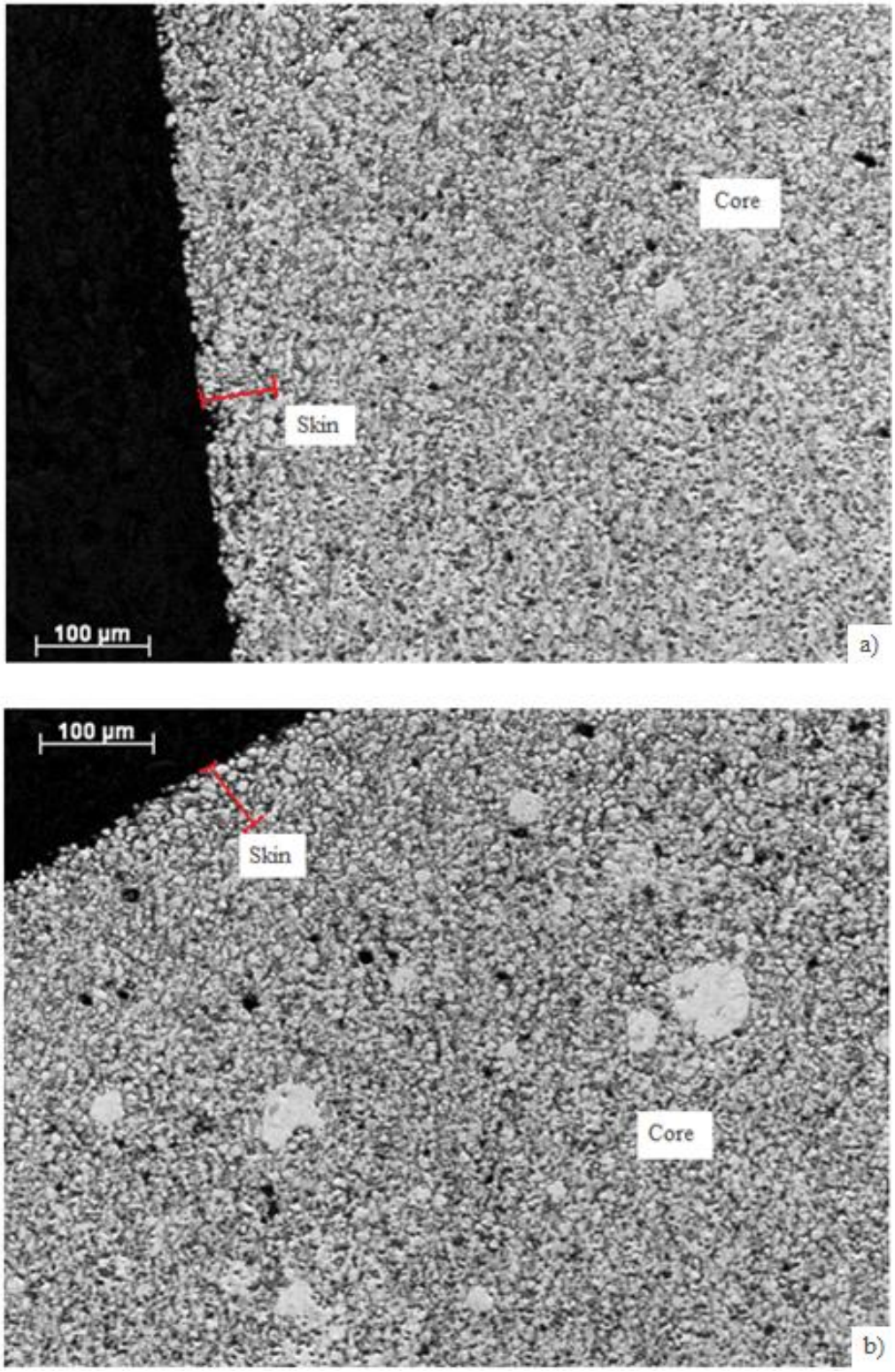

Figure 4.48: Optical micrograph showing the skin and the core of the a) longitudinal and b) transverse section of a sample sintered at 550°C 1h in an atmosphere of nitrogen.

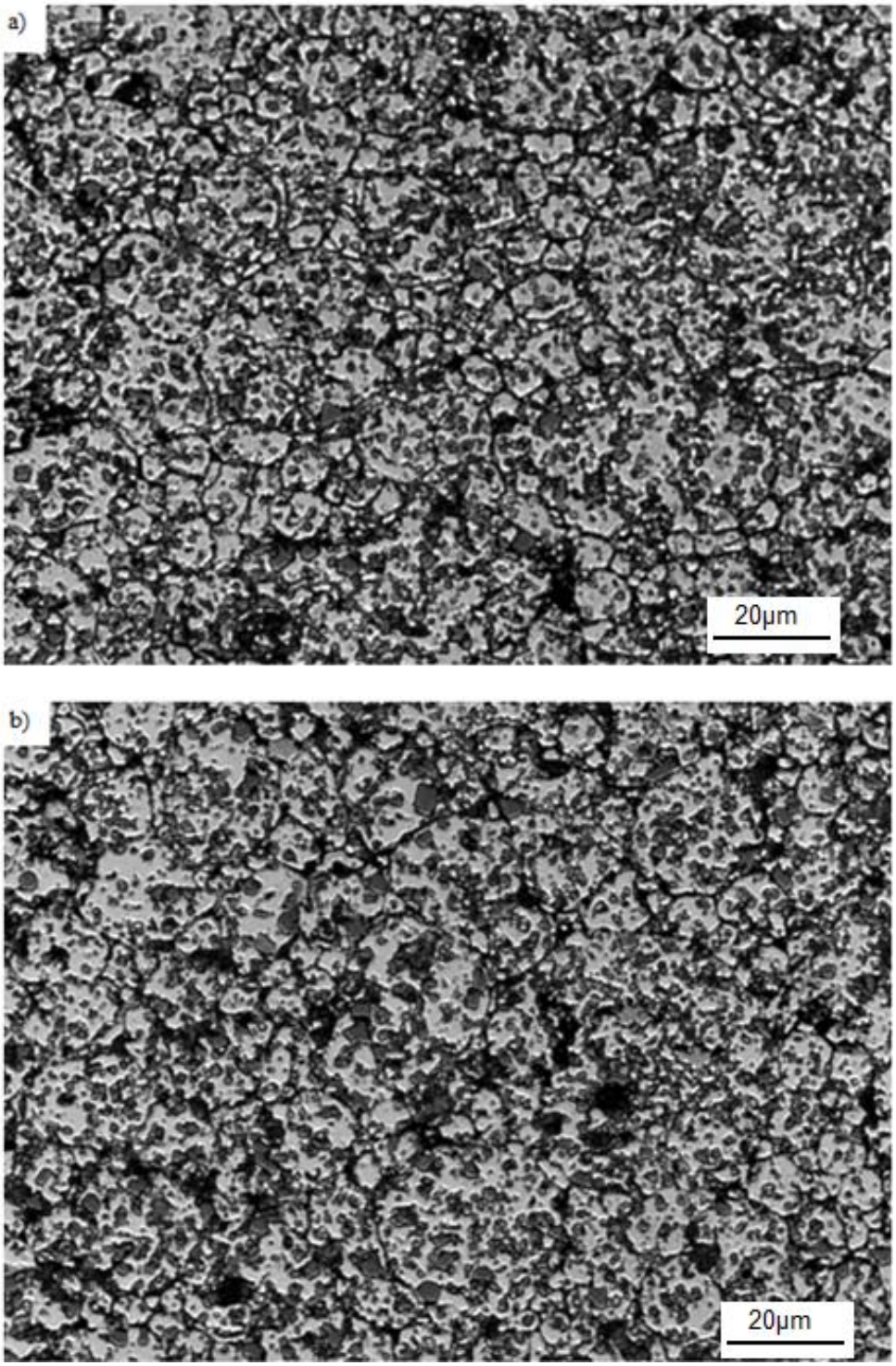

Figure 4.49: Etched optical micrograph of the a) longitudinal and b) transverse sections of the sample sintered at 500°C 1h used to attain aluminium grain size measurements.

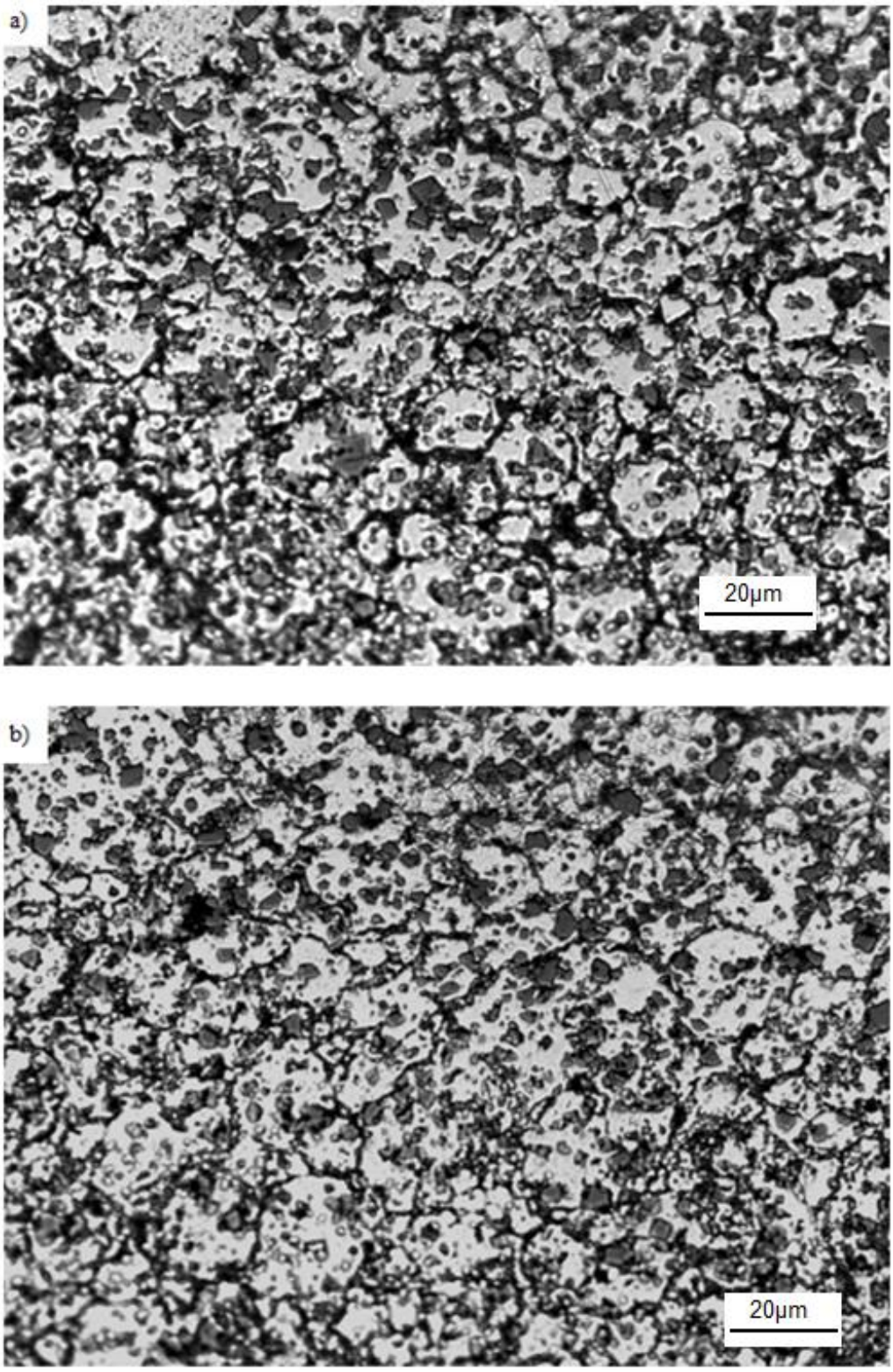

Figure 4.50: Etched optical micrograph of the a) longitudinal and b) transverse sections of the sample sintered at 500°C 10h used to attain aluminium grain size measurements.

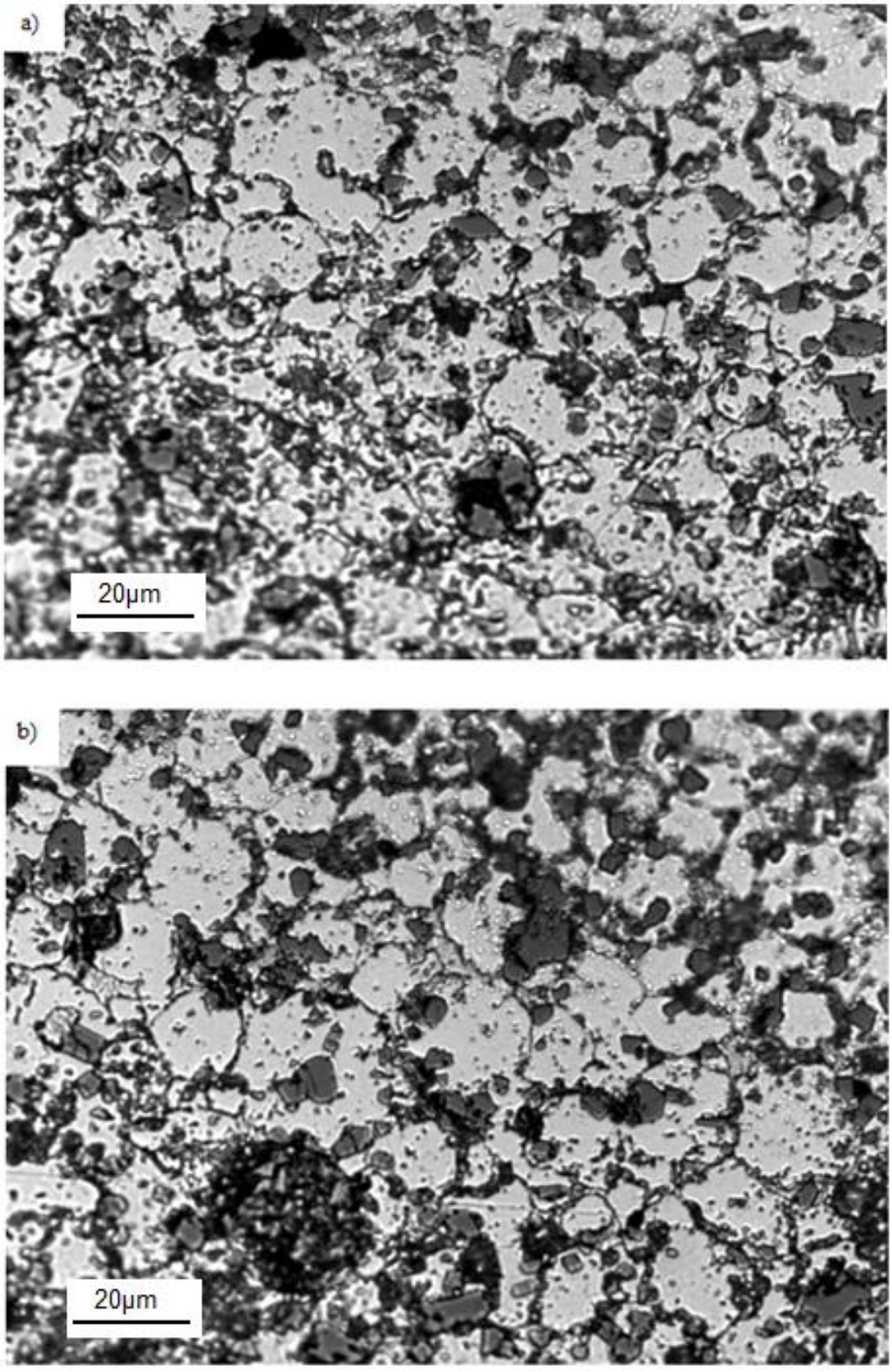

Figure 4.51: Etched optical micrograph of the a) longitudinal and b) transverse sections of the sample sintered at 550°C 10h used to attain aluminium grain size measurements.

Table 4.20: The length, width and ECD of the aluminium grain sizes for the sintered samples.

Sample	Length µm		Width µm		Aspect ratio		ECD µm	
	Longitudinal	Transverse	Longitudinal	Transverse	Longitudinal	Transverse	Longitudinal	Transverse
Sintered 500°C 1h	11.91 ± 7.42	15.64 ± 10.76	8.6 ± 5.44	11.38 ± 7.61	0.72	0.73	9.83 ± 5.95	12.77 ± 8.07
Sintered 500°C 10h	16.36 ± 8.06	18.87 ± 8.63	12.38 ± 5.97	14.03 ± 6.44	0.76	0.74	13.48 ± 6.47	15.32 ± 6.68
Sintered 550°C 1h	19.07 ± 11.43	20.69 ± 11.13	13.17 ± 8.03	14.46 ± 7.91	0.69	0.70	15 ± 8.62	16.26 ± 8.38

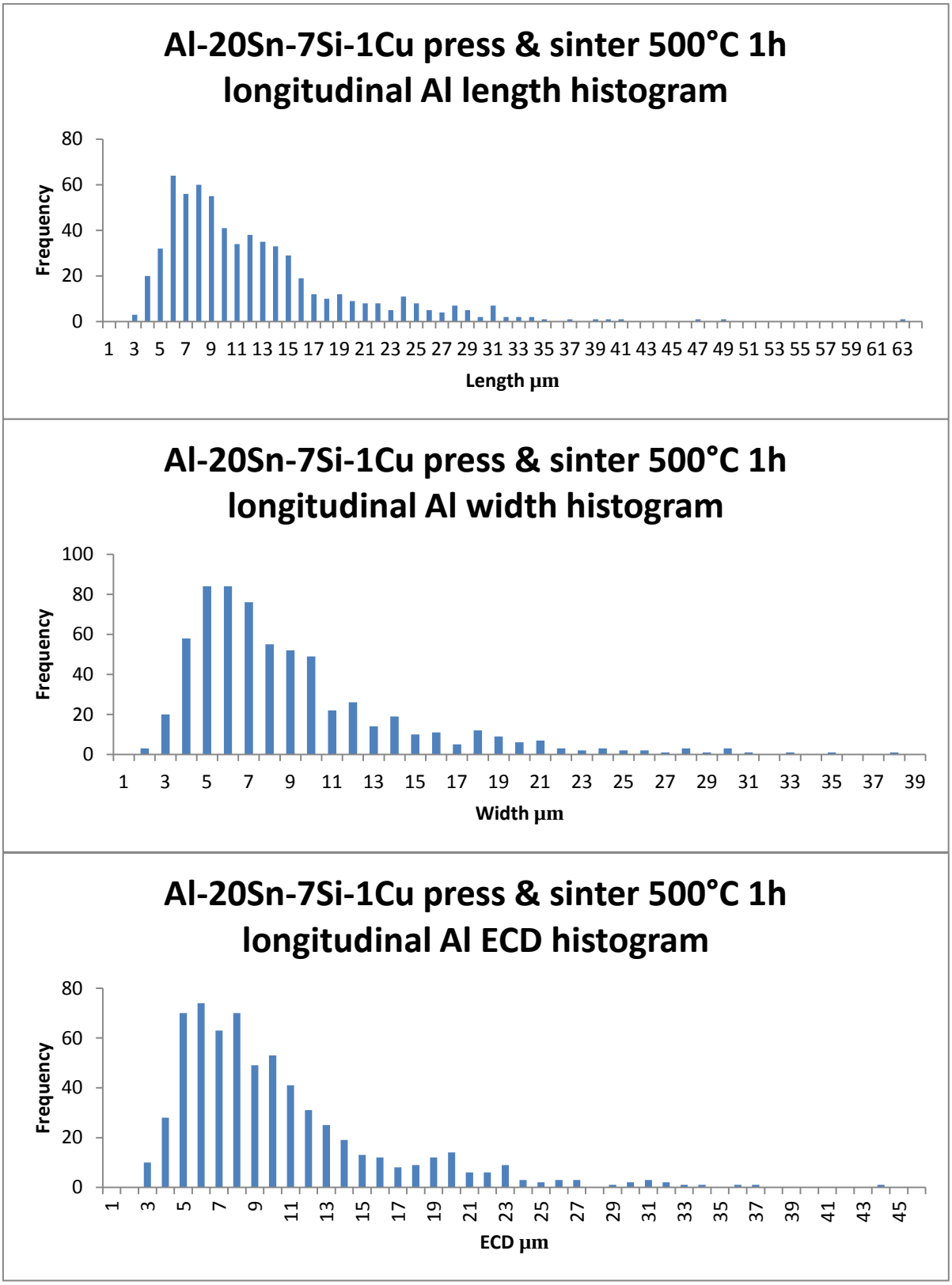

Figure 4.52: Histograms for the length, width and ECD of the aluminium grains in the longitudinal section of samples sintered at 500C for 1h.

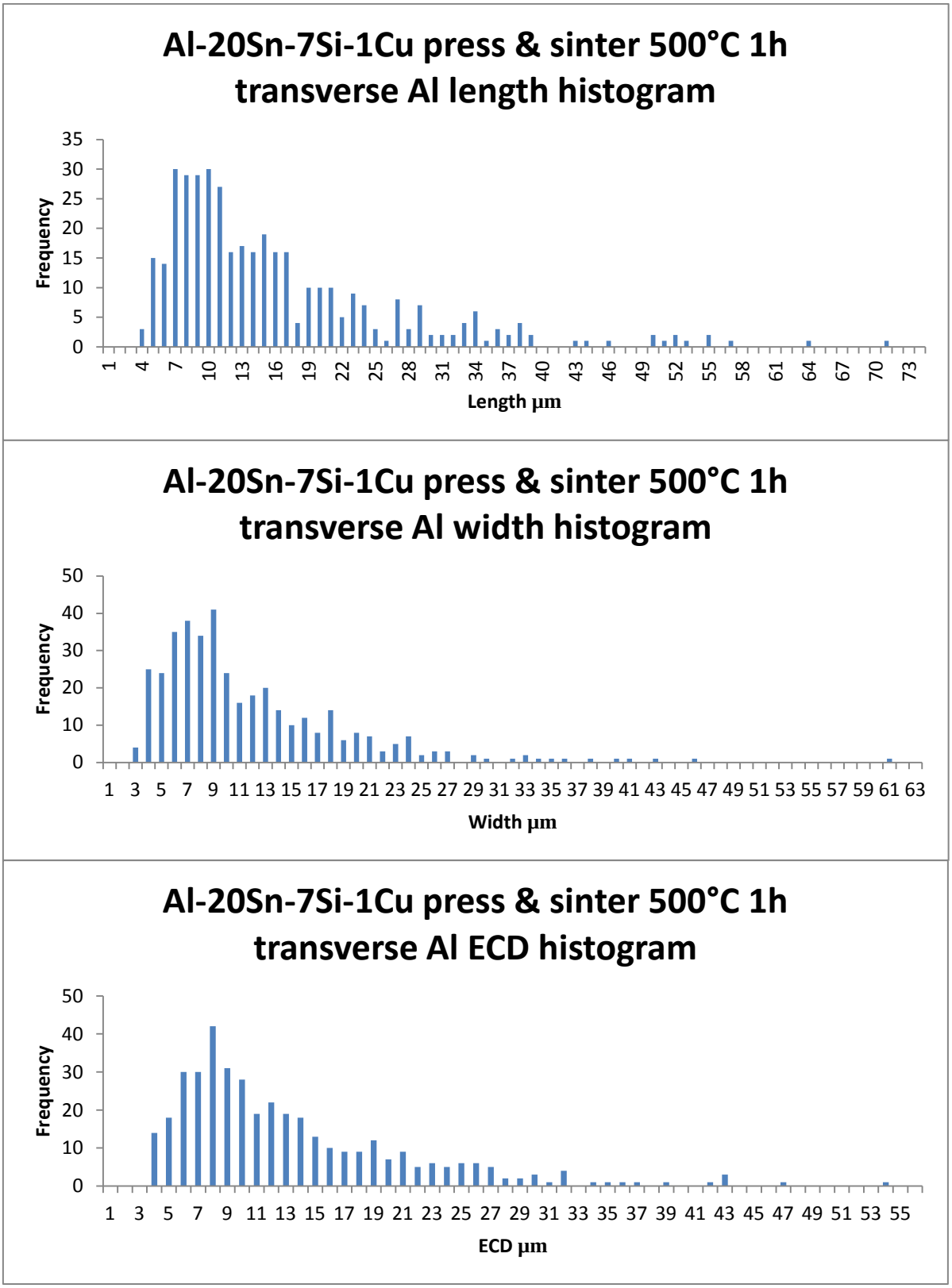

Figure 4.53: Histograms for the length, width and ECD of the aluminium grains transverse section of samples sintered at 500C for 1h.

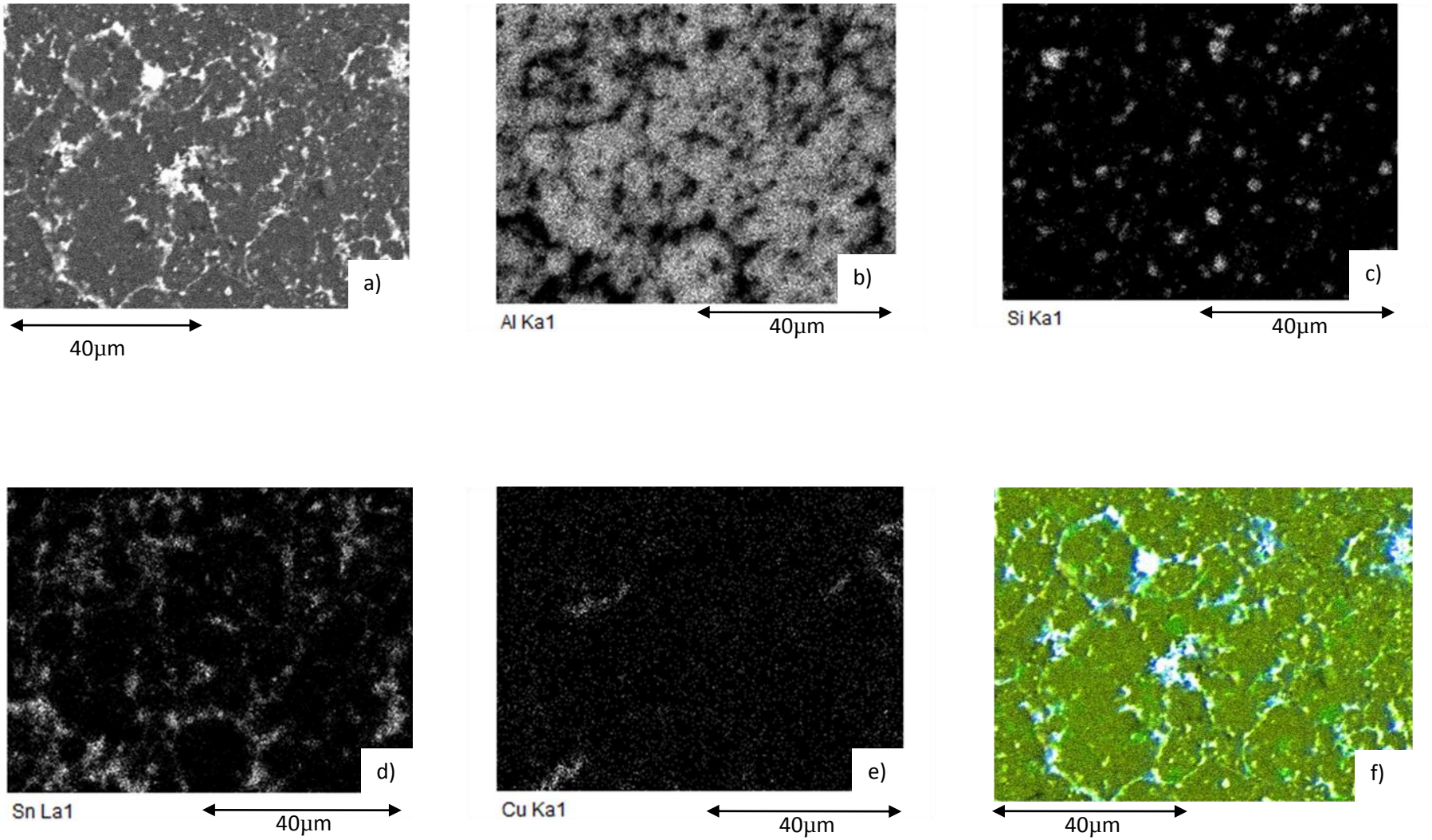

Figure 4.54: EDX of the longitudinal section of samples sintered at 500C 1h; a) SEM; b) Al map; c) Si map; d) Sn map; e) Cu map; f) Coloured map where dark green represents Al, lighter green represents Si, blue/white represents Sn and light brown represents Cu.

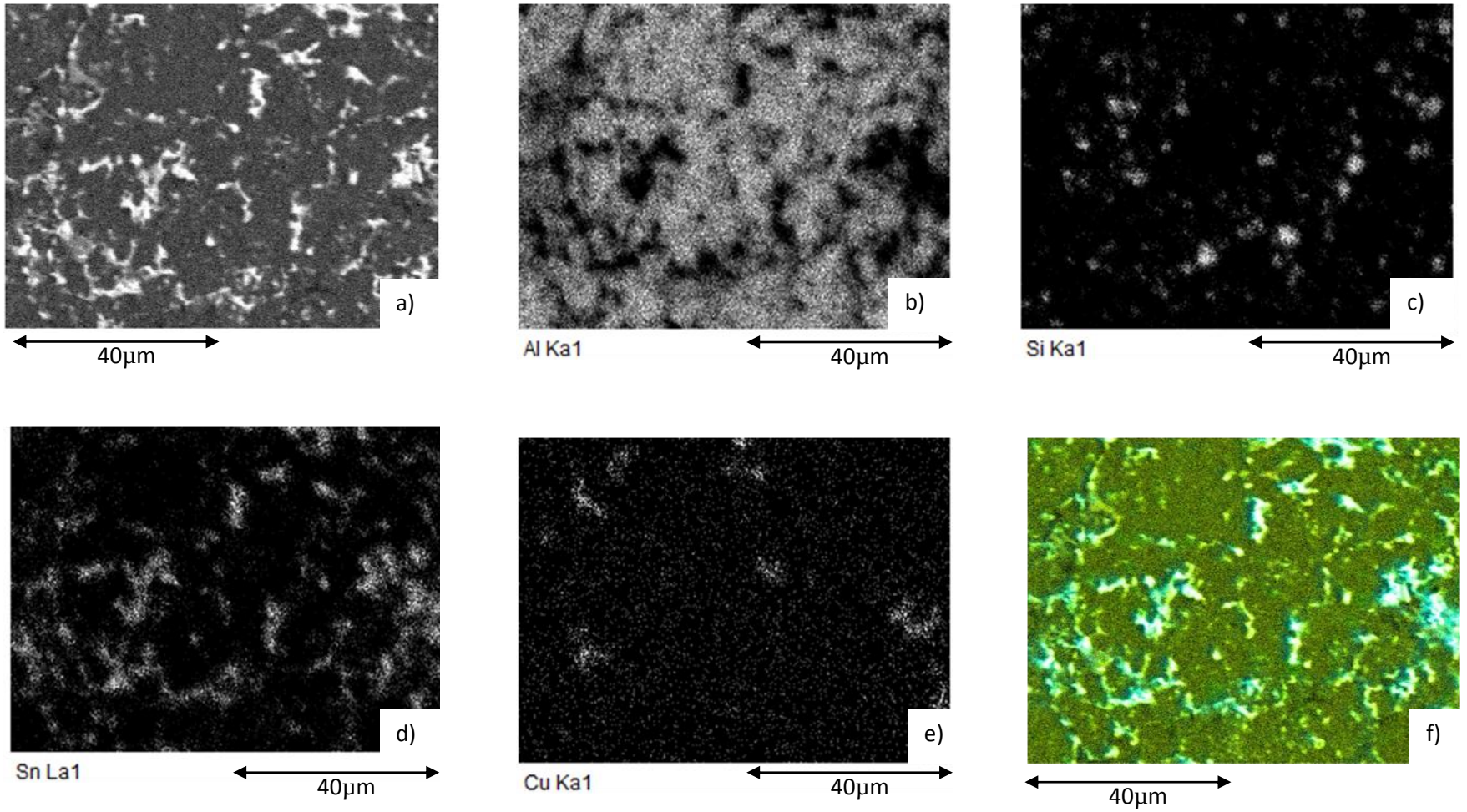

Figure 4.55: EDX of the transverse section of samples sintered at 500C 1h; a) SEM; b) Al map; c) Si map; d) Sn map; e) Cu map; f) Coloured map where dark green represents Al, lighter green represents Si, blue/white represents Sn and light brown represents Cu.

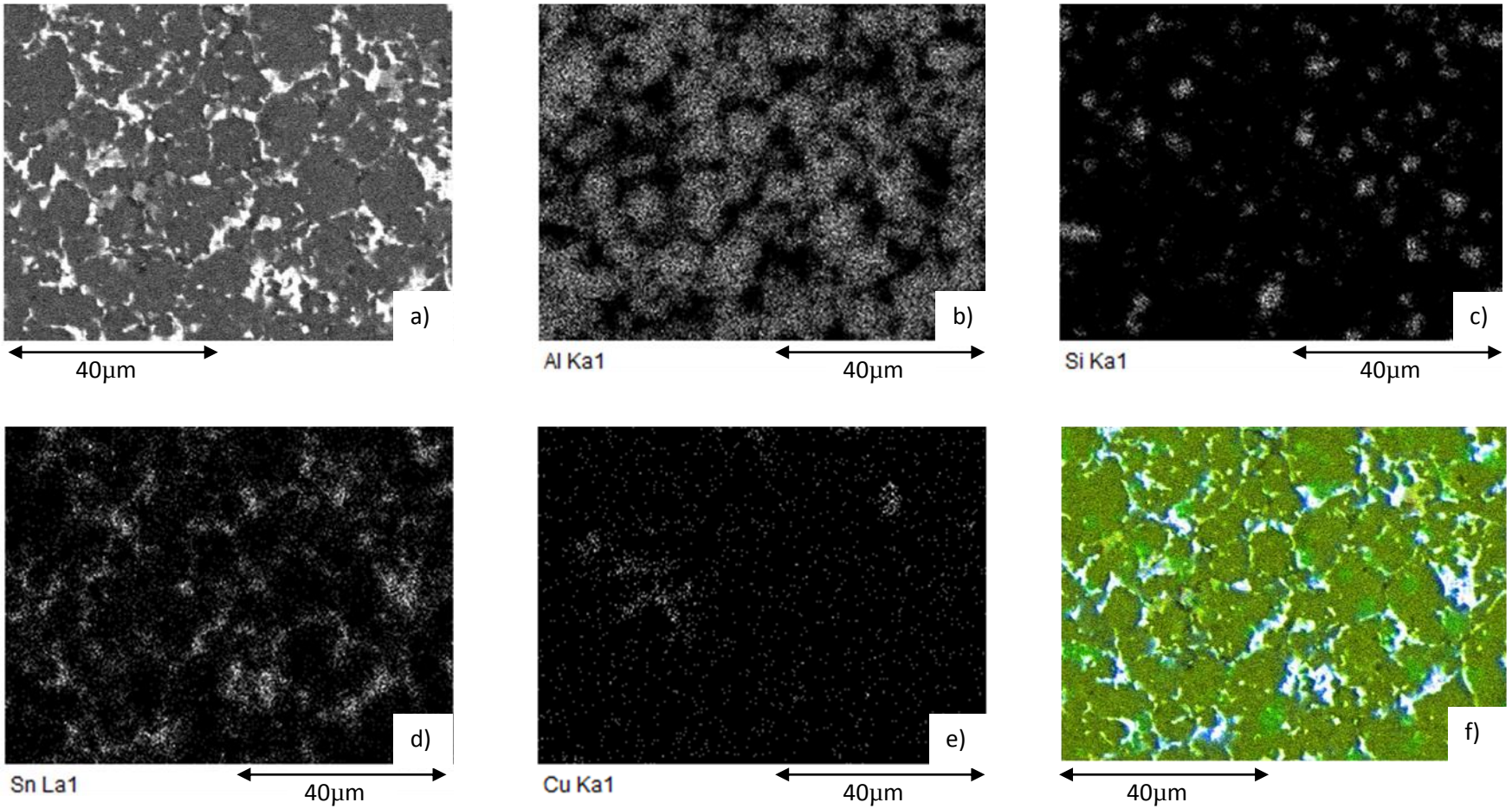

Figure 4.56: EDX of the longitudinal section of samples sintered at 500C 10h; a) SEM; b) Al map; c) Si map; d) Sn map; e) Cu map; f) Coloured map where dark green represents Al, lighter green represents Si, blue/white represents Sn and light brown represents Cu.

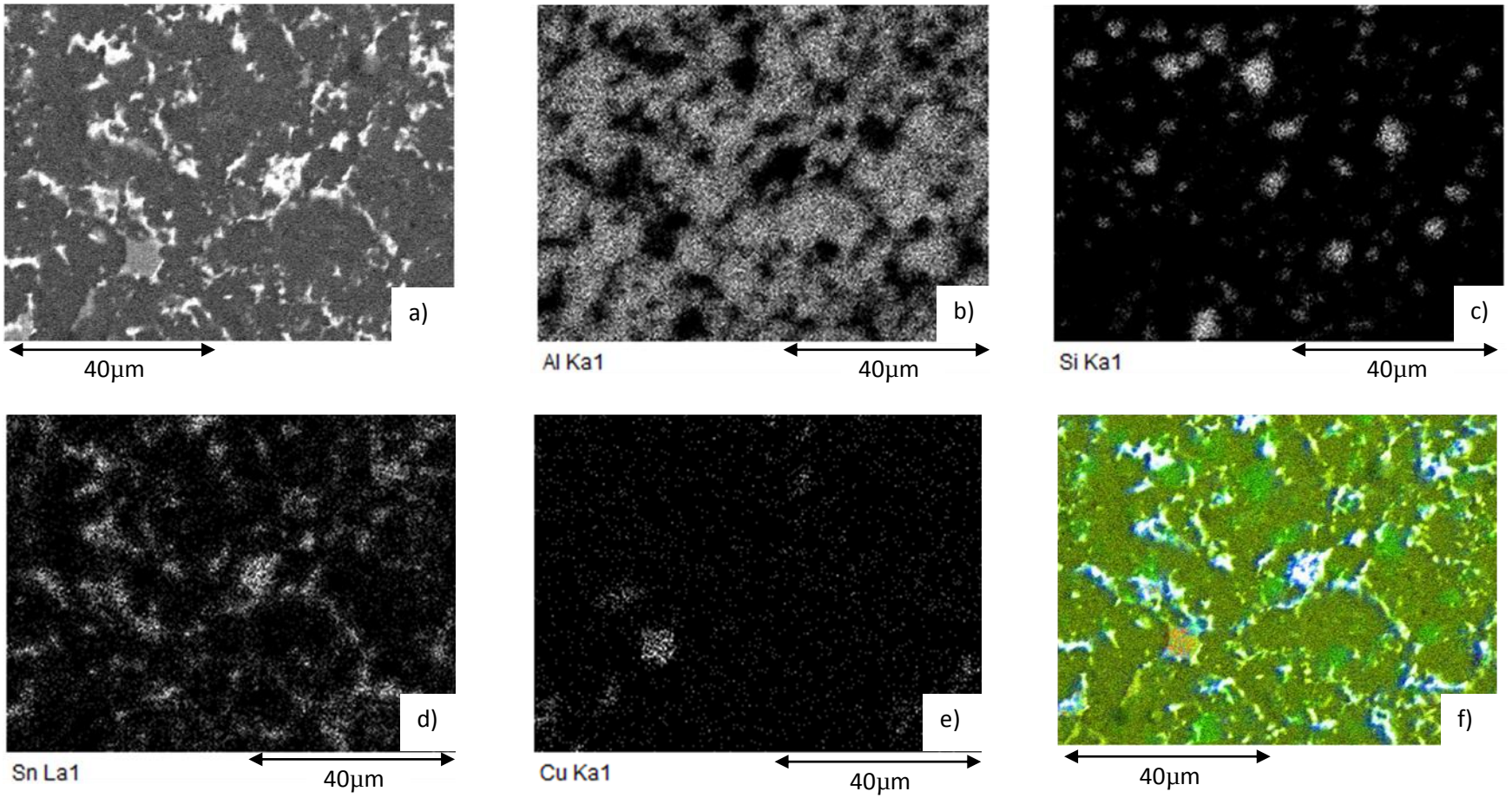

Figure 4.57: EDX of the transverse section of samples sintered at 500C 10h; a) SEM; b) Al map; c) Si map; d) Sn map; e) Cu map; f) Coloured map where dark green represents Al, lighter green represents Si, blue/white represents Sn and light brown represents Cu.

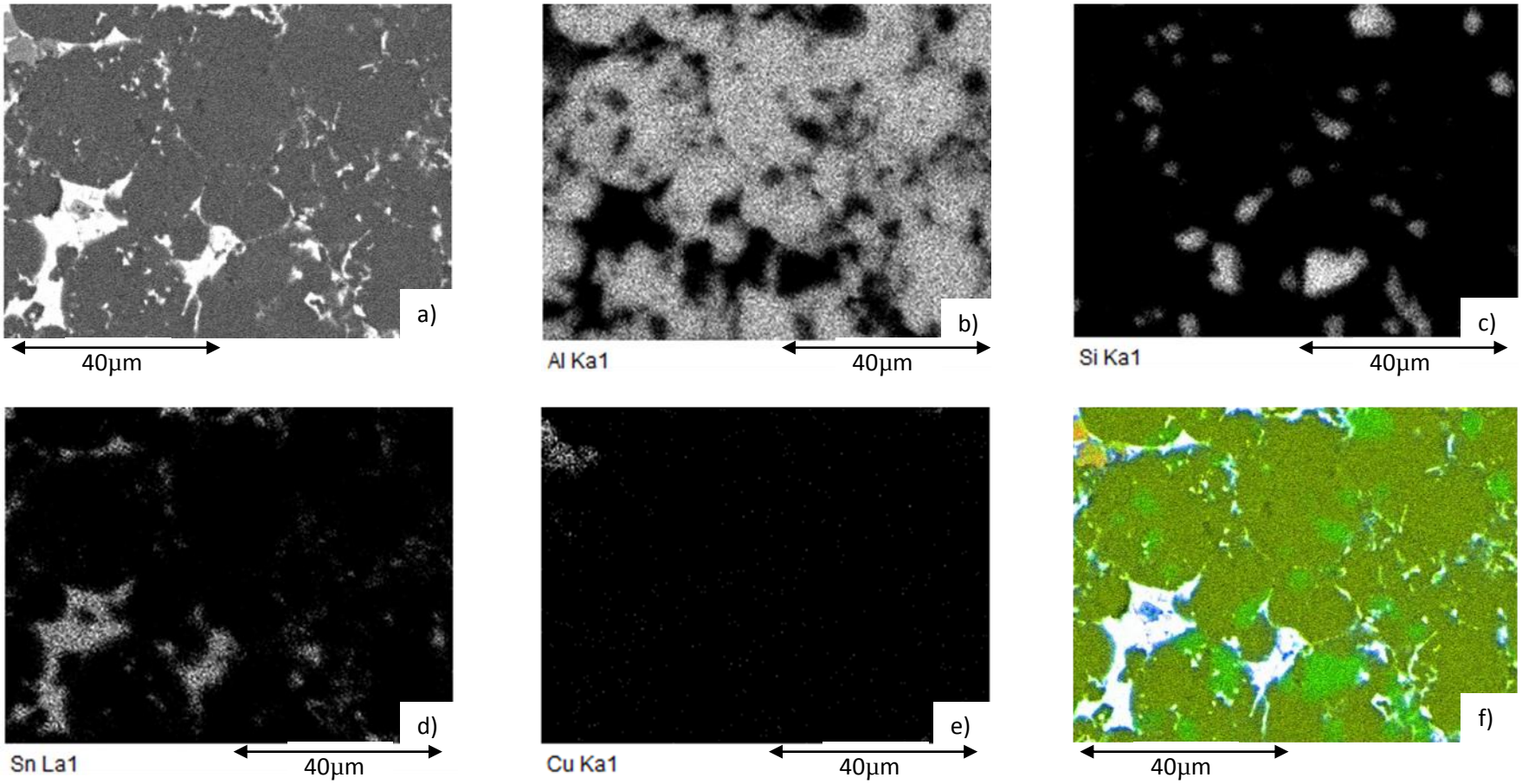

Figure 4.58: EDX of the longitudinal section of samples sintered at 550C 1h; a) SEM; b) Al map; c) Si map; d) Sn map; e) Cu map; f) Coloured map where dark green represents Al, lighter green represents Si, blue/white represents Sn and light brown represents Cu.

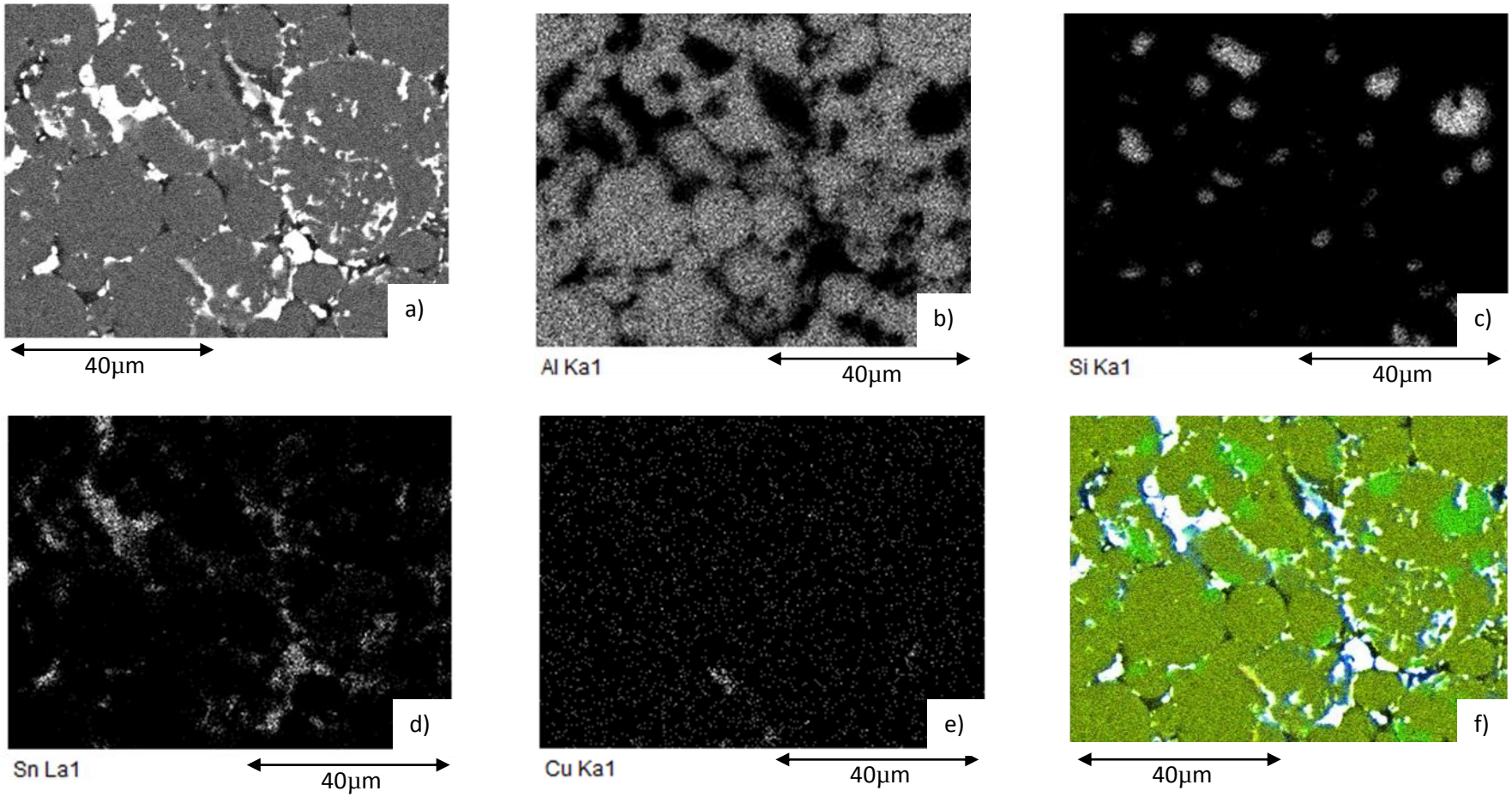

Figure 4.59: EDX of the transverse section of samples sintered at 550C 1h; a) SEM; b) Al map; c) Si map; d) Sn map; e) Cu map; f) Coloured map where dark green represents Al, lighter green represents Si, blue/white represents Sn and light brown represents Cu.

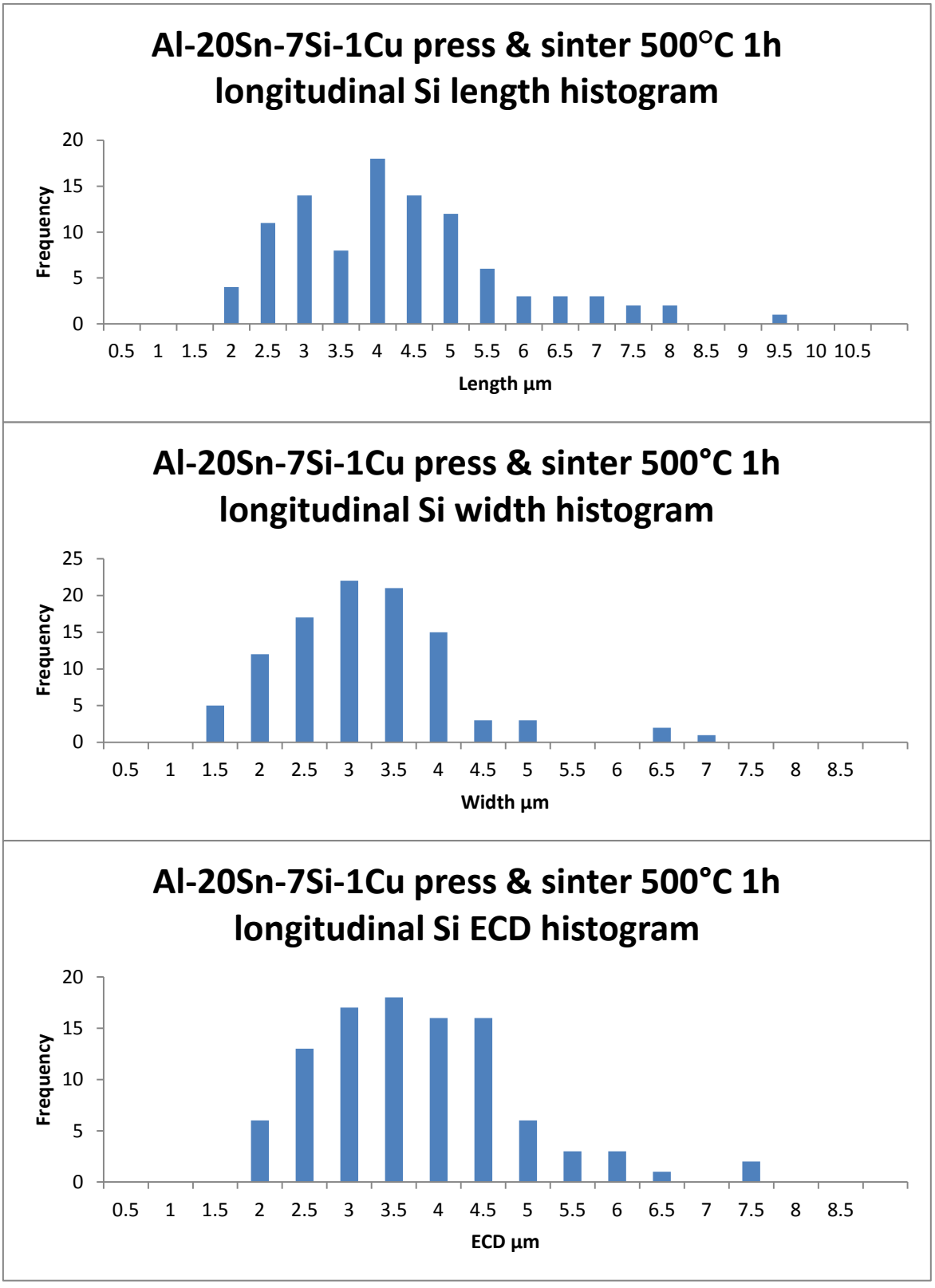

Figure 4.60 Histograms for length, width and ECD of the silicon particles in the longitudinal section of samples sintered at 500C for 1h.

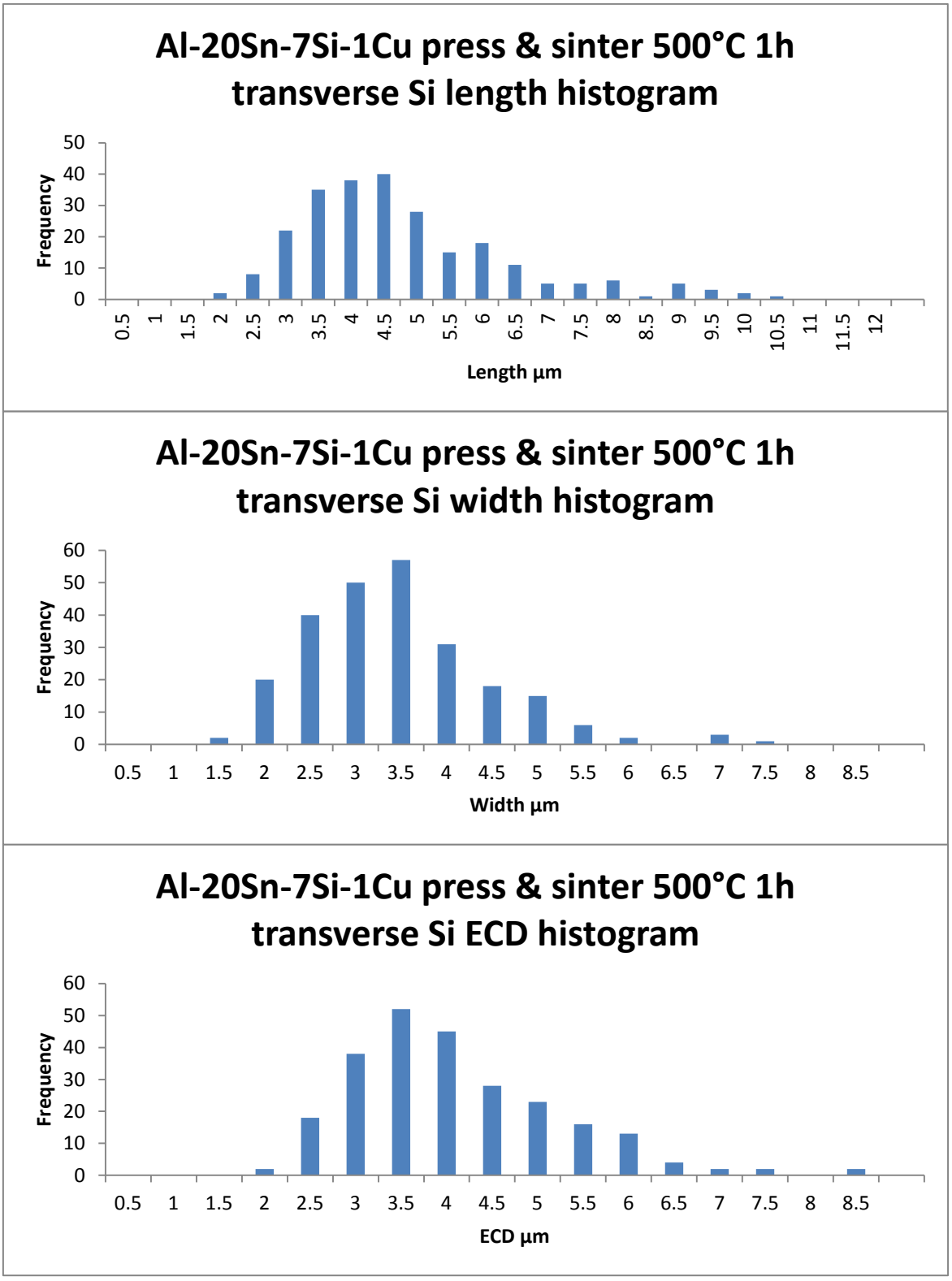

Figure 4.61: Histograms for length, width and ECD of the silicon particles in the transverse section of samples sintered at 500C for 1h.

Table 4.21: The silicon particle sizes for the sintered samples.

Sample	Length µm		Width µm		Aspect ratio		ECD µm	
	Longitudinal	Transverse	Longitudinal	Transverse	Longitudinal	Transverse	Longitudinal	Transverse
Sintered 500°C 1h	4.06 ± 1.47	4.55 ± 1.64	2.93 ± 0.99	3.21 ± 1.01	0.72	0.71	3.51 ± 1.1	3.86 ± 1.14
Sintered 500°C 10h	4.44 ± 1.57	5.05 ± 1.89	3.34 ± 1.06	3.64 ± 1.26	0.75	0.72	4.5 ± 1.15	4.3 ± 1.41
Sintered 550°C 1h	6.08 ± 2.94	6.59 ± 2.86	3.99 ± 1.68	4.65 ± 1.97	0.66	0.71	4.89 ± 1.96	5.52 ± 2.19

4.3.3.3. Sintered hardness

The hardness values for the sintered samples are shown in Table 4.22. The hardness of the sintered samples decreased from the cold compacted hardness of approximately 61$HV_{2.5kg}$ to 33.68 ± 1.2$HV_{2.5kg}$ and 34.8 ± 0.99$HV_{2.5kg}$ in the longitudinal and transverse sections respectively of the sample sintered at 500°C for 1h. The hardness reduced slightly to 32.43 ± 0.69$HV_{2.5kg}$ and 32.6 ± 0.71$HV_{2.5kg}$ in the longitudinal and transverse sections respectively for the sample sintered at 500°C for 10h. The hardness reduced further to 24.6 ± 1$HV_{2.5kg}$ and 26.3 ± 0.6$HV_{2.5kg}$ in the longitudinal and transverse sections respectively for the sample sintered at 550°C for 1h.

Table 4.22: Vickers hardness values of the sintered samples.

Sample	**Hardness $HV_{2.5kg}$**	
	Longitudinal	Transverse
500°C 1h	33.68 ± 1.2	34.8 ± 0.99
500°C 10h	32.43 ± 0.69	32.6 ± 0.71
550°C 1h	24.6 ± 1	26.3 ± 0.6

4.3.4. ECAP response

4.3.4.1. Density of ECAP samples

The densities of the samples after one pass of ECAP are shown in Table 4.23. The density increased from the cold compacted density of 2.67 ± 0.04g/cm^3 to 2.96 ± 0.01g/cm^3, 3.03 ± 0.02g/cm^3 and 3.04 ± 0.01g/cm^3 for the samples pre-sintered at 500°C for 1 & 10 hours and 550°C for 1h respectively.

Table 4.23: The density measurements of the sintered samples after one pass of ECAP

Sample	Density g/cm^3	Density %
500°C 1h → RT ECAP	2.96 ± 0.01	96.16 ± 0.37
500°C 10h → RT ECAP	3.03 ± 0.02	98.4 ± 0.84
550°C 1h → RT ECAP	3.04 ± 0.01	98.57 ± 0.24

4.3.4.2. Microstructure of ECAP samples

Macroscopic images of the ECAP samples are shown in Figure 4.62 to Figure 4.64. Two distinct regions developed after one pass, which can be seen as a reflective region, termed the "skin" and a lighter grey, matte region which appeared towards the centre of the sample, termed "core". Both of these regions appeared in the transverse and longitudinal sections.

Etched optical micrographs of the ECAP sample pre-sintered at 500°C 1h & 10h and 550°C for 1h in the longitudinal and transverse sections are shown in Figure 4.65 to Figure 4.70 for measurement of aluminium grain sizes. For the longitudinal section, the aluminium grains appear elongated in the core region compared to the relatively equiaxed grains of the skin region. For the transverse section, the aluminium grains are relatively equiaxed in both the skin and the core region. Another observation from the core region was the existence of 'whiskers' of material extruding from the surface. EDX revealed these features to be tin as shown from Figure 4.71 to Figure 4.82. These tin whiskers were seen in all of the ECAP samples after one pass in the core region. The silicon maps from EDX were used to measure the silicon sizes.

The length, width and ECD of the aluminium particles after one pass of ECAP are shown in Table 4.24 and there is a large scatter of data around the mean. For comparative purposes, the transverse section gives a better representation of grain size changes. After ECAP, the samples pre-sintered at 500°C 1h had an ECD of 8.94 ± 4.05μm in the skin region and 7.77 ± 4.24μm in the core region. For the samples pre-sintered at 500°C for 10h, the ECD was 6.92 ± 4.21μm in the skin region and 6.59 ± 3.86μm in the core region. For the samples pre-sintered at 550°C for 1h, the ECD was 11.08 ± 5.26μm and 11.22 ± 5.11μm for the skin and core region respectively. Histograms for the length, width and ECD of aluminium grain sizes in the longitudinal skin and core regions of the 500°C 1h ECAP sample are shown in Figure 4.83 and Figure 4.84 respectively and for the transverse section in Figure 4.85 and Figure 4.86 respectively. The corresponding aluminium grain size histograms for the samples pre-sintered at 10h and 550°C 1h are shown in Appendix 6-24 to Appendix 6-31 respectively.

The length, width and ECD of the silicon particles after one pass of ECAP are shown in Table 4.25. After ECAP, in the skin region of the sample pre-sintered at 500°C for 1h, the silicon ECD was 3.19 ± 1.06µm and 2.99 ± 1.09µm in the longitudinal and transverse sections respectively. In the core region, these were 2.83 ± 1.12µm and 2.9 ± 1.09µm in the longitudinal and transverse section respectively. In the skin region of the sample pre-sintered at 500°C for 10h, the silicon ECD was 2.95 ± 1.21µm and 2.86 ± 1.28µm in the longitudinal and transverse section respectively. In the core region of this sample, the ECD was 2.81 ± 1.24µm and 3.04 ± 1.34µm in the longitudinal and transverse section respectively. In the skin region of the samples pre-sintered at 550°C for 1h, the silicon ECD was 3.69 ± 1.44µm and 4.04 ± 1.86µm in the longitudinal and transverse sections respectively. In the core region of the samples pre-sintered at 550°C for 1h, the silicon ECD was 3.77 ± 1.72µm and 4.45 ± 2.24µm in the longitudinal and transverse sections respectively. It is also observed that the silicon particles remained relatively equiaxed and embedded in the aluminium matrix after one pass of ECAP, whereas the tin is more elongated between the aluminium grains.

Histograms for the length, width and ECD of silicon sizes in the longitudinal and transverse skin and core regions of the 500°C 1h ECAP sample are shown in Figure 4.87 to Figure 4.90 respectively. The corresponding histograms for the samples pre-sintered at 500°C for 10h and 550°C for 1h are shown in Appendix 6-32 and Appendix 6-39.

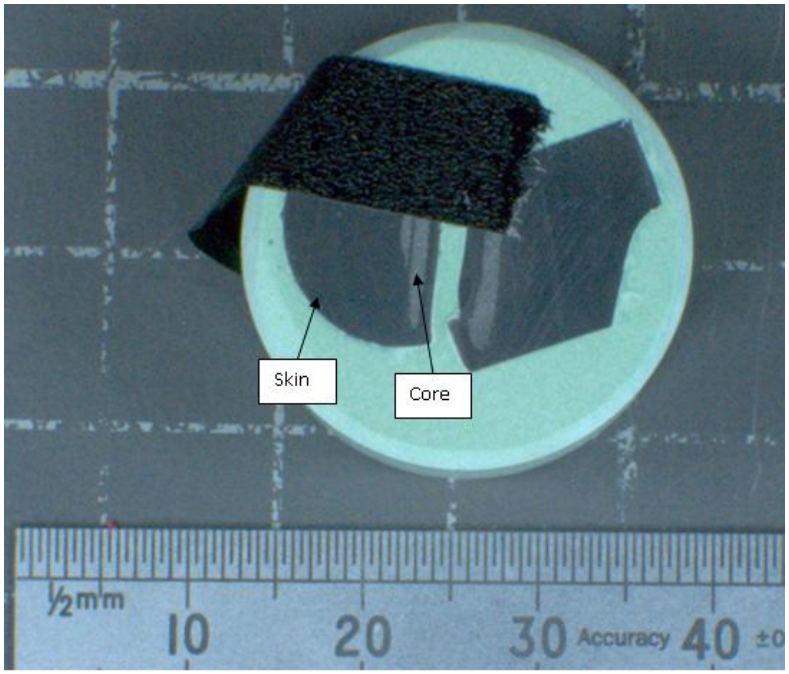

Figure 4.62: Macroscopic image of the 500C 1h sample processed by one pass of ECAP showing the brighter, skin region and matte core region. The transverse section is on the left and the longitudinal on the right.

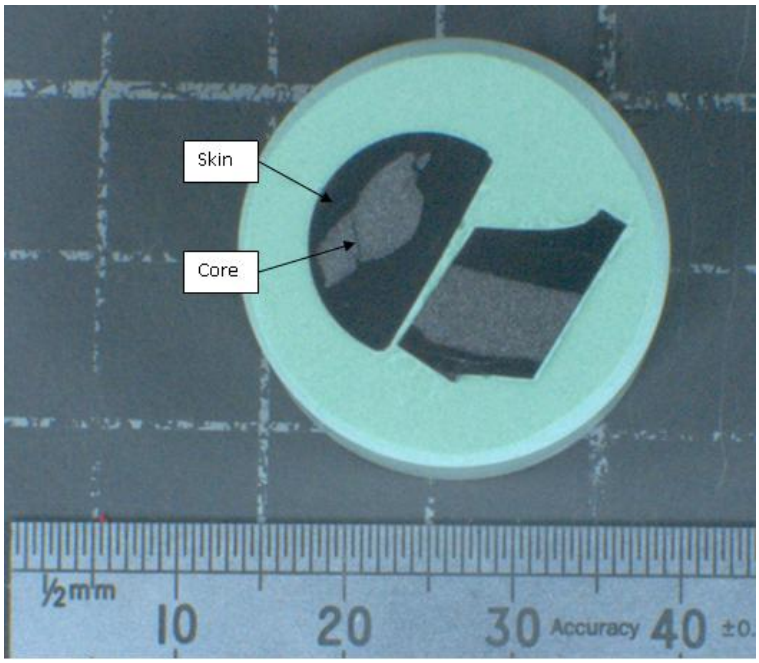

Figure 4.63: Macroscopic image of the 500C 10h sample after one pass of ECAP. The transverse section is on the left, the longitudinal on the right.

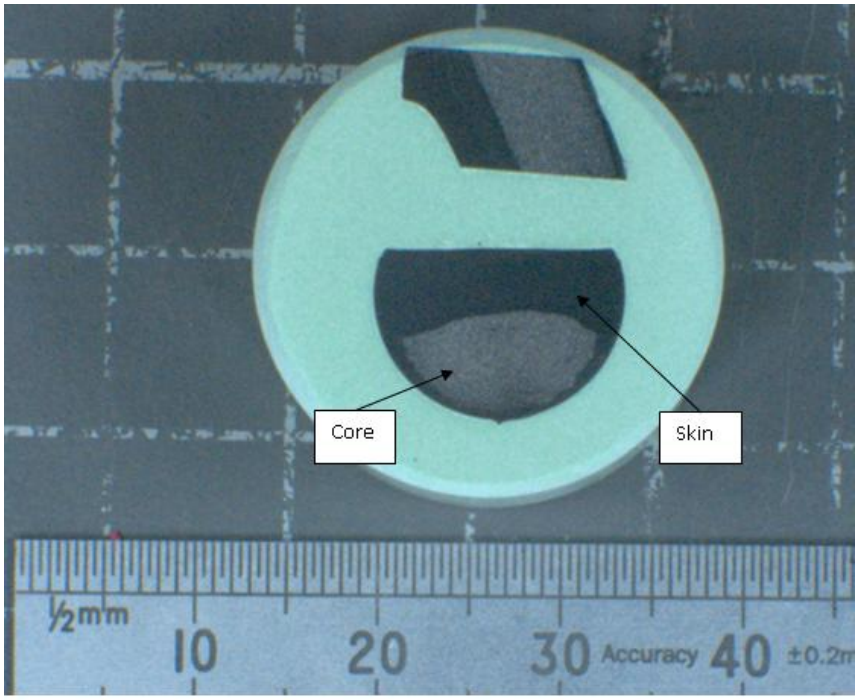

Figure 4.64: Macroscopic image of the 550 C 1h sample after one pass of ECAP. The transverse section is at the bottom and the longitudinal at the top.

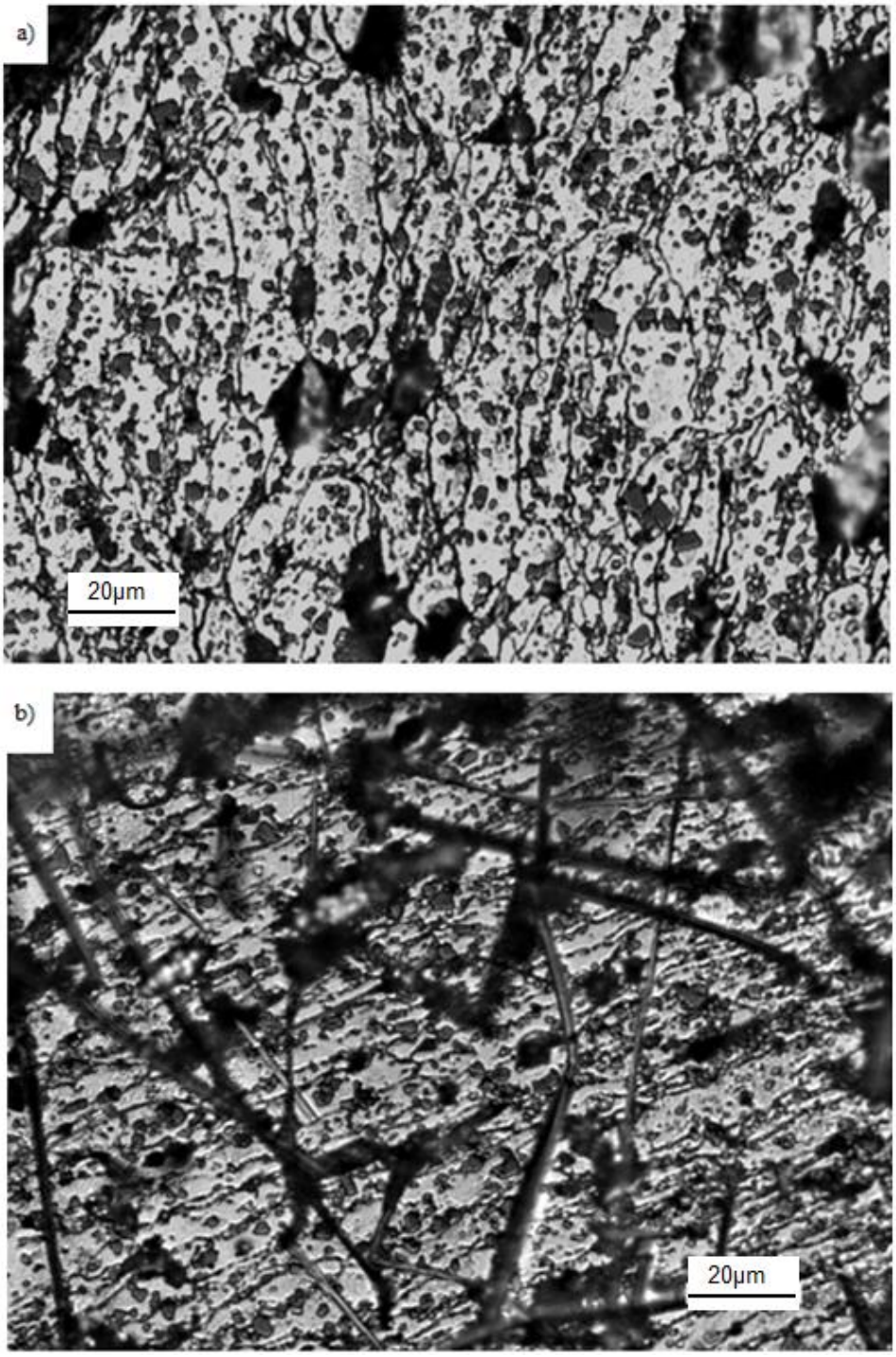

Figure 4.65: Etched optical micrograph of the longitudinal section of the 500C 1h sample after one pass of ECAP where; a) is the "skin" region from Figure 4.62 and; b) is the "core" region from Figure 4.62.

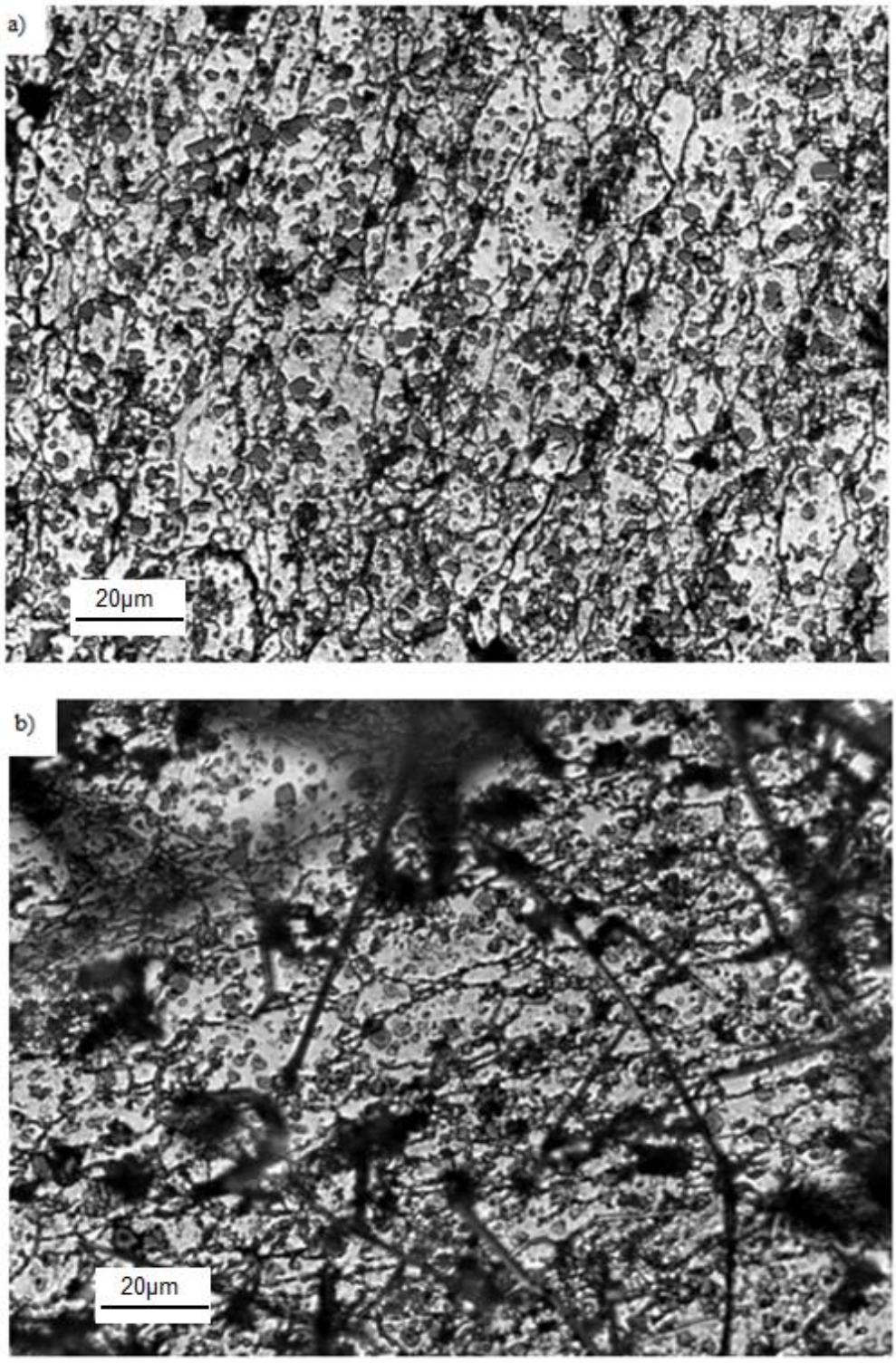

Figure 4.66: Etched optical micrograph of the transverse section of the 500C 1h sample after one pass of ECAP, where; a) is the "skin" region from Figure 4.62 and; b) is the "core" region from Figure 4.62.

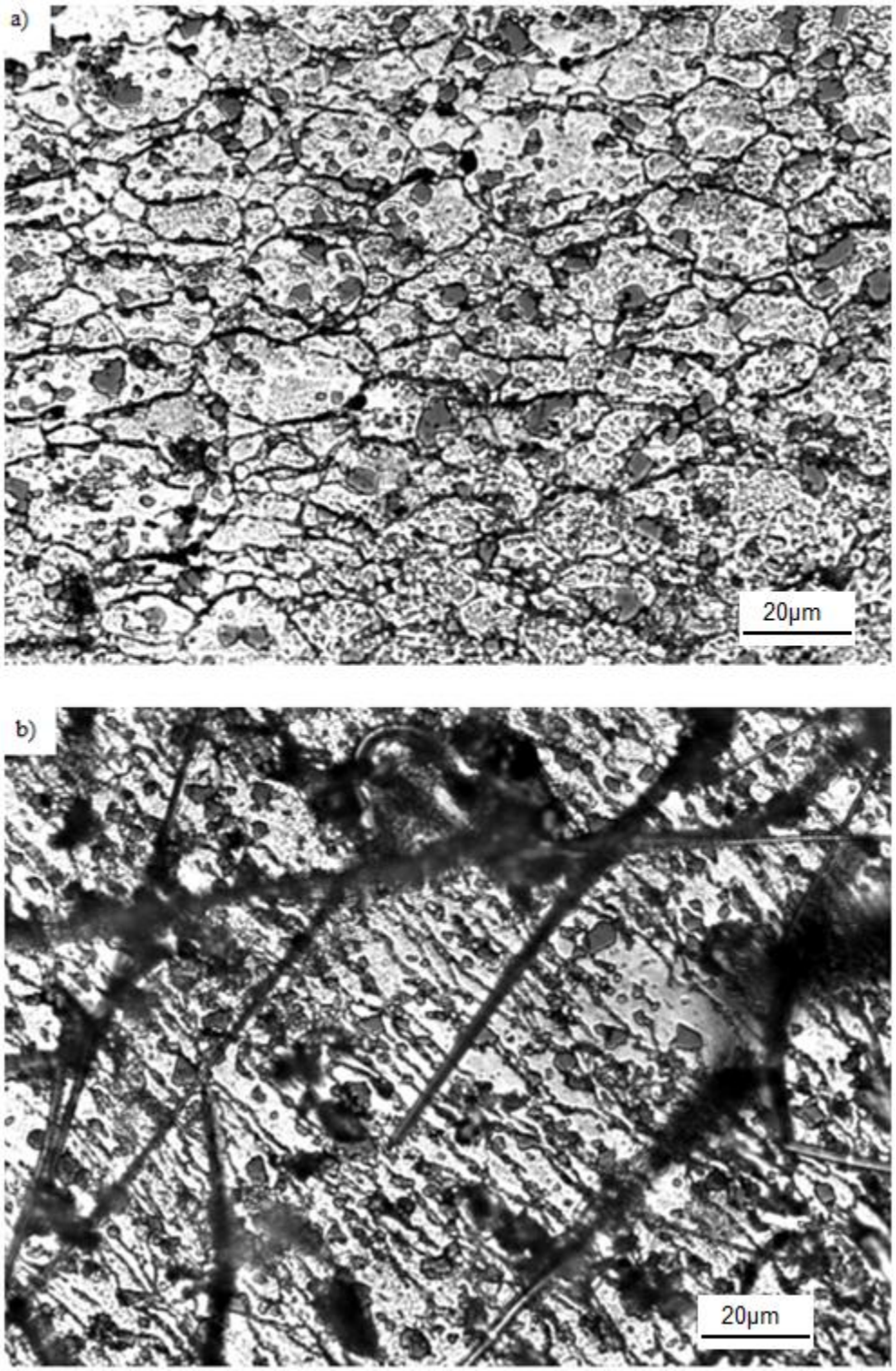

Figure 4.67: Etched optical micrograph of the longitudinal section of the 500C 10h sample after one pass of ECAP where; a) is the "skin" region from Figure 4.63 and; b) is the "core" region from Figure 4.63.

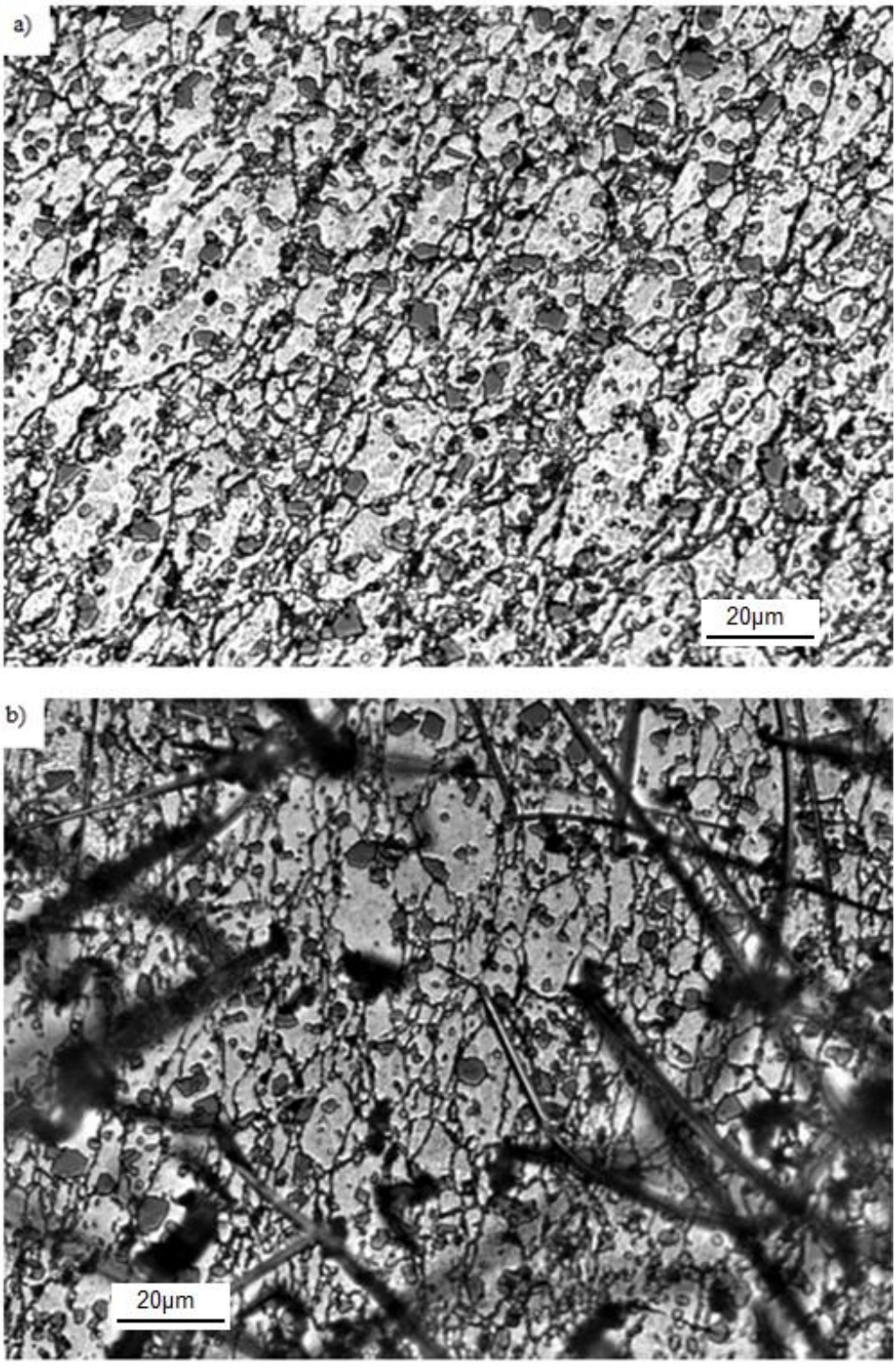

Figure 4.68: Etched optical micrograph of the transverse section of the 500C 10h sample after one pass of ECAP where; a) is the "skin" region from Figure 4.63 and; b) is the "core" region from Figure 4.63.

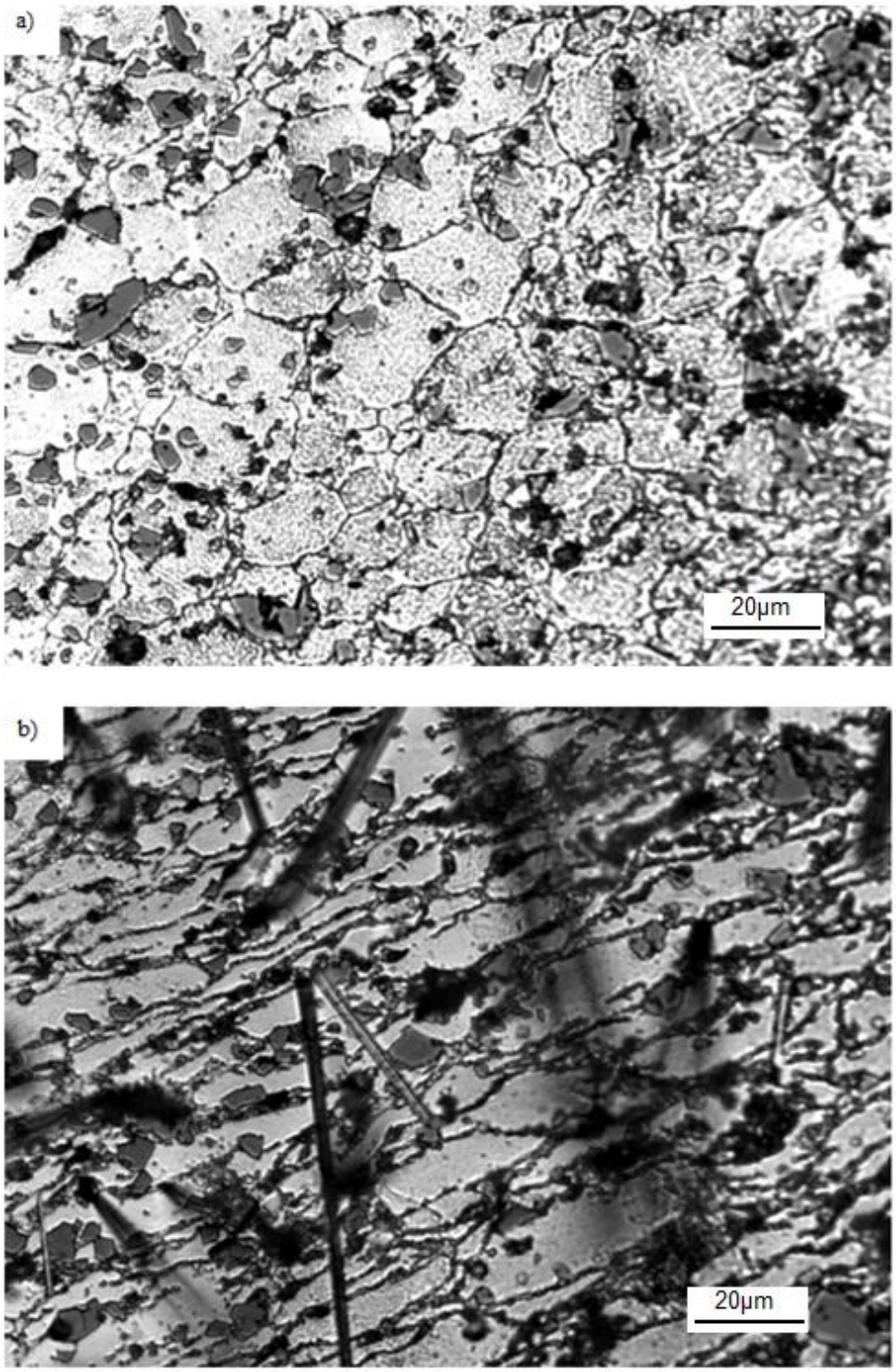

Figure 4.69: Etched optical micrograph of the longitudinal section of the 550C 1h sample after one pass of ECAP where; a) is the "skin" region from Figure 4.64 and; b) is the "core" region from Figure 4.64.

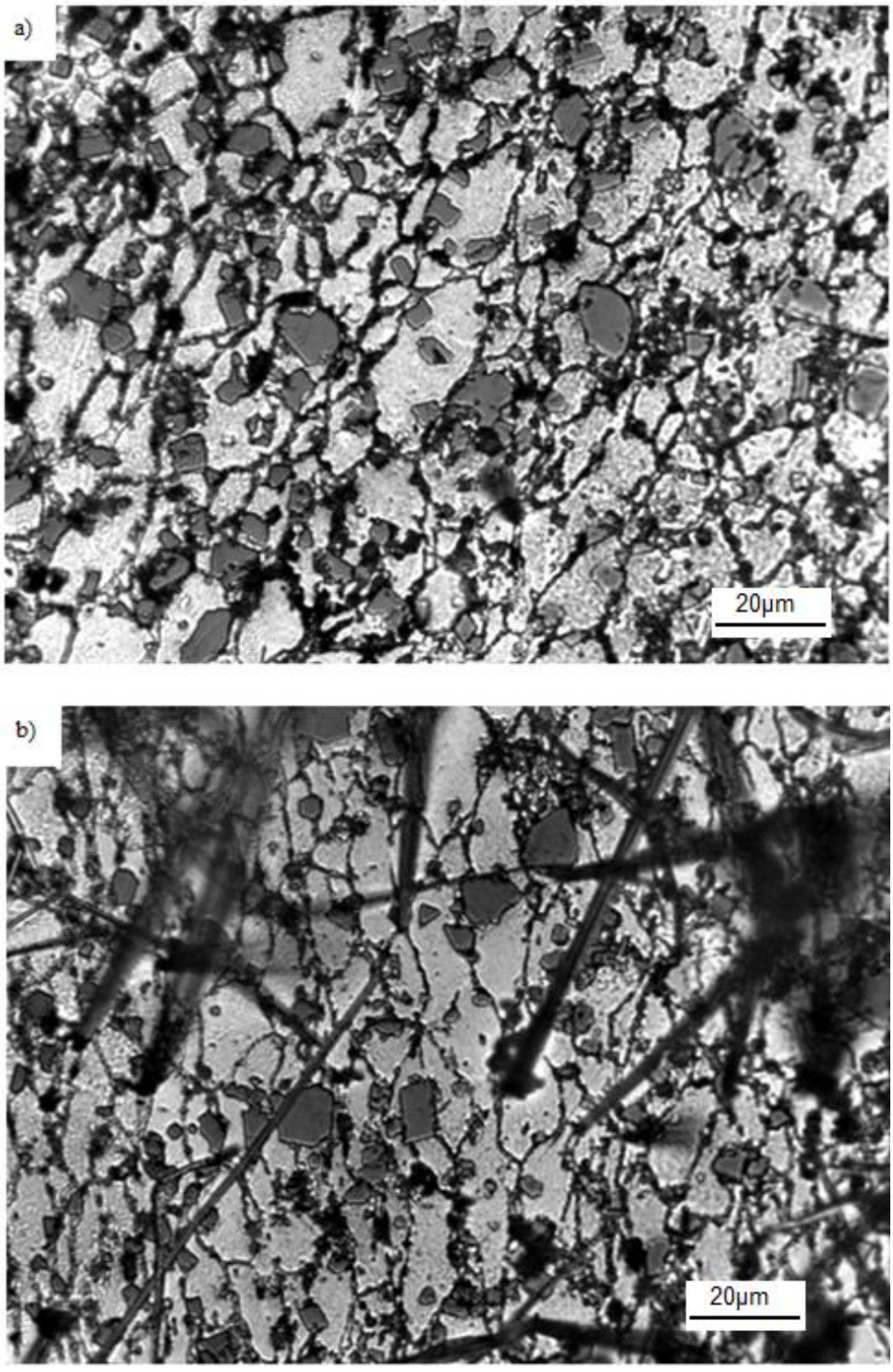

Figure 4.70: Etched optical micrograph of the transverse section of the 550C 1h sample after one pass of ECAP where; a) is the "skin" region from Figure 4.64 and; b) is the "core" region from Figure 4.64.

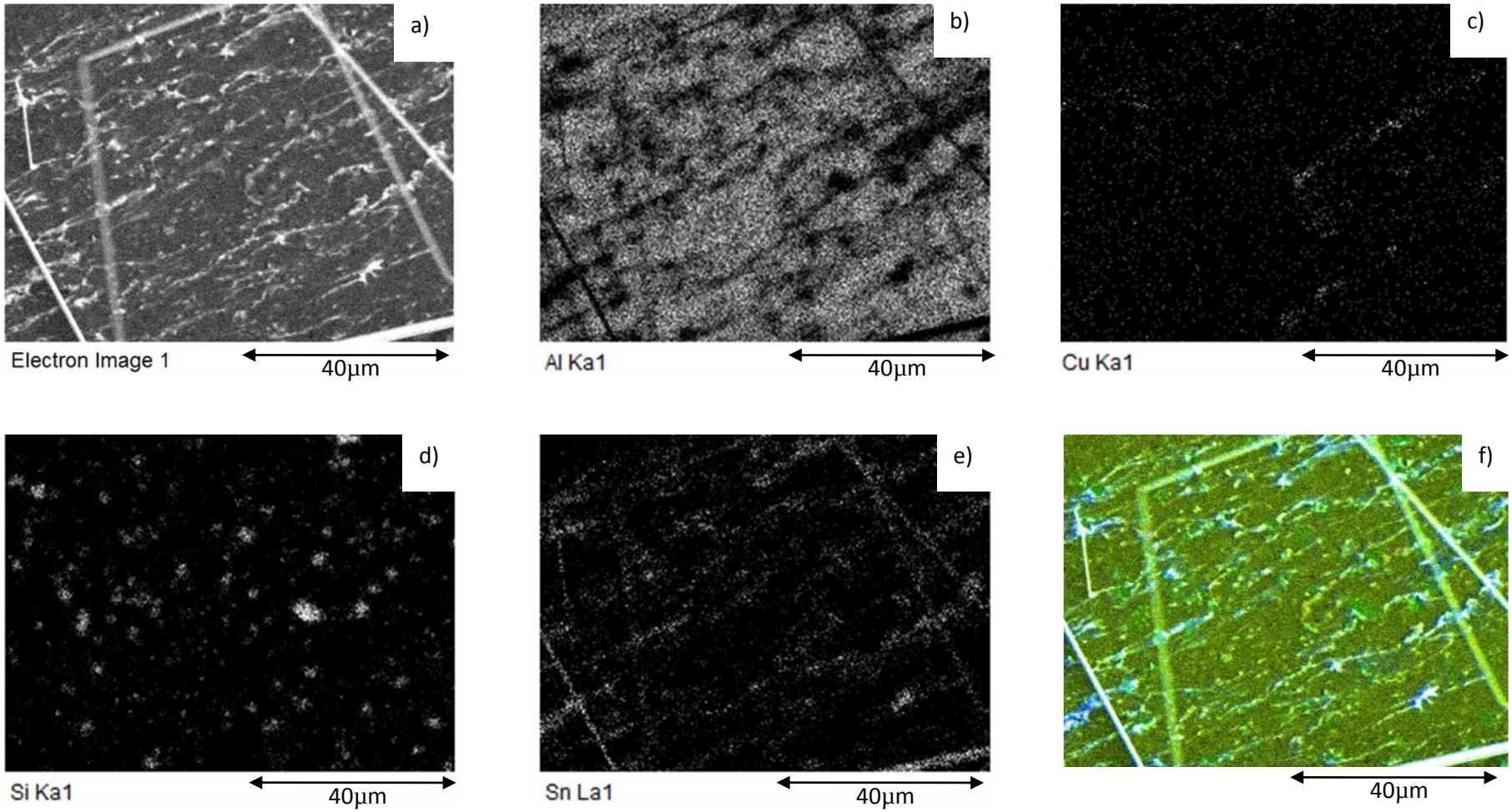

Figure 4.71: EDX analysis of the sintered 500C 1h sample after one ECAP pass in the core region of the longitudinal section, where; a) is the SEM image; b) is the Al map; c) is the Cu map; d) is the Si map; e) is the Sn map and; f) is the colour map with blue/white representing tin, dark green representing aluminium, lighter green representing silicon and the light brown representing copper.

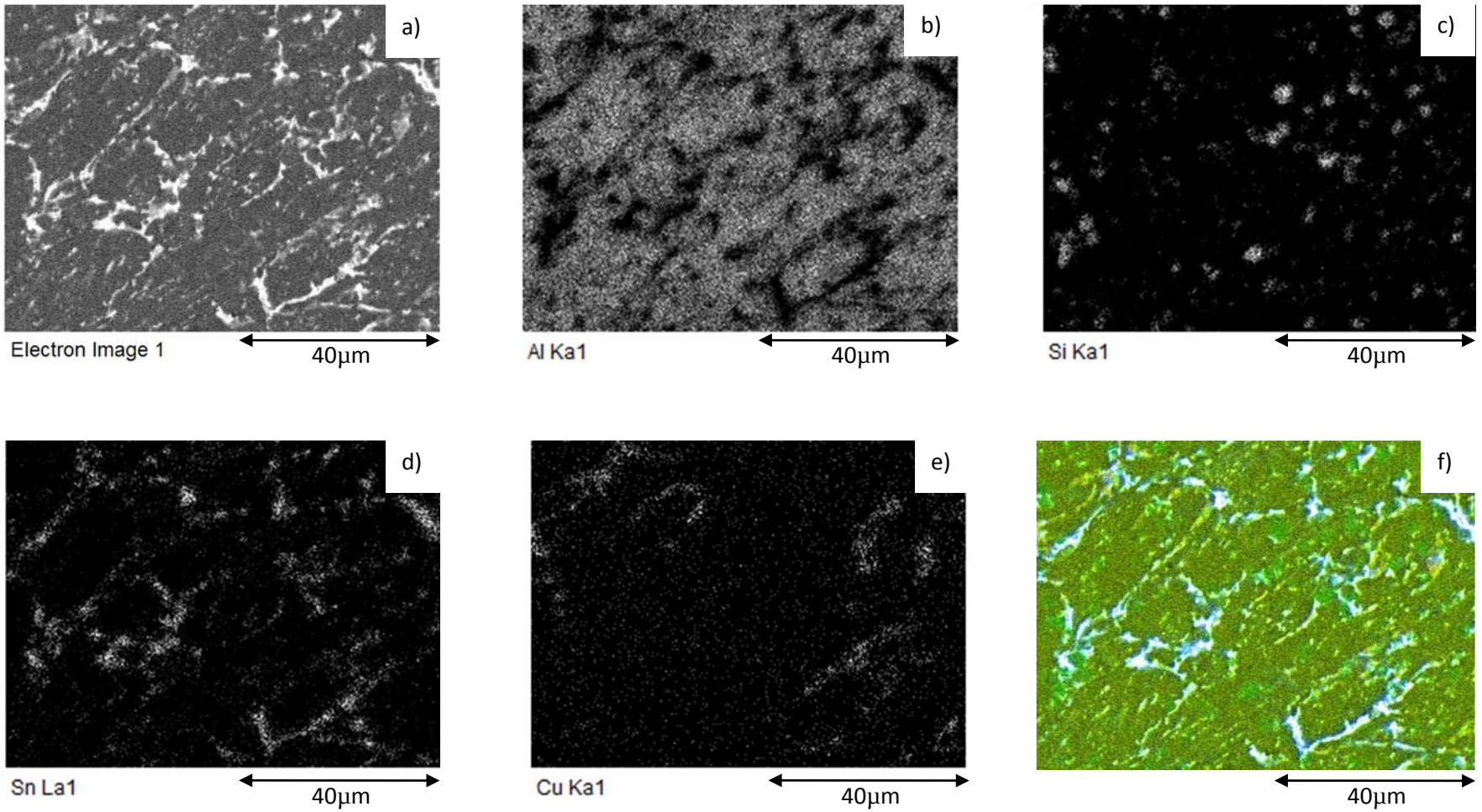

Figure 4.72: EDX analysis of the sintered 500C 1h sample after one ECAP pass in the skin region of the longitudinal section, where; a) is the SEM image; b) is the Al map; c) is the Cu map; d) is the Si map; e) is the Sn map and; f) is the colour map with blue/white representing tin, dark green representing aluminium, lighter green representing silicon and the light brown representing copper.

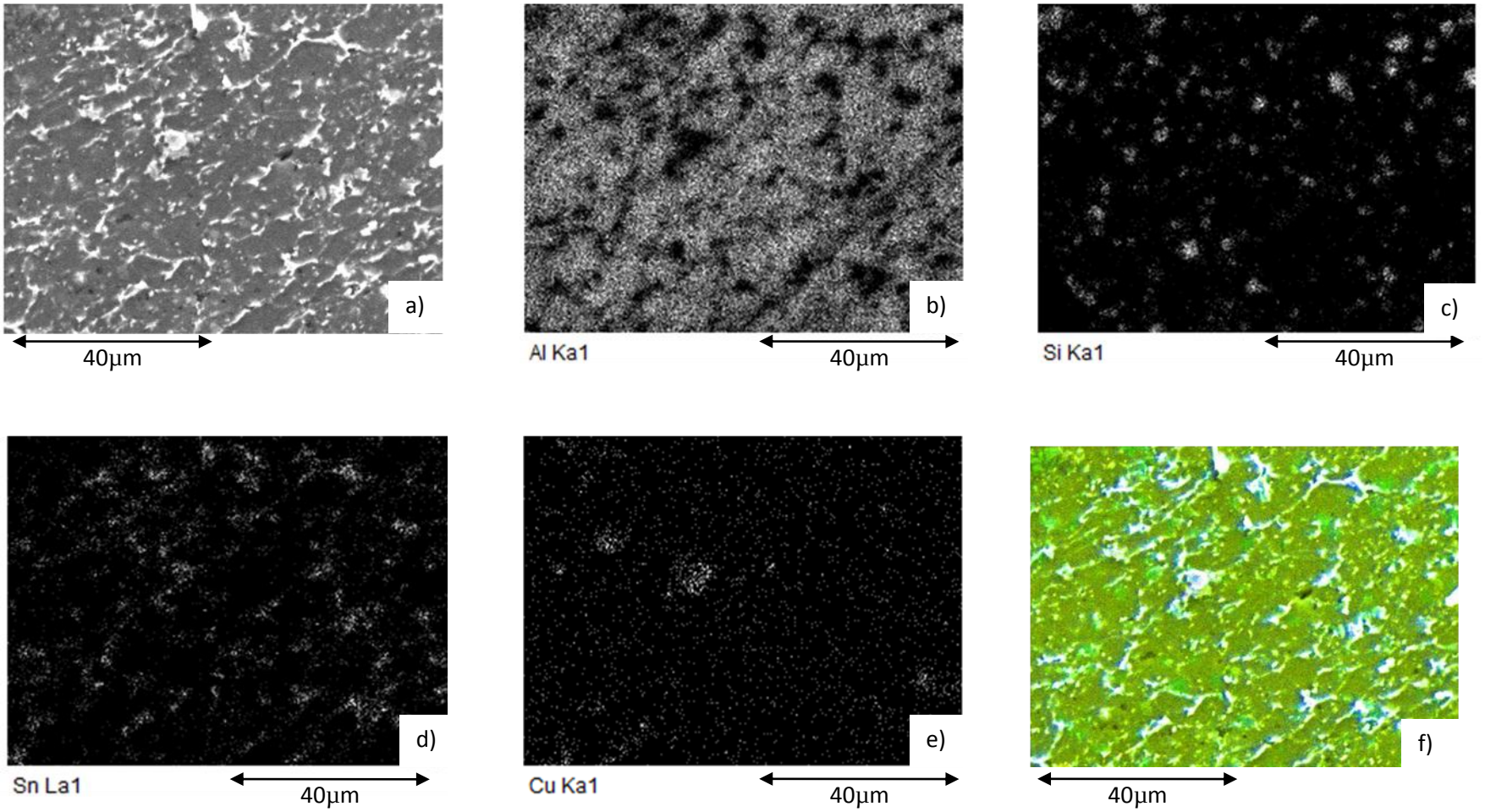

Figure 4.73: EDX analysis of the sintered 500C 1h sample after one ECAP pass in the core region of the transverse section, where; a) is the SEM image; b) is the Al map; c) is the Cu map; d) is the Si map; e) is the Sn map and; f) is the colour map with blue/white representing tin, dark green representing aluminium, lighter green representing silicon and the light brown representing copper.

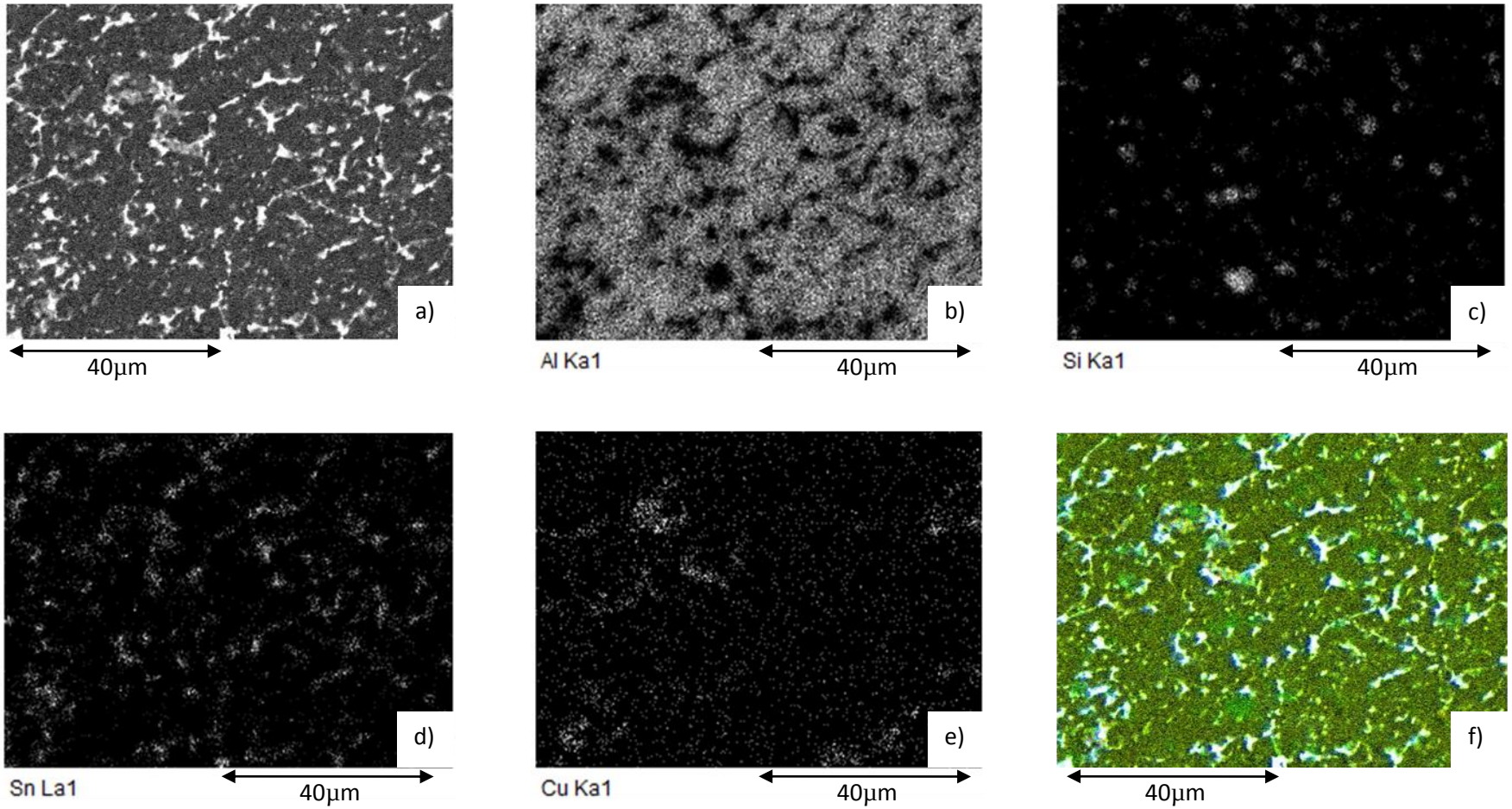

Figure 4.74: EDX analysis of the sintered 500C 1h sample after one ECAP pass in the skin region of the transverse section, where; a) is the SEM image; b) is the Al map; c) is the Cu map; d) is the Si map; e) is the Sn map and; f) is the colour map with blue/white representing tin, dark green representing aluminium, lighter green representing silicon and the light brown representing copper.

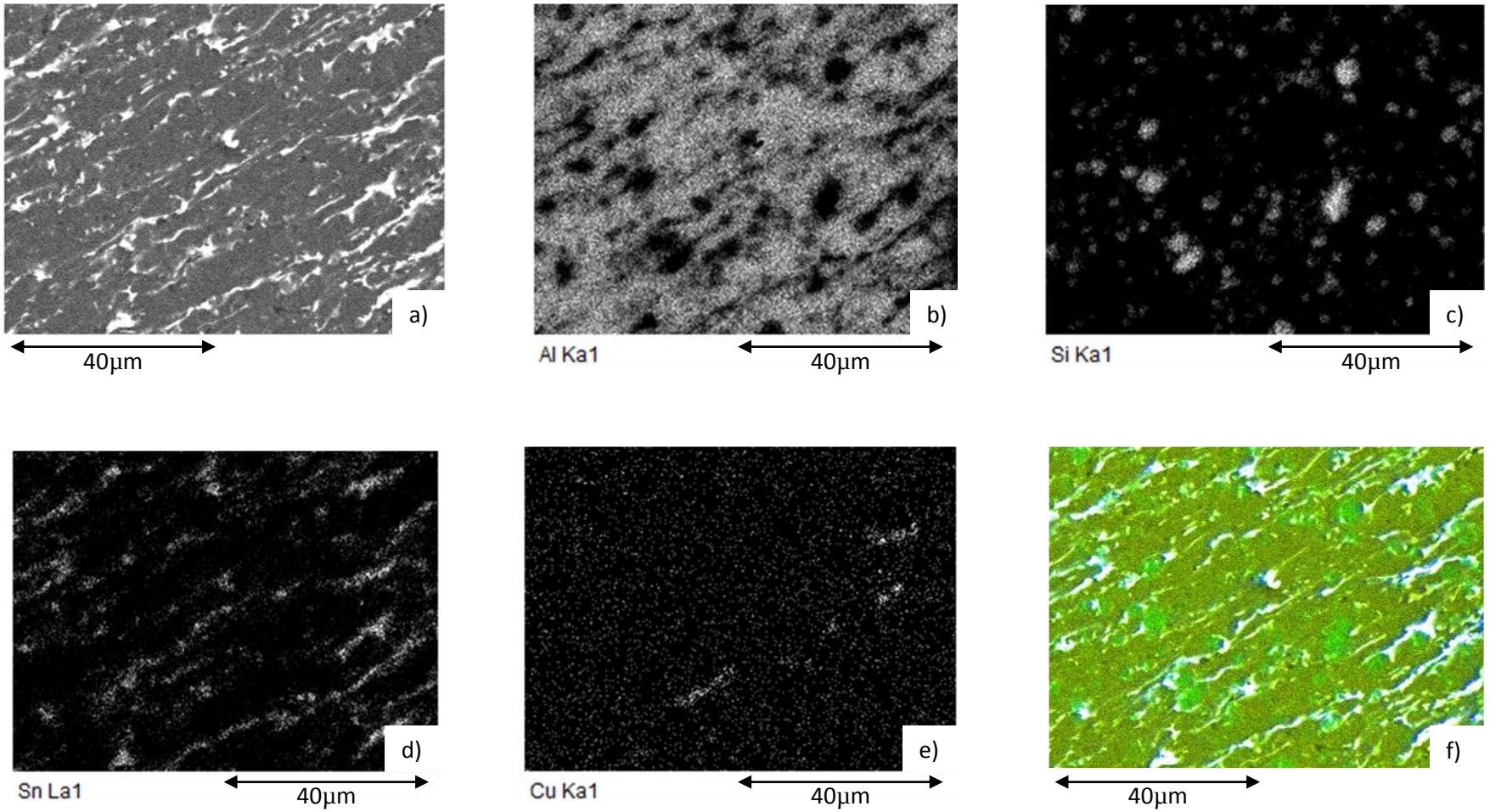

Figure 4.75: EDX analysis of the sintered 500C 10h sample after one ECAP pass in the core region of the longitudinal section, where; a) is the SEM image; b) is the Al map; c) is the Cu map; d) is the Si map; e) is the Sn map and; f) is the colour map with blue/white representing tin, dark green representing aluminium, lighter green representing silicon and the light brown representing copper.

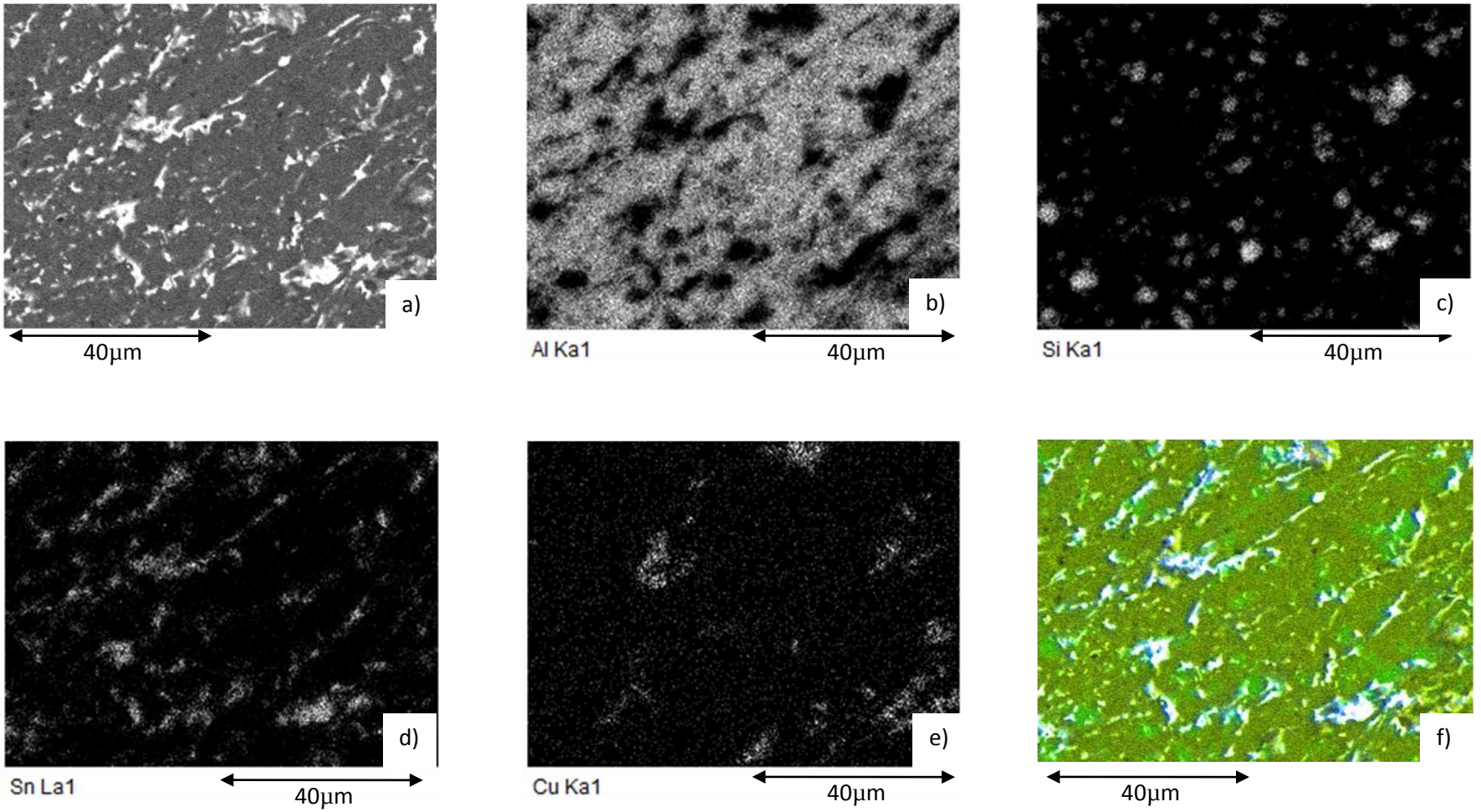

Figure 4.76: EDX analysis of the sintered 500C 10h sample after one ECAP pass in the skin region of the longitudinal section, where; a) is the SEM image; b) is the Al map; c) is the Cu map; d) is the Si map; e) is the Sn map and; f) is the colour map with blue/white representing tin, dark green representing aluminium, lighter green representing silicon and the light brown representing copper.

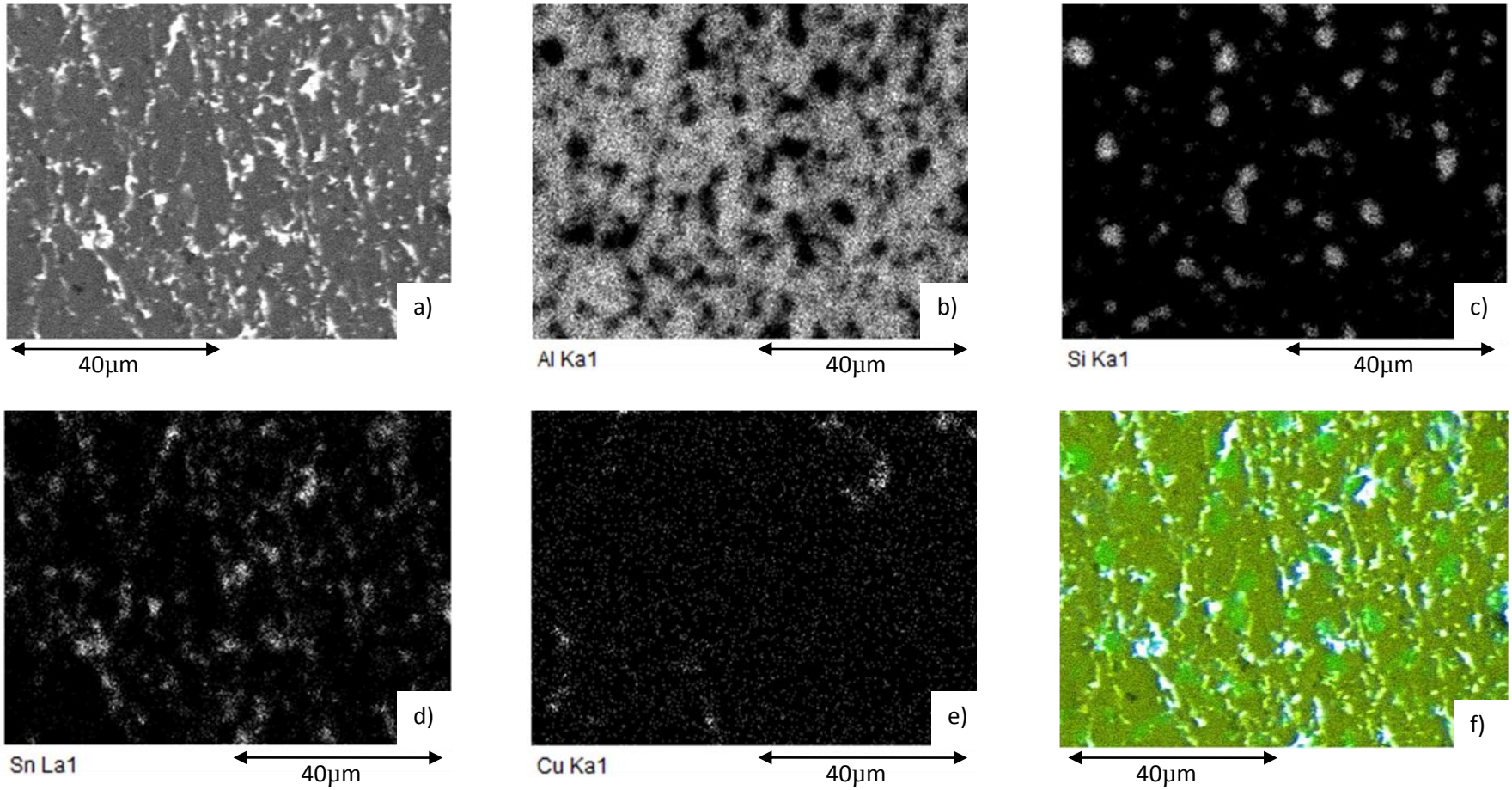

Figure 4.77: EDX analysis of the sintered 500C 10h sample after one ECAP pass in the core region of the transverse section, where; a) is the SEM image; b) is the Al map; c) is the Cu map; d) is the Si map; e) is the Sn map and; f) is the colour map with blue/white representing tin, dark green representing aluminium, lighter green representing silicon and the light brown representing copper.

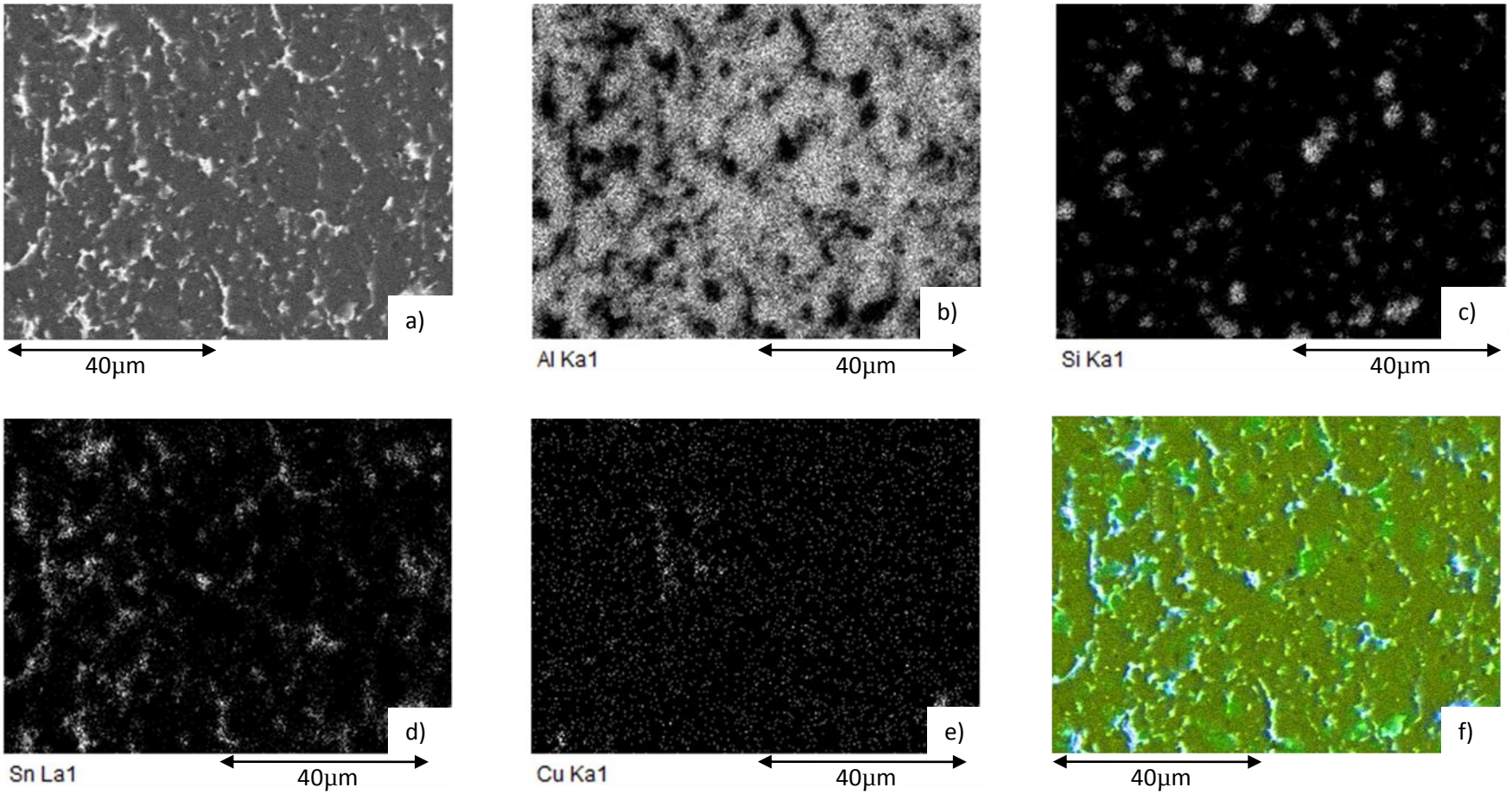

Figure 4.78: EDX analysis of the sintered 500C 10h sample after one ECAP pass in the skin region of the transverse section, where; a) is the SEM image; b) is the Al map; c) is the Cu map; d) is the Si map; e) is the Sn map and; f) is the colour map with blue/white representing tin, dark green representing aluminium, lighter green representing silicon and the light brown representing copper.

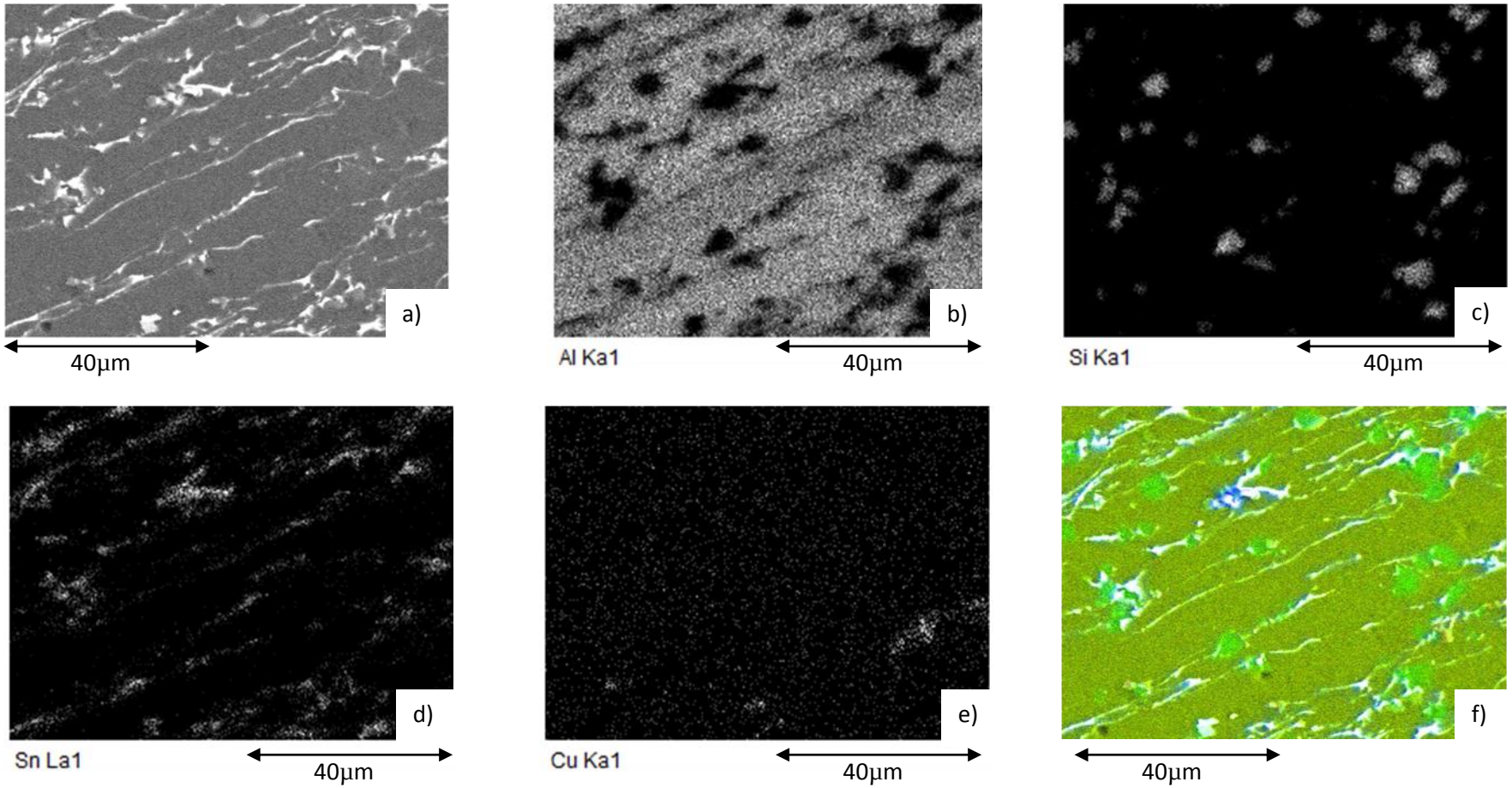

Figure 4.79: EDX analysis of the sintered 550C 1h sample after one ECAP pass in the core region of the longitudinal section, where; a) is the SEM image; b) is the Al map; c) is the Cu map; d) is the Si map; e) is the Sn map and; f) is the colour map with blue/white representing tin, dark green representing aluminium, lighter green representing silicon and the light brown representing copper.

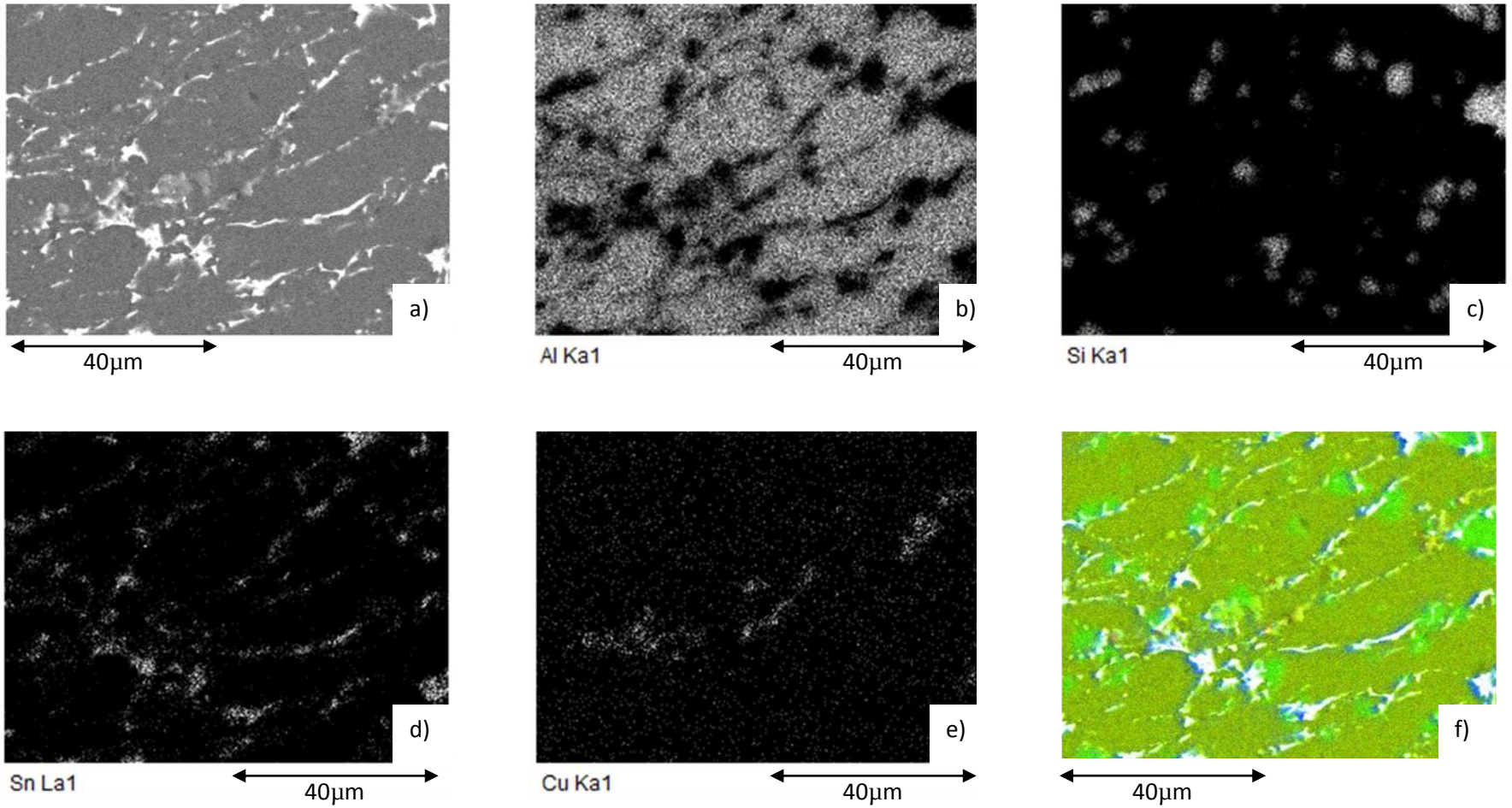

Figure 4.80: EDX analysis of the sintered 550C 1h sample after one ECAP pass in the skin region of the longitudinal section, where; a) is the SEM image; b) is the Al map; c) is the Cu map; d) is the Si map; e) is the Sn map and; f) is the colour map with blue/white representing tin, dark green representing aluminium, lighter green representing silicon and the light brown representing copper.

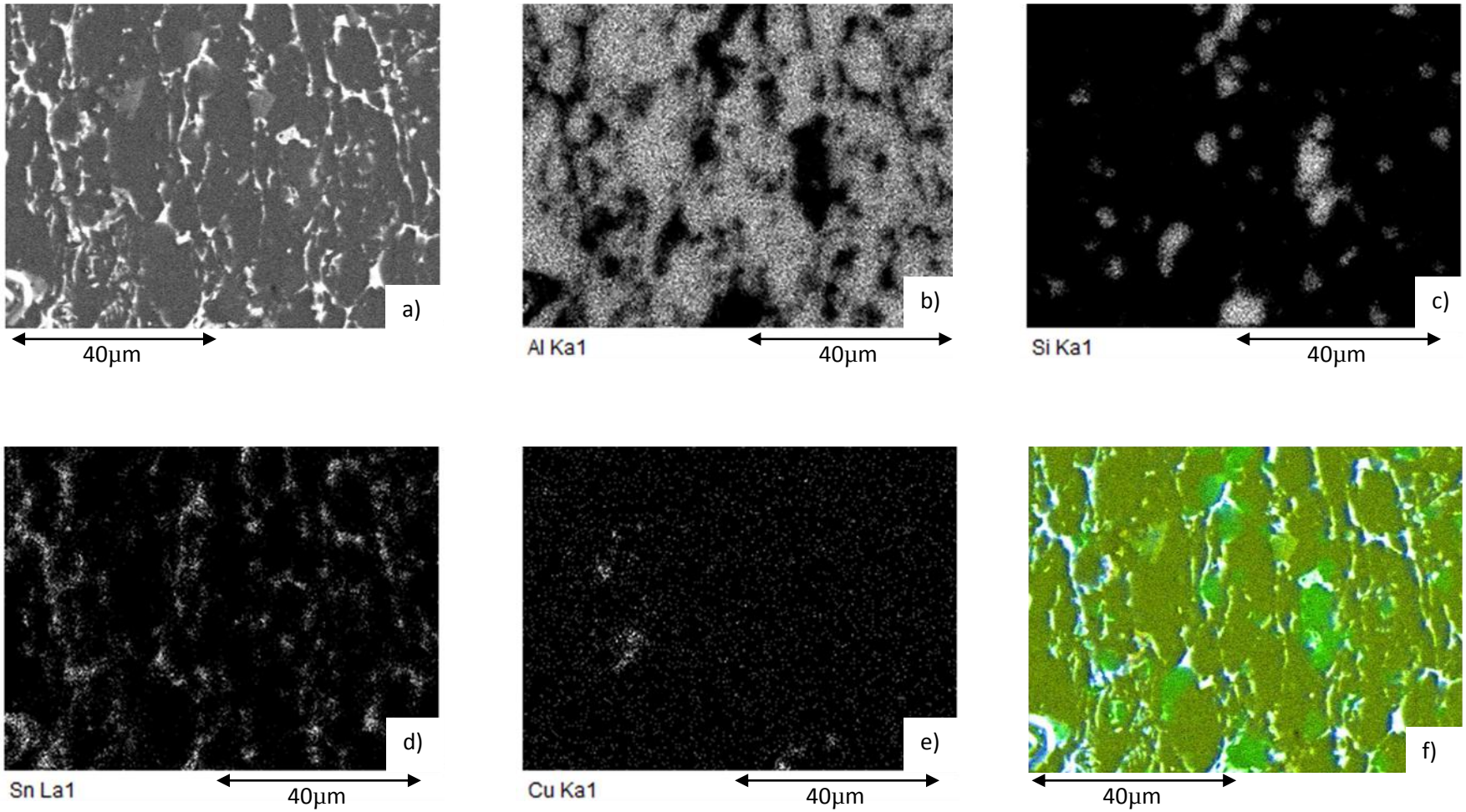

Figure 4.81: EDX analysis of the sintered 550C 1h sample after one ECAP pass in the core region of the transverse section, where; a) is the SEM image; b) is the Al map; c) is the Cu map; d) is the Si map; e) is the Sn map and; f) is the colour map with blue/white representing tin, dark green representing aluminium, lighter green representing silicon and the light brown representing copper.

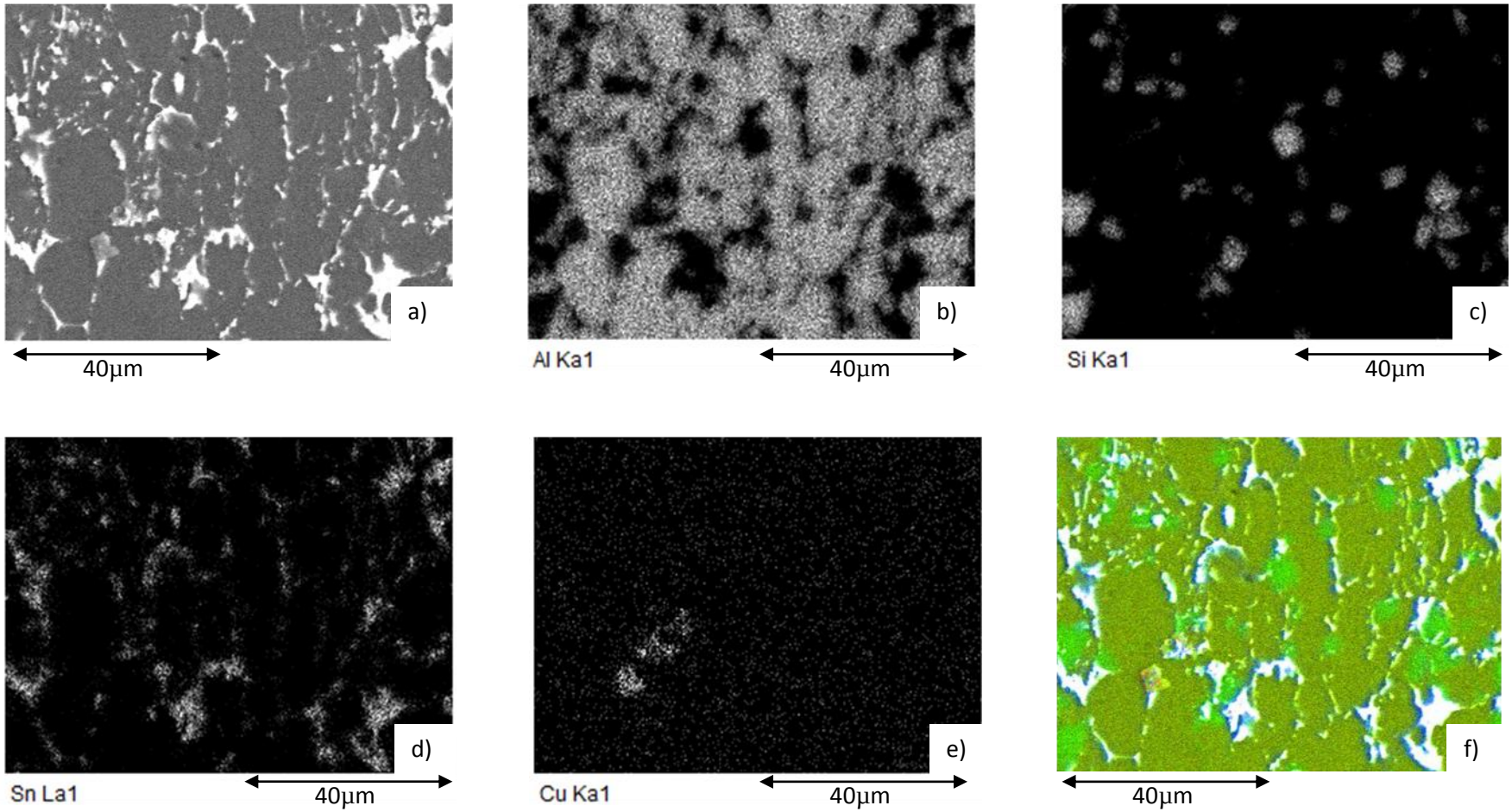

Figure 4.82: EDX analysis of the sintered 550C 1h sample after one ECAP pass in the skin region of the transverse section, where; a) is the SEM image; b) is the Al map; c) is the Cu map; d) is the Si map; e) is the Sn map and; f) is the colour map with blue/white representing tin, dark green representing aluminium, lighter green representing silicon and the light brown representing copper.

Table 4.24: The length, width and ECD for the aluminium grains of the ECAP samples. The spread around the mean values is quite large, indicating a large scattering of the data.

Sample	Length µm		Width µm		Aspect ratio		ECD µm	
	Longitudinal	**Transverse**	**Longitudinal**	**Transverse**	**Longitudinal**	**Transverse**	**Longitudinal**	**Transverse**
Sintered at 500°C 1h								
Skin region	13.99 ± 11.03	10.28 ± 6.74	4.9 ± 3.42	5.34 ± 3.42	0.35	0.52	7.79 ± 5.43	8.94 ± 4.05
Core region	18.68 ± 10.15	11.62 ± 7.27	4.86 ± 1.92	5.78 ± 3.13	0.26	0.50	7.08 ± 4.38	7.77 ± 4.24
Sintered at 500°C 10h								
Skin region	13.28 ± 8.66	10.07 ± 6.42	6.95 ± 4.22	5.19 ± 3.32	0.52	0.51	9.2 ± 5.58	6.92 ± 4.21
Core region	15.16 ± 9.8	9.92 ± 6.33	4.23 ± 1.97	4.67 ± 2.8	0.28	0.47	7.46 ± 3.74	6.59 ± 3.86
Sintered at 550°C 1h								
Skin region	31.33 ± 20.14	17.5 ± 9.5	11.72 ± 5.03	9.53 ± 5.2	0.37	0.54	14.53 ± 6.02	11.08 ± 5.26
Core region	21.6 ± 10.14	15.73 ± 7.36	8.86 ± 3.76	9.1 ± 4.66	0.41	0.58	14.2 ± 6.48	11.22 ± 5.11

Table 4.25: The length, width and ECD of the silicon particles after one pass of ECAP of the sintered specimens.

Sample	Length µm		Width µm		Aspect ratio		ECD µm	
	Longitudinal	**Transverse**	**Longitudinal**	**Transverse**	**Longitudinal**	**Transverse**	**Longitudinal**	**Transverse**
Sintered at 500°C 1h								
Skin region	3.7 ± 1.46	3.45 ± 1.47	2.61 ± 0.96	2.19 ± 0.96	0.71	0.63	3.19 ± 1.06	2.99 ± 1.09
Core region	3.21 ± 1.46	3.37 ± 1.47	2.33 ± 1.05	2.45 ± 0.98	0.81	0.73	2.83 ± 1.12	2.9 ± 1.09
Sintered at 500°C 10h								
Skin region	3.3 ± 1.53	3.34 ± 1.71	2.46 ± 1.1	2.29 ± 1.13	0.75	0.69	2.95 ± 1.21	2.86 ± 1.28
Core region	3.22 ± 1.63	3.53 ± 1.74	2.29 ± 1.1	2.5 ± 1.21	0.71	0.71	2.81 ± 1.24	3.04 ± 1.34
Sintered at 550°C 1h								
Skin region	4.3 ± 2.05	4.87 ± 2.43	3.05 ± 1.25	3.25 ± 1.63	0.71	0.67	3.69 ± 1.44	4.04 ± 1.86
Core region	5.43 ± 3.19	3.65 ± 1.96	4.41 ± 2.2	3.13 ± 1.56	0.81	0.86	3.77 ± 1.72	4.45 ± 2.24

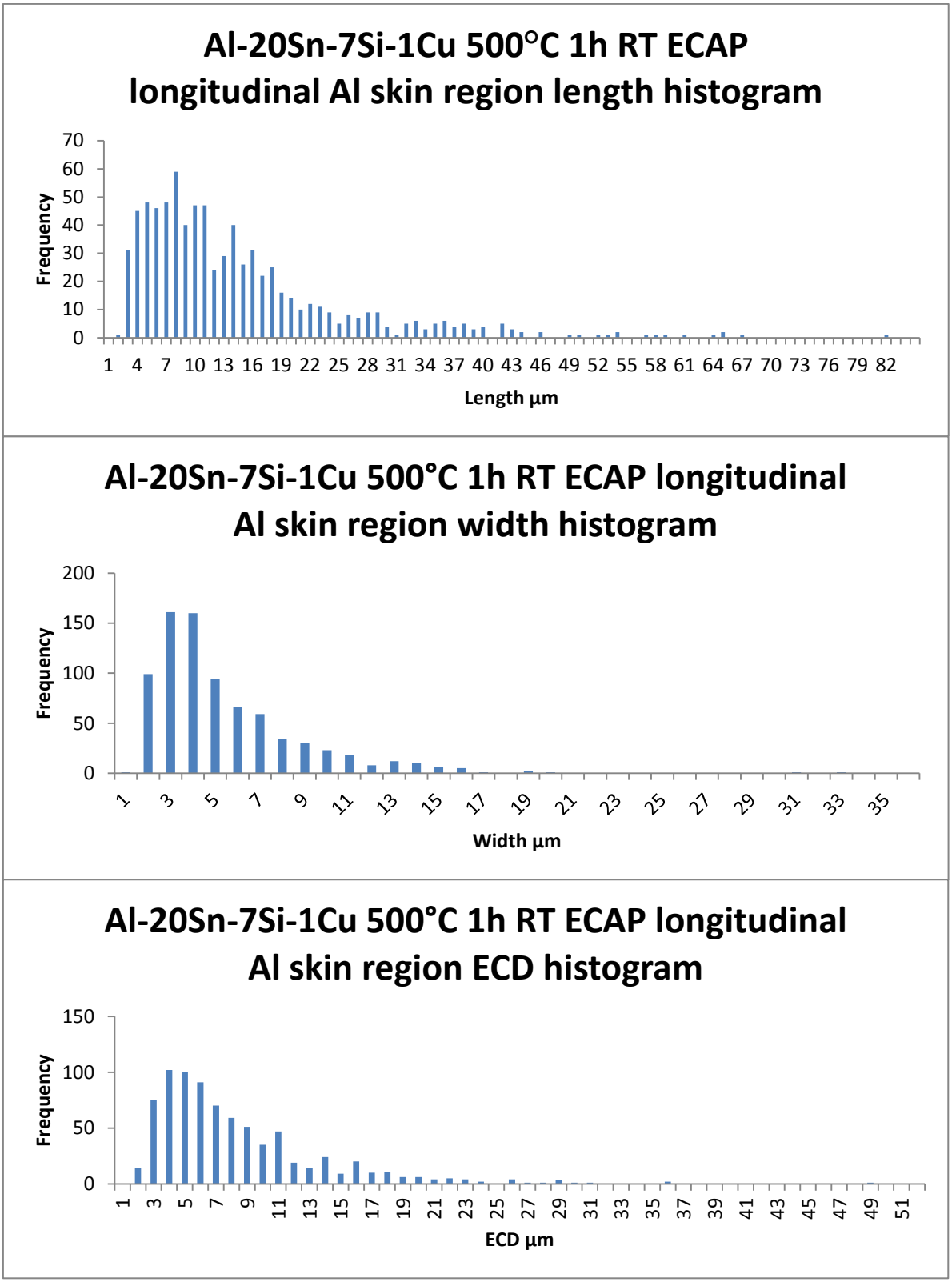

Figure 4.83: Histograms for length, width and ECD of aluminium grains in the skin region of the longitudinal section after 1 pass of ECAP of samples pre-sintered at 500°C 1h.

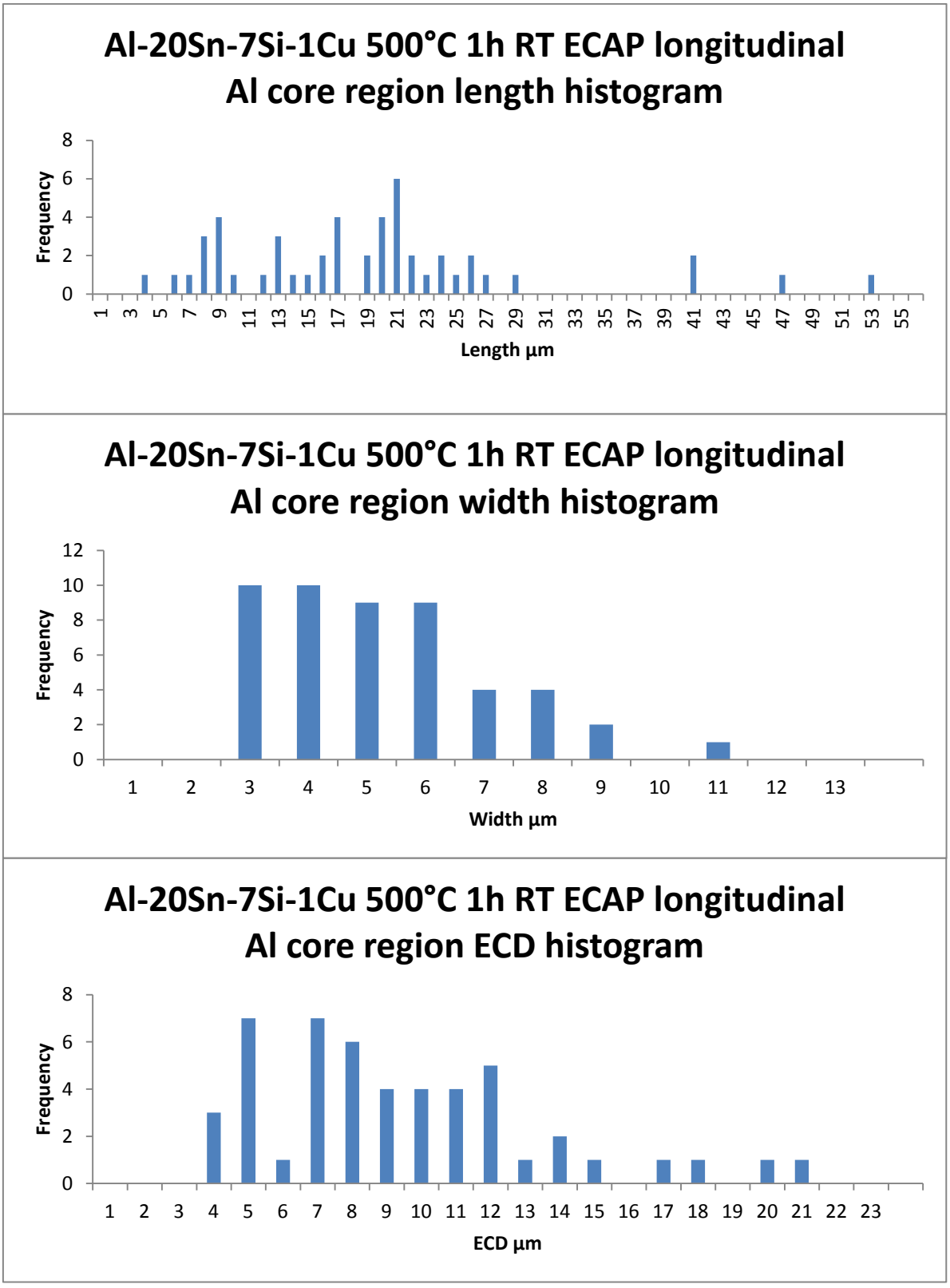

Figure 4.84: Histograms for length, width and ECD of aluminium grains in the core region of the longitudinal section after 1 pass of ECAP of samples pre-sintered at 500°C 1h.

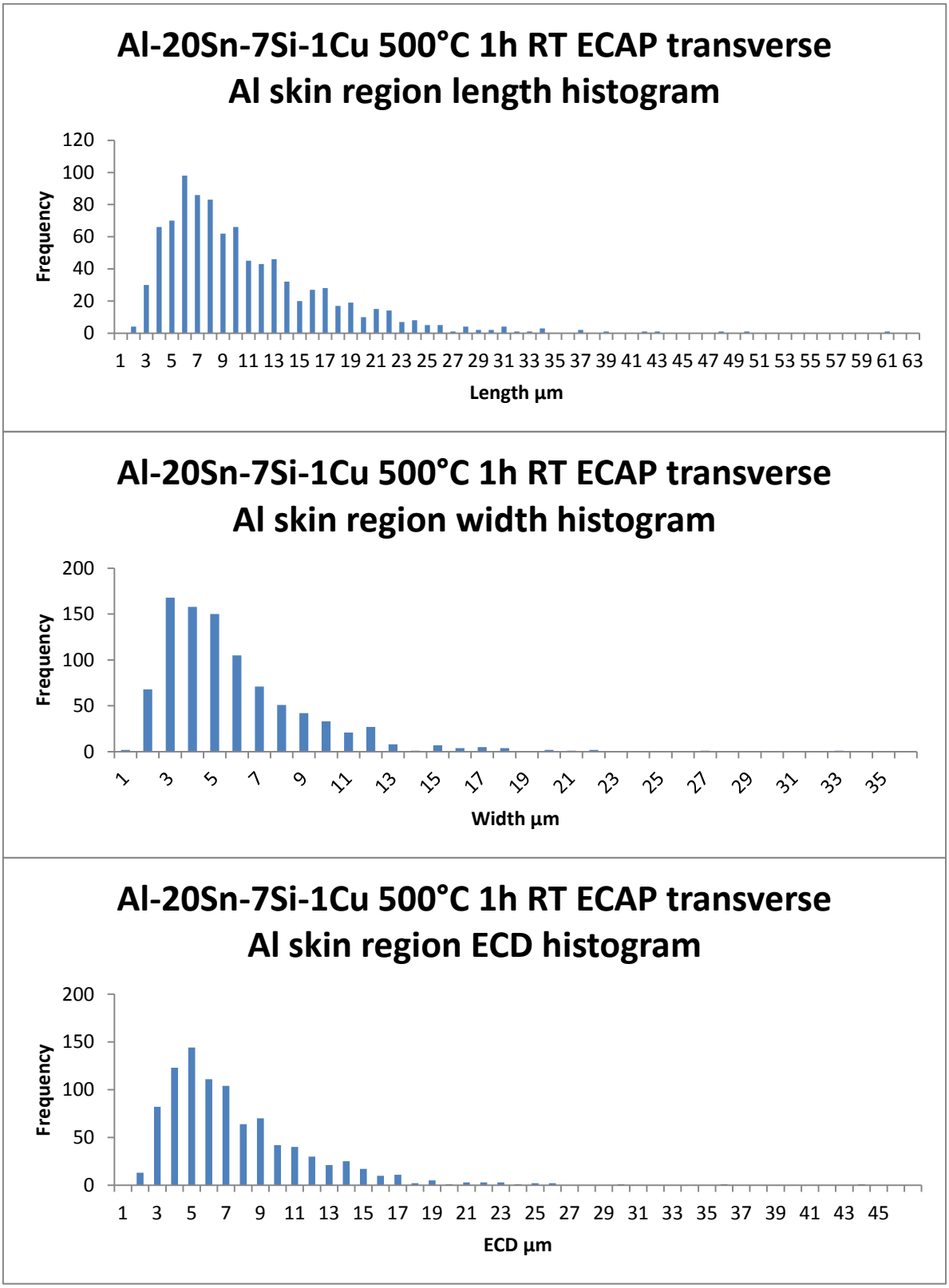

Figure 4.85: Histograms for length, width and ECD of aluminium grains in the skin region of the transverse section after 1 pass of ECAP of samples pre-sintered at 500°C 1h.

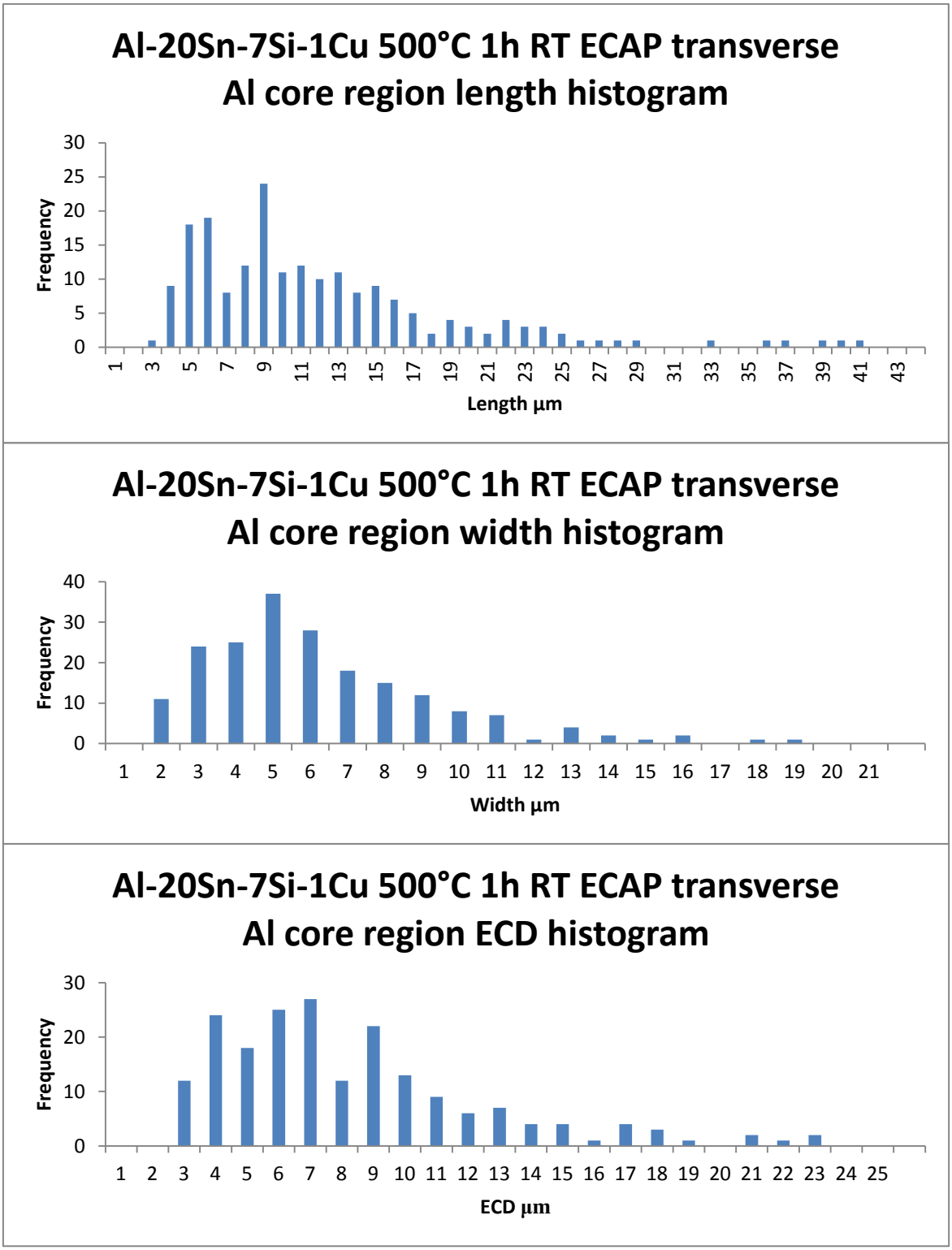

Figure 4.86: Histograms for length, width and ECD of aluminium grains in the core region of the transverse section after 1 pass of ECAP of samples pre-sintered at 500°C 1h.

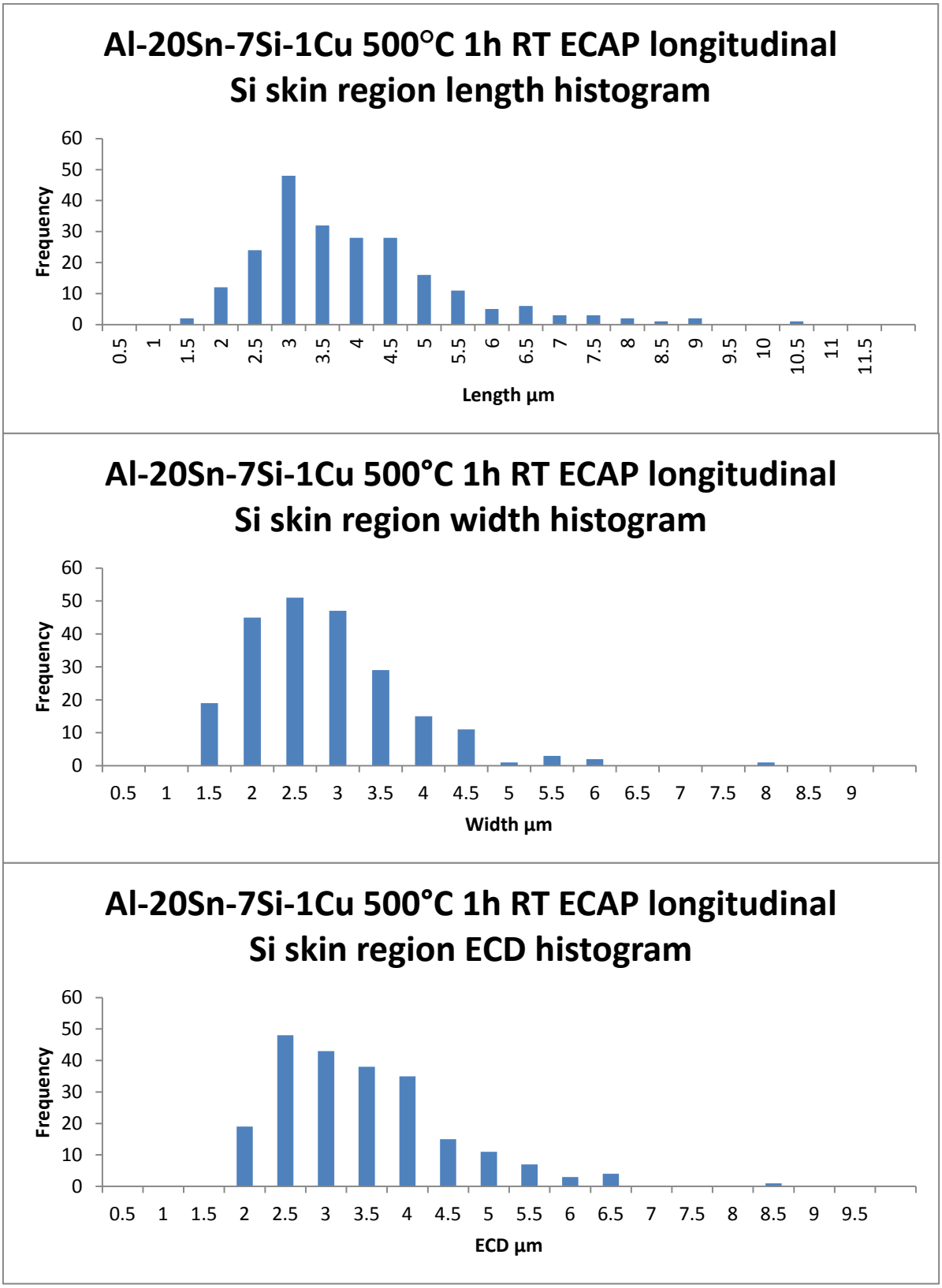

Figure 4.87: Histograms for length, width and ECD of silicon particles in the skin region of the longitudinal section after 1 pass of ECAP of samples pre-sintered at 500°C 1h.

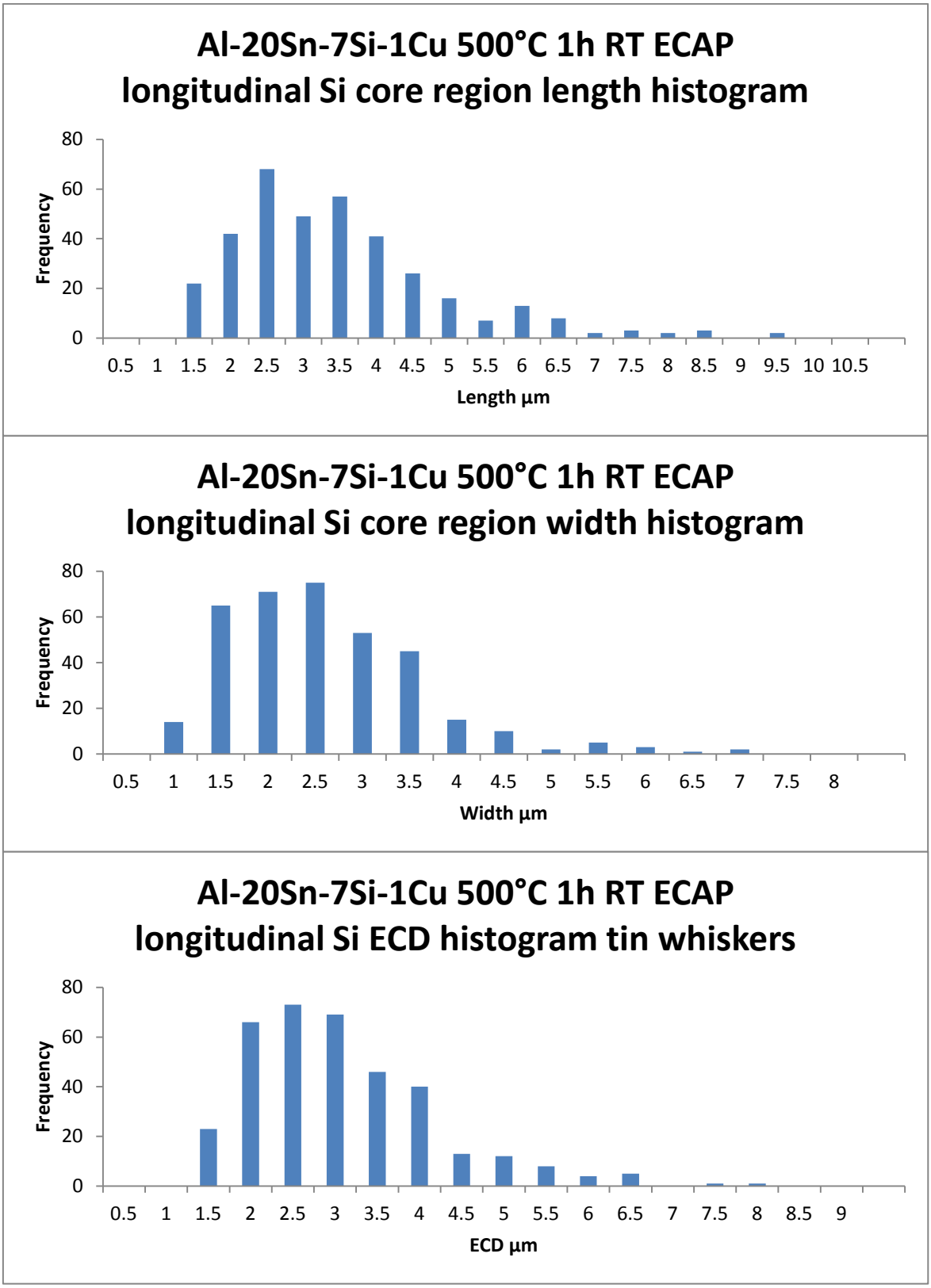

Figure 4.88: Histograms for length, width and ECD of silicon particles in the core region of the longitudinal section after 1 pass of ECAP of samples pre-sintered at 500°C 1h.

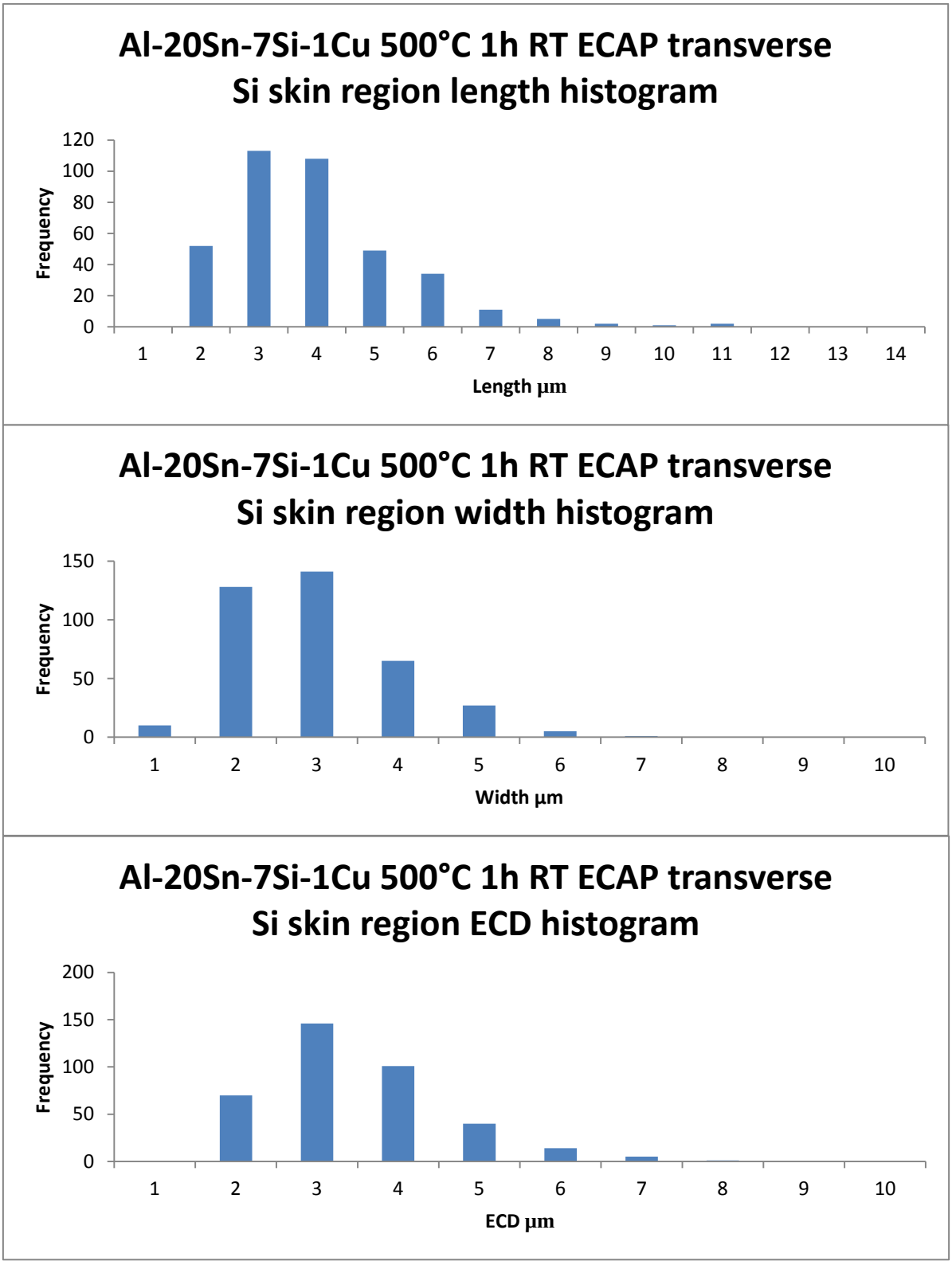

Figure 4.89: Histograms for length, width and ECD of silicon particles in the skin region of the transverse section after 1 pass of ECAP of samples pre-sintered at 500°C 1h.

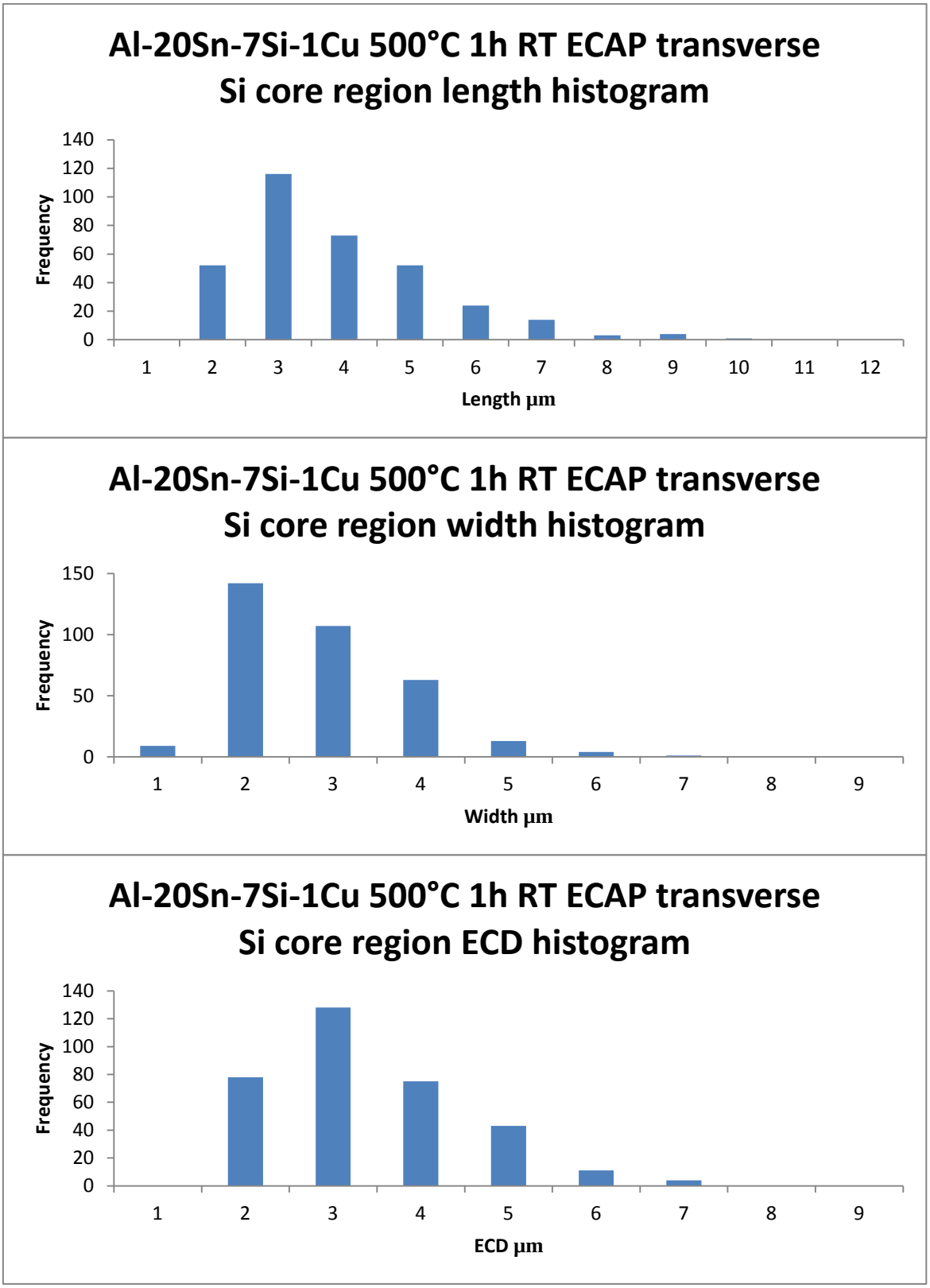

Figure 4.90: Histograms for length, width and ECD of silicon particles in the core region of the transverse section after 1 pass of ECAP of samples pre-sintered at 500°C 1h.

4.3.4.3. ECAP hardness

The hardness after one pass of ECAP in the skin and core region is shown in Table 4.26. After ECAP, the hardness of the skin region in the sample pre-sintered at 500°C for 1h was $69.3 \pm 4.7HV_{2.5kg}$ and $68.3 \pm 8.5HV_{2.5kg}$ in the longitudinal and transverse sections respectively. This increased to $76.9 \pm 0.97HV_{2.5kg}$ and $77.9 \pm 1.53HV_{2.5kg}$ in the core region of the longitudinal and transverse sections respectively. The hardness of the skin region in the sample pre-sintered at 500°C for 10h was $74.26 \pm 1.05HV_{2.5kg}$ and $73.66 \pm 0.97HV_{2.5kg}$ for the longitudinal and transverse sections respectively. In the core region, the hardness increased to $78.08 \pm 1.22HV_{2.5kg}$ and $76.7 \pm 1.77HV_{2.5kg}$ in the longitudinal and transverse sections respectively. For the sample pre-sintered at 550°C for 1h, the hardness of the skin region after ECAP was $70.12 \pm 2.71HV_{2.5kg}$ and $74.46 \pm 2.05HV_{2.5kg}$ in the longitudinal and transverse sections respectively. In the core region, this increased to $79.12 \pm 1.2HV_{2.5kg}$ and $76.26 \pm 1.03HV_{2.5kg}$ in the longitudinal and transverse sections respectively.

Table 4.26: The Vickers Hardness of the samples after one pass of ECAP in the transverse and longitudinal sections of the skin and core regions.

Sample	Longitudinal $HV_{2.5kg}$	Transverse $HV_{2.5kg}$
Sintered at 500°C 1h		
Skin	69.3 ± 4.7	68.3 ± 8.5
Core	76.9 ± 0.97	77.9 ± 1.53
Sintered at 500°C 10h		
Skin	74.26 ± 1.05	73.66 ± 0.97
Core	78.08 ± 1.22	76.7 ± 1.77
Sintered at 550°C 1h		
Skin	70.12 ± 2.71	74.46 ± 2.05
Core	79.12 ± 1.2	76.26 ± 1.03

4.4. Al-20Sn-7Si-1Cu bearing alloy discussion

4.4.1. Powder and compacted microstructure

4.4.1.1. Starting powder

The back scattered electron image of the starting material in Figure 4.32 showed that the pre-alloyed powders are mainly spherical with a D_{100} size of 54.36µm. The spherical morphology of the powders was a result of the gas atomisation process and depends on cooling rate and surface tension [4, 38, 42, 43, 45]. The cooling rate in gas atomisation is much lower as a result of the lower surface tension of the particles, which allows time for spheroidisation of the particles to occur during solidification [4, 45, 50, 139, 240].

As cooling progresses, the dendritic microstructure of Al-Si cells seen in Figure 4.37 forms via nucleation and growth of solid phases from the liquid droplet [4, 256]. On the surface of particles larger than 40µm diameter, protrusions of tin appear, observed in Figure 4.32. This is a result of tin having the lowest melting point of the elements in the alloy causing it to remain liquid as the other constituents solidify [103, 154, 155, 165]. As the other parts of the droplet solidify, they apply a slight compressive force on the liquid region and squeeze it out of the particle, which then solidify to leave the particle structure as shown in Figure 4.32 [4, 50, 52, 256, 257].

4.4.1.2. Density and Heckel relationship

The compressibility curve in Figure 4.33 shows the same trend as that seen with the pure aluminium samples, where the density increases with increasing compaction pressure before it plateaus. The reason for this is similar to the pure aluminium compaction trend, where by densification happens sequentially. The fundamental stages of densification involve particle re-arrangement, followed by plastic deformation of the particles until the compaction pressure is reached, which has been explained previously in section **4.2.3.1** [8, 17, 65, 87-90].

Using the Heckel relationship the yield strength of the Al-20Sn-7Si-1Cu compact can be determined. A graph of $ln\frac{1}{1-D}$ against P is shown in Figure 4.91 and the gradient of the graph is 0.002576, which gives a yield stress of 129.4MPa. This is lower than the yield stress of ~210MPa of an Al-20Sn-7Si-1Cu thermally sprayed coating that has been heat treated for 30 minutes at 300°C [165, 258]. This can be attributed to the low density of the green compact containing porosity, which weakens the microstructure [19, 23-25]. Furthermore, the particles are quite fine, which means that they are more resistant to plastic deformation and do not deform in to the voids left behind during die fill. This subsequently reduces the density and increases the gradient of the Heckel plot, thus lowering the calculated yield strength.

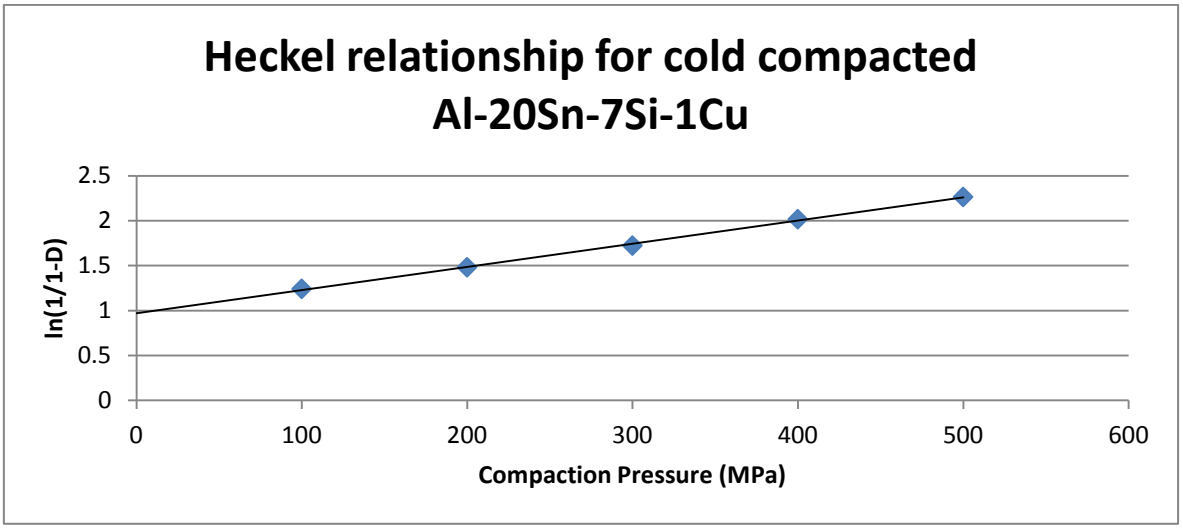

Figure 4.91: The Heckel relationship for the cold compacted Al-20Sn-7Si-1Cu samples

4.4.1.3. Porosity variation

The Al-20Sn-7Si-1Cu as-pressed samples also exhibited non-uniform transmission of pressure with the development of skin and core regions in Figure 4.34. This was approximately 3mm in the longitudinal section compared to up to 0.2mm in the longitudinal section of the pure aluminium samples shown in Figure 4.6. Under optical microscopy, the outer skin region contained higher amounts of porosity compared with that of the central core region, seen in Figure 4.35. This variation in porosity has been attributed to the high friction at the die wall, preventing adequate die fill when compared to the centre, even when die wall lubricant was applied [72, 73, 83, 100]. The transmission of the force through the powder is therefore non-uniform and hence these regions are seen.

Furthermore, the starting powder particles were relatively fine with a D_{100} of 54.36µm. As was noted in the pure aluminium samples, finer particles have higher frictional forces due to large surface areas and are harder to deform according to the Hall-Petch equation, thus do not transmit the compaction force efficiently [35, 62, 69]. Also, the Al-20Sn-7Si-1Cu particles had higher yield strength from the Heckel relationship of 129.4MPa than the coarse, medium and fine pure aluminium samples of 52.64MPa, 66.15MPa and 44.88MPa respectively. The aluminium matrix is supersaturated with silicon and copper as a result of solid solution strengthening and dispersion hardening, which increased the hardness of the materials and thus the transmission of force through the particles is less effective due to inability of particles to deform into voids, consequently leading to a thicker porous region [72, 73, 83].

4.4.1.4. Grain size and shape

After compaction, the ECD of the particles decreased from the D_{100} of 54.36µm to between 12.43 ± 7.25µm and 13.9 ± 8.65µm in the longitudinal and transverse sections respectively. The reason for this decrease in particle size can be attributed to the plastic deformation of the particles during the compaction process, which was mentioned in more detail in section **4.2.3.1**. The second stage of densification involves plastic deformation of the particles, therefore an associated reduction in grain size was expected as compaction pressure is applied [76, 87, 90].

When compared to the difference in grain size after compaction of the fine pure aluminium particles, the bearing alloy material is finer than the fine size range. From the sieve analysis supplied by AlPoCo in Table 4.14, it can be seen that the D_{50} is 21.70µm and D_{10} is 6.46µm. When analysing the longitudinal and transverse ECD histograms of the cold compacted bearing alloy powder in Figure 4.39 and Figure 4.40 respectively, the majority of the particles sizes are seen between 5-13µm. With the fine pure aluminium powders, the ECD in the longitudinal and transverse sections was 31.82 ± 15.53µm and 28.41 ± 13.6µm respectively as shown in Table 4.4. The spread of these measurements for the fine aluminium powder is seen in Appendix 6-3 for the longitudinal section and Appendix 6-4 for the transverse section. The majority of the ECD measurements are between 13-49µm for the longitudinal section and between 10-51µm in the transverse section. Therefore there are a greater number of finer particles in the bearing alloy compared to that in the fine size range of the pure aluminium leading to a smaller average particle size.

4.4.1.5. Grain structure

The cold compacted cross-section is shown in an optical image in Figure 4.37 and EDX analysis in Figure 4.38, which reveals an Al-Si dendritic structure and isolated regions of Sn. The formation of the Al-Si dendrite structures occurs first during cooling. The formation of this phase repels the liquid tin, creating pools in various regions of the particle, identified by the light phase in the backscattered image in Figure 4.38 [151, 165]. Due to tin having the lowest melting temperature of the constituents of 232°C, it is the last material to solidify [103, 154, 155].

EDX mapping of the cold compacted sample also showed that a few pure aluminium particles were present in the supplied powder with a majority of the pre-alloyed powder containing Sn phases. There was a uniform distribution of Si phase observed in the EDX analysis, thus suggesting that, during atomisation, the silicon was dissolved in the aluminium matrix due to the formation of a supersaturated solid solution from the rapid solidification process [4, 50, 52, 165, 256, 257].

4.4.1.6. Hardness

The hardness of the cold compacted samples was between 60.19$HV_{2.5kg}$ ± 2.27 and 62.2$HV_{2.5kg}$ ± 1.95 for the longitudinal and transverse sections respectively, which was lower than the 77.7$HV_{0.15kg}$ ± 1.71 for the as received powder. Even though the grain size was reduced as a result of plastic deformation, the green compact contained a few soft pure aluminium particles, which decreased hardness. In addition, the pre-alloyed powders are supersaturated with silicon in the aluminium matrix, which increased the hardness of the powders via solid solution hardening [165, 259]. Finally, porosity had an influence on the hardness of the material by increasing stress concentrations leading to facilitation of crack propagation [19, 23-25]. As porosity existed in the green compact, due to it being only 86.76 ± 1.16% of the theoretical density, it is likely that the presence of pores also lowered the hardness to below that of the starting powder.

The hardness of the cold compacted pure aluminium particles was ~39.8$HV_{2.5kg}$ for the coarse size range, ~44$HV_{2.5kg}$ for the medium size range and ~46$HV_{2.5kg}$ for the fine size range. These values are lower than that seen for the cold compacted bearing alloy hardness of ~61$HV_{2.5kg}$. One reason for this is that the average measured ECD of the bearing alloy particles is much smaller than that of the pure aluminium particles, which, according the to the Hall-Petch equation, means that the yield strength and hardness of the bearing alloy particles is higher due to restriction of movement of dislocations in the finer particles. Another reason is because of the addition of silicon and copper, which are supersaturated in the aluminium matrix, causing hardening by solid solution strengthening and thus increasing the hardness.

4.4.2. Sintering response – the effect of sintering temperature

4.4.2.1. Density

The density of the bearing alloy before and after sintering was shown in Table 4.16 and Table 4.19 respectively. The density of the cold compacted sample was 2.67 ± 0.04g/cm^3, which remained at 2.67 ± 0.01g/cm^3 after sintering at 500°C for 1h and decreased to 2.6 ± 0.01g/cm^3 after sintering at 550°C for 1h. As was illustrated in Figure 4.41, tin exuded out of the sample at the elevated sintering temperature of 550°C for 1h, whereas tin remained in the sample sintered at 500°C for 1h. The exuded tin meant that pores were left behind at the aluminium grain boundaries as shown in Figure 4.59, which reduced the density, whereas the tin remained in the sample sintered at 500°C for 1h and so the density was higher at this sintering temperature.

The reason that the tin was exuded out of the sample sintered at 550°C for 1h was due to the liquid being less viscous at this temperature compared to 500°C for 1h. It was discussed in section **2.3.3** that the wetting angle is important as it relates to the equilibrium between solid, liquid and vapour phases in sintering, shown in equation (2.4) [102, 103, 107]. Decreasing the contact angle between the liquid and the solid causes the liquid to spread and encourage capillary forces, which attract particles together and enhance the densification mechanisms. However, increasing the contact angle between the liquid tin and the solid aluminium particles causes the liquid to retreat from the solid and when the viscosity of the liquid was low enough, it was exuded out of the sample as was the case for the 550°C sintered sample [102, 103, 107].

Furthermore, the aluminium oxide layer has a negative effect on sintering as it prevents good wetting behaviour and as tin was unable to wet the aluminium, there was no improvement in density [102, 108, 109]. It was discussed in section **2.4.2.3** that tin prevents aluminium nitride formation as it moves to the surface of the aluminium particles. AlN creates a pressure difference between the pores and the gaps between the particles, which aids pore filling and it is likely that the formation of AlN was prevented, therefore the density did not improve [115, 156, 157].

4.4.2.2. Aluminium grain size

It could be argued that there is a slight increase in average aluminium particle ECD with sintering temperature from 9.83 ± 5.95µm and 12.77 ± 8.07µm in the longitudinal and transverse section respectively to 15 ± 8.62µm and 16.26 ± 8.38µm in the longitudinal and transverse section respectively of the samples sintered at 500°C 1h and 550°C for 1h respectively. It was discussed in section **2.3.7.5** that increasing sintering temperature causes the viscosity of the liquid phase to decrease, meaning that the rate of material transport is increased due to higher diffusion rates [141, 143, 144]. It is possible that in the 550°C sintered samples, the material from neighbouring aluminium grains is transported and deposited more rapidly, which lead to the marginal increases in grain size.

On the other hand, when comparing the sintered aluminium ECD to the cold compacted aluminium ECD in Table 4.17, they are within the spread of data for all samples where the cold compacted ECD is 12.43 ± 7.25µm and 13.9 ± 8.65µm in the longitudinal and transverse sections respectively, implying that the effect of sintering on the aluminium grain size was negligible. As mentioned in sections **2.3.3** and **4.4.2.1**, the wetting angle is significant for densification and causing particles to be attracted together. A high wetting angle caused the liquid tin to move away from the aluminium grains and, from Figure 4.54 and Figure 4.55 of the sample sintered at 500°C 1h and Figure 4.58 and Figure 4.59 of the sample sintered at 550°C 1h, the EDX images show that tin flowed out of the pre-alloyed powder particle and around the aluminium grain boundaries. Therefore, the tin was unable to wet the aluminium sufficiently, which did not break down the oxide layer and prevented the liquid phase sintering kinetics mentioned in section **2.3.4** from occurring [115, 156, 157].

4.4.2.3. Silicon growth

After sintering, discrete silicon particles were observed, which formed in and around the Al grains as shown in Figure 4.54 and Figure 4.55 of the sample sintered at 500°C 1h and Figure 4.58 and Figure 4.59 of the sample sintered at 550°C 1h. The growth of silicon from the Al-Si dendritic structure in the pre-alloyed starting particles is usually seen in heat treatments in both casting and P/M processing [145, 260, 261].

For the samples sintered at 500°C for 1h, the silicon particles grew to between 3.5µm ± 1.21 and 3.86µm ± 1.14 in the longitudinal and transverse sections respectively and after sintering at 550°C for 1h, they grew to between 4.89µm ± 1.96 and 5.52µm ± 2.19 in the longitudinal and transverse sections respectively. The driving force for the silicon particles to form in this way is to reduce the free energy and they form via Ostwald ripening, where the smaller particles grow at the expense of the larger ones, a phenomenon that has been observed during sintering of Al-Si alloys [102, 146, 262, 263]. The silicon particles appear to be slightly coarser in the sample sintered at 550°C for 1h compared to sintering at 500°C for 1h. The higher sintering temperature increases atomic activity, meaning that the silicon is able to move faster through the material and grow at a faster rate compared to the lower sintering temperature. Hence larger silicon sizes are seen at higher sintering temperatures [141, 143, 144].

4.4.2.4. Hardness

After sintering, the hardness of the compacts had decreased from the cold compacted hardness to between 33.68$HV_{2.5kg}$ ± 1.2 and 34.8$HV_{2.5kg}$ ± 0.99 in the longitudinal and transverse sections respectively of the samples sintered at 500°C for 1h and a further reduction to between 24.6$HV_{2.5kg}$ ± 1 to 26.3$HV_{2.5kg}$ ± 0.6 for the samples sintered at 550°C. Prior to sintering, the silicon was evenly dispersed throughout the pre-alloyed particle microstructure, which resulted in a high hardness value as a result of solid solution strengthening.

After sintering, this microstructure had been replaced by aluminium with tin located at the boundaries as well as formation of distinct silicon particles. Therefore, the solid solution hardening mechanism had been removed from the compact and thus reduced the hardness [102, 146, 262, 263].

Another factor contributing to the lower hardness was recovery and re-crystallisation effects, which was mentioned in section **4.2.4.3**. The powders absorb strain energy as they are plastically deformed in cold compaction, creating dislocations that become entangled thus increasing the hardness [190-192]. During heating, the thermal energy allows the atoms to move via the driving force of the strain energy [245, 250-252]. The entangled dislocations then become re-arranged into low-angle grain boundaries that are relatively free of dislocations, indicating recovery [245, 250-252].

The changes seen in the hardness are likely to be caused by re-crystallisation, where new, non-deformed grains nucleate and grow, reducing the dislocation density to the original value and reducing the hardness [245, 250-252]. Additionally, at 550°C the hardness was slightly lower than the samples sintered at 500°C due to a lower density. The tin was exuded out of the compacts at the higher temperature, leaving porosity where the tin was situated, thus decreased the hardness values [19, 23-25].

4.4.3. Sintering response – the effect of sintering time

4.4.3.1. Density

The density of the cold compacted sample was 2.67 ± 0.04g/cm^3, which remained at 2.67 ± 0.01g/cm^3 after sintering at 500°C for 1h and marginally decreased to 2.66 ± 0.01g/cm^3 after sintering at 500°C for 10h. The minimal change in density between 1h and 10h indicates that sintering for longer times does not provide any benefit towards densification of this alloy. As has been mentioned in sections **2.3.3** and **4.4.2.1**, the wetting angle is important as it relates to the equilibrium between the solid, liquid and vapour phases in sintering, which was shown in equation (2.4) [102, 103, 107]. The tin is unable to wet the aluminium grains as the oxide layer is a barrier to sintering therefore there is no densification of the alloy even with increased sintering time.

The effect of sintering time was described in section **2.3.7.4** and it is important to allow adequate time for sintering mechanisms to take place. The majority of densification occurs in the first 20 minutes, with longer times aiding further pore elimination [110]. Conversely, having too long a sintering time can lead to microstructural coarsening and decrease in the strength of the final sintered material [110]. However, there was no densification of the material after sintering for any length of time as a result of the tin being unable to wet the aluminium.

4.4.3.2. Aluminium grain size

Again, it could be argued that there is a slight increase in average aluminium ECD with sintering temperature from 9.83 ± 5.95μm and 12.77 ± 8.07μm in the longitudinal and transverse section respectively of the sample sintered at 500°C 1h to 13.48 ± 6.47μm and 15.32 ± 6.68μm in the longitudinal and transverse section respectively of the sample sintered at 500°C for 10h. This may be due to the 10h condition allowing more time for the transport of material from neighbouring aluminium grains, which lead to the marginal increases in grain size.

However, a similar observation to the comparison of sintering temperature was seen when evaluating the sintered aluminium ECD and the cold compacted aluminium ECD in Table 4.17. The measurements are within the spread of data for all samples where the cold compacted ECD is 12.43 ± 7.25µm and 13.9 ± 8.65µm in the longitudinal and transverse sections respectively, implying that the effect of sintering time on the aluminium grain size was also negligible. This has been attributed to a high wetting angle between the liquid tin and the solid aluminium particles, which caused the liquid to be pushed away from the aluminium grains. EDX of the sample sintered at 500°C for 1h in Figure 4.54 and Figure 4.55 and of the sample sintered at 500°C 10h in Figure 4.56 and Figure 4.57 show a very similar microstructure where tin flowed out of the pre-alloyed powder particle and around the aluminium grain boundaries. The tin was unable to wet the aluminium sufficiently regardless of sintering time and did not break down the oxide layer, which prevented the liquid phase sintering kinetics mentioned in section **2.3.4** from occurring [115, 156, 157].

4.4.3.3. Silicon growth

Silicon particles were also observed in and around the Al grains as shown in Figure 4.54 and Figure 4.55 of the sample sintered at 500°C 1h and Figure 4.56 and Figure 4.57 of the sample sintered at 500°C 10h. The growth of silicon from the Al-Si dendritic structure in the pre-alloyed starting particles is usually seen in heat treatments in both casting and P/M processing [145, 260, 261].

After sintering at 500°C for 1h, the silicon particles grew to between 3.5µm ± 1.21 and 3.86µm ± 1.14 in the longitudinal and transverse section respectively and after sintering at 500°C for 10h, they grew to between 4.5µm ± 1.15 and 4.3µm ± 1.41 in the longitudinal and transverse sections respectively. The driving force for the silicon particles to form in this way is to reduce free energy and they form via Ostwald ripening, where the smaller particles grow at the expense of the larger ones [102, 146, 262, 263]. The silicon particles appear to be slightly coarser in the sample sintered at 500°C for 10h compared to sintering at 500°C for 1h. Sintering for longer meant that there was more time for the silicon particles to move and coalesce as the free energy of the material is reduced. Hence a larger silicon size is seen at longer sintering times [140, 141].

4.4.3.4. Hardness

After sintering, the hardness of the compacts decreased from the cold compacted hardness to between 33.68$HV_{2.5kg}$ ± 1.2 and 34.8$HV_{2.5kg}$ ± 0.99 in the longitudinal and transverse sections respectively of the samples sintered at 500°C for 1h. There was a slight reduction to 32.43$HV_{2.5kg}$ ± 0.69 to 32.6$HV_{2.5kg}$ ± 0.71 in the longitudinal and transverse sections respectively for the samples sintered at 500°C for 10h. Prior to sintering, the pre-alloyed powders contained a dendritic Al-Si composition, which resulted in a high hardness value as a result of solid solution strengthening. However, after sintering, this dendritic microstructure had disappeared and been replaced by an aluminium matrix with tin located at the grain boundaries as well as dissolution and formation of silicon particles at boundaries. Therefore, the solid solution hardening mechanism had been removed from the compact and thus a lower hardness was observed [102, 146, 262, 263].

Similar to the discussion of the effect of sintering temperature, the lower hardness is likely to be a result of recovery and re-crystallisation effects, which was mentioned in section **4.2.4.3**. The dislocation accumulation from plastic deformation during compaction is removed when temperature is applied during sintering, which decreases the hardness to below that seen from cold compaction [245, 250-252]. At 500°C for 10h, the hardness was slightly lower than those samples sintered at 500°C for 1h due to a slightly lower density [19, 23-25].

4.4.4. Aluminium-copper precipitates

The EDX images revealed copper rich regions in all sintered conditions. This was expected as aluminium-copper precipitates commonly form in aluminium alloys containing small amounts of copper [150]. After silicon and tin have moved out of the original particles during sintering, the only phases left are copper and aluminium. From the magnified region of the Al-Cu phase diagram in Figure 4.92, it can be seen that at the sintering temperatures of 500°C and 550°C, the Al-1%Cu exists as a solid solution, given by α. There is a decrease in solid solubility of the α-phase (Al-1%Cu) as the temperature is decreased and once the temperature cools to below approximately 375°C, the Al-Cu (θ) precipitates form separately from the α-phase [220, 221, 253-255, 264]

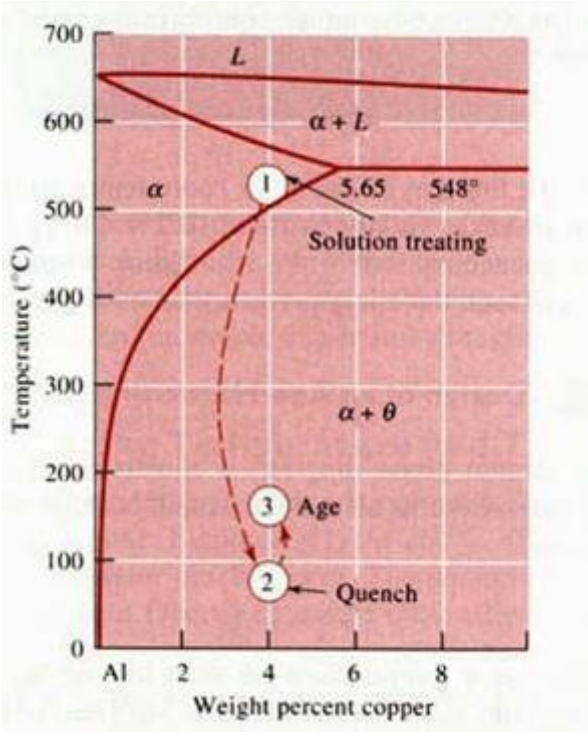

Figure 4.92: Magnified Al-Cu phase diagram [264]

4.4.5. ECAP response

4.4.5.1. Density

After one ECAP pass, the density had significantly improved from both sintering and cold compaction to approximately 3g/cm^3 for all ECAP samples as shown in Table 4.23. This is a result of the shear strain applied to the material as it is pushed through the die. The strain imposed caused severe plastic deformation of the softer aluminium particles and tin phases, leading to the closure of pores created from cold compaction [220, 221, 253-255].

As was mentioned in section **2.5.5** and **4.2.5.1**, the oxide layer was broken down as a result of the severe plastic deformation of the aluminium particles, which exposed fresh particle surfaces that bonded together with back pressure from the samples in the die [8, 70, 71, 76, 90]. In cold compaction, plastic deformation of the powder particles at contact points causes the particles to begin closing off the porous network until the compaction pressure is reached [220, 221, 253-255]. When severe plastic deformation occurs, the isolated porous networks are almost eliminated as the particles spread in to them, which subsequently leads to an increase in density [72, 73, 83]. The effect of sintering temperature and time prior to ECAP had no effect on the final density achieved after ECAP.

4.4.5.2. Macro and microstructure

After one pass of ECAP, the macro images revealed two distinct regions as shown in Figure 4.62 to Figure 4.64. This non-uniform microstructure showed; a reflective skin region where there were no elongated grains in the longitudinal sections of the samples and; a matte core region where EDX revealed the protrusion of fine ‘whiskers’ of tin in both longitudinal and transverse sections, with elongation of the aluminium particles in the longitudinal section.

The cause of these two regions can be attributed to the non-uniform densification resulting from the cold compaction stage. As mentioned in section **4.2.3**, more friction occurs at the die wall in compaction, leading to increased areas of porosity at the edges of the sample and higher density at the central core region [220, 221, 253-255]. Sintering did not have a significant influence on the homogenisation of the microstructure after one pass of ECAP, therefore the two distinct regions remained.

In the longitudinal section of each sample processed by ECAP, the core region showed elongation of aluminium grains, indicating that they underwent severe plastic deformation. However, in the skin region, this was not the case as the particles seemed to be relatively equiaxed, indicating that the strain from ECAP caused pore closure and densification. Despite the different regions after ECAP, a reduction in the ECD of all the pre-sintered samples was seen in the transverse sections, which is expected due to the severe plastic deformation imposed on them [4, 79, 265].

The protrusion of tin in the core region can be explained by the increase of internal stresses resulting from the deformation and elongation of the aluminium grains compared to the skin region. These internal stresses were higher in the matte region than the reflective region. Tin is softer and more ductile than aluminium and it surrounded the aluminium grain boundaries after sintering. When ECAP was applied, the internal stresses increased due to the aluminium grains deforming in the matte region, therefore when the samples were sectioned, the tin moved to the outside of the surface [191, 192]. These tin whiskers did not appear in the reflective region of the sample as there was less deformation at the skin due to frictional effects. It should also be noted that these tin protrusions could be wiped away without reoccurrence even after polishing.

The ECD of the silicon particles sizes were not significantly reduced after one pass of ECAP for all pre-sintered samples, which indicates a resistant to fracture. This is expected as the silicon phase is a harder material and the SEM and EDX analysis indicates that ECAP caused the softer aluminium and tin phases to deform around the harder silicon phase.

4.4.5.3. ECAP Hardness

After one pass of ECAP, the hardness of the samples was higher than that observed for the sintered compacts. Furthermore, the hardness in the core region of the sample was slightly increased although the difference is not so significant in the samples pre-sintered at 500°C 10h. This higher hardness in the core region compared to the skin region is due to the higher deformation seen in the aluminium particles. A reduction in grain size via severe plastic deformation causes an increase in hardness by restricting the movement of dislocations [115, 158].

One possibility for the hardness of the sample pre-sintered at 500°C for 10h not varying as much as the other pre-sintered samples between the core and skin region is that the time was longer for the tin to be more homogenously distributed throughout the compact during sintering. This would cause a slightly more uniform microstructure and when comparing the grain sizes in the core and skin region of the 500°C 10h ECAP sample, there is very little difference between the length, width and ECD in the longitudinal section.

5. CONCLUSIONS & FUTURE WORK

5.1. Conclusions

ECAP has been demonstrated to consolidate pure aluminium and aluminium bearing alloy powders with grain refinement and improvements in density and hardness after one pass as a secondary process.

Cold compaction produces a non-uniform distribution of density, with a more porous region on the outside of the samples as a result of increased die wall friction.

Solid state sintering of pure aluminium is not effective for densification due to the oxide layer preventing adequate particle to particle contact. ECAP caused elongation of the grains in the longitudinal section and a relatively equiaxed microstructure in the transverse section. The grains were refined and density and hardness was increased.

For the Al-20Sn-7Si-1Cu material, sintering at 500°C between 1 and 10 hours did not improve density as the liquid tin is unable to wet the aluminium. Instead it remained at the particle boundaries, weakened the material and did not homogenise the microstructure. Increasing sintering temperature to 550°C for 1h only caused the liquid tin to be exuded from the sample due to lower viscosity at higher temperatures. Silicon particles developed from the pre-alloyed powder into sizes between 3-5µm due to Ostwald Ripening.

After ECAP, there were two distinct regions; a denser, deformed core region and a more equiaxed skin region. The core region had tin whiskers protruding from the surface and the skin region showed pore closure.

5.2. Future work

Developing the Al-20Sn-7Si-1Cu alloy would be essential so that liquid phase sintering can be optimised. Research of alloying additions such as magnesium to break down the aluminium oxide layer and aid sintering would be beneficial for this alloy. Also, investigating the effects of sintering temperature and time would provide more insight in to how the behaviour of the alloy changes under these conditions. Quenching could also be applied to the alloys to see if Al-Cu precipitates form during cooling at slow rate or if they can be prevented using high cooling rates. Varying the amount of magnesium in the Al-20Sn-7Si-1Cu-xMg to optimise the properties of the sintered alloy could be another future investigation.

Other powder consolidation methods such as cold isostatic pressing and hot isostatic pressing could be considered. These processes might overcome density variation from uni-axial compaction, which would help in optimising the final mechanical properties and microstructures in this particular alloy. Also applying these methods to the alloy with the addition of magnesium for comparative purposes would be beneficial.

The scaling up of ECAP has been mentioned in the literature review section. Another potential study would be to scale up ECAP of this and the magnesium containing alloy to an industrial level, where larger parts, up to 40-60mm diameter, can be passed and then machined afterwards. This would require careful die design to ensure longevity of parts.

6. APPENDIX

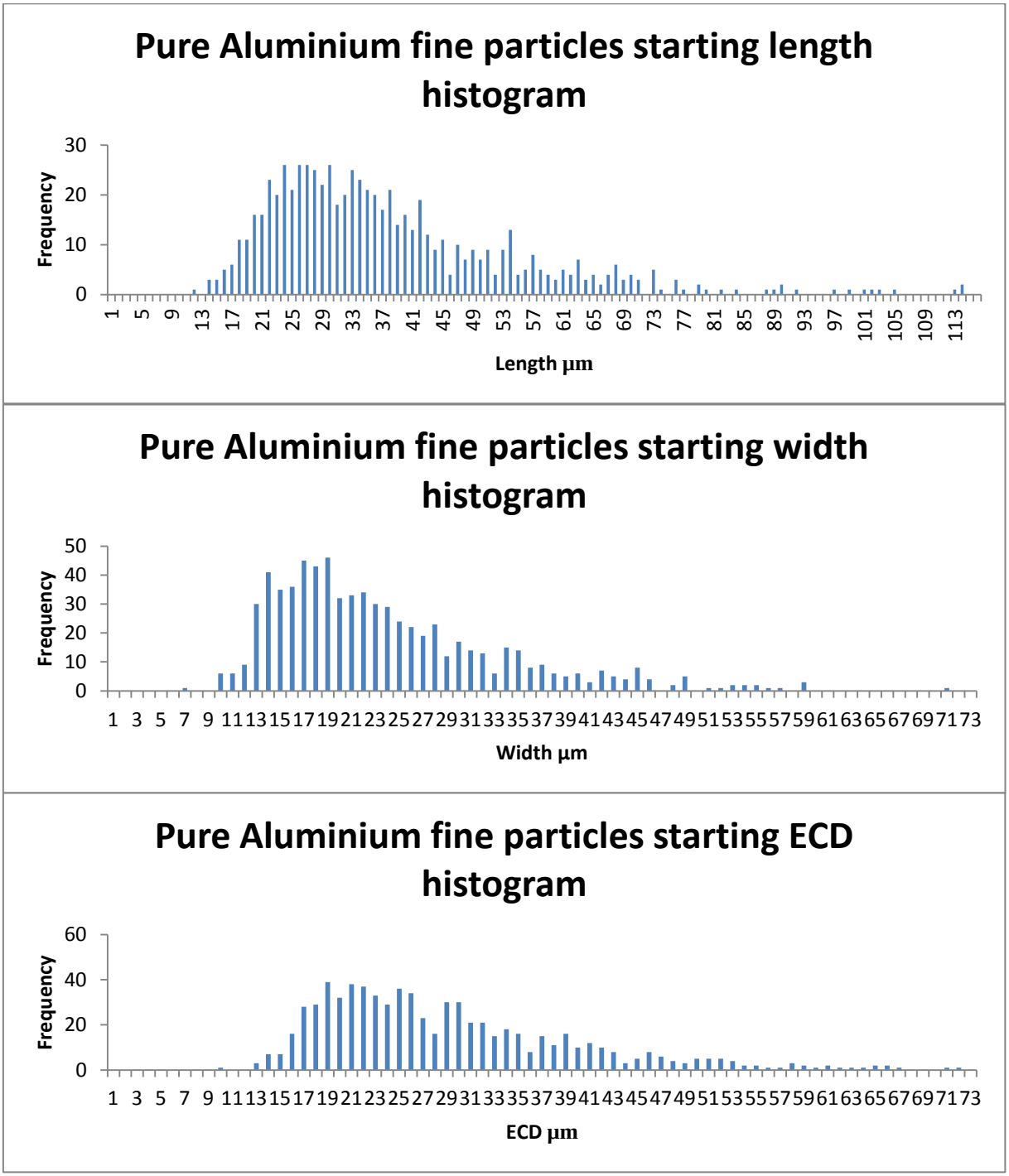

Appendix 6-1: Length, width and ECD histograms for the pure aluminium fine starting powder

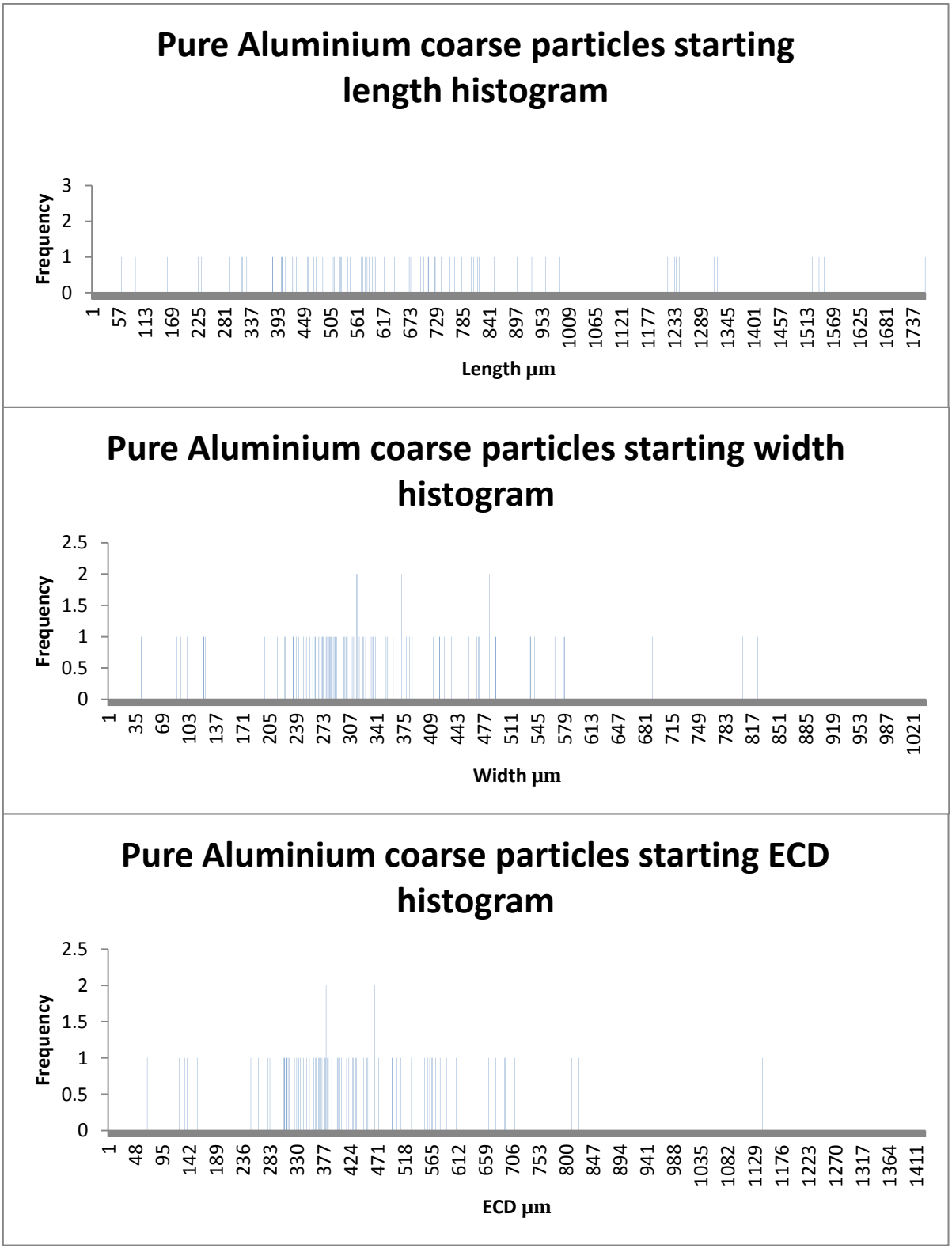

Appendix 6-2: Length, width and ECD histograms for the pure aluminium coarse starting powder

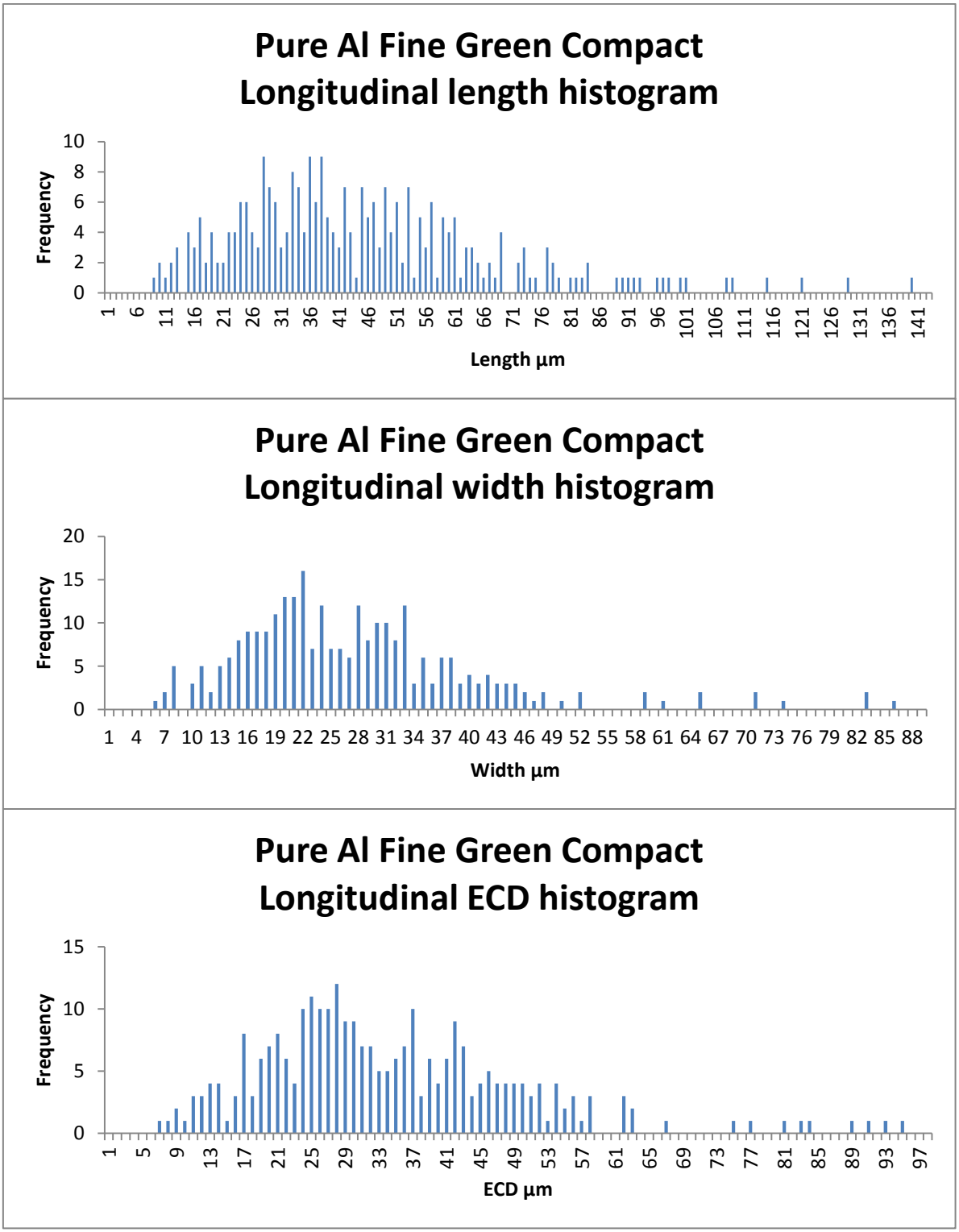

Appendix 6-3: Histograms for length, width and ECD of the pure aluminium fine particles in the longitudinal section

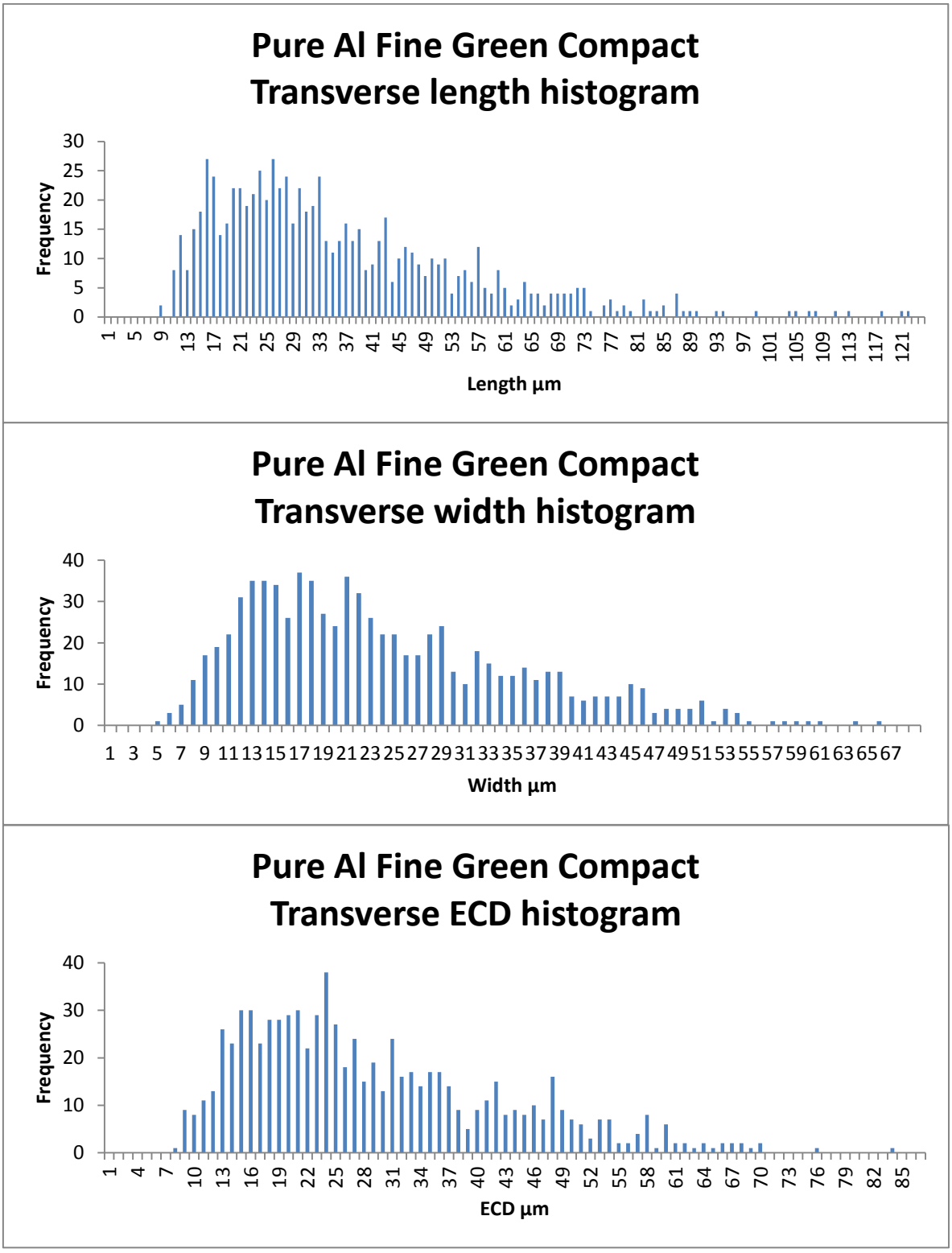

Appendix 6-4: Histograms for length, width and ECD of the pure aluminium fine particles in the transverse section

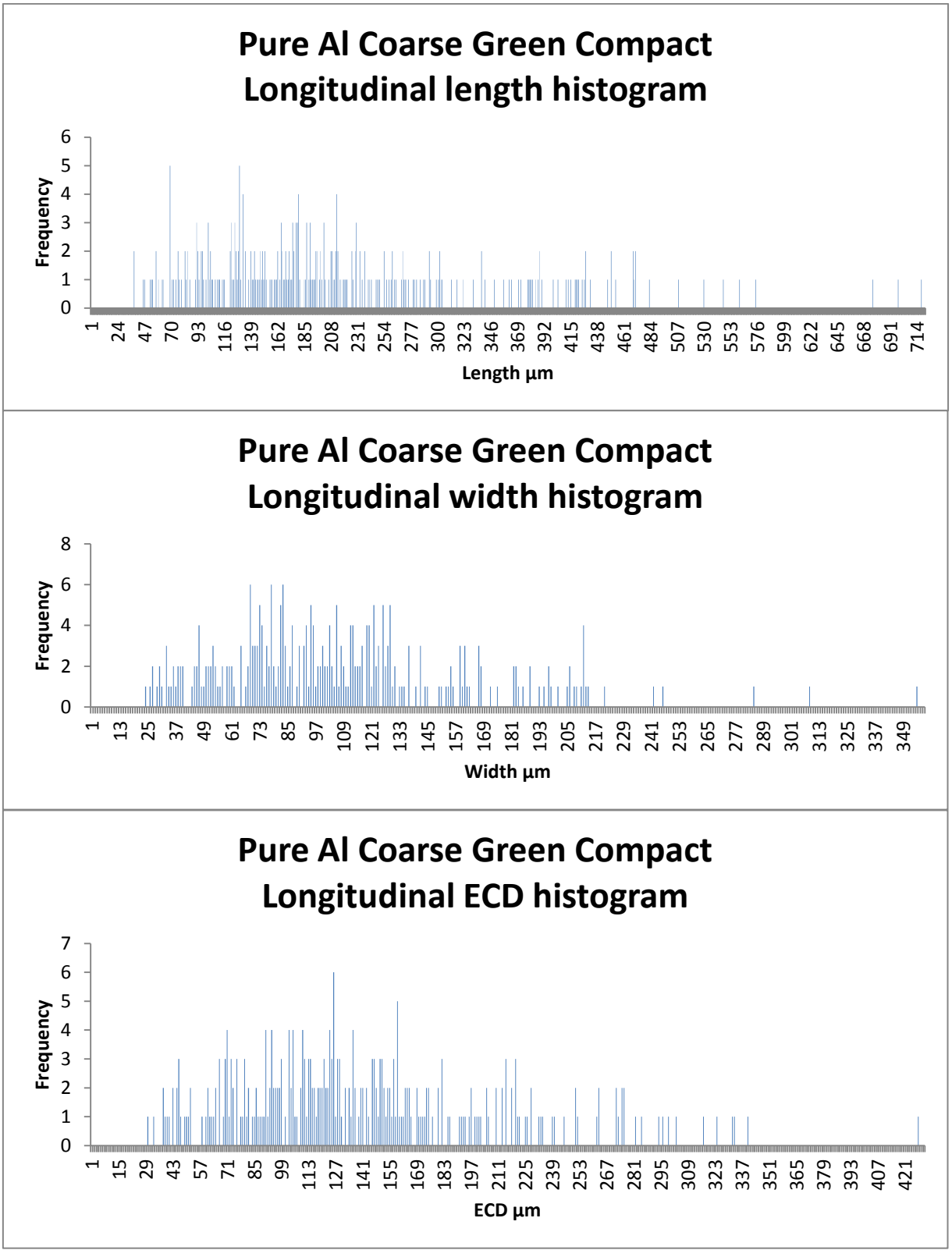

Appendix 6-5: Histograms for length, width and ECD of the pure aluminium coarse particles in the longitudinal section

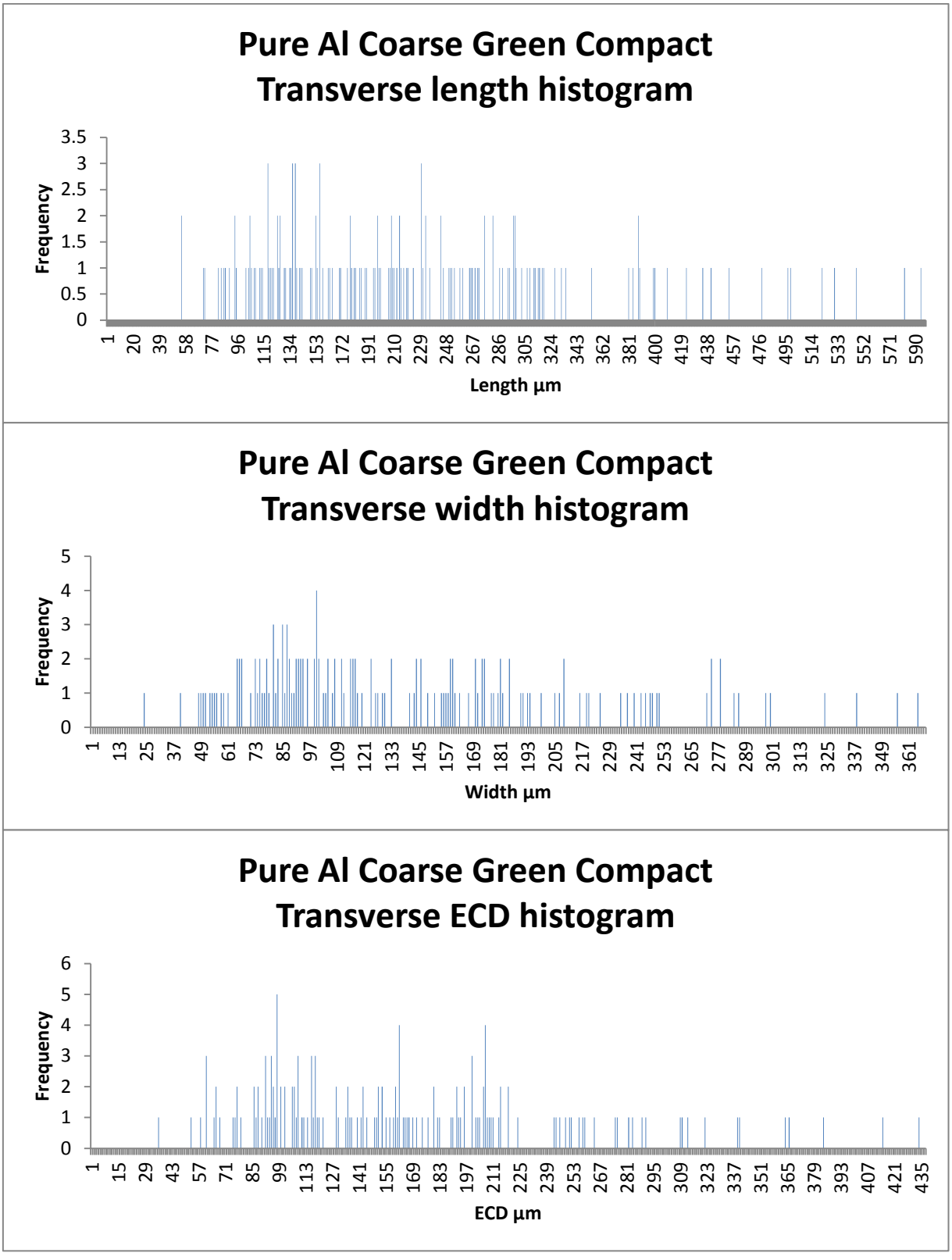

Appendix 6-6: Histograms for length, width and ECD of the pure aluminium coarse particles in the transverse section

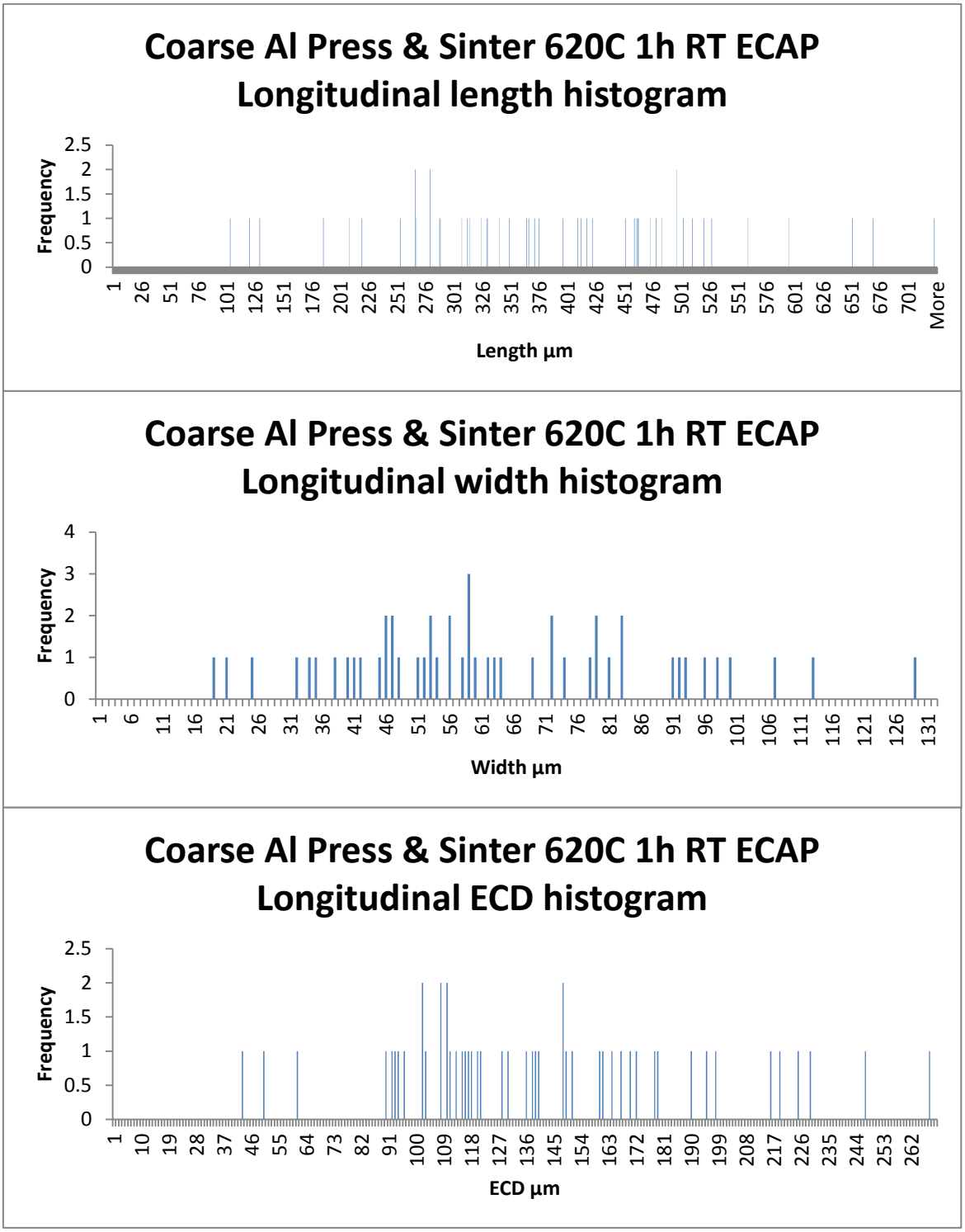

Appendix 6-7: Longitudinal length, width and ECD histograms for the coarse aluminium particles pre-sintered at 620C 1h after one pass of ECAP

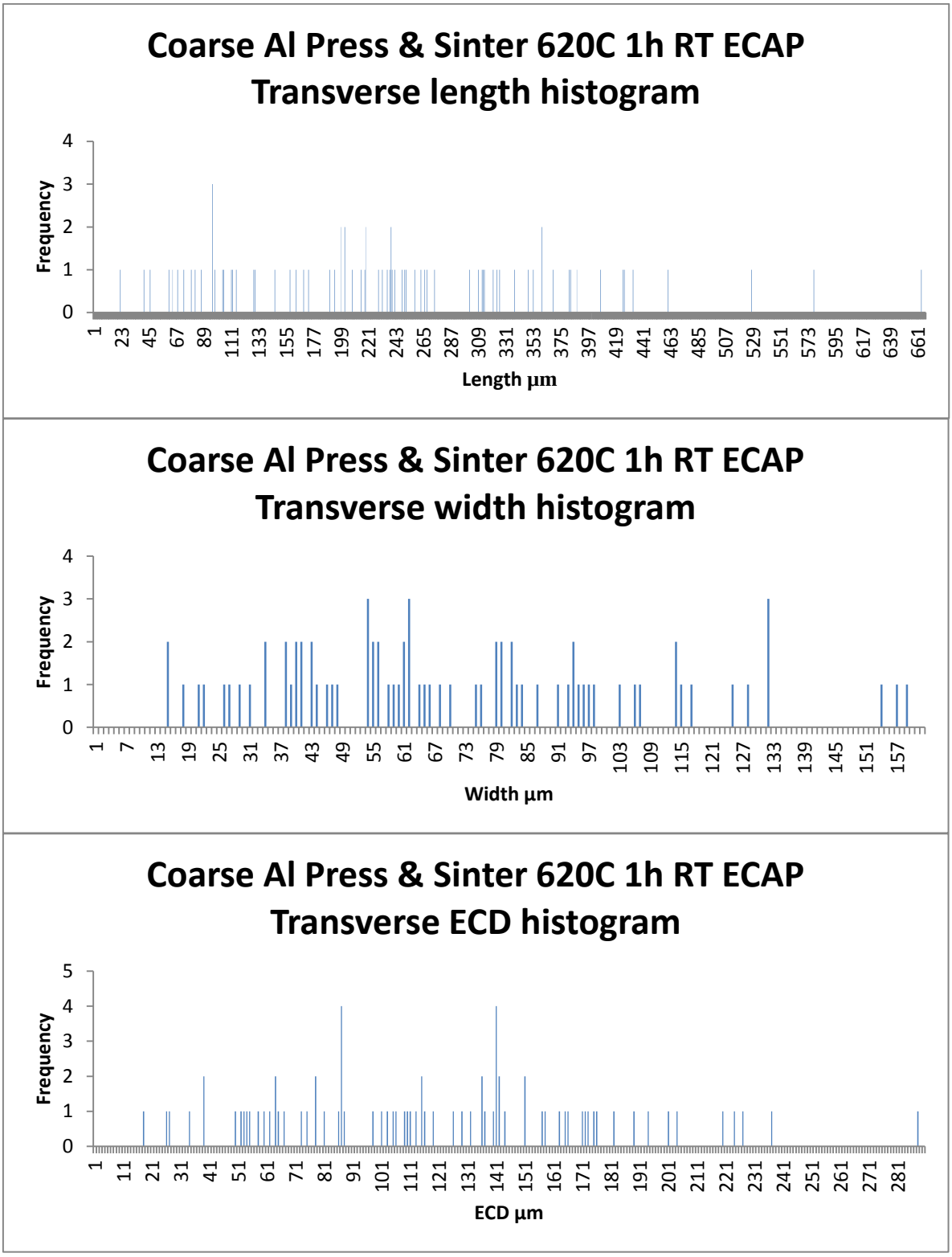

Appendix 6-8: Transverse length, width and ECD histograms for the coarse aluminium particles pre-sintered at 620C 1h after one pass of ECAP.

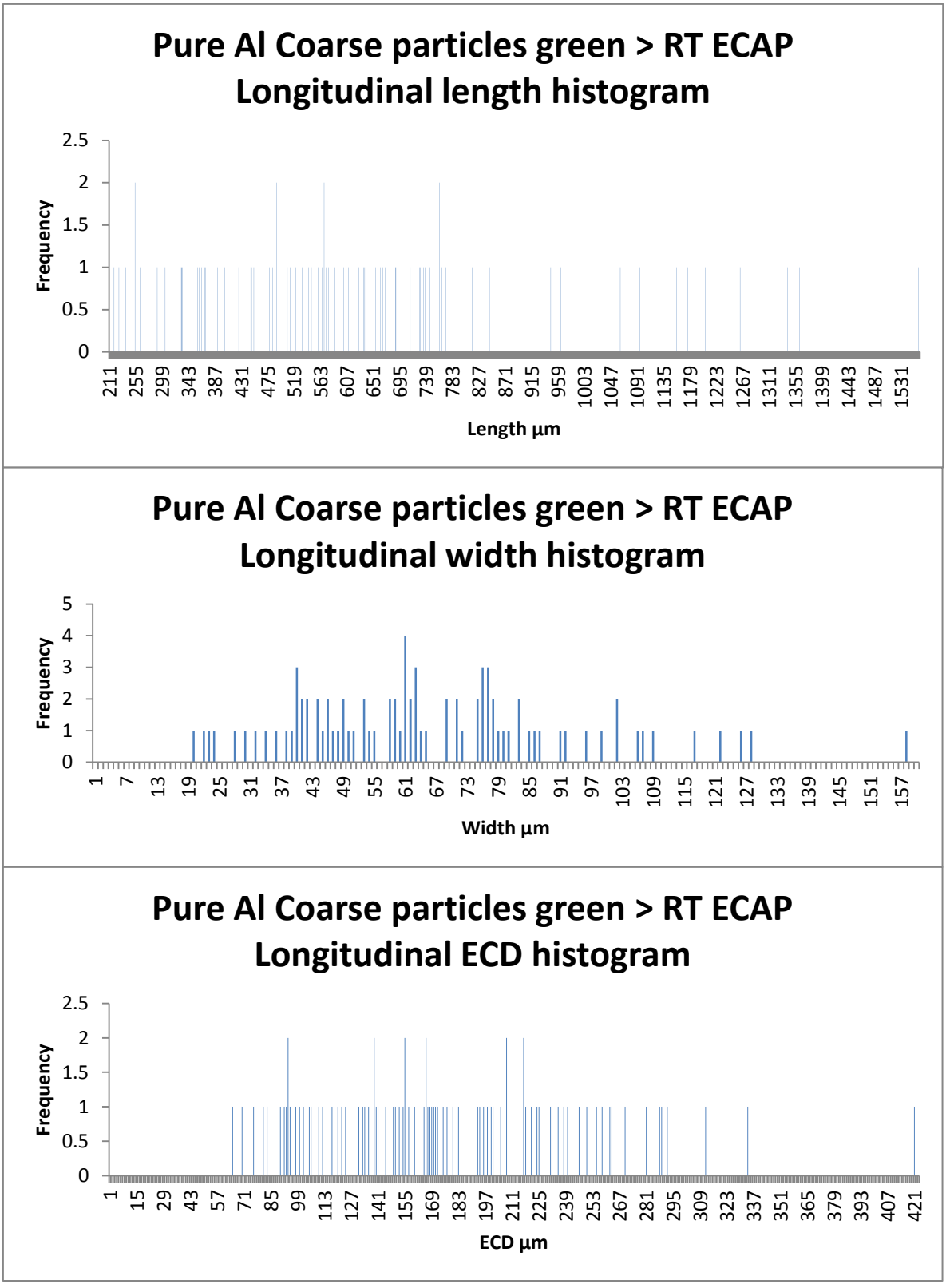

Appendix 6-9: Longitudinal length, width and ECD histograms for the coarse aluminium particles pre-compacted then subject to one pass of ECAP.

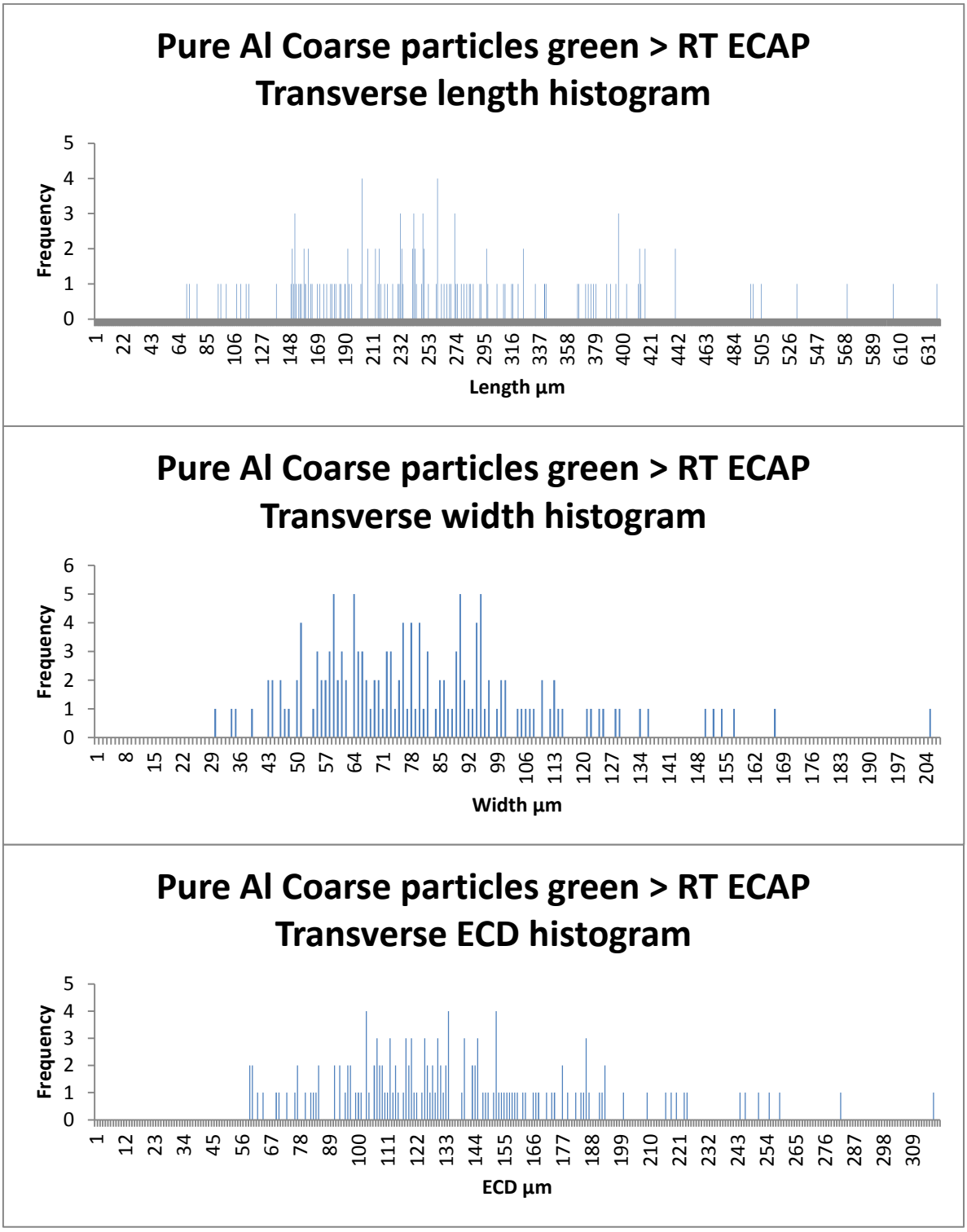

Appendix 6-10: Longitudinal length, width and ECD histograms for the coarse aluminium particles pre-compacted then subject to one pass of ECAP.

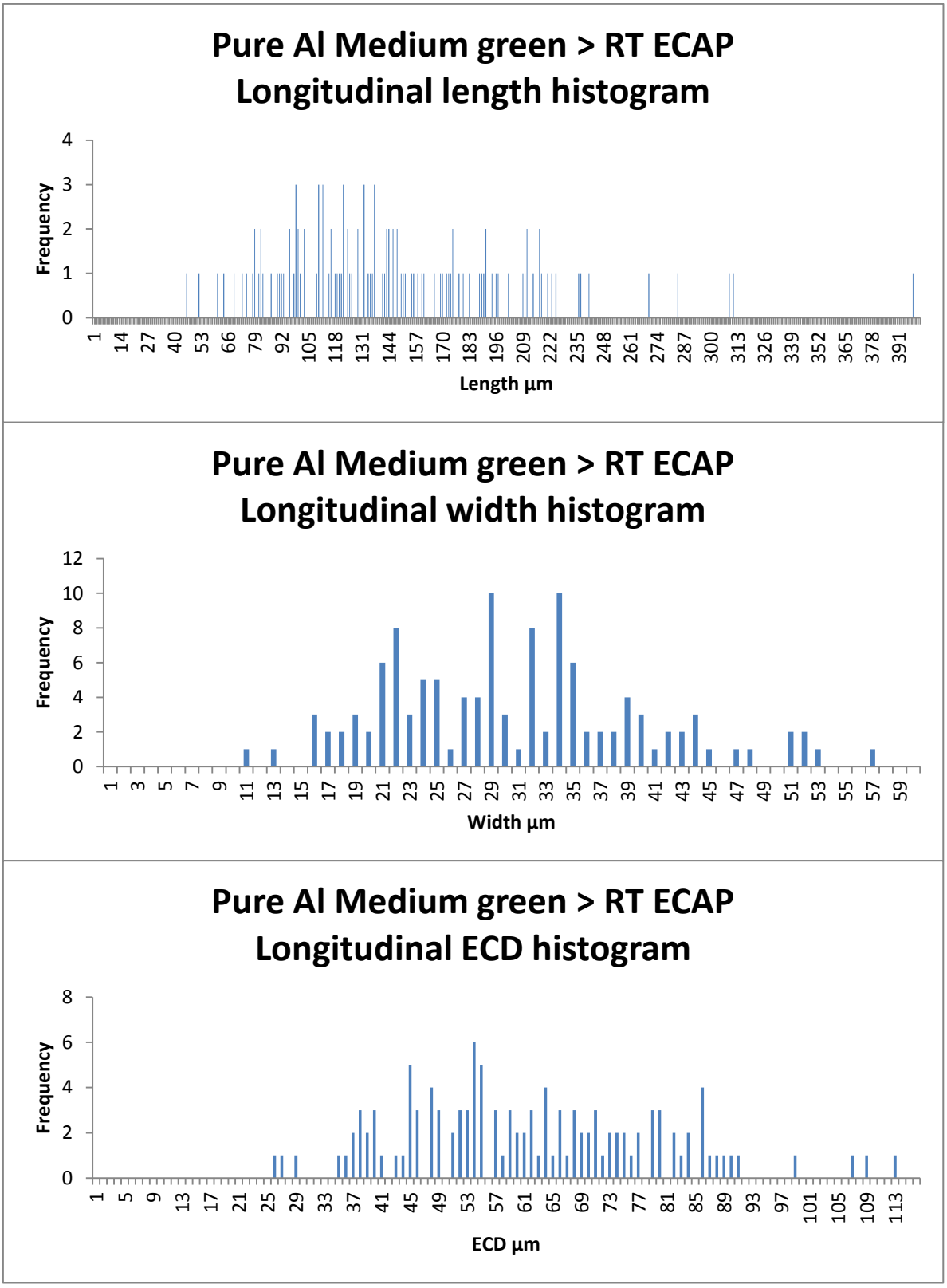

Appendix 6-11: Longitudinal length, width and ECD histograms for the medium aluminium particles pre-compacted then subject to one pass of ECAP.

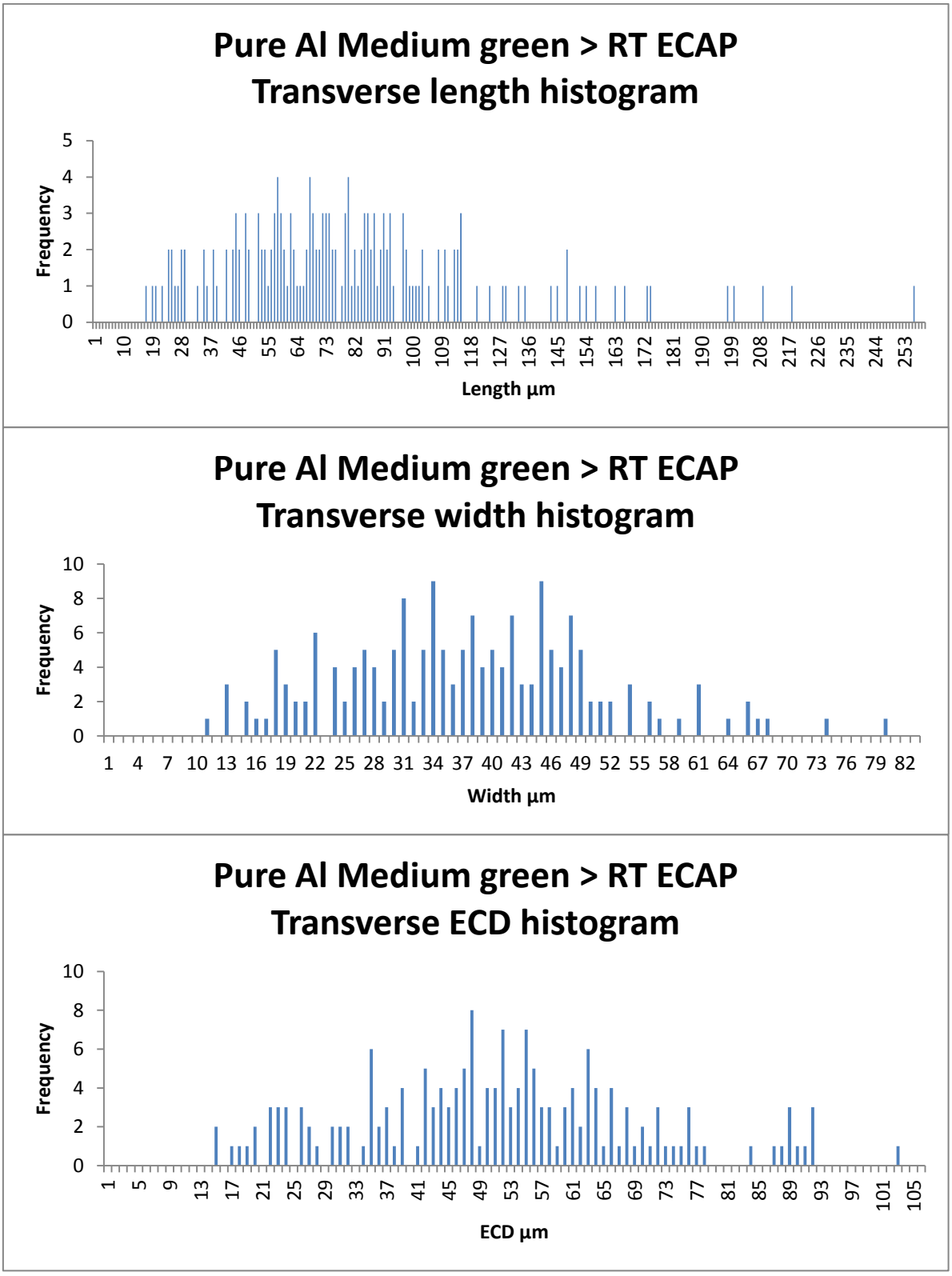

Appendix 6-12: Transverse length, width and ECD histograms for the medium aluminium particles pre-compacted then subject to one pass of ECAP.

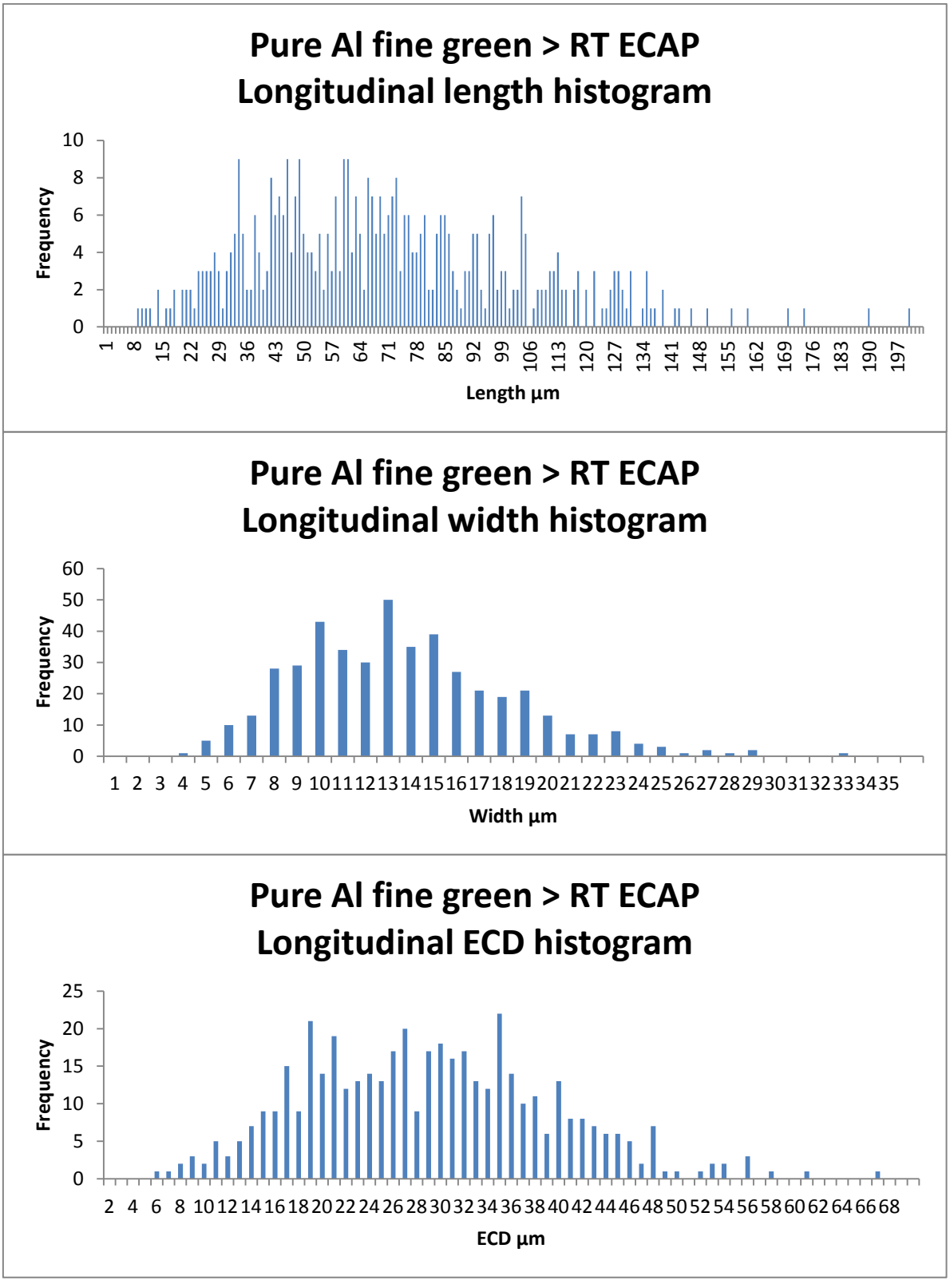

Appendix 6-13: Longitudinal length, width and ECD histograms for the fine aluminium particles pre-compacted then subject to one pass of ECAP.

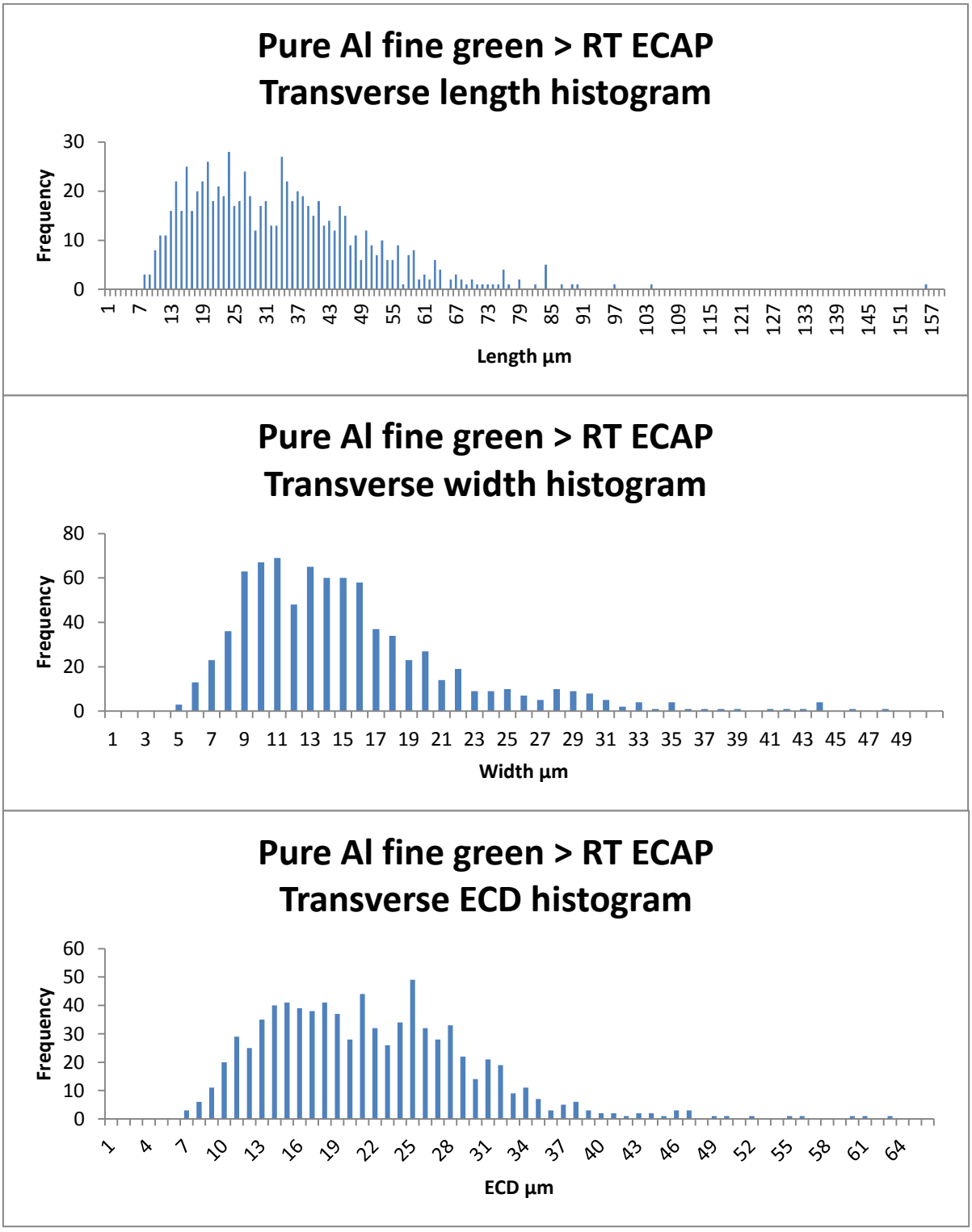

Appendix 6-14: Transverse length, width and ECD histograms for the fine aluminium particles pre-compacted then subject to one pass of ECAP.

Appendix 6-15: Calculation of theoretical density

Using equation (6.1), the density of the alloy can be calculated:

$$\rho = \frac{m}{v} \tag{6.1}$$

Where ρ is the density, m is the mass and v is the volume. For a mass of 100g, the volume can be worked out from the densities of the alloying elements shown Appendix Table 1.

Appendix Table 1: Mass and density of given elements in the Al-20Sn-7Si-1Cu pre-alloyed powder.

Mass	Density
$m_{aluminium}$ = 72g	$\rho_{aluminium}$ = 2.7g/cm^3
m_{tin} = 20g	ρ_{tin} = 7.365 g/cm^3
$m_{silicon}$ = 7g	$\rho_{silicon}$ = 2.329 g/cm^3
m_{copper} = 1g	ρ_{copper} = 8.94 g/cm^3

The total volume of the alloy can be calculated as follows:

$$v = \frac{m}{\rho} = \frac{72}{2.7} + \frac{20}{7.365} + \frac{7}{2.329} + \frac{1}{8.94}$$

$$\therefore v = 26.\dot{6} + 2.716 + 3.01 + 0.11$$

$$\therefore v = 32.51 cm^3$$

$$\rho = \frac{100}{32.51}$$

This gives a theoretical density for the Al-20Sn-7Si-1Cu alloy of 3.08g/cm^3.

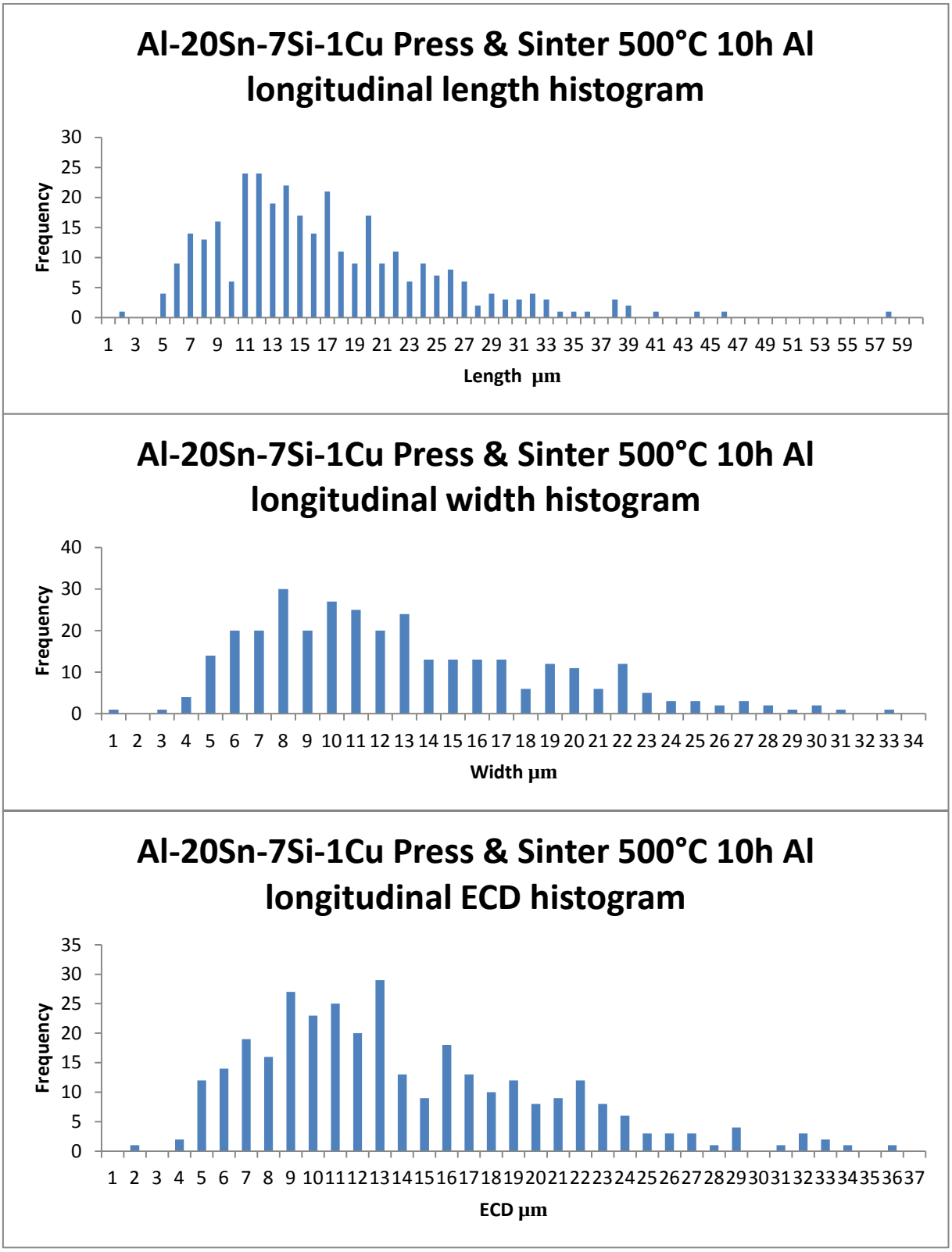

Appendix 6-16: Histograms for the length, width and ECD of the aluminium grains of the longitudinal section of samples sintered at 500C for 10h.

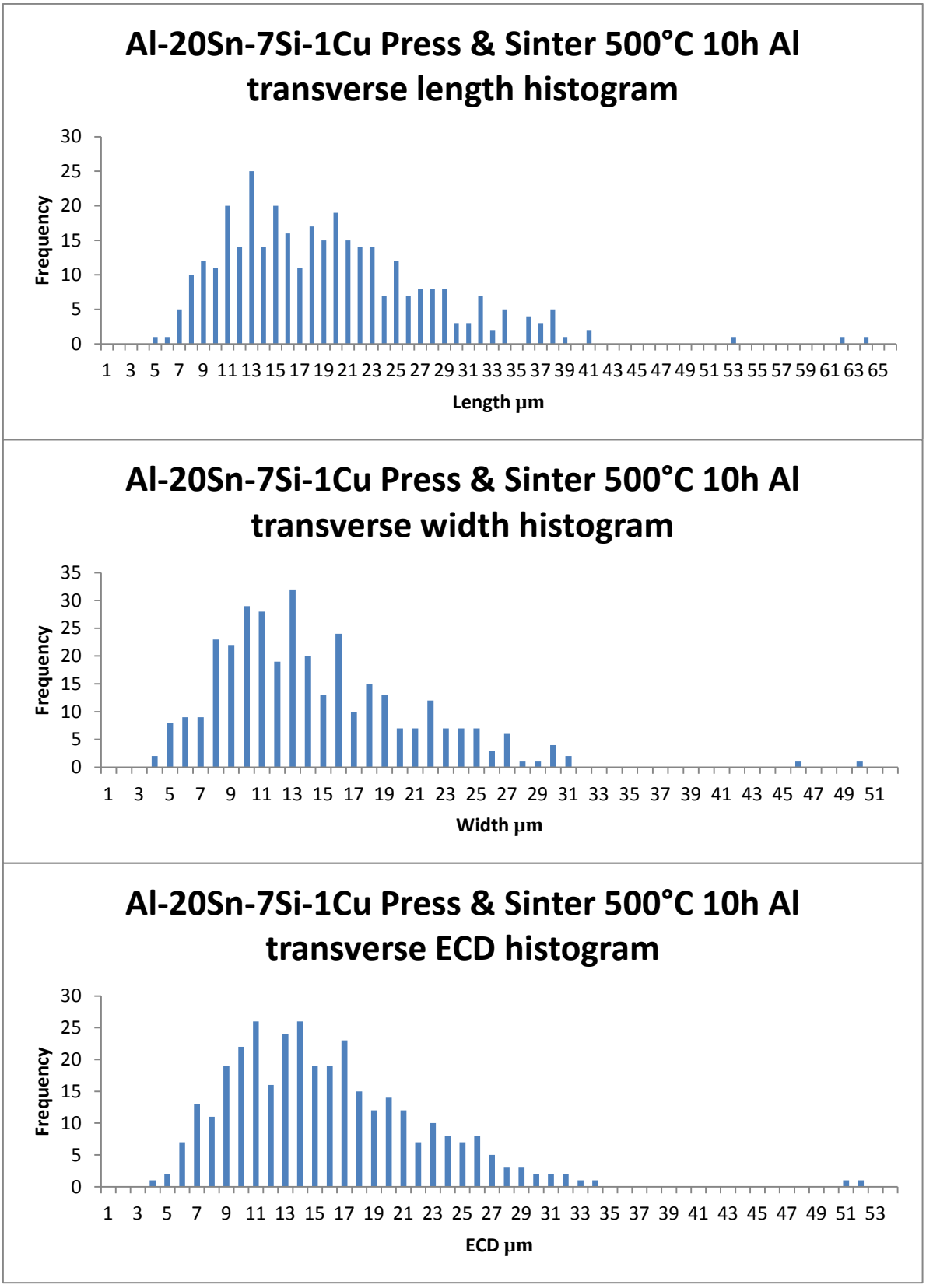

Appendix 6-17: Histograms for the length, width and ECD of the aluminium grains of the transverse section of samples sintered at 500C for 10h.

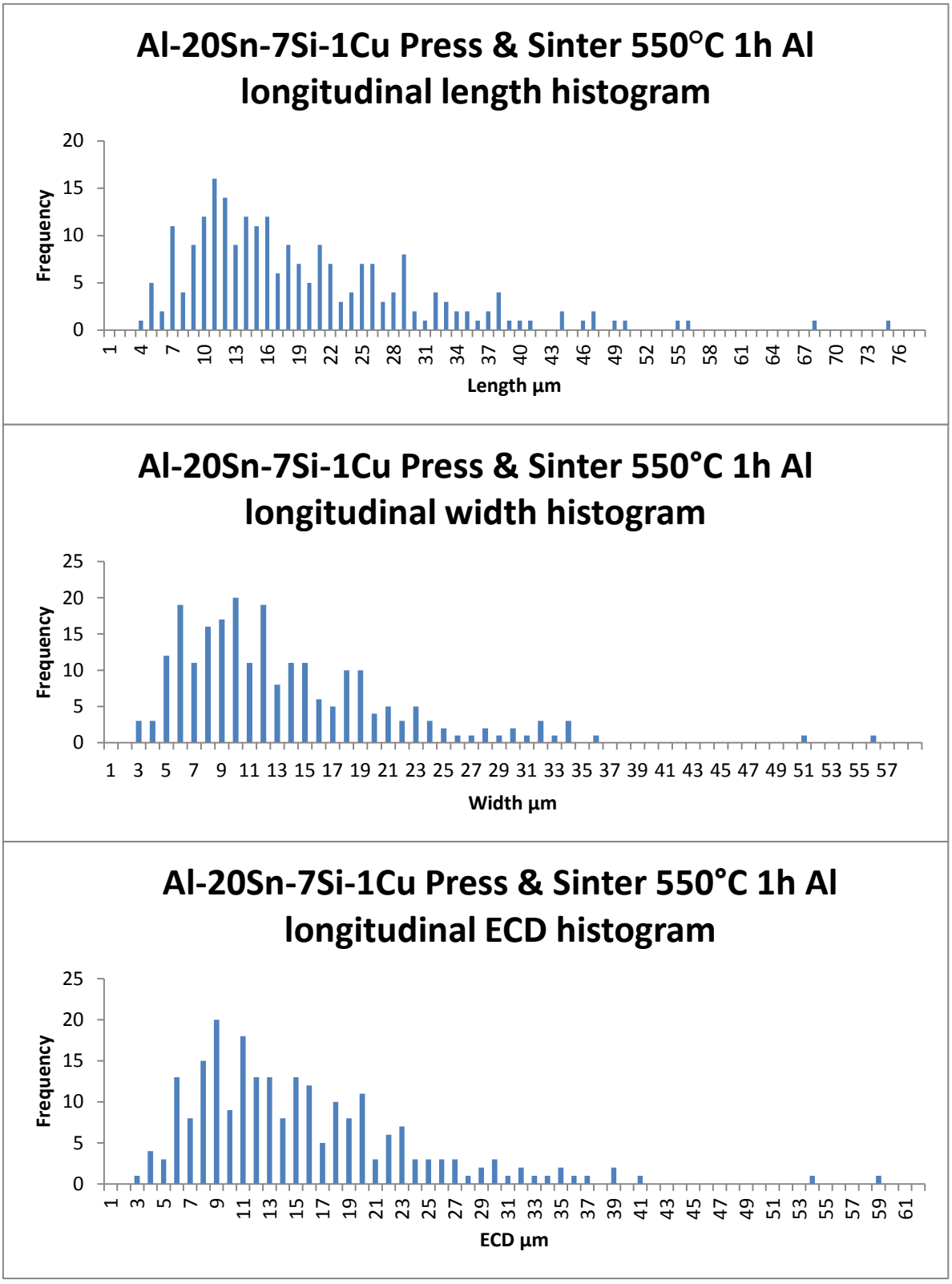

Appendix 6-18: Histograms for the length, width and ECD of the aluminium grains in the longitudinal section of samples sintered at 550C for 1h.

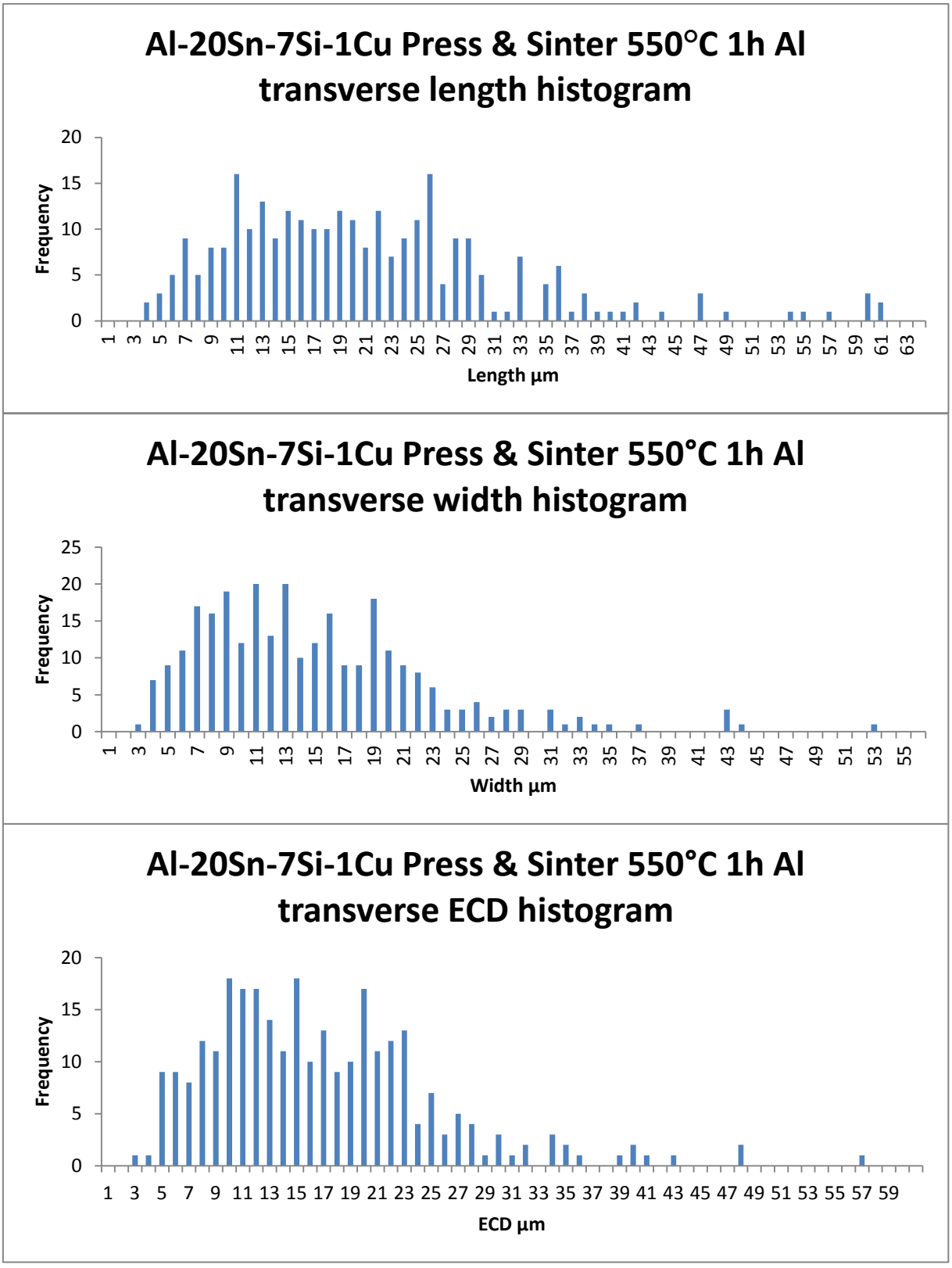

Appendix 6-19: Histograms for the length, width and ECD of the aluminium grains in the transverse section of samples sintered at 550C for 1h.

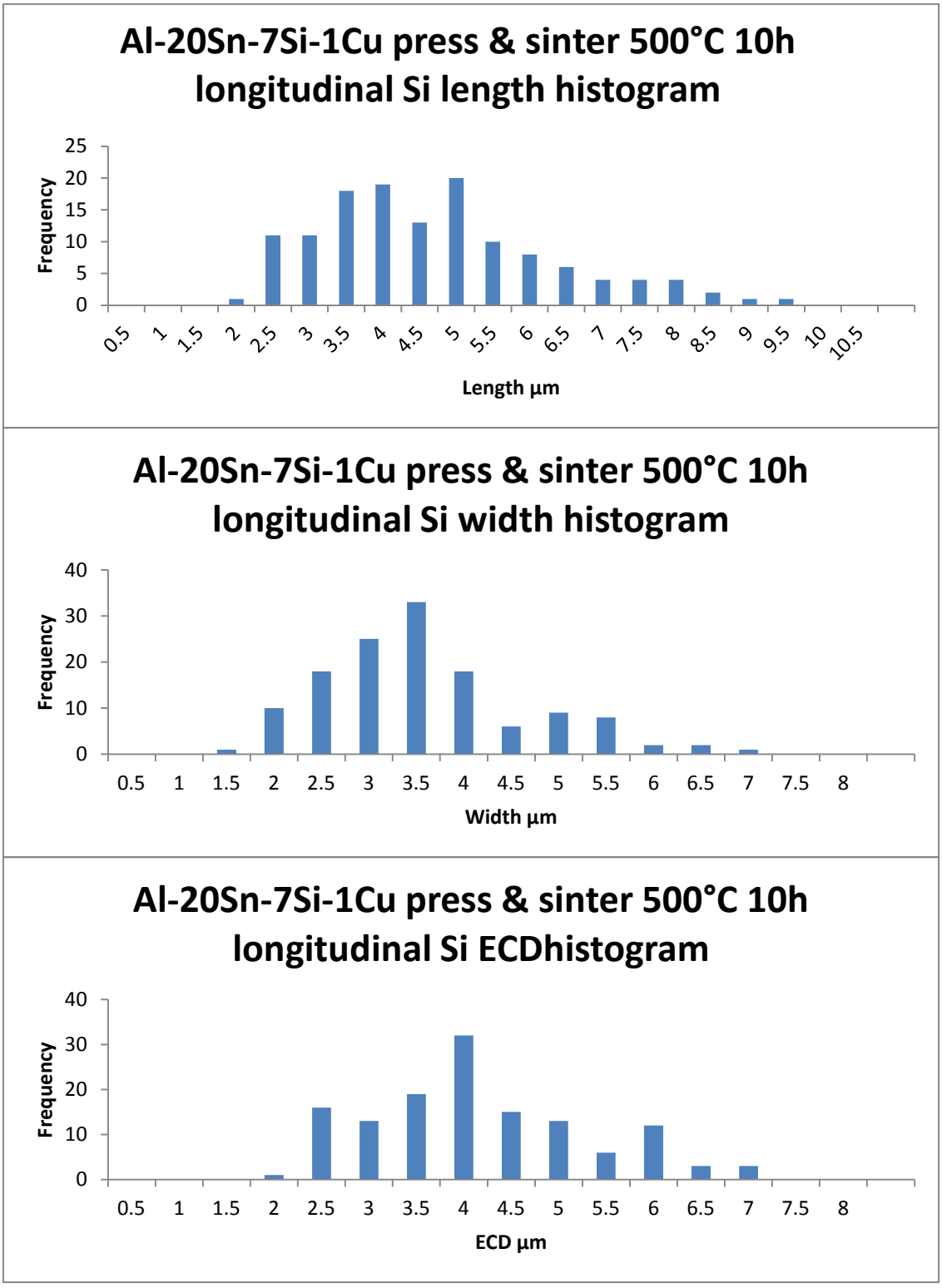

Appendix 6-20: Histograms for the length, width and ECD of the silicon particles in the longitudinal section of samples sintered at 500C for 10h.

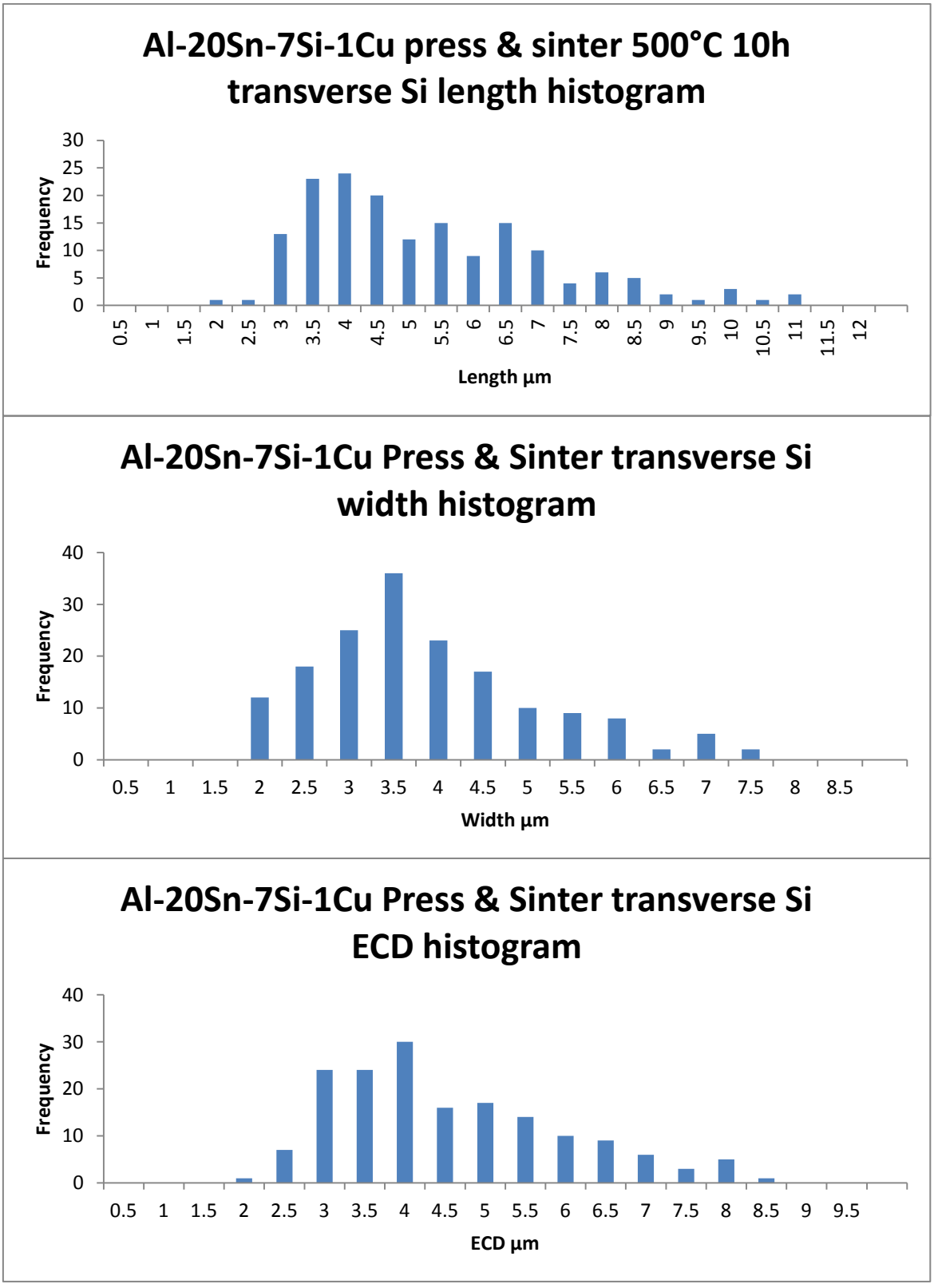

Appendix 6-21: Histograms for the length, width and ECD of the silicon particles in the transverse section of samples sintered at 500C for 10h.

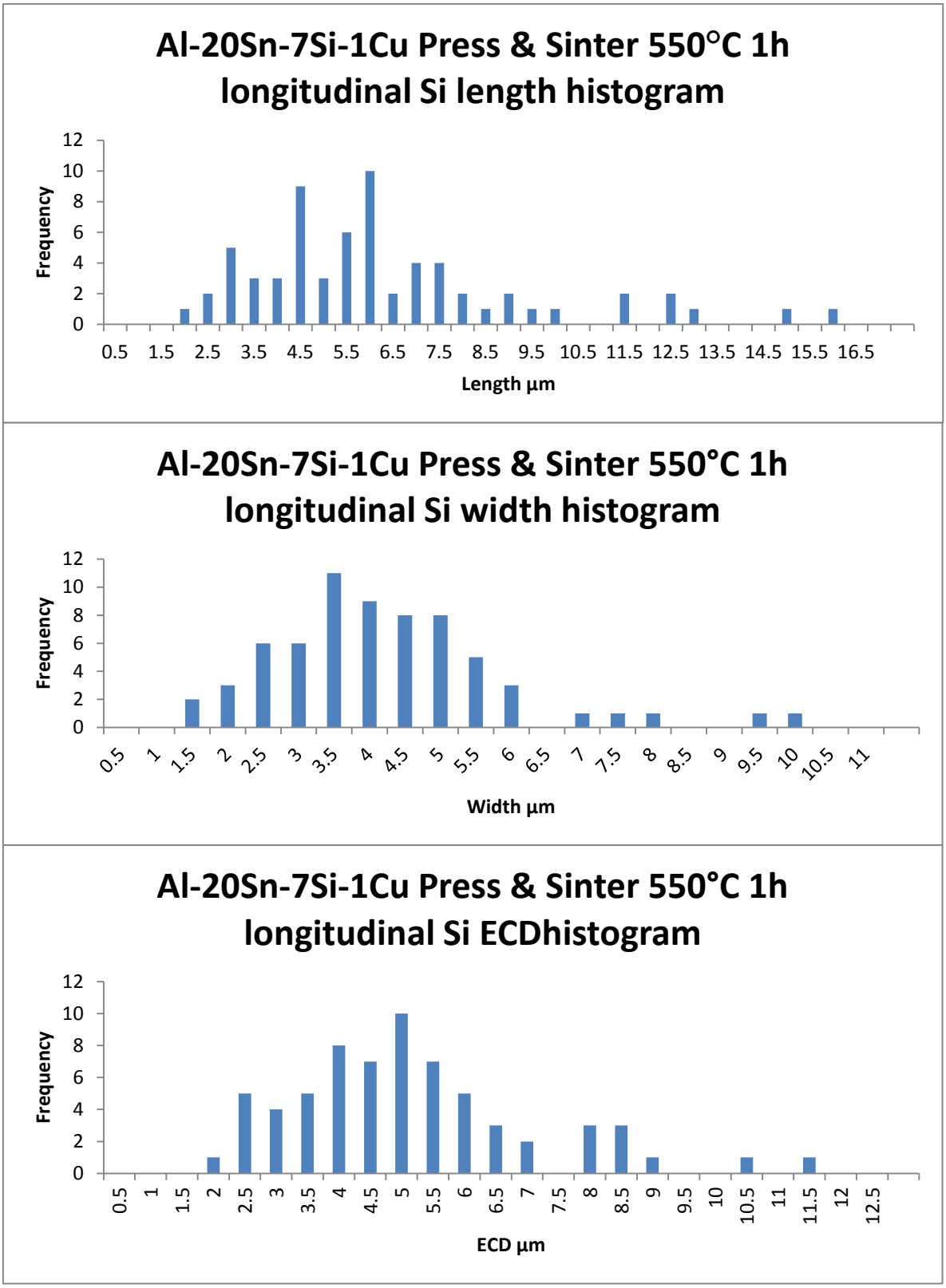

Appendix 6-22: Histograms for the length, width and ECD of the silicon particles in the longitudinal section of samples sintered at 550C for 1h.

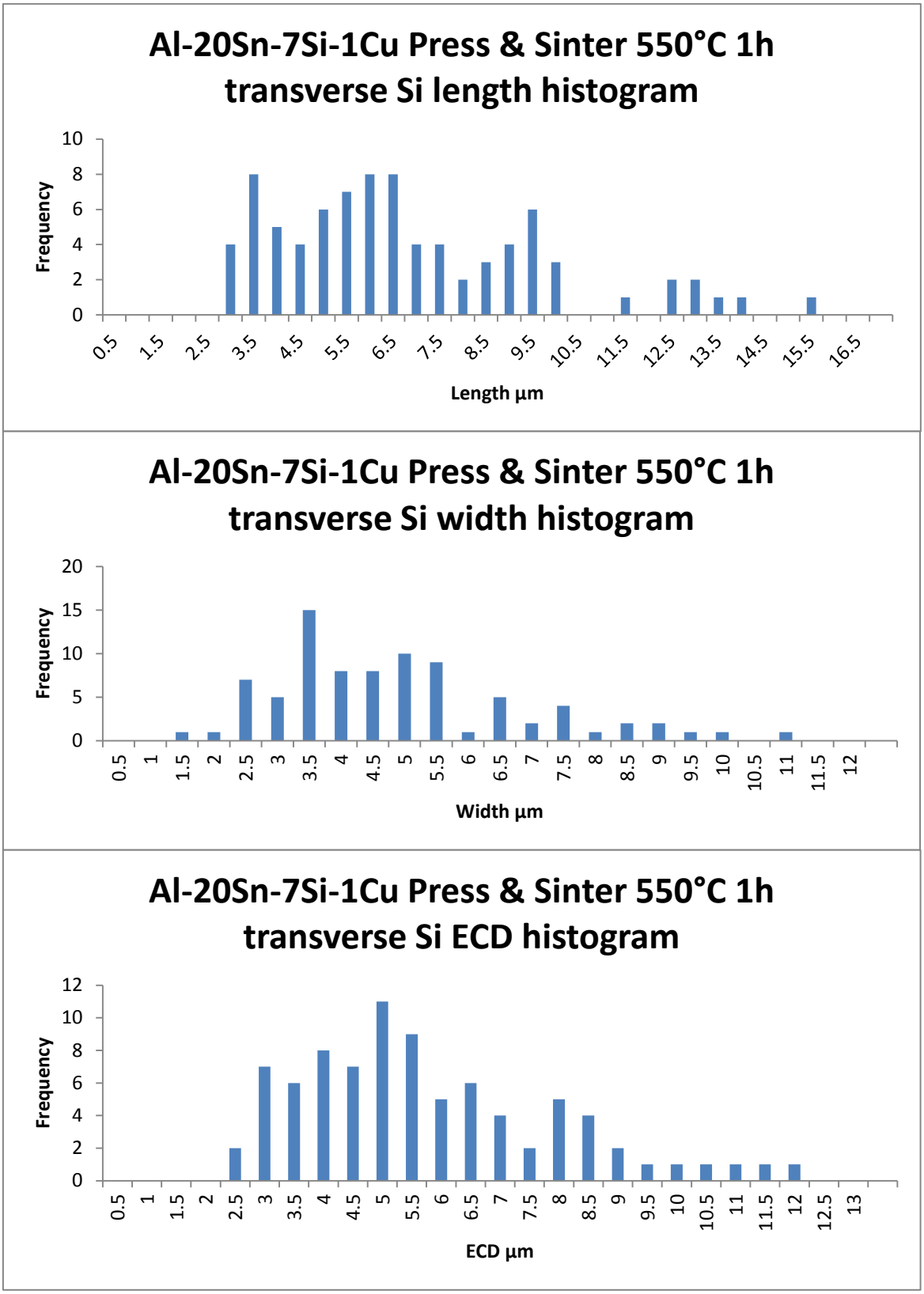

Appendix 6-23: Histograms for the length, width and ECD of the silicon particles in the transverse section of samples sintered at 550C for 1h.

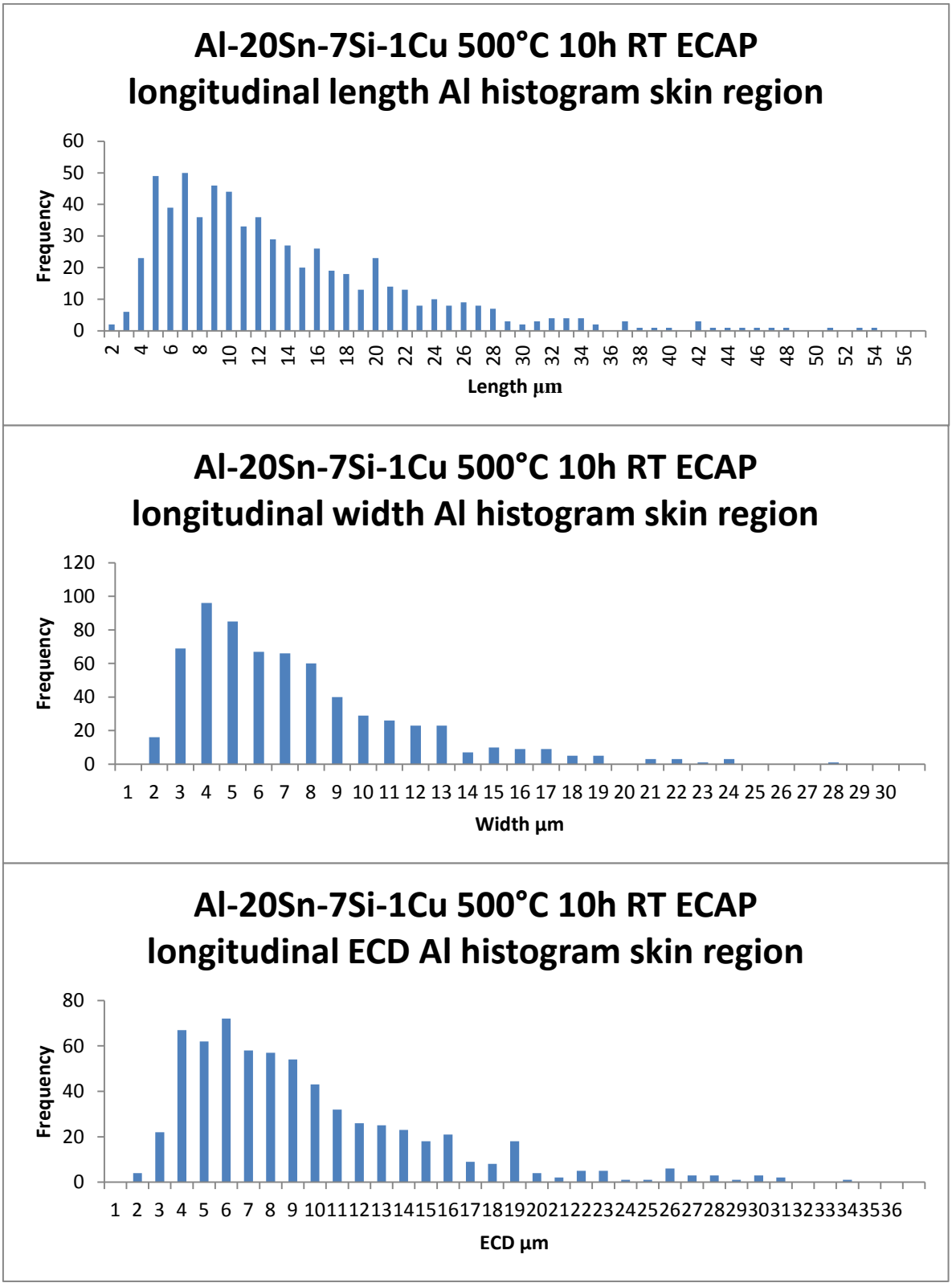

Appendix 6-24: Histograms for length, width and ECD of the aluminium grains in the longitudinal section of the skin region of the samples pre-sintered at 500°C 10h and subject to ECAP.

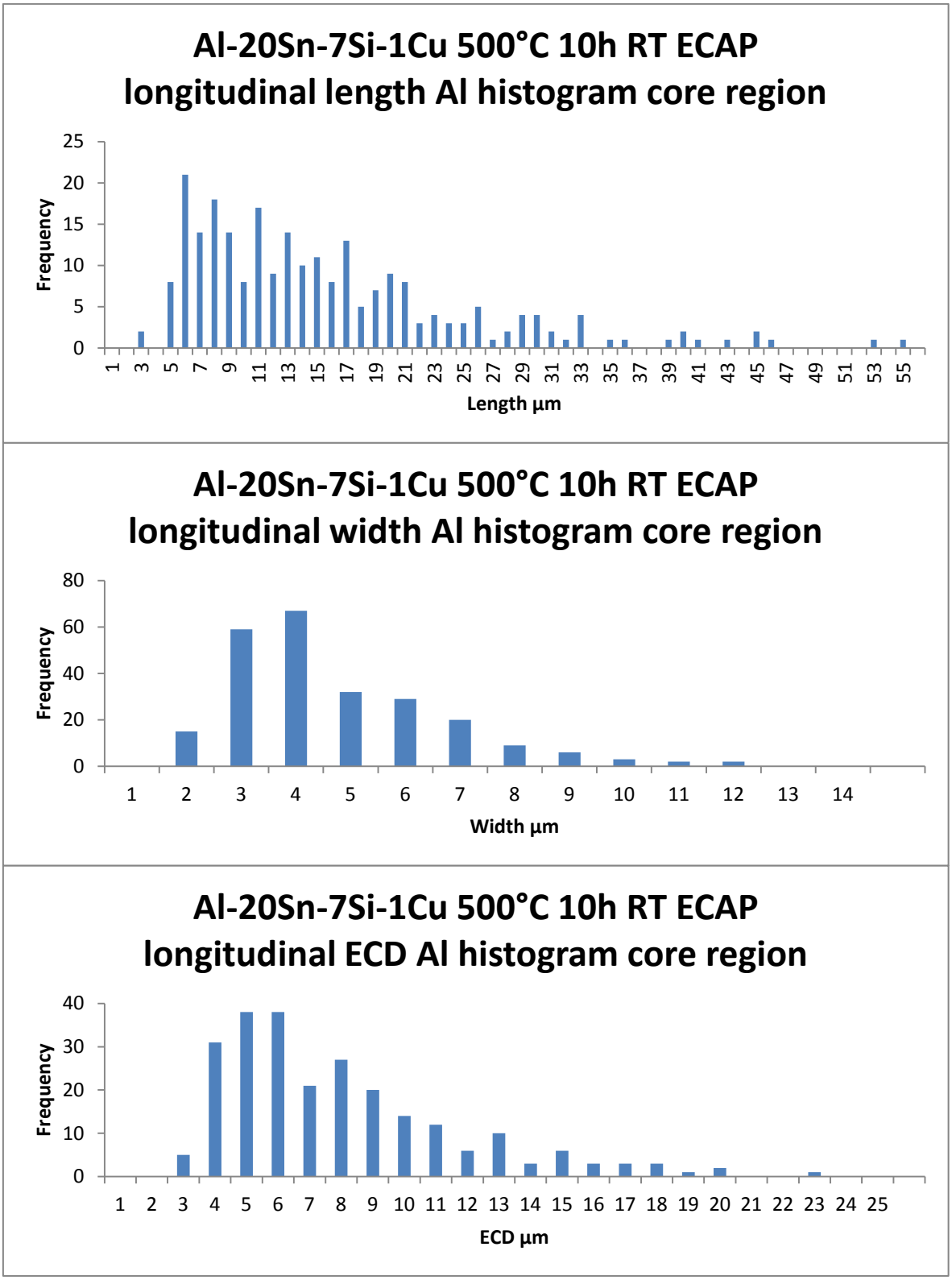

Appendix 6-25: Histograms for length, width and ECD of the aluminium grains of the longitudinal section of the core region of the samples pre-sintered at 500°C 10h and subject to ECAP.

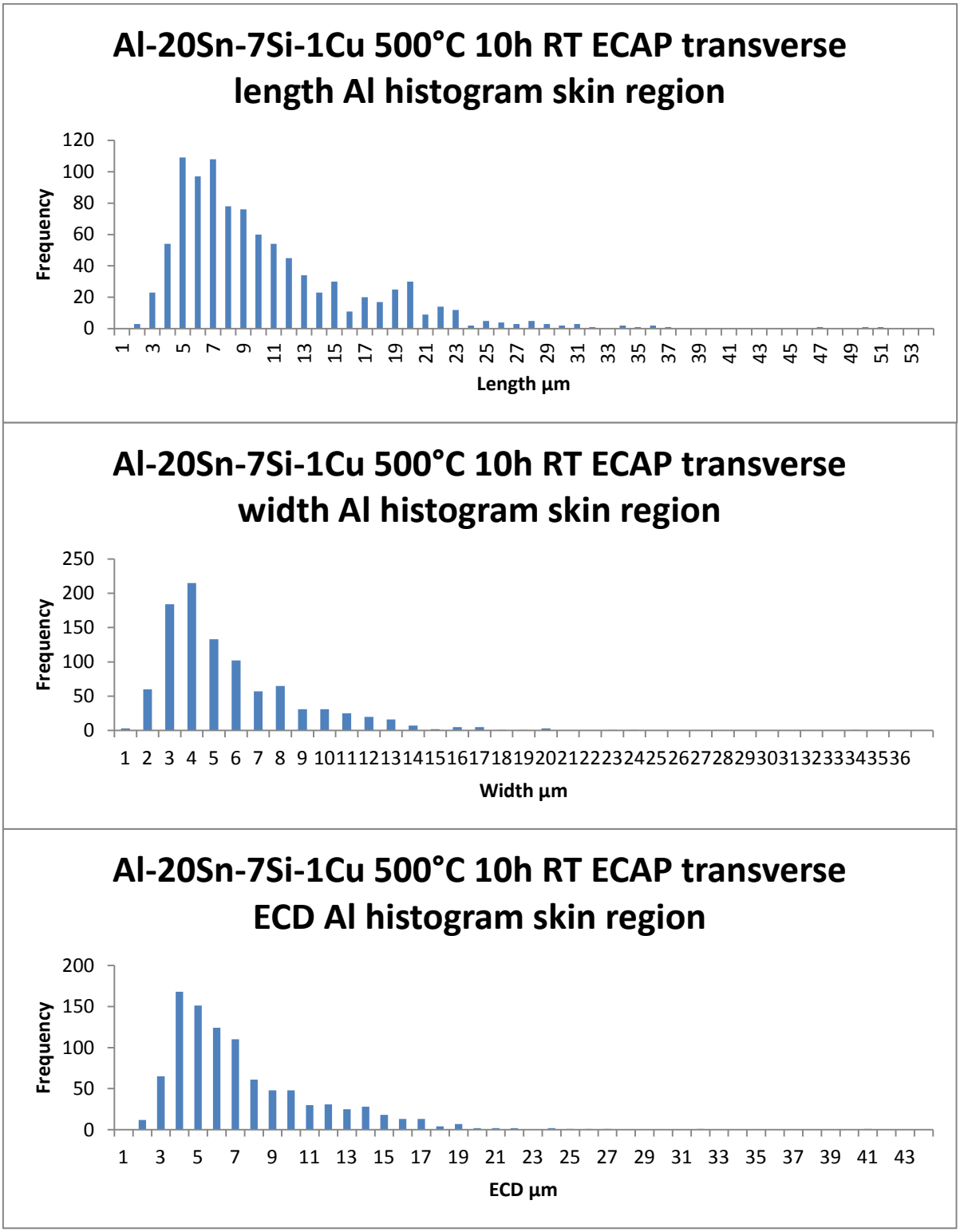

Appendix 6-26: Histograms for length, width and ECD of the aluminium grains of the transverse section of the skin region of the samples pre-sintered at 500°C 10h and subject to ECAP.

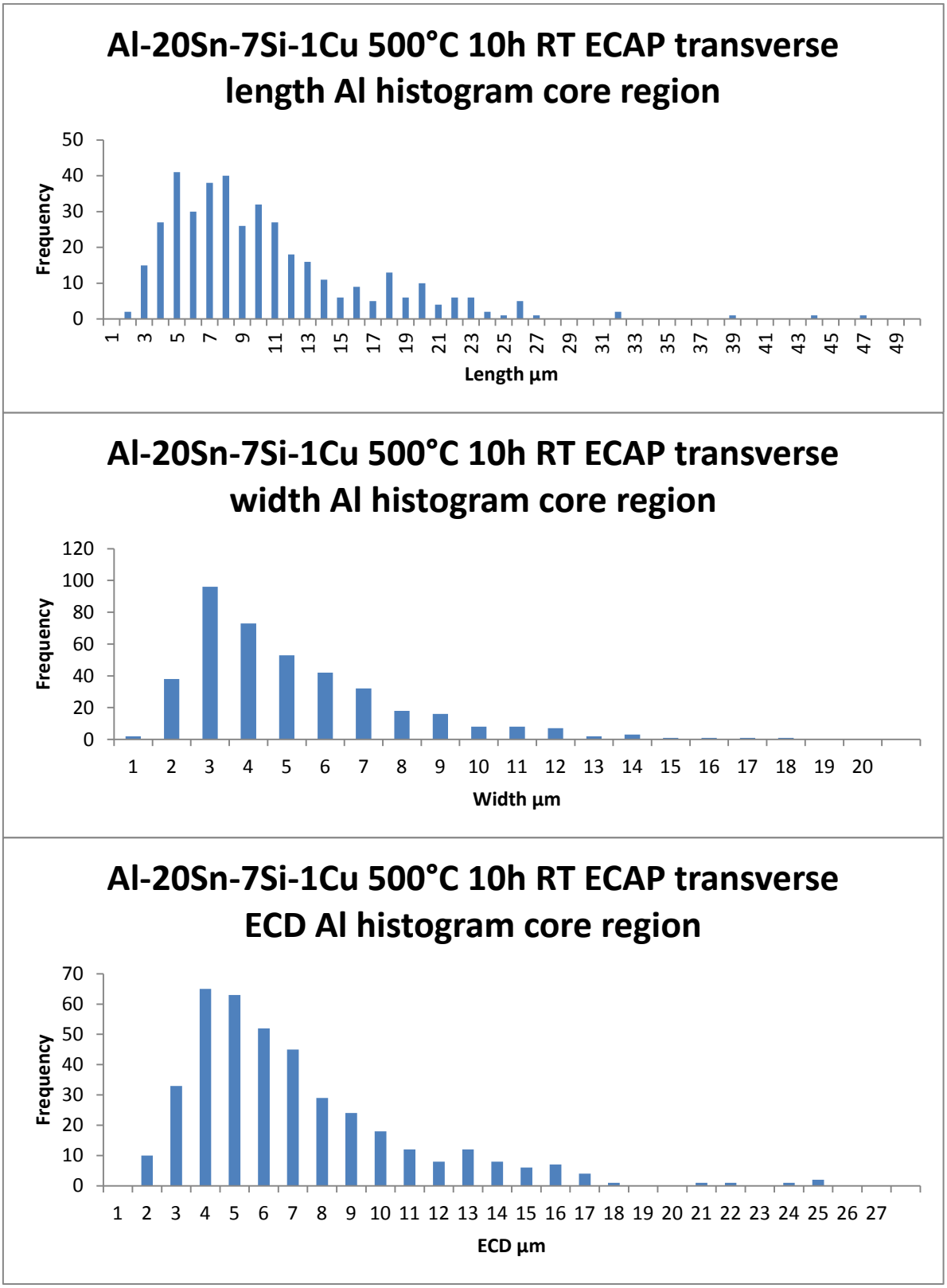

Appendix 6-27: Histograms for length, width and ECD of the aluminium grains in the transverse section of the core region of the samples pre-sintered at 500°C 10h and subject to ECAP.

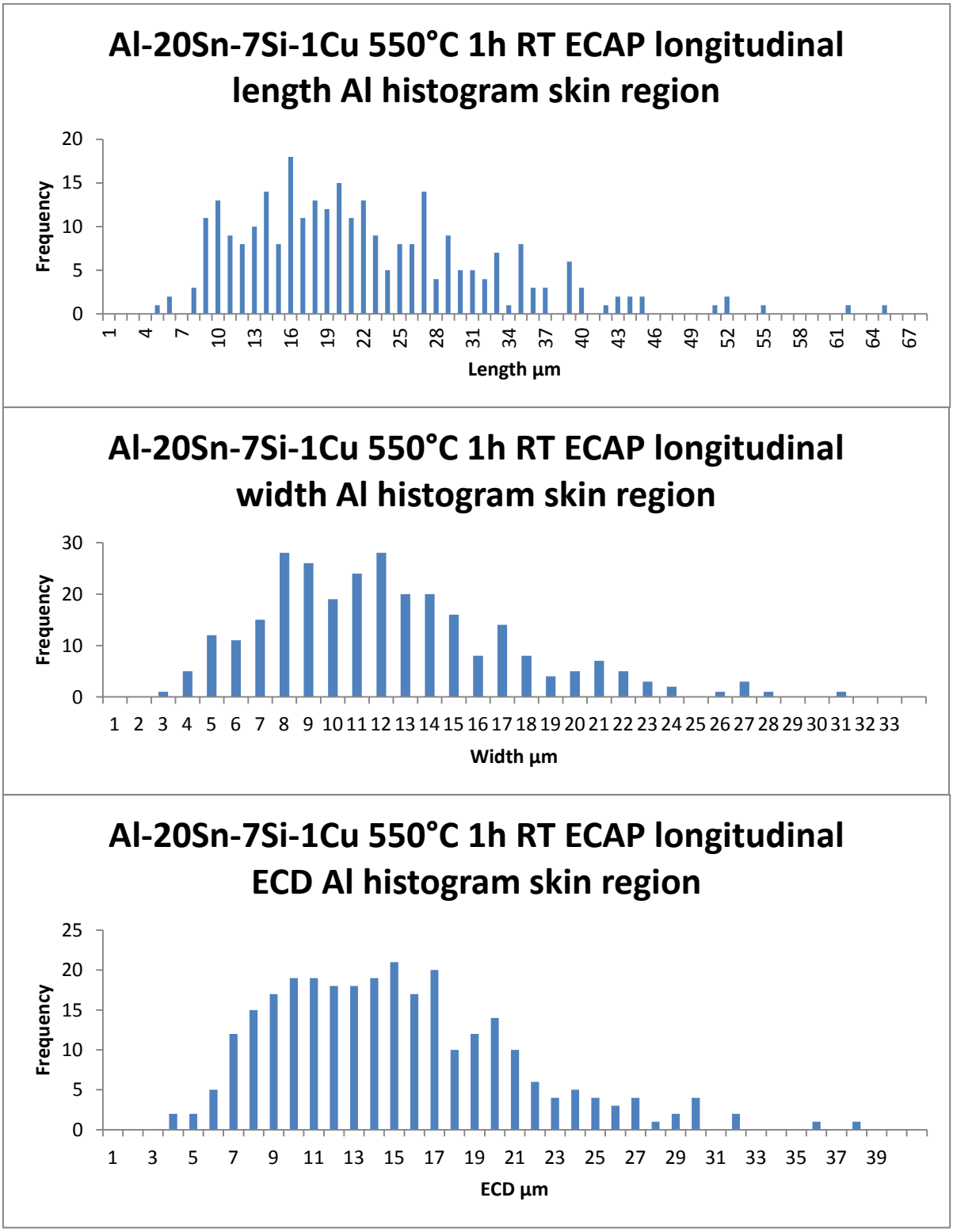

Appendix 6-28: Histograms for length, width and ECD of the aluminium grains in the longitudinal section of the skin region of the samples pre-sintered at 550°C 1h and subject to ECAP.

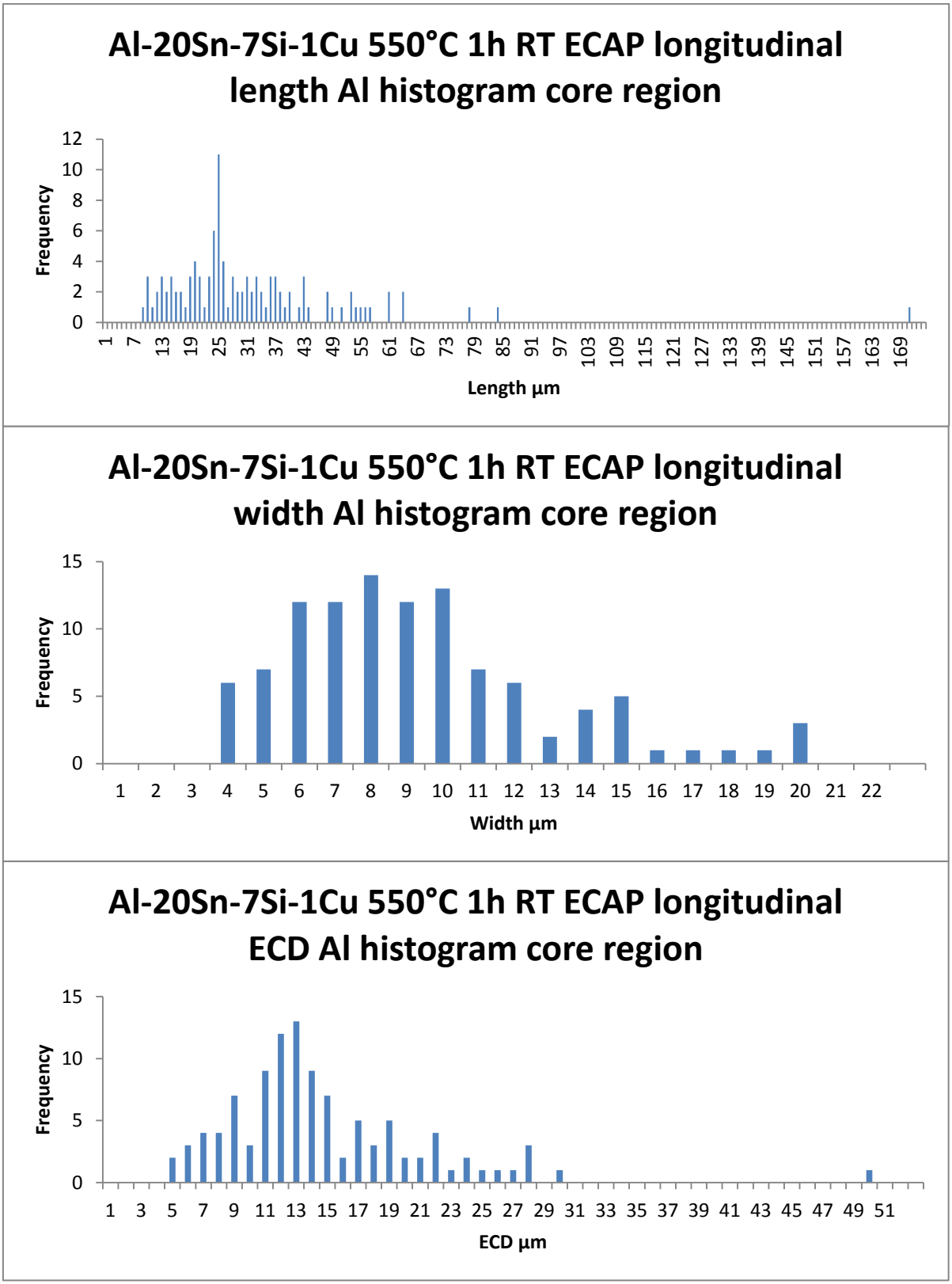

Appendix 6-29: Histograms for length, width and ECD of the aluminium grains in the longitudinal section of the core region of the samples pre-sintered at 550°C 1h and subject to ECAP.

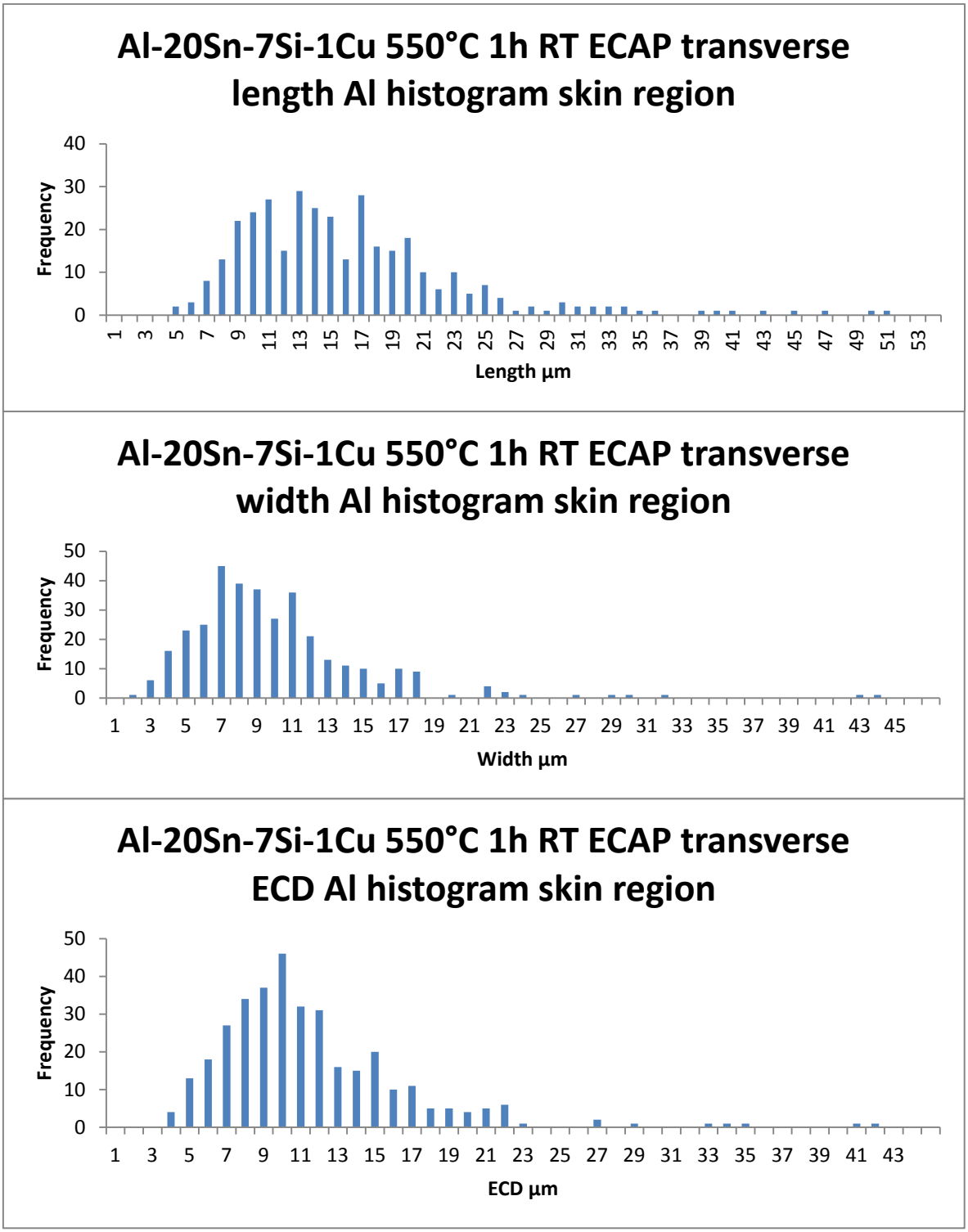

Appendix 6-30: Histograms for length, width and ECD of the aluminium grains in the transverse section of the skin region of the samples pre-sintered at 550°C 1h and subject to ECAP.

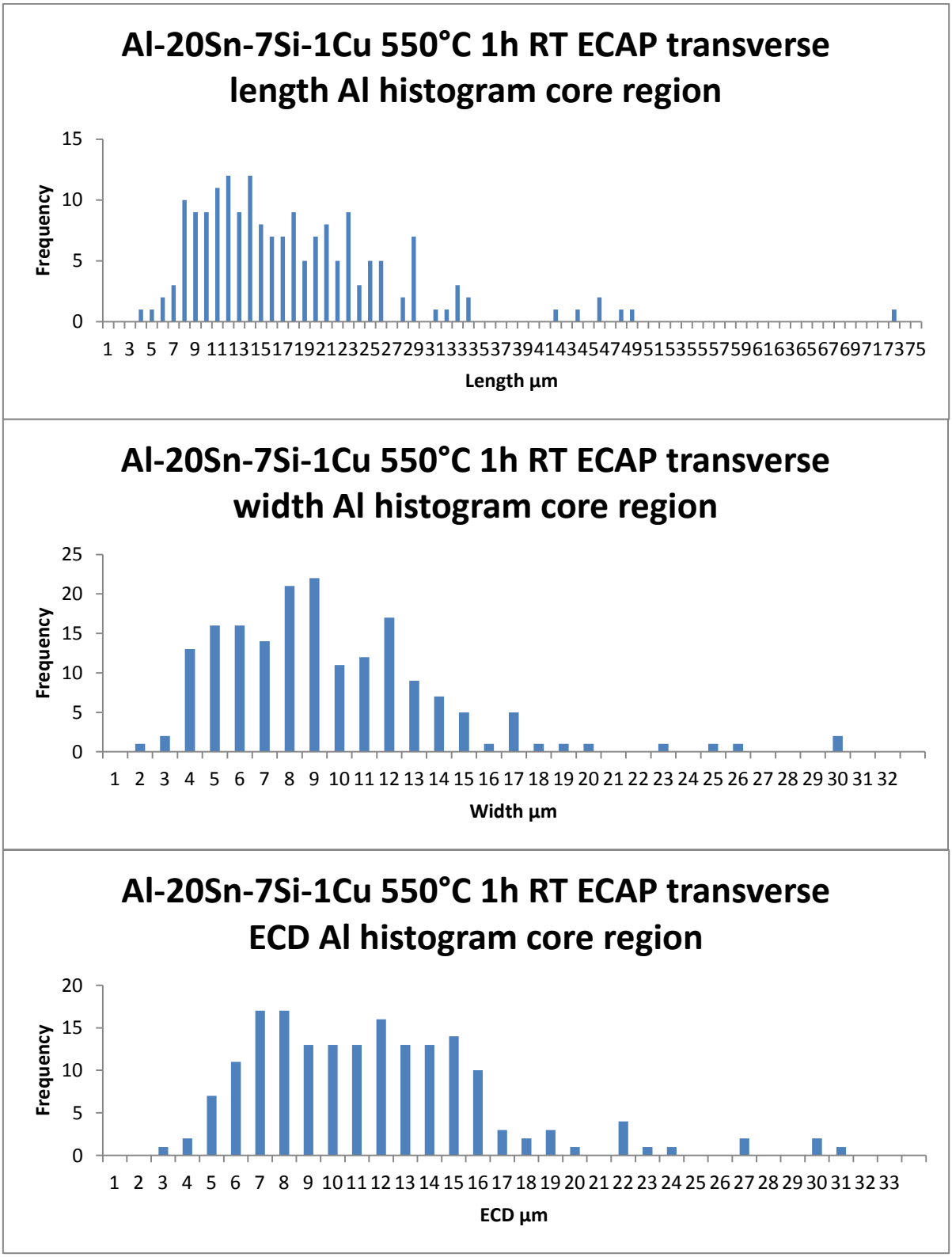

Appendix 6-31: Histograms for length, width and ECD of the aluminium grains in the transverse core region of the samples pre-sintered at 550°C 1h and subject to ECAP.

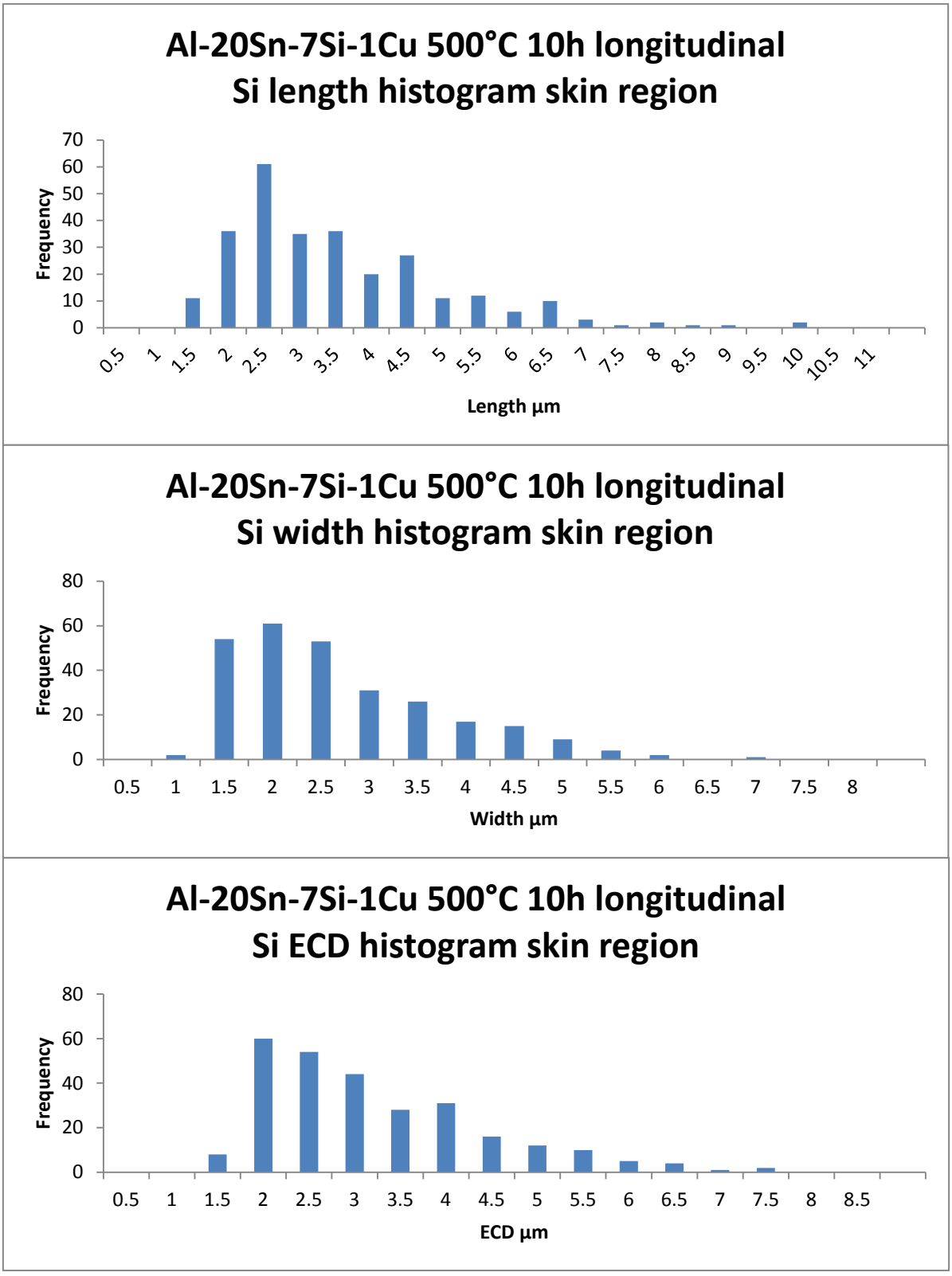

Appendix 6-32: Histograms for length, width and ECD of the Si particles in the longitudinal section of the skin region of the samples pre-sintered at 500°C 10h and subject to ECAP.

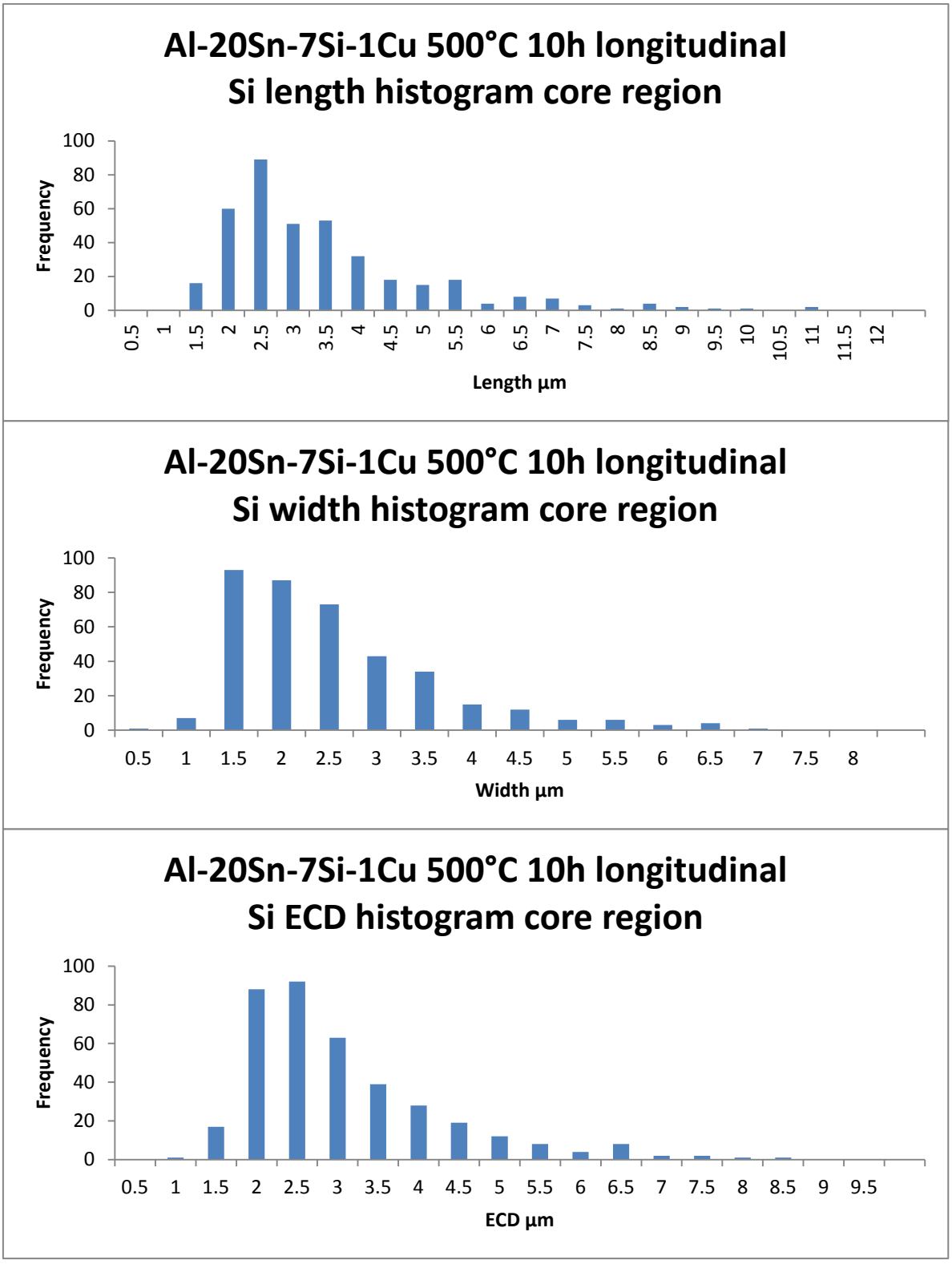

Appendix 6-33: Histograms for length, width and ECD of the Si particles in the longitudinal section of the core region of the samples pre-sintered at 500°C 10h and subject to ECAP.

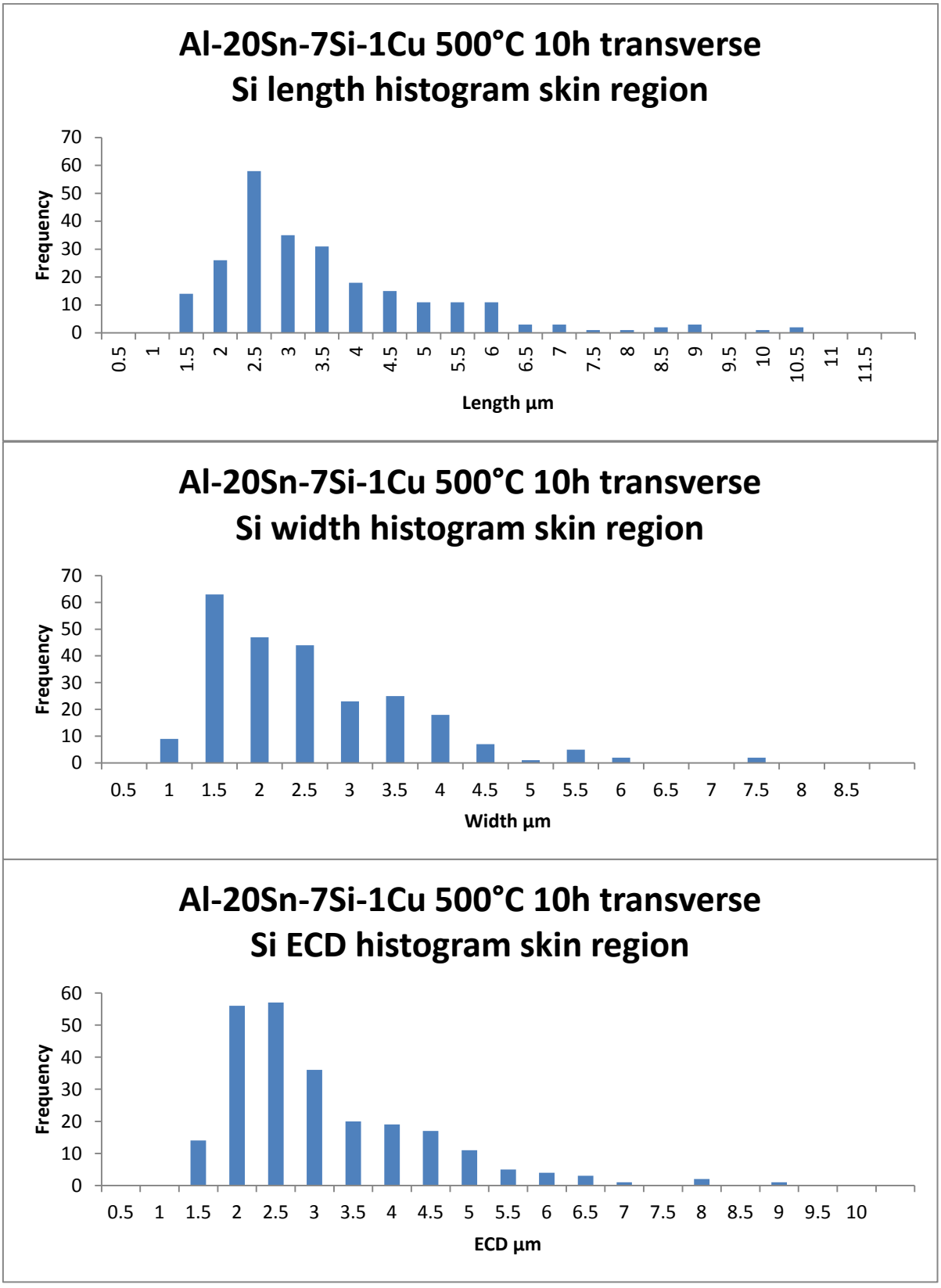

Appendix 6-34: Histograms for length, width and ECD of the Si particles in the transverse section of the skin region of the samples pre-sintered at 500°C 10h and subject to ECAP.

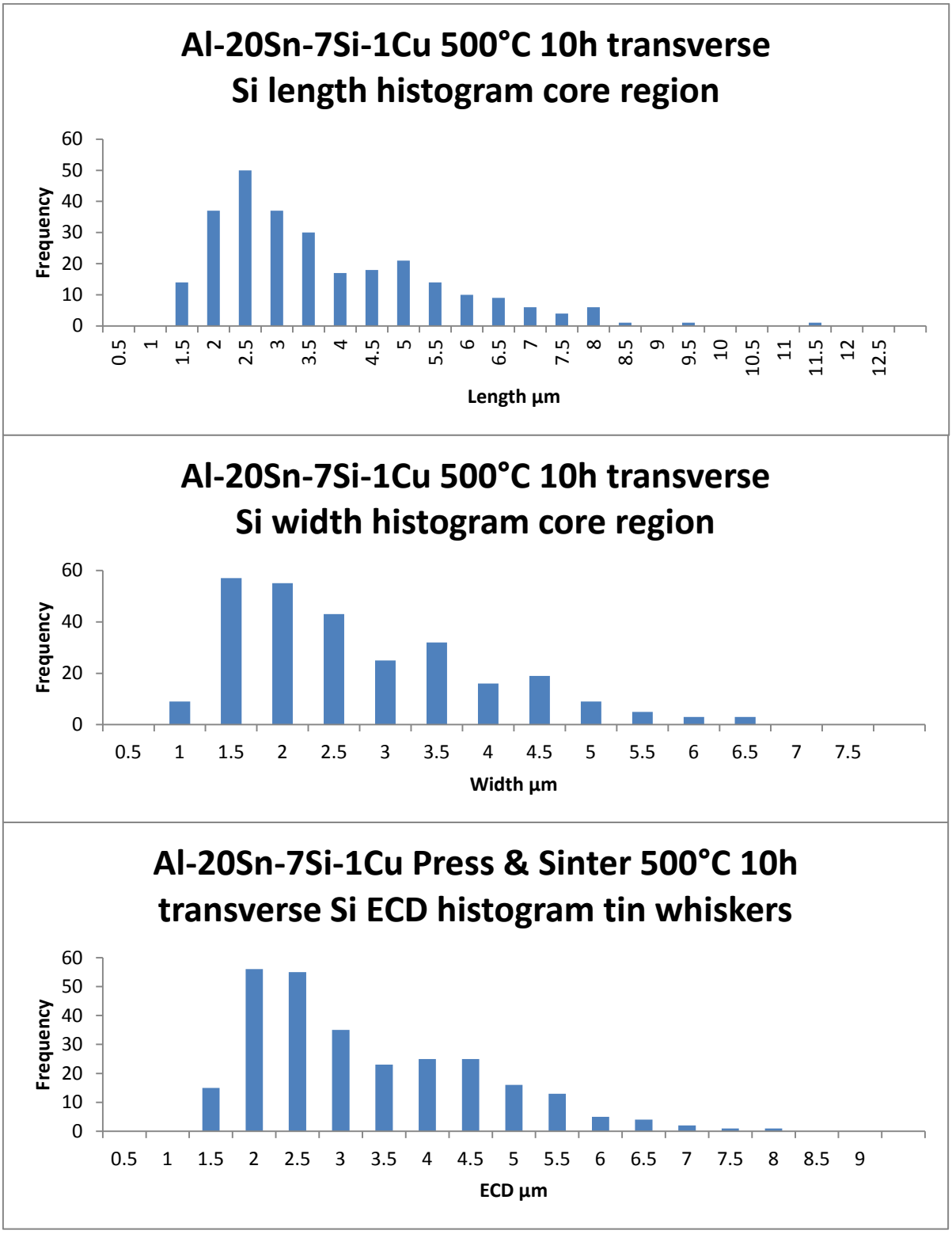

Appendix 6-35: Histograms for length, width and ECD of the Si particles in the transverse section of the core region of the samples pre-sintered at 500°C 10h and subject to ECAP.

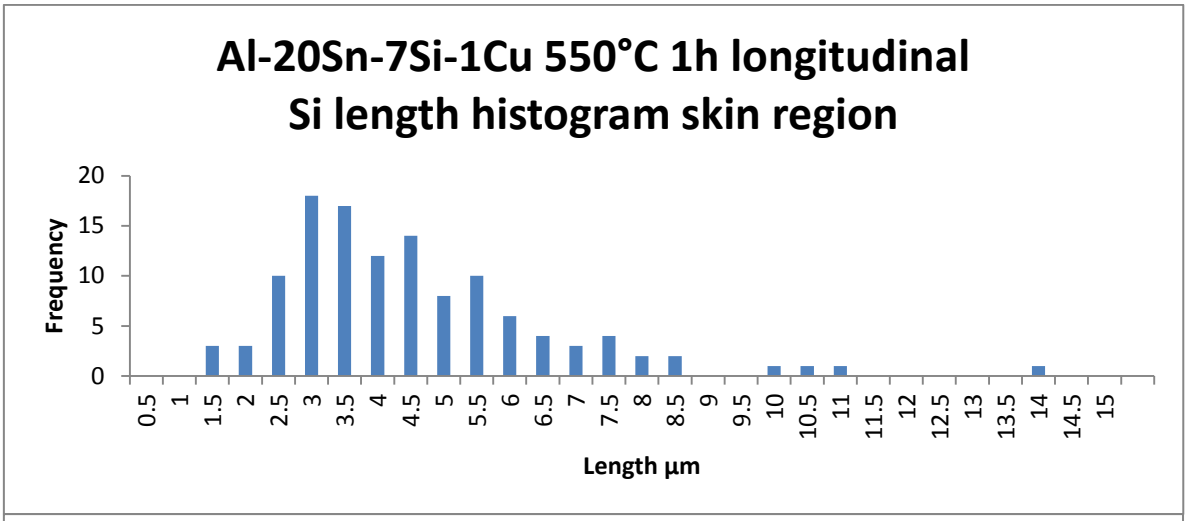

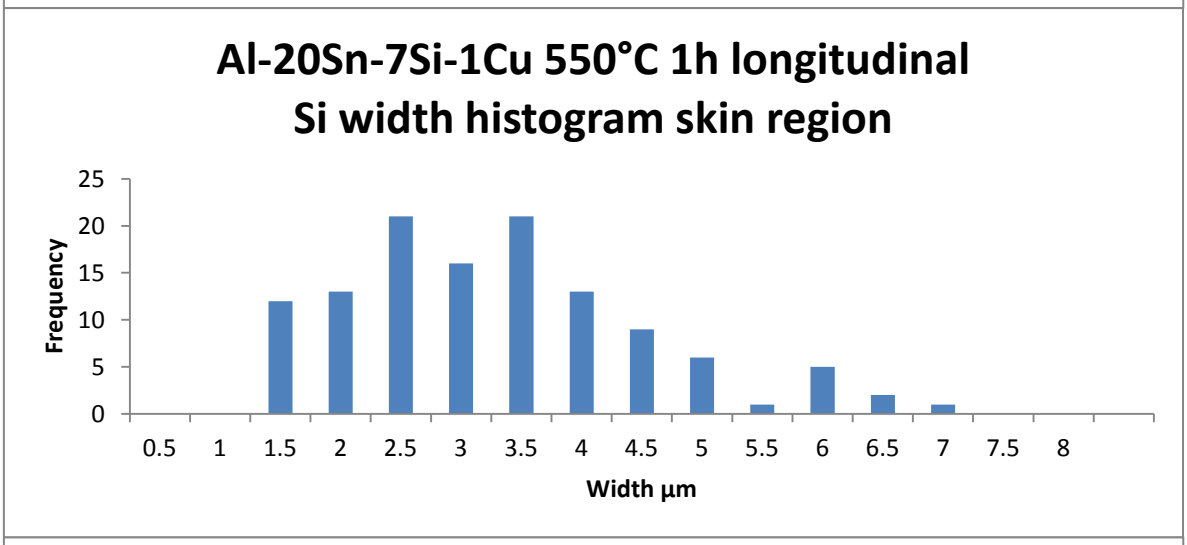

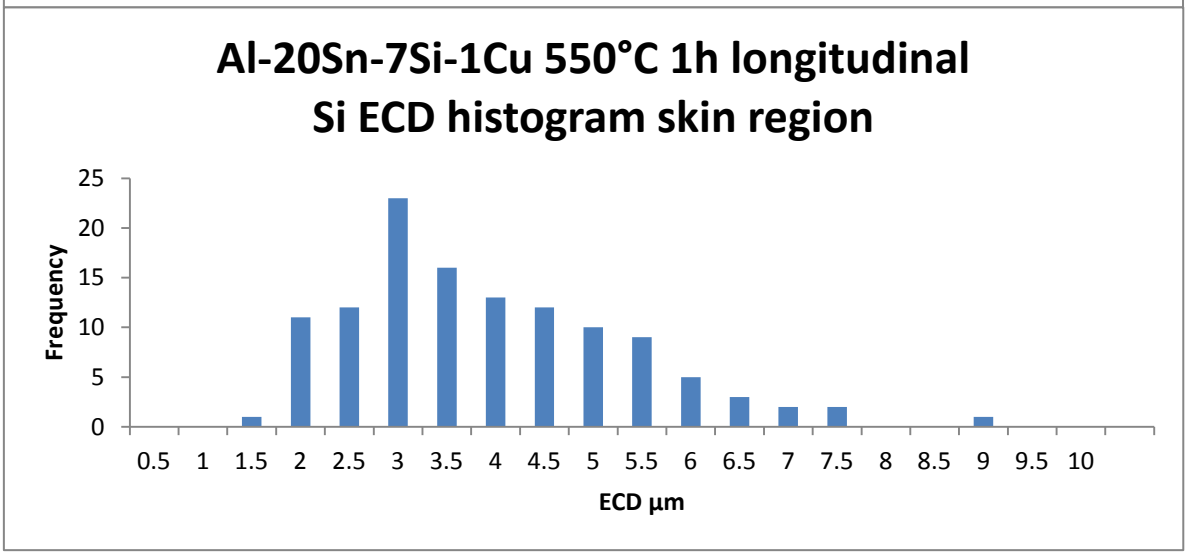

Appendix 6-36: Histograms for length, width and ECD of the Si particles in the longitudinal section of the skin region of the samples pre-sintered at 550°C 1h and subject to ECAP.

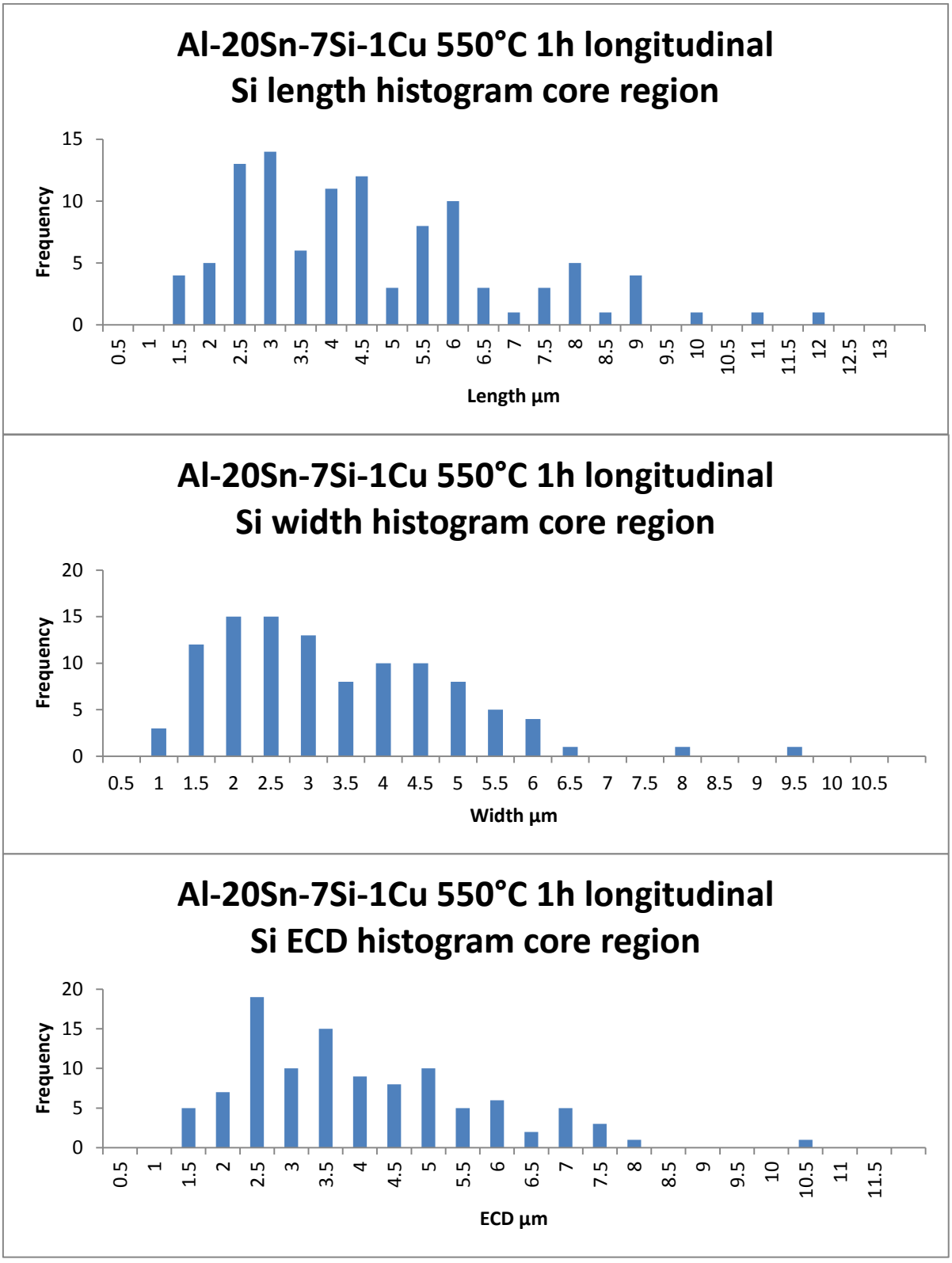

Appendix 6-37: Histograms for length, width and ECD of the Si particles in the longitudinal section of the core region of the samples pre-sintered at 550°C 1h and subject to ECAP.

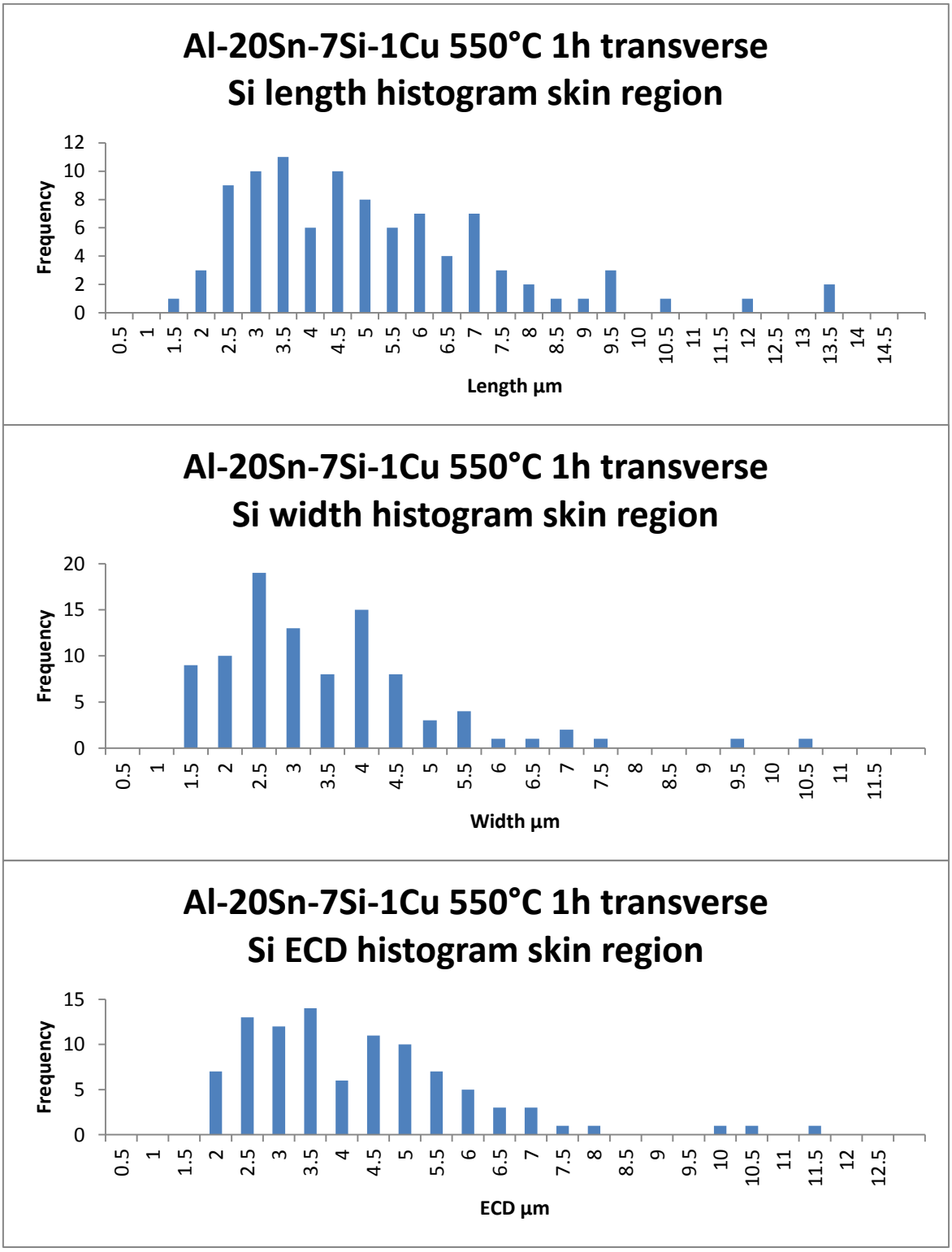

Appendix 6-38: Histograms for length, width and ECD of the Si particles in the transverse section of the skin region of the samples pre-sintered at 550°C 1h and subject to ECAP.

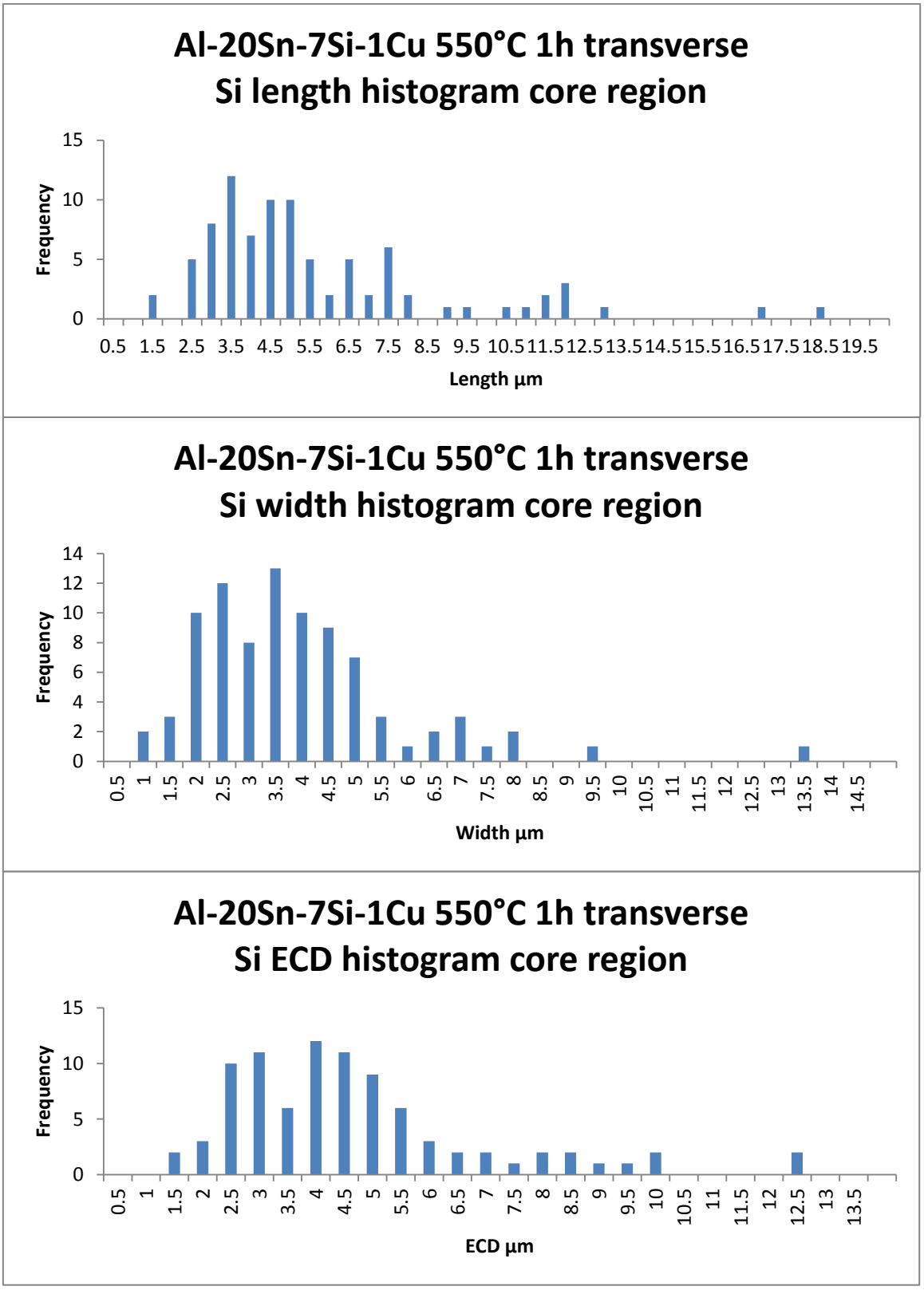

Appendix 6-39: Histograms for length, width and ECD of the Si particles in the transverse section of the core region of the samples pre-sintered at 550°C 1h and subject to ECAP.

7. REFERENCES

1. Hirschhorn, J.S., *Introduction to Powder Metallurgy*. 1969, Princetown, New Jersey: American Powder Metallurgy Institute.
2. Dowson, G., *Powder Metallurgy: the process and its products*. 1990, Michigan: A. Hilger. 167.
3. LaDelpha, A.D.P., Mosher, M.P., Caley, W.F., Kipouros, G.J., Bishop, D.P., *On the simulation of wrough AA4032 via P/M processing.* Materials Science and Engineering A, 2008. **479**: p. 1-9.
4. Thümmler, F., Oberacker, R., *Introduction to Powder Metallurgy*. The Institute of Materials Series on Powder Metallurgy, ed. I. Jenkins, Wood, J.V. 1993, Cambridge: The Institute of Materials.
5. Ramakrishnan, P., *History of powder metallurgy.* Indian Journal of History of Science, 1983. **18**(1): p. 109-114.
6. Buturla, D.E., *Powder Metallurgy*. 2009.
7. Assinter. *Powder Metallurgy Components: Production Cycle*. in *EPMA Summer School 2010*. 2010. Madrid.
8. Akisanya, A.R., Cocks, A.C.F., *Stage I compaction of cylindrical particles under non-hydrostatic loading.* Journal of the Mechanics and Physics of Solids, 1995. **43**(4): p. 605-636.
9. The Aluminium Association, I., *Aluminium Powder Metallurgy*, I. Marketing and the Technical & Standards Committees of the Pigments and Powder Division of The Aluminium Association, Editor. 2011.
10. Furukawa, M., Horita, M. Nemoto, M., Langdon, T.G., *Review: processing of metals by equal channel angular pressing.* Journal of Materials Science, 2001. **36**: p. 2835-2843.
11. Beyerlein, I.J., Tóth, L.S., *Texture evolution in equal-channel angular extrusion.* Progress in Materials Science, 2009: p. 427-510.
12. Segal, V.M., *Equal channel angular extrusion: from macromechanics to structure formation.* Materials Science and Engineering A, 1999. **271**: p. 322-333.
13. Hunt, W.H.J., *New directions in aluminium-based P/M materials for automotive applications.* International Journal of Powder Metallurgy, 2000. **36**(6): p. 51-60.
14. Beaumont, F., *Aluminum P/M: Past, present and future.* International Journal of Powder Metallurgy, 2000. **36**(6): p. 41-44.
15. Levina, D.A., Chernyshev, L. I., Mikhaylovskaya, N. V., *Powder metallurgy in North America continues to grow.* Powder Metallurgy and Metal Ceramics, 2006. **45**(7-8): p. 400-404.
16. Fujiki, A., *Present state and future prospects of powder metallurgy parts for automotive applications.* Materials Chemistry and Physics, 2001. **67**: p. 298-306.
17. Bocchini, G.F., *Warm compaction of metal powders: why it works, why it requires a sophisticated engineering approach.* Powder Metallurgy, 1999. **42**(2): p. 171-180.
18. Pohl, A., *PM aluminium drives forward in a new BMW breakthrough.* Metal Powder Report, 2006. **61**(2): p. 13-15.
19. Pohl, A., *Wear resistant sintered aluminium parts for automotive applications.* Powder Metallurgy, 2006. **49**(2): p. 104-106.
20. Schubert, T., Weißgärber, T., Kieback, B., Balzer, H., Neubing, H.C., Baum, U., Braun, R., *Aluminium PM 'is a challenge that industry can overcome'.* Metal Powder Report, 2005. **5**: p. 32-36.
21. Showaiter, N., Youseffi, M., *PM processing of elemental and pre-alloyed 6061 aluminium alloy with and without common lubricants and sintering aids.* Powder Metallurgy, 2006. **49**(3): p. 240-252.
22. (EPMA), E.P.M.A., *Economic Advantages of Powder Metallurgy*. 2014.

23. Puscas, T.M.S., M., Molinari, A., Strafelini, G., *Image analysis investigation of the effect of the process variables on the porosity of sintered chromium steels.* Materials Characterisation, 2001. **50**(1): p. 1-10.
24. Rutz, H.G., Hanejko, F.G. *High density processing of high performance ferrous materials*. in *1994 International Conference & Exhibition on Powder Metallurgy & Particulate Materials*. 1994. Toronto, Riverton, New Jersey.
25. Exner, H.E., Muller, C., Wincierz, C., Broszeit, E., *Effects of microstructure on wear of aluminium bearing alloys with systematic variation of hard and soft phases.* Materialwissenschaft und Werkstofftechnik (Material Science and Material Technology), 2000. **31**: p. 215-224.
26. Crossin, E., Yao, J.-Y., Schaffer, G.B., *Swelling during liquid phase sintering of Al-Mg-Si-Cu alloys.* Powder Metallurgy, 2007. **50**(4): p. 354-358.
27. Lumley, R.N., Schaffer, G.B., *The effect of additive particle size on the mechanical properties of sintered aluminium-copper alloys.* Scripta Materialia, 1998. **39**(8): p. 1089-1094.
28. Lumley, R.N., Schaffer, G.B., *The effect of solubility and particle size on liquid phase sintering.* Scripta Materialia, 1996. **35**(5): p. 589-595.
29. Valiev, R.Z., Langdon T.G., *Principles of equal channel angular pressing as a processing tool for grain refinement.* Progress in Materials Science, 2006. **51**: p. 881-981.
30. Patel, J., Morsi, K., *Effect of mechanical alloying on the microstructure and properties of Al-Sn-Mg.* Journal of Alloys and Compounds, 2012. **540**: p. 100-106.
31. Sutherland, J.W., *Milling*, in *Manufacturing Education Page*, Michigan Technological University: Michigan.
32. Senna, M., Kuno, H., *Polymorphic transformation of PbO by isothermal wet ball-milling.* Journal of the American Ceramic Society, 1971. **54**(5): p. 259-262.
33. Suryanarayana, C., *Mechanical alloying and milling.* Progress in Materials Science, 2001. **46**: p. 1-84.
34. Koch, C.C., *Milling of Brittle and Ductile Materials*, in *ASM Handbook - Powder Metal Technologies and Applications*, A. International, Editor. 1998, ASM International. p. 134-165.
35. Schatt, W., Wieters, K.-P, *Powder Metallurgy: Processing and Materials*. 1997, Düsseldorf, Germany: European Powder Metallurgy Association (EPMA).
36. Esawi, A.M.K., Morsi, K., Sayed, A., Gawad, A. A., Borah, P., *Fabrication and properties of dispersed carbon nanotube-aluminum composites.* Materials Science and Engineering A, 2009. **508**: p. 167-173.
37. Webster, O., *Effect of lithium on the mechanical properties and microstructures of SiC whisker reinforced aluminium alloys.* Metallurgical and Materials Transactions A, 1982. **13**(3): p. 1511-1519.
38. Dunkley, J.J., *Atomization*, in *ASM Handbook Volume 7 - Powder Metal Technologies and Applications*. 1998, ASM Handbook: Sheffield, England. p. 89-133.
39. Neikov, O.D., *Atomization and Granulation*, in *Handbook of Non-Ferrous Metal Powders: Technologies and Applications*. 2009, Elsevier: Amsterdam. p. 102-142.
40. Jones, H., *Gas-atomised aluminium alloy powders and their products: an update 1996-2001.* Materials Science and Engineering A, 2004. **375-377**: p. 104-111.
41. Neikov, O.D., Milman, Y. V., Sirko, A. I., Sameljuk, A. V., Krajnikov, A. V., *Elevated temperature aluminum alloys produced by water atomization.* Materials Science and Engineering A, 2008. **477**(1-2): p. 80-85.
42. German, R.M., *Powder Metallurgy Science*. Second Edition ed. 1994, Princeton, New Jersey: Metal Powder Industries Federation. 472.
43. Reinshagen, J., Neupaver, A., *Principles of Atomization*, in *Physical Chemistry of Powder Metals Production and Processing*, W.M. Small, Editor. 1989, The Minerals, Metals and Materials Society.

44. Colton, D.J., *Metal Powder Processing*, George W. Woodruff School of Mechanical Engineering, Georgia Institute of Technology: Atlanta.
45. Ünal, A., Leon, D.D., Gurganus, T.B., Hildeman, G.J., Aluminium Company of America, *Production of Aluminium and Aluminium-Alloy Powder*, in *ASM Handbook Volume 7: Powder Metal Technologies and Applications*, A. International, Editor. 1998, ASM International. p. 353-380.
46. Flumerfelt, J.F., Anderson, I.E., *High purity aluminium powder processed using high pressure gas atomisation.* Advances in Powder Metallurgy & Particulate Materials, 1996. **1**: p. 87-96.
47. Anderson, I.E., Foley, J.C., *Determining the role of surfaces and interfaces in the powder metallurgy processing of aluminum alloy powderse.* Surface & Interface Analysis, 2001. **31**: p. 599-608.
48. Seki, Y., Takigawa, H., Kawai, N., *Effect of atomization variables on powder characteristics.* Metal Powder Report, 1990. **45**(1): p. 38-40.
49. Ghanim, A.N., *Atomization of aluminum by unique air nozzle.* Journal of Babylon University: Pure and Applied Sciences, 2011. **19**(3): p. 1255-1267.
50. Neikov, O.D., *Advanced Aluminum Alloy Powders*, in *Handbook of Non-Ferrous Metal Powders*. 2009, Elsevier: Amsterdam. p. 284-313.
51. Neikov, O.D. *Rapidly solidified aluminium alloy powders*. in *1998 Powder Metallurgy World Congress*. 1998. Granada, Spain: European Powder Metallurgy Association.
52. Neikov, O.D., Vasilieva, G.I., Sameljuk, A. V., Krajnikov, *Water atomised aluminium alloy powders.* Materials Science and Engineering A, 2004. **383**: p. 7-13.
53. Totten, G.E., Mackenzie, D.S., *Handbook of Aluminum: Physical Metallurgy and Processes*. Vol. 1. 2003, New York, NY: Marcel Dekker, INC.
54. Iacocca, R.G., *Particle size and size distribution in metal powders*, in *ASM Handbook Volume 7: Powder Metal Technologies and Applications*, A. International, Editor. 1998, ASM Internation. p. 541-550.
55. Merkus, G.H., *Particle Size Measurements: Fundamentals, Practice, Quality*. 2009: Springer. 536.
56. Irani, R., Callis, C. F., *Particle Size: Measurement, Interpretation, and Application*. 1963, New York: Wiley. 165.
57. Bernhardt, C., *Particle Size Analysis: Classification and Sedimentation Methods*. 1 ed. 1994, London: Chapman & Hall.
58. Barth, H.G., *Modern Methods of Particle Size Analysis*. 1984, New York: John Wiley & Sons. 320.
59. Allen, T., *Particle Size Measurement: Powder Sampling and Particle Size Measurement*. 5 ed. Vol. 1. 1996, London: Springer.
60. Sheikhaliev, S.M., Sheikhalieva, Z.I., Dunkley, J.J., *Spin atomisation makes tighter, safer aluminium.* Metal Powder Report, 2008. **63**(2): p. 28-30.
61. Bytnar, J.H., Parent, J.O.G., Henein, H., Iyengar, J., *Macro-segregation diagram for dry blending particulate metal-matrix composites.* International Journal of Powder Metallurgy, 1995. **31**(1): p. 37-50.
62. Carson, J.W., Pittenger, B. H., *Bulk Properties of Powders*, in *ASM Handbook - Powder Metal Technologies and Applications*, A. International, Editor. 1998, ASM International. p. 665-725.
63. Coube, O., Cocks, A.C.F., Wu, C.-Y., *Experimental and numerical study of die filling, powder transfer and die compaction.* Powder Metallurgy, 2005. **48**(1): p. 68-76.
64. Wu, C.-y., Guo, Y., *Numerical modelling of suction filling using DEM/CFD.* Chemical Engineering Science, 2012. **73**: p. 231-238.
65. Wu, C.-Y., Cocks, A.C.F, *Flow behaviour of powders during die filling.* Powder Metallurgy, 2004. **47**(2): p. 127-136.

66. (MPIF), M.P.I.F., *Standard Test Methods for Metal Powders and Powder Metallurgy Products, 2012 Edition*. 2012 ed. 2012: Metal Powder Industries Federation.
67. Iacocca, R.G., German, R.M., *The experimental evaluation of die compaction lubricants using deterministic chaos theory.* Powder Technology, 1999. **102**: p. 253-265.
68. Marinelli, J.C., J.W., *Solve solids flow problems in bins, hoppers and feeders.* Chemical Engineering Progress, 1992: p. 22-28.
69. Fischer, J.J., *Solid-solid blending.* Chemical Engineering, 1960. **67**(8): p. 107-128.
70. Ferguson, B.L., *Powder Shaping Technologies*, in *ASM Handbook - Powder Metal Technologies and Applications*, A. International, Editor. 1998, ASM Internation. p. 727-744.
71. Ogbonna, N., Fleck, N.A., *Compaction of an array of spherical particles.* Acta Metallurgica et Materialia, 1995. **43**(2): p. 603-620.
72. Lefebvre, L.-P., Thomas, Y., *Evaluation of a polyehylene lubricant for aluminium P/M applications.* International Journal of Powder Metallurgy, 1999. **35**(5): p. 45-53.
73. Liu, L.X., Schaffer, G.B., Lister, J.D., *Binder-treated segregation-free aluminium-alloy powders.* International Journal of Powder Metallurgy, 2005. **41**(1): p. 42-49.
74. Showaiter, N., Youseffi, M., *Compaction, sintering and mechanical properties of elemental 6061 Al powder with and without sintering aids.* Materials and Design, 2008. **29**: p. 752-762.
75. Tien, Y.-M., Wu, P.-L., Huang, W.-H., Kuo, M.-F., Chu, C.-A., *Wall friction measurement and compaction characteristics of bentonite powders.* Powder Technology, 2007. **173**(2): p. 140-151.
76. Wei, X.S., Vekshin, B., Kraposhin, V., Huang, Y.J., Shen, J., Xia, K., *Full density consolidation of pure aluminium powders by cold hydro-mechanical pressing.* Materials Science and Engineering A, 2011. **528**: p. 5784-5789.
77. Enneti, R.K., Lusin, A., Kumar, S., German, R.M., Atre, S.V., *Effects of lubricant on green strength, compressibility and ejection of parts in die compaction process.* Powder Technology, 2013. **233**: p. 22-29.
78. Bonnefoy, V., Doremus, P., Puente, G., *Investigations on friction behaviour of treated and coated tools with poorly lubricated powder mixes.* Powder Metallurgy, 2003. **46**(3): p. 224-228.
79. Melúch, L., *Warm Compaction of Aluminium Alloy Alumix 123*, in *Department of Metallurgy and Materials*. 2009, University of Birmingham: Birmingham. p. 237.
80. Hasegawa, K. *High density compaction method for soft magnetic composites (SMCs)*. in *PM2012 World PM Congress*. 2012. Yokohama, Japan: Japan Powder Metallurgy Association.
81. Lefebvre, L.-P., Thomas, Y., White, B., *Effects of lubricants and compacting pressure on the processability and properties of aluminum P/M parts.* Journal of Light Metals, 2002. **2**: p. 239-246.
82. Li, Y.Y., Ngai, T.L., Zhang, D.T., Long, Y. and Xia, W., *Effect of die wall lubrication on warm compaction powder metallurgy.* Journal of Materials Processing Technology, 2002. **129**: p. 354-358.
83. Larsson, M., Ramstedt, M., *Lubricants for compaction of P/M components*, Höganäs, Editor. 2005, Höganäs.
84. Hoeganas AB, S., *Material Safety Data Sheet for Kenolube P11, MSDS code: 027575*.
85. St-Laurent, S., Azzi, L., Thomas, Y. *High Performance Lubricants for Demanding PM Applications*. in *Proceedings of the 2006 Advances in Powder Metallurgy & Particulates Materials Conference*. 2006. Princeton: MPIF.
86. IMS Company, O., *Materials Safety Data Sheet for Acrawax C, V50, V150*.
87. Lee, S.C., Kim, K.T., *Densification behaviour of aluminium alloy powder under cold compaction.* International Journal of Mechanical Sciences, 2002. **44**: p. 1295-1308.

88. Kim, K.T., Lee, S.C., Ryu, H.S., *Densification behavior of aluminum alloy powder mixed with zirconia powder inclusion under cold compaction.* Materials Science and Engineering A, 2003. **340**(1-2): p. 41-48.
89. Al-Qureshi, H.A., Soares, M. R. F., Hotza, D., Alves, M. C., Klein, A. N., *Analyses of the fundamental parameters of cold die compaction of powder metallurgy.* Journal of Materials Processing Technology, 2008. **199**: p. 417-424.
90. Fleck, N.A., *A crystal plasticity view of powder compaction.* Acta Metallurgica et Materialia, 1995. **43**(8): p. 3177-3184.
91. Sridhar, I., Fleck, N.A., Akisanya, A.R., *Cold compaction of an array of cylindrical fibres.* International Journal of Mechanical Sciences, 2001. **43**: p. 715-742.
92. Kim, I., Kim, J., Shin, D.S., Lee, C.S., Hwang, S.K., *Effects of equal channel angular pressing temperature on deformation structures of pure Ti.* Materials Science and Engineering A, 2003. **342**: p. 302-310.
93. Moreno, M.F., González Oliver, C. J. R., *Densification of Al powder and Al-Cu matrix composite (reinforced with 15% saffil short fibres) during axial cold compaction.* Powder Technology, 2011. **206**: p. 297-305.
94. Sonnergaard, J.M., *A critical evaluation of the Heckel equation.* International Journal of Pharmaceutics, 1999. **193**: p. 63-71.
95. Heckel, R.W., *Density pressure relationship in powder compaction.* Transactions of the Metallurgical Society of AIME, 1961. **221**: p. 671-675.
96. Augsburger, L.L., Muller, F.X., *The role of the displacement-time waveform in the determination of heckel behaviour under dynamic conditions in a compaction simulator and a fully instrumental rotary tablet machine.* Journal of Pharmacy and Pharmacology, 1994. **46**: p. 468-475.
97. Sjödahla, M., Siviourb, C.R., Forsberga, F., *Digital volume correlation applied to compaction of granular materials.* Procedia IUTAM, 2012. **4**: p. 179-195.
98. Lee, S.C., Kim, K.T., *A study on the cap model for metal and ceramic powder under cold compaction.* Materials Science and Engineering A, 2007. **445-446**: p. 163-169.
99. Jiang, G., Daehn, G.S., Lannutti, J.J., Fu, Y. Wagoner, R.H., *Effects of lubrication and aspect ratio on the consolidation of metal matrix composites under cyclic pressure.* Acta Materialia, 2001. **49**: p. 1471-1477.
100. Zhao, C., Jain, M.K., Bruhis, M., Lawcock, R., *An integrated study of die powder fill, transfer and compaction process using digital image correlation method.* Powder Technology, 2011. **208**: p. 225-230.
101. Khoei, A.R., Keshavarz, Sh., Khaloo, A.R., *Modeling of large deformation frictional contact in powder compaction processes.* Applied Mathematical Modelling, 2008. **32**: p. 775-801.
102. Kang, S.-K.L., *Sintering: Densification, Grain Growth & Microstructure*. 2005, Oxford: Elsevier Butterwoth-Heinemann. 261.
103. Schaffer, G.B., Sercombe, T.B., Lumley, R.N., *Liquid phase sintering of aluminium alloys.* Materials Chemistry and Physics, 2001. **67**: p. 85-91.
104. Sands, R.L., Shakespeare, C.R., *Powder Metallurgy*. 1966, London: William Clows and Sons. 78-81.
105. Rahaman, M.N., *Ceramic Processing*. 2006: CRC / Taylor & Francis. 376.
106. Park, E.J., *Chapter 3 - Solid-State Sintering Fundamentals*. 2007.
107. Liu, J., German, R. M., *Microstructure effect on dihedral angle in liquid-phase sintering.* Metallurgical and Materials Transactions A, 2001. **32**(1): p. 165-169.
108. Lee, S.-M., Kang, S.-J.L., *Theoretical analysis of liquid phase sintering: pore filling theory.* Acta Materialia, 1998. **46**: p. 3191-3202.
109. Kang, S.-J.L., Kim, K.-H., Yoon, D.N., *Densification and shrinkage during liquid phase sintering.* Journal of the American Ceramic Society, 1991. **74**: p. 425-427.

110. German, R.M., Suri, P., Park, S.J., *Review: liquid phase sintering.* Journal of Materials Science, 2009. **44**: p. 1-39.
111. Tang, F., Anderson, I.E., Biner, S.B., *Solid state sintering and consolidation of Al powders and Al matrix composites.* Journal of Light Metals, 2002. **2**: p. 201-214.
112. Lumley, R.N., Sercombe, T.B., Schaffer, G.M., *Surface oxide and the role of magnesium during the sintering of aluminum.* Metallurgical and Materials Transactions A, 1999. **30**(2): p. 457-463.
113. Ralph, J., Chau, I., *Spinel: Spinel mineral information and data*. 1993-2013.
114. Schaffer, G.B., J.-Y. Yao, Bonner, S.J., Crossin, E., Pas, S.J., Hill, A.J., *The effect of tin and nitrogen on liquid phase sintering of Al-Cu-Mg-Si alloys.* Acta Materialia, 2008. **56**: p. 2615-2624.
115. MacAskill, I.A., Hexemer, R.L., Donaldson, I.W., Bishop, D.P., *Effects of magnesium, tin and nitrogen on the sintering response of aluminium powder.* Journal of Materials Processing Technology, 2010. **210**: p. 2252-2260.
116. Rahaman, M.N., *Ceramic Processing and Sintering*. 2nd ed. 2003: CRC Press.
117. Nakajima, H., *The discovery and acceptance of the Kirkendall Effect: the result of a short research career.* Journal of Metals, 1997. **49**(6): p. 15-19.
118. Timofeev, N.S., Savitskii, A.P., *Volumetric changes in powder bodies in liquid-phase sintering of the aluminum-magnesium system.* Soviet Powder Metallurgy and Metal Ceramics, 1990. **29**(3): p. 188-192.
119. Savitskii, A.P., Romanov, G.N., Gopienko, V.G., *Influence of solubility in the solid phase on volume changes in liquid-phase sintering of aluminum-base powder metallurgy specimens.* Soviet Powder Metallurgy and Metal Ceramics, 1988. **27**(7): p. 568-571.
120. Lee, S.-M., Kang, S.-K.L., *Evaluation of densification mechanisms of liquid phase sintering.* Z. Metallkd., 2001. **92**: p. 669-674.
121. Lee, S.-M., Chaix, J.-M., Martin, C.L., Allibert, C.H., Kang, S.-J., *Computer simulation of particle rearrangement in the presence of liquid.* Metals and Materials, 1999. **5**: p. 197-203.
122. Huppmann, W.J., Riegger, H., *Modelling of rearrangement processes in liquid phase sintering.* Acta Metallurgica, 1975. **23**: p. 965-971.
123. Kang, S.-J.L., Kaysser, W.A., Petzow, G., Yoon, D.N., *Elimination of pores during liquid phase sintering of Mo-Ni.* Powder Metallurgy, 1984. **27**: p. 97-100.
124. German, R.M., *Sintering Theory and Practice*. 1996, New York: Wiley. 568.
125. Marion, J.E., Hsueh, C.H., Evans, A.G., *Liquid-phase sintering of ceramics.* Journal of the American Ceramic Society, 1987. **70**(10): p. 708-713.
126. McNaught, A.D., Wilkinson, A., *Compendium of Chemical Terminology, 2nd Edition*. 2nd ed. 1997, Oxford: Blackwell Scientific Publications. 1824.
127. Park, H.-H., Kwon, O.-J., Yoon, D.N., *The critical grain size for liquid flow into pores during liquid phase sintering.* Metallurgical and Materials Transactions A, 1986. **17A**: p. 1915-1919.
128. German, R.M., Dunlap, J.W., *Processing of iron-titanium powder mixtures by transient liquid phase sintering.* Metallurgical Transactions A, 1986. **17**(2): p. 205-213.
129. Huppman, W.J., *Sintering to high density.* The International Journal of Powder Metallurgy and Powder Technology, 1985. **21**: p. 184-185.
130. German, R., *Supersolidus liquid-phase sintering of prealloyed powders.* Metallurgical and Materials Transactions A, 1997. **28**: p. 1553-1567.
131. Lal, A., Iacocca, R., German, R., *Densification during the supersolidus liquid-phase sintering of nickel-based prealloyed powder mixtures.* Metallurgical and Materials Transactions A, 1999. **30**: p. 2201-2208.
132. Tandon, R., German, R.M., *Supersolidus-transient liquid phase sintering using superalloy powders.* The International Journal of Powder Metallurgy and Powder Technology, 1994. **30**: p. 435-443.

133. Kwon, O.-H., Messing, G.L., *Kinetic analysis of solution-precipitation during liquid-phase sintering of alumina.* Journal of the American Ceramic Society, 1990. **73**: p. 275-281.
134. Cahn, J.W., Heady, R.B., *Analysis of capillary forces in liquid-phase sintering of jagged particles.* Journal of the American Ceramic Society, 1970. **53**: p. 406-409.
135. Liu, Z.Y., Sercombe, T.B., Schaffer, G.B., *The effect of particle shape on the sintering of aluminum.* Metallurgical and Materials Transactions A, 2007. **38**(1351-1357).
136. Schaffer, G.B., Hall, B.J., Bonner, S.J., Huo, S.H., Sercombe, T.B., *The effect of the atmosphere and the role of pore filling on the sintering of aluminium.* Acta Materialia, 2006. **54**(1): p. 131-138.
137. Martín, J.M., Castro, F., *Liquid phase sintering of P/M aluminium alloys: effect of processing conditions.* Journal of Materials Processing Technology, 2003. **143-144**: p. 814-821.
138. Fabian, R., *Vacuum Technology: Practical Heat Treating and Brazing*, ed. A. International. 1993. 179.
139. Angelo, P.C., Subramanian, R., *Powder Metallurgy: Science, Technology and Applications (Easter economy edition)*. 2008, New Delhi: PHI Learning Pvt Ltd. 312.
140. German, r.M., Olevsky, E.A., *Modeling grain growth dependence on the liquid content in liquid-phase-sintered materials.* Metallurgical and Materials Transactions A, 1998. **29**: p. 3057-3067.
141. Fang, Z.Z., Wang, H., *Densification and grain growth during sintering of nanosized particles.* International Materials Reviews, 2008. **53**(6): p. 326-352.
142. Voorhees, P.W., Schaefer, R.J., *In situ observation of particle motion and diffusion interactions during coarsening.* Acta Metallurgica, 1987. **35**(2): p. 327-339.
143. German, R.M., *Liquid Phase Sintering*. 1985, New York: Springer. 240.
144. Rahimian, M., Ehsani, N., Parvin, N., Baharvandi, H.R., *The effect of particle size, sintering temperature and sintering time on the properties of Al-Al2O3 composites made by powder metallurgy.* Journal of Materials Processing Technology, 2009. **209**: p. 5387-5393.
145. Yuan, G.C., Li, Z.J., Lou, X.Y., Zhang, X.M., *Study on crystallization and microstructure for new series of Al-Sn-Si alloys.* Materials Science and Engineering A, 2000. **280**: p. 108-115.
146. Arribas, I., Martín, J.M., Castro, F., *The initial stage of liquid phase sintering for an Al-14Si-2.5Cu-0.5Mg (wt%) P/M alloy.* Materials Science and Engineering A, 2010. **527**: p. 3949-3966.
147. Farzin Nia, F., Davies, B.L., *Production of Al-Cu and Al-Cu-Si alloys by PM methods.* Powder Metallurgy, 1982. **25**(4): p. 209-215.
148. Murray, J.L., *Al-Cu (Aluminum - Copper)*, in *ASM Metals Handbook Volume 3 - Alloy Phase Diagrams*. 1992, ASM International. p. 1762.
149. Heard, D.W., Donaldson, I.W., Bishop, D.P., *Metallurgical assessment of a hypereutectic aluminum-silicon P/M alloy.* Journal of Materials Processing Technology, 2009. **209**: p. 5902-5911.
150. Dhokey, N.B., Athavale, V.A., Narkhede, N., Kamble, M., *Effect of processing conditions on transient liquid phase sintering of premixed aluminium alloy powders.* Advanced Materials Letters, 2013. **4**(3): p. 235-240.
151. Massalski, T.B., *Binary Alloy Phase Diagrams*. Vol. 1. 1986: American Society for Metals.
152. King, F., *Aluminum and its alloys*. 1987, New York: Ellis Horwood Limited.
153. Gupta, M., Ling, S., *Microstructure and mechanical properties of hypo/hyper-eutectic Al-Si alloys synthesized using a near-net shap forming technique.* Journal of Alloys and Compounds, 1999. **287**: p. 284-294.
154. McAlister, A.J., Kahan, D.J., *Al-Sn (Aluminum-Tin)*, in *ASM Metals Handbook Volume 3 - Alloy Phase Diagrams*, A. International, Editor. 1983, ASM International. p. 327.
155. *Springer Materials: The Landolt-Börnstein Database*.
156. Kondoh, K., Kimura, A., Watanabe, R., *Effect of Mg on sintering phenomenon of aluminium alloy powder particle.* Powder Metallurgy, 2001. **44**(2): p. 161-164.

157. Sercombe, T.B., Schaffer, G.B., *On the role of tin in the nitridation of aluminium powder.* Scripta Materialia, 2006. **55**(4): p. 323-326.
158. Li, J.G., Chatain, D., Coudurier, L., Eustathopoulos, *Wettability of sapphire by Sn-Al alloys.* Journal of Materials Science Letters, 1988. **7**(9): p. 961-963.
159. Sercombe, T.B., Schaffer, G.B., *The effect of trace elements on the sintering of Al-Cu alloys.* Acta Materialia, 1999. **47**(2): p. 689-697.
160. Dean, R.R., Evans, C.J., *Plain bearing materials: the role of tin.* Tribology International, 1976. **9**(3): p. 101-108.
161. Lepper, K., James, M., Chashechkina, J., Rigney, D.A., *Sliding behavior of selected aluminium alloys.* Wear, 1997. **203-204**: p. 46-56.
162. Desaki, T., Kamiya, S., *Development of a new aluminum alloy bearing for small-sized diesel engines.* Japan Society of Automotive Engineers, 2000. **21**: p. 143-147.
163. Kumada, Y., Hashizume, K., Kimura, Y., *Performance of plain bearings with circumferential microgrooves.* Tribology Transactions, 1996. **39**(1): p. 81-86.
164. Ratke, L., Ågren, J., Ludwig, A., Babette, T., Gránásy, L., Mathiesen, R., Arnberg, L., Anger, G., Reifenhäuser, B., Lauer, M., Garen, R., Gust, E. *Lead-free bearing alloys for engine applications*. in *Microgravity applications programme: successful teaming of science and industry*. 2005. Noordwijk: ESA Publications Division.
165. Marrocco, T., Driver, L.C., Harris, S.J., McCartney, D.G., *Microstructure and properties of thermallly sprayed Al-Sn-based alloys for plain bearing applications.* Journal of Thermal Spray Technology, 2006. **15**(4): p. 634-639.
166. Stuczynski, T., *Metallurgical problems associated with the production of aluminium-tin alloys.* Materials and Design, 1997. **18**(4): p. 369-372.
167. Polmear, I.J., *Wrought Aluminium Alloys*, in *Light Alloys: From Traditional Alloys to Nanocrystals 4th Edition*. 2005, Butterworth Heinemann: Melbourne, Australia. p. 193-195.
168. Abis, S., Onofrio, G., Signorelli, E., *New bearing Al-based alloys: evolution of advanced materials.* Associazione Italiana Di Metallurgica, 1989: p. 511-516.
169. Liu, X., Zeng, M.Q., Ma, Y., Zhu, M., *Melting behaviour and the correlation of Sn distribution on hardness in a nano-structured Al-Sn alloy.* Materials Science and Engineering A, 2009. **506**: p. 1-7.
170. Munda, P., Dube, R.K., Basu, B., Koria, S.C., *Friction and wear properties of steel backed Al-10Sn-4Si-1Cu metallic strips prepared via spray atomization-deposition-rolling route.* Surface & Coatings Technology, 2009. **203**: p. 3541-3548.
171. Tripathy, M.R., Dube, R.K., Koria, S.C., *Rolling behaviour of steel backed spray deposited Al-Sn strip.* Journal of Materials Processing Technology, 2007. **190**: p. 342-349.
172. Söderberg, S., *On fretting maps.* Wear, 1988. **126**(2): p. 131-147.
173. Fukuoka, T. *Fatigue and life of plain bearings under alternating and rotating loads*. in *Proceedings of the Japanese Society of Lubrication Engineers International Tribology Conference*. 1985. Tokyo, Japan: Elsevier.
174. Kopeliovich, D., *Requirements to Engine Bearing Materials*, SubsTech, Editor. 2012.
175. Pratt, G.C., *Materials for plain bearings.* International Metallurgical Reviews, 1973. **18**(2): p. 62-88.
176. Torabian, H., Pathak, J.P., Tiwari, S.N., *On wear characteristics of leaded aluminium-silicon alloys.* Wear, 1994. **177**(1): p. 47-54.
177. Desaki, T., Kamiya, S., Sato, K., Okauchi, Y., Nukami, T., *Aluminum alloy for sliding bearing and its production method*, J. Toyota, Editor. 2004, Taiho Kogyo Co., Ltd. & Toyota Jidosha Kabushiki Kaisha: USA.
178. Segal, V.M., *Materials processing by simple shear.* Materials Science and Engineering A, 1995. **197**: p. 157-164.

179. Horita, Z., Fujinami, T., Langdon, T.G., *The potential for scaling ECAP: effect of sample size on grain refinement and mechanical properties.* Materials Science and Engineering A, 2001. **318**: p. 34-41.
180. Srinivasan, R., Cherukuri, B., Chaudhury, P.K., *Scaling up of equal channel angular pressing (ECAP) for the production of forging stock.* Materials Science Forum, 2006. **503-504**: p. 371-378.
181. Stolyarov, V.V., Zhu, Y.T., Raab, G.I., Zharikov, A.I., Valiev, R.Z., *Effect of initial microstructure on the microstructural evolution and mechanical properties of Ti during cold rolling.* Materials Science and Engineering A, 2004. **385**(1-2): p. 309-313.
182. Langdon, T.G., *The principles of grain refinement in equal-channel angular pressing.* Materials Science and Engineering A, 2007. **462**: p. 3-11.
183. Xia, K., *Bulk ultrafine and nanostructured materials from consolidation of particles by severe plastic deformation.* Materials Science Forum, 2008. **579**: p. 61-74.
184. Valiev, R.Z., Krasilnikov, N.A., Tsenev, N.K., *Plastic deformation of alloys with submicron-grained structure.* Materials Science and Engineering A, 1991. **137**: p. 35-40.
185. Verlinden, B. *Severe Plastic Deformation of Metals*. in *2nd International Conference: Deformation Processing and Structure of Materials*. 2005. Belgrade, Serbia and Montenegro.
186. Iwahashi, Y., Wang, J., Horita, Z., Nemoto, M., Langdon, T. G., *Principle of equal-channel angular pressing for the processing of ultra-fine grained materials.* Scripta Materialia, 1996. **35**(2): p. 143-146.
187. Lee, D.N., *An upper-bound solution of channel angular deformation.* Scripta Materialia, 2000. **43**(2): p. 115-118.
188. Aida, T., Matsuki, K., Horita, Z., Langdon, T.G., *Estimating the equivalent strain in equal-channel angular pressing.* Scripta Materialia, 2001. **44**(4): p. 575-579.
189. Furuno, K., Akamatsu, H., Oh-ishi, K., Furukawa, M., Horita, Z., Langdon, T.G., *Microstructural development in equal channel angular pressing using a 60° die.* Acta Materialia, 2004. **52**: p. 2497-2507.
190. Gedeon, M., *Grain size and material strength.* Technical Tidbits, 2010(15): p. 1-2.
191. Gedeon, M., *Material Yielding.* Technical Tidbits, 2000. **2**(8): p. 2-4.
192. Ashby, M.F., Jones, D.R.H., *Engineering Materials 1*. 2 ed. 1996, Oxford: Butterworth-Heinemann. 306.
193. Valiev, R.Z., *Structure and mechanical properties of ultrafine-grained metals.* Materials Science and Engineering A, 1997. **234-236**: p. 59-66.
194. Asushima, A. *Trend of ultrafine grained steel*. in *Proceedings of the 245th Symposium on Technology of Plasticity*. 2003. Japan.
195. Azushima, A., Kopp, R., Korhonen, A., Yang, D.Y., Micari, F., Lahoti, G.D., Groche, P., Yanagimoto, J., Tsuji, N., Rosochowski, A., Yanagida, A., *Severe plastic deformation (SPD) for metals.* CIRP Annuals - Manufacturing Technology, 2008. **57**: p. 716-735.
196. Humphreys, F.J., *Review: Grain and subgrain characterisation by electron backscatter diffraction.* Journal of Materials Science, 2001. **3**(6): p. 3833-3854.
197. Instruments, O., *Introduction to EBSD*. 2013.
198. Xu, C., Horita, Z., Langdon, T.G., *Microstructural evolution in an aluminum solid solution alloy processed by ECAP.* Materials Science and Engineering A, 2011. **528**: p. 6059-6065.
199. Nakashima, K., Horita, Z., Nemoto, M., Langdon, T., *Development of a multi-pass facility for equal-channel angular pressing to high total strains.* Materials Science and Engineering A, 2000. **281**: p. 82-87.
200. Lee, S., Langdon, T.G., *Influence of equal-channel angular pressing on the superplastic properties of commercial aluminum alloys.* MRS Proceedings, 1999. **601**: p. 359-364.

201. Nakashima, K., Horita, Z., Nemoto, M., Langdon, T., *Influence of channel angle on the development of ultrafine grains in equal-channel angular pressing.* Acta Materialia, 1998. **46**(5): p. 1589-1599.
202. Semiatin, S.L., Segal, V.M., Goforth, R.E., Frey, N.D., DeLo, D.P., *Workability of commercial-purity titanium and 4340 steel during equal channel angular extrusion at cold working temperatures.* Metallurgical and Materials Transactions A, 1999. **30**(5): p. 1425-1435.
203. Akata, H.E., *Application of separated die design to production of ECAP dies.* Advanced Materials Research, 2012. **445**: p. 120-124.
204. Shan, A., Moon, I.-G., Park, J.-W., *Estimation of friction during equal channel angular (ECA) pressing of aluminium alloys.* Journal of Materials Processing Technology, 2002. **122**: p. 255-259.
205. Pei, Q.X., Hu, B.H., Lu, C., Wang, Y.Y., *A finite element study of the temperature rise during equal channel angular pressing.* Scripta Materialia, 2003. **49**: p. 303-308.
206. Srinivasan, R., *Computer simulation of the equichannel angular extrusion (ECAE) process.* Scripta Materialia, 2001. **44**: p. 91-96.
207. Suh, J.-Y., Kim, H.-S., Park, J.-W., Chang, J.-Y., *Finite element analysis of material flow in equal channel angular pressing.* Scripta Materialia, 2001. **44**: p. 677-681.
208. Prangnell, P.B., Harris, C., Roberts, S.M., *Finite element modelling of equal channel angular extrusion.* Scripta Materialia, 1997. **37**(7): p. 983-989.
209. Lapovok, R.Y., *The role of back-pressure in equal channel angular extrusion.* Journal of Materials Science, 2005. **40**: p. 341-346.
210. Berbon, P.B., Furukawa, M., Horita, Z., Nemoto, M., Langdon, T.G., *Influence of pressing speed in microstructural development in equal-channel angular pressing.* Metallurgical and Materials Transactions A, 1999. **30**: p. 1989-1994.
211. Yamashita, A., Yamaguchi, D., Horita, Z., Langdon, T.G., *Influence of pressing temperature on microstructural development in equal-channel angular pressing.* Materials Science and Engineering A, 2000. **287**: p. 100-106.
212. Chen, Y.C., Huang, Y.Y., Chang, C.P., Kao, P.W., *The effect of extrusion temperature on the development of deformation microstructures in 5052 aluminium alloy processed by equal channel angular extrusion.* Acta Materialia, 2003. **51**: p. 2005-2015.
213. Goloborodko, A., Sitdikov, O., Kaibyshev, R., Miura, H., Sakai, T., *Effect of pressing temperature on fine-grained structure formation in 7475 aluminum alloy during ECAP.* Materials Science and Engineering A, 2004. **381**: p. 121-128.
214. Wang, Y.Y., Sun, P.L., Kao, P.W., Chang, C.P., *Effect of deformation temperature on the microstructure developed in commercial purity aluminum processed by equal channel angular extrusion.* Scripta Materialia, 2004. **50**: p. 613-617.
215. Balog, M., Simancik, F., Bajana, O., Guillermo, R., *ECAP vs. direct extrusion- techniques for consolidation of ultra-fine Al particles.* Materials Science and Engineering A, 2009. **504**: p. 1-7.
216. Semiatin, S.L., Delo, D.P., Shell, E.B., *The effect of material properties and tooling design on deformation and fracture during equal channel angular extrusion.* Acta Materialia, 2000. **48**(8): p. 1841-1851.
217. Wu, Y., Baker, I., *An experimental study of equal channel angular extrusion.* Scripta Materialia, 1997. **37**(4): p. 437-442.
218. DeLo, D.P., Semiatin, S.L., *Finite-element modeling of nonisothermal equal-channel angular extrusion.* Metallurgical and Materials Transactions A, 1999. **30**(5): p. 1391-1402.
219. Valiev, R.Z., Alexandrov, I.V., Zhu, Y.T., Lowe, T.C., *Paradox of strength and ductility in metals processed by severe plastic deformation.* Journal of Materials Research, 2002. **17**(1): p. 5-8.
220. Mani, B., Jahedi, M., Paydar, M.H., *Consolidation of commercial pure aluminum powder by torsional-equal channel angular pressing (T-ECAP) at room temperature.* Powder Technology, 2012. **219**: p. 1-8.

221. Matsuki, K., Aida, T., Takeuchi, T., Kusui, J., Yokoe, K., *Microstructural characteristics and superplastic-like behavior in aluminum powder alloy consolidated by equal-channel angular pressing.* Acta Materialia, 2000. **48**: p. 2625-2632.
222. Derakhshandeh. H, R., Jenabali Jahromi, A., *An investigation on the capability of equal channel angular pressing for consolidation of aluminum and aluminum composite powder.* Materials and Design, 2011. **32**: p. 3377-3388.
223. Xia, K., Wu, X., *Back pressure equal channel angular consolidation of pure Al particles.* Scripta Materialia, 2005. **53**: p. 1225-1229.
224. Xu, W., Wu, X., Honma, T., Ringer, S.P., Xia, K., *Nanostructured Al-Al2O3 composite formed in situ during consolidation of ultrafine Al particles by back pressure equal channel angular pressing.* Acta Materialia, 2009. **57**(14): p. 4321-4330.
225. Xu, W., Honma, T., Wu, X., Ringer, S.P., Xia, K., *High strength ultrafine/nanostructured aluminum produced by back pressure equal channel angular processing.* Applied Physics Letters, 2007. **91**: p. 031901.
226. Lapovok, R., Tomus, D., Muddle, B.C., *Low-temperature compaction of Ti-6Al-4V powder using equal channel angular extrusion with back pressure.* Materials Science and Engineering A, 2008. **490**(1-2): p. 171-180.
227. Wu, X., Xu, W., Xia, K., *Pure aluminum with different grain size distributions by consolidation of particles using equal-channel angular pressing with back pressure.* Materials Science and Engineering A, 2008. **493**: p. 241-245.
228. Nieh, T.G., Luo, P., Nellis, W., Lesuer, D., Benson, D., *Dynamic compaction of aluminum nanocrystals.* Acta Materialia, 1996. **44**(9): p. 3781-3788.
229. Gupta, N., Ravisankar, B., Kumaran, *Densification of Al-2024 and Al-2024/Al2O3 powders by conventional P/M route and ECAP: a comparative study.* Transactions - Indian Institute of Metals, 2012. **65**(4): p. 381-386.
230. Haghighi, R.D., Jahromi, S.A.J., Moresedgh, A., Khorshid, M.T., *A comparison between ECAP and conventional extrusion for consolidation of aluminum metal matrix composite.* Journal of Materials Engineering and Performance, 2012. **21**(9): p. 1885-1892.
231. Nagasekhar, A.V., Tick-Hon, Y., Ramakanth, K.S., *Mechanics of single pass equal channel angular extrusion of powder in tubes.* Applied Physics A, 2006. **85**(2): p. 185-194.
232. Lapovok, R., *Damage evolution under severe plastic deformation.* International Journal of Fracture, 2002. **115**(2): p. 159-172.
233. Wang, X., Xue, K., Li, P., Wu, Z., Li, Q., *Equal channel angular pressing and torsion of pure al powder in tubes.* Advanced Materials Research, 2010. **97-101**: p. 1109-1115.
234. Paydar, M.H., Reihanian, M., Bagherpour, E., Sharifzadeh, M., Zarinejad, M., Dean, T.A., *Equal channel angular pressing-forward extrusion (ECAP-FE) consolidation of Al particles.* Materials and Design, 2009. **30**: p. 429-432.
235. Pieczonka, T., Schubert, T., Baunack, S., Kieback, B., *Dimensional behaviour of aluminium sintered in different atmospheres.* Materials Science and Engineering A, 2008. **478**: p. 251-256.
236. Gökçe, A., Findik, F., *Mechanical and physical properties of sintered aluminium powders.* Journal of Achievements in Materials and Manufacturing Engineering, 2008. **30**(2): p. 157-164.
237. Walker, R., *SI Water*. 2011.
238. Technologies, P., *Metallographic Etchants - Aluminium*. 2010.
239. Zaidi, M.A., *Microstructure of rapidly solidified aluminum alloy powders for elevated temperature applications.* Materials Science and Engineering, 1988. **98**: p. 221-226.
240. Mehrotra, S.P., *Mathematical modelling of gas atomization process for metal powder production.* Powder Metallurgy International, 1981. **13**: p. 80-85.
241. Narayanan, R.G., *Powder Metallurgy - basics and applications*. 2013: Guwahati.

242. Pickens, J.R., *Conventional Aluminium Powder Metallurgy Alloys*, in *ASM Handbook - Powder Metal Technologies and Applications*, A. International, Editor. 1998, ASM International. p. 2083-2095.
243. Wu, Y., Kim, G.-Y., *Compaction behavior of Al6061 powder in the semi-solid state.* Powder Technology, 2011. **214**(2): p. 252-258.
244. Brandes, E.A., Brook, G.B., *Mechanical Properties of Aluminium and Aluminium alloys*, in *Smithells Metals Reference Book Seventh Edition*, E.A. Brandes, Brook, G.B., Editor. 1992, Butterworth-Heinemann: Oxford. p. 22-1 to 22-26.
245. Ashby, M.F., Jones, D.R.H., *Engineering Materials 2*. 2 ed. 1998, Oxford: Butterworth-Heinemann. 381.
246. AALCO, *Technical Information - Aluminium Alloy // Commercial Alloy // 1050 H14*. 2013.
247. Munir, Z.A., *Surface oxides and sintering of metals.* Powder Metallurgy, 1981. **4**: p. 177-180.
248. Guo, R.Q., Rohatgi, P.K., *Preparation of aluminium-fly ash particulate composite by powder metallurgy technique.* Journal of Materials Science, 1997. **32**: p. 3971-3974.
249. Schaffer, G.B., Hall, B.J., *The influence of the atmosphere on the sintering of aluminum.* Metallurgical and Materials Transactions A, 2002. **33**(10): p. 3279-3284.
250. Cama, H., Ricks, R., Hamerton, R., Humphreys, J., *Recovery: Introduction*, U.o. Liverpool, Editor. 2001-2010, aluMATTER: Liverpool.
251. Lambe, D., *Recovery, Recrystallisation & Grain Growth*. 2013.
252. Humphreys, F.J., Hatherly, M., *Recrystallisation and Related Annealing Phenomena*. 1995, Great Yarmouth: Pergamon.
253. Galanty, M., Kazanowski, P., Kansuwan, P., Misiolek, W.Z., *Consolidation of metal powders during the extrusion process.* Journal of Materials Processing Technology, 2002. **125-126**: p. 491-496.
254. Esawi, A.M.K., Borady, M.E., *Carbon nanotube-reinforced aluminium strips.* Composites Science and Technology, 2008. **68**(2): p. 486-492.
255. Bidulská, J., Kvačkaj, T., Bidulský, R., Actis Grande, M., *The porosity evaluation during ECAP in aluminium PM alloy.* Acta Physica Polonica A, 2012. **122**(3): p. 553-556.
256. Perepezko, J.H., Sebright, J.L., Höckel, P.G., Wilde, G., *Undercooling and solidification of atomized liquid droplets.* Materials Science and Engineering A, 2002. **326**: p. 144-153.
257. Murakami, Y., *Aluminum-based alloys.* Materials Science and Technology, 1996. **8**: p. 213-276.
258. Alumatter, *Hardness*. 2008.
259. AluMATTER, *Quench sensitivity*. 2013.
260. Chiang, C.-H., Tsao, C.Y.A., *Si coarsening of spray-formed high loading hypereutectic Al-Si alloys in the semisolid state.* Materials Science and Engineering A, 2005. **396**: p. 263-270.
261. Lee, K., Kwon, Y.N., Lee, S., *Effects of eutectic silicon particles on tensile properties and fracture toughness of A356 aluminum alloys fabricated by low-pressure-casting, casting-forging, and squeeze-casting processes.* Journal of Alloys and Compounds, 2008. **461**: p. 532-541.
262. So, H., Li, W.C., Hsieh, H.K., *Assessment of the powder extrustion of silicon-aluminium alloy.* Journal of Materials Processing Technology, 2001. **114**(1): p. 18-21.
263. Martín, J.M., Castro, F., *Sintering response & microstructural evolution of an Al-Cu-Mg-Si premix.* International Journal of Powder Metallurgy, 2007. **43**(6): p. 59-69.
264. Metals, K.t., *Precipitation hardening of aluminium alloys*. 2010.
265. Sinha, A.K., *Powder Metallurgy*. 1995, New Delhi: Dhanpat Rai & Sons.